COMPARATIVE KBOLOGY: USING SURFACE SPECTRA OF TRITON, PLUTO, AND CHARON TO INVESTIGATE ATMOSPHERIC, SURFACE, AND INTERIOR PROCESSES ON KUIPER BELT OBJECTS

by

BRYAN JASON HOLLER

B.S., Astronomy (High Honors), University of Maryland, College Park, 2012

B.S., Physics, University of Maryland, College Park, 2012

M.S., Astronomy, University of Colorado, 2015

A thesis submitted to the

Faculty of the Graduate School of the

University of Colorado in partial fulfillment

of the requirement for the degree of

Doctor of Philosophy

Department of Astrophysical and Planetary Sciences

2016

This thesis entitled:
Comparative KBOlogy: Using spectra of Triton, Pluto, and Charon to investigate atmospheric, surface, and interior processes on KBOs
written by Bryan Jason Holler
has been approved for the Department of Astrophysical and Planetary Sciences

_____
Dr. Leslie Young

_____
Dr. Fran Bagenal

Date_____

The final copy of this thesis has been examined by the signatories, and we find that both the content and the form meet acceptable presentation standards of scholarly work in the above mentioned discipline.

ABSTRACT

Holler, Bryan Jason (Ph.D., Astrophysical and Planetary Sciences)

Comparative KBOlogy: Using spectra of Triton, Pluto, and Charon to investigate atmospheric, surface, and interior processes on KBOs

Thesis directed by Dr. Leslie Young

This thesis presents analyses of the surface compositions of the icy outer Solar System objects Triton, Pluto, and Charon. Pluto and its satellite Charon are Kuiper Belt Objects (KBOs) while Triton, the largest of Neptune's satellites, is a former member of the KBO population. Near-infrared spectra of Triton and Pluto were obtained over the previous 10+ years with the SpeX instrument at the IRTF and of Charon in Summer 2015 with the OSIRIS instrument at Keck. The Charon data were reduced by spectrophotometry using code that I wrote for this purpose. I present evidence of short-term volatile transport and the presence of the non-methane hydrocarbon ethane on Pluto and Triton, as well as uniform temperature and ammonia ice distributions on Charon. Based on previous laboratory work and the results of my analysis, I conclude that cryovolcanism is not necessary to explain the high percentage of crystalline water ice on Charon. The three "geologic" bodies, those previously visited by spacecraft, provide context for understanding the larger population of KBOs, the "astronomical" bodies that may never be visited by spacecraft. Observations of the geologic bodies can be used to better understand the atmospheric, surface, and interior processes on all KBOs through what I term "comparative KBOlogy." Next-generation observatories, both in space and on the ground, will further contribute to our knowledge of the dominant processes that shape the surface evolution of KBOs.

To Leslie:

For giving me a chance.

ACKNOWLEDGMENTS

Thesis: I would like to take this first sentence to thank my wife, Kelsey, for her tolerance over the past few years, especially during the late nights, early mornings, weird sleep schedules, 40 straight days in Hawaii, and the last few weeks of writing this thesis. My parents have encouraged my interest in astronomy since that fateful trip to the public library back in August 2003. My grandfather, a World War II veteran, had the courage and forethought to go to college on the G.I. Bill after the war ended, and was the first Holler to earn a college degree. My aunt was the first Holler to earn her Masters, and I am proud to continue the legacy with this thesis. I do not envy my children, who will need two PhDs to keep the trend going. There are many other people to thank for helping me get to this point, certainly more than would be proper to include here, but I will do it anyway: Susan Armstrong, Fran Bagenal, Gerbs Bauer, Rick Binzel, Dave Brain, Marc Buie, Mark Bullock, Bonnie Buratti, Marsha Burch, Bobby Bus, Bryan Butler, Nancy Chanover, Jason Cook, Dale Cruikshank, Jeremy Darling, Francesca DeMeo, Larry Esposito, Will Grundy, Michelle Hamernik, Tim Lister, Jim Lyke, Steve Mojzsis, Cathy Olkin, Silvia Protopapa, Henry Roe, Amanda Sickafoose, John Stansberry, Alan Stern, Stephen Tegler, Henry Throop, Chad Trujillo, Anne Verbiscer, Eliot Young, and Leslie Young. And finally, a great big “thank you” to all the new friends and colleagues I made here in Boulder. You guys helped keep me sane. It’s been real. It’s been fun. Sometimes it’s even been real fun.

Chapter II: We graciously thank the staff of the IRTF for their assistance over the past 12+ years, especially, W. Golisch, D. Griep, P. Sears, E. Volquardsen, J. T. Rayner, A. T. Tokunaga, and B. Cabreira. A special thanks to the reviewers whose comments significantly improved this paper. We wish to recognize and acknowledge the significant cultural role and reverence of the summit of Mauna Kea within the indigenous Hawaiian community and to express our appreciation for the opportunity to observe from this special mountain. This work was funded by NASA PAST NNX13AG06G and NASA NESSF 14-PLANET14F-0045.

Chapter III: The authors would like to specially thank Bobby Bus for his illuminating questions and advice during the 2013 DPS poster session. Mark Bullock deserves a special thanks for adding an extra and necessary dimension to the evaluation of the results of this paper. We graciously thank the staff of the IRTF for their assistance over the past 13 years, especially W. Golisch, D. Griep, P. Sears, E. Volquardsen, J.T. Rayner, A.T. Tokunaga, and B. Cabreira. We wish to recognize and acknowledge the significant cultural role and reverence of the summit of Mauna Kea within the indigenous Hawaiian community and to express our appreciation for the opportunity to observe from this special mountain. Special thanks also to Fran Bagenal, Dale Cruikshank, Francesca DeMeo, Stephen Tegler, and Eliot Young for guidance and advice. Many thanks to the two reviewers for their perceptive comments that were used to significantly strengthen the arguments made in this paper. This work was funded by NASA PAST NNX13AG06G.

Chapter IV: A very special thanks to everyone who was part of the schedule reorganization in July 2015, including S. Dahm, A. Howard, C. Jordan, H. Knutson, G. Marcy, and M. Rich. We would also like to thank the Support Astronomers and Observing Assistants at the W. M. Keck Observatory, without whom this work would not have been possible: R. Campbell, S. Dahm, G. Doppman, H. Hershey, J. McIlroy, J. Rivera, and H. Tran. Bobby Bus and Rick Binzel provided useful advice for ensuring an effective telluric correction. The data presented herein were obtained at the W.M. Keck Observatory, which is operated as a scientific partnership among the California Institute of Technology, the University of California, and the National Aeronautics and Space Administration. The Observatory was made possible by the generous financial support of the W.M. Keck Foundation. A portion of the data presented herein were obtained using the UCI Remote Observing Facility, made possible by a generous gift from John and Ruth Ann Evans. We wish to recognize and acknowledge the significant cultural role and reverence of the summit of Mauna Kea within the indigenous Hawaiian community and to express our appreciation for the opportunity to observe from this special mountain. This work was funded by NASA PAST NNX13AG06G, NASA NESSF 14-PLANET14F-0045, and NASA NESSF 15-PLANET15R-0023.

CONTENTS

TABLES

CHAPTER II

Table

CHAPTER III

Table

CHAPTER IV

Table

FIGURES

CHAPTER I

Figure

CHAPTER II

Figure

CHAPTER III

Figure

CHAPTER IV

Figure

CHAPTER I

INTRODUCTION

A Short History of Outer Solar System Studies

At the cutting edge of planetary science is the study of Kuiper Belt Objects (KBOs), a disk of bodies composed of rock and ice found beyond the orbit of Neptune (>30 AU). This diverse population of objects provides valuable information in regards to Solar System formation and evolution, chemical and physical processes at low temperature, and the origins of life. Over 1500 KBOs have been identified since the discovery of the first, Pluto, in 1930. This story of ongoing discovery does not begin with Pluto, however, but instead with Sir William Herschel.

The Discovery of Uranus, Neptune, and Triton. The word "planet" is derived from the Ancient Greek word for "wanderer," an accurate description for the movement of Solar System objects against the background stars as seen from Earth. It was on the night of March 13, 1781 that Sir William Herschel serendipitously discovered the first celestial wanderer since antiquity, Uranus. After years of astrometry to improve the calculation of Uranus' orbit, discrepancies in the predicted and measured locations of Uranus were noticed. Two mathematicians, John Couch Adams of Great Britain and Urbain Jean Joseph Le Verrier of France, independently determined that an unseen planet was gravitationally influencing the orbit of Uranus. British and French astronomers were largely uninterested in following up on the predictions of Adams and Le Verrier, so the latter contacted Johann Galle at the Berlin Observatory to undertake a search for a new planet.

Galle, together with Heinrich D'Arrest, discovered Neptune on September 23, 1846 (Herschel, 1846). Shortly thereafter, on October 10, 1846, William Lassell discovered the largest moon of Neptune, Triton, in a synchronous, retrograde orbit (Lassell, 1846). The presence of Triton allowed for a calculation of Neptune's mass and a correction to Uranus' orbit. The Solar System was once again orderly and predictable, at least for a little while.

Discovery of Pluto. Percival Lowell became interested in the possibility of a trans-Neptunian planet around the turn of the 20th century (Hoyt, 1980). Further discrepancies in the position of Uranus had been identified that were not attributable to Neptune, based on the value of its mass known at that time. Lowell began a campaign to search for what he called "Planet X." He passed away in 1916 without discovering Planet X and the project was largely forgotten until 1929 when Vesto Slipher, the director of Lowell Observatory, hired Clyde W. Tombaugh to continue the search. Using a blink comparator to quickly flash images of the same location of sky from different nights (Fig. 1), Tombaugh discovered Pluto on February 18, 1930 (Slipher, 1930). The elusive Planet X had been found, and Pluto's mass was assumed to be large enough to account for Uranus' orbital discrepancies.

Discovery of Charon. It was not until 1978, nearly a half-century after the discovery of Pluto, that Pluto's mass was accurately calculated. On June 22 of that year, James Christy and Robert Harrington of the U.S. Naval Observatory serendipitously discovered Pluto's largest satellite, Charon (Christy and Harrington, 1978). Charon and Pluto are triply synchronous, meaning that the two

objects' rotation periods and Charon's orbital period are identical (~6.4 days). With approximately 12% of Pluto's mass, Pluto and Charon were known as the "Double Planet" and the system barycenter is found outside Pluto's surface (Tholen et al., 2008). However, Pluto's mass was found to be significantly smaller than needed to perturb Uranus' orbit and was therefore not the alleged Planet X. With the Voyager 2 flyby through the Neptune system in August 1989, the Planet X idea was put to rest with a new, more accurate determination of Neptune's mass (Standish, 1993). But the idea that something else might be orbiting beyond Neptune and Pluto had already piqued the interest of planetary scientists.

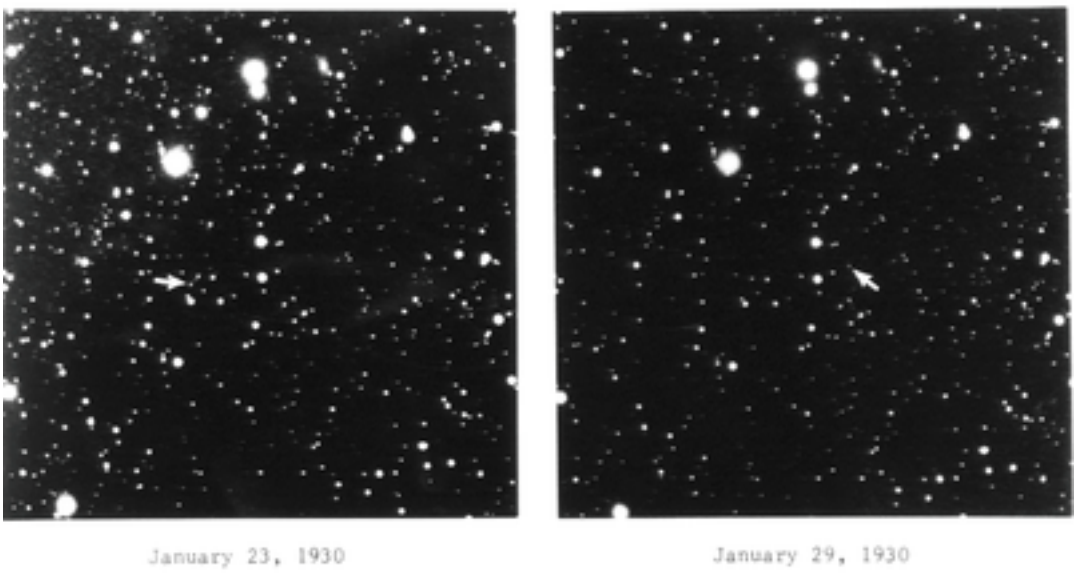

Figure 1: Blink comparator images used by Clyde W. Tombaugh to discover Pluto on March 13, 1930. Tombaugh would have flipped between the two images in the comparator, using his brain's ability of pattern-recognition to identify differences between the two images. The white arrows mark the position of Pluto on two different nights. (Credit: Lowell Observatory Archives)

Kuiper Belt Hypothesis. Qualitative speculation following the discovery of Pluto suggested that Pluto might not be alone in the far reaches of the outer Solar System. The more quantitative work of Kenneth E. Edgeworth and Gerard P. Kuiper in the 1940s and 1950s provided theoretical proof for a disk of icy objects beyond Neptune (Davies et al., 2008). Both argued for the formation of small, icy planetesimals beyond Pluto's orbit where the original solar nebula would have been less dense; the lack of material prevented a larger planet from forming. Due to the pioneering work of both astronomers, this disk is sometimes referred to as the "Edgeworth-Kuiper Belt," but I will continue to refer to it as the more colloquial "Kuiper Belt" for the remainder of this document. The object that proved Edgeworth and Kuiper correct was not discovered until 1992. This KBO, 1992 QB_1, is estimated to be only 200 km in diameter, yet revolutionized the field of outer Solar System studies (Jewitt and Luu, 1992). For comparison, Pluto is ~2400 km and Charon is ~1200 km in diameter. According to the IAU Minor Planet Center, as of May 1, 2016, there are 1532 KBOs known in our Solar System, with numerous associated satellites.

The Dwarf Planets. Three other prominent members of the Kuiper Belt are the dwarf planets Eris, Makemake, and Haumea, all discovered by Michael Brown, Chad Trujillo, and David Rabinowitz in the early 2000s (Brown et al., 2005a). In particular, the discovery of Eris, thought at the time to be larger than Pluto, magnified the ongoing debate since 1992 about Pluto's status as a planet, ultimately resulting in its demotion to the newly created "dwarf planet" category. Regardless of

how one labels Pluto, it remains the historically important culmination of a 150-year effort to rectify planetary orbits in the Solar System and an object of continued scientific fascination.

Further Discovery in the Outer Solar System. Now, after nearly a quarter century, the idea of another planet in the outer Solar System has resurfaced. The discovery of long-period KBOs such as Sedna (Brown et al., 2004), 2012 VP_{113}

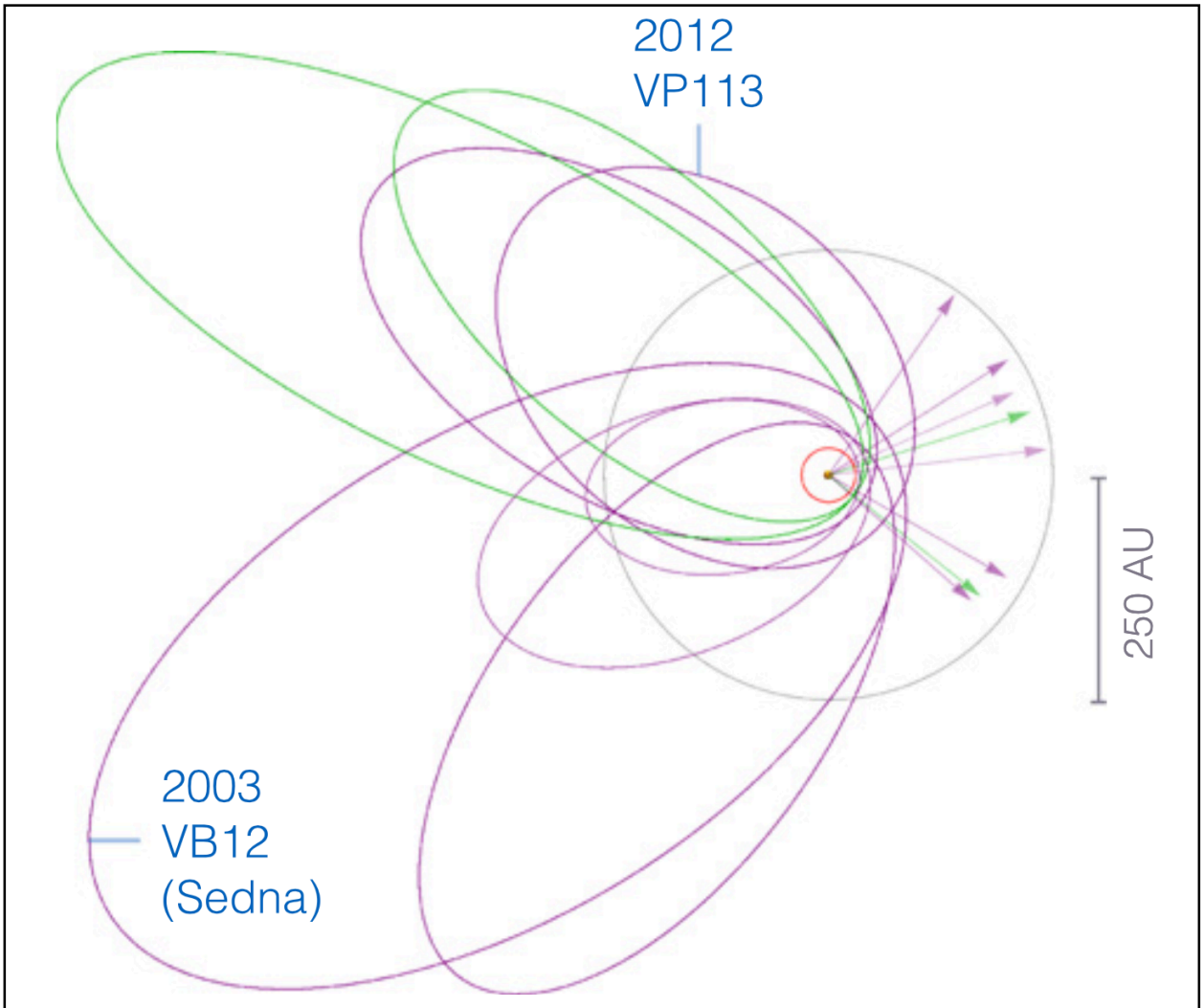

Figure 2: Orbits of all KBOs with semi-major axes greater than 250 AU and dynamically stable KBOs with semi-major axes greater than 150 AU. Note the clustering of arguments of perihelia. (From Batygin and Brown (2016))

(Trujillo and Sheppard, 2014), and others has ushered in a new era in Kuiper Belt studies. The argument of perihelion (the angle between the ascending node, where the orbit crosses the ecliptic plane, and perihelion) of these "detached objects" is similar (Fig. 2). This clustering apparently cannot be explained by chance or observational bias (Batygin and Brown, 2016). Following the same historical pattern that resulted in the discovery of Neptune and Pluto, their work suggests the presence of another planet at an extremely large distance from the Sun. A Uranus- or Neptune-sized planet, orbiting in the same plane as the detached objects and with a longitude of perihelion offset by 180° from those of the detached objects, has been invoked to describe the orbits of these distant KBOs (Batygin and Brown, 2016). The planetary science community is still undecided about the validity of this theory (e.g., Lawler et al., 2016), but the possibility of detecting another planet in our own Solar System is an exciting prospect, and one that carries on the legacy of discovery of the past 250 years.

Overview of the Kuiper Belt

The over 1500 KBOs currently known are a statistically useful population that can be divided into smaller sub-classes based on dynamical behavior. These groups in turn provide boundary conditions for models of Solar System formation. The presence of binary KBOs enables in-depth study of the physical properties of individual objects. Kuiper Belt analogs have even been identified around a handful of other stars, and there is reason to believe that the dynamical, physical, and

chemical processes at work in our Kuiper Belt should apply to those as well. The work of the past quarter century qualifies our Kuiper Belt as the key to understanding the formation and evolution of planetary systems, and is summarized in the following pages.

Dynamical Classification of KBOs. The surface evolution of a KBO can be significantly influenced by its dynamical evolution, especially in terms of the radiation and impact environments. Additionally, the formation circumstances of a KBO are vital to understanding what changes have occurred over the past 4.5 Gyr, and the current dynamical class can provide clues about dynamical evolution and, ultimately, KBO origins. The dynamical scheme proposed by Gladman et al. (2008) defines a Kuiper Belt Object as any minor body with a semi-major axis, a, between 30 and 2000 AU, a perihelion distance, q, greater than 7.5 AU, and a Tisserand parameter with respect to Jupiter, T_J, greater than 3.05. The semi-major axis constraints require the minor body to have an average distance from the Sun between Neptune's orbit (~30 AU) and the Oort Cloud (~2000 AU, though this number is arbitrary). Any object that satisfies the semi-major axis criterion but has a perihelion distance less than 7.5 AU is considered a Centaur. The Tisserand parameter is used to distinguish different kinds of orbits from each other, for example, Main Belt asteroids from Jupiter-family comets (JFCs), and is defined as:

$$T_J = \frac{a_J}{a} + 2cosi\sqrt{\frac{a}{a_J}(1-e^2)}\,, \tag{1}$$

where a_J is the semi-major axis of Jupiter in AU, i is the inclination of the object's orbit in degrees, and e is the eccentricity of the object's orbit. Objects with Tisserand

parameters less than 3.05, likely because of a larger eccentricity, are considered JFCs. With these constraints, the Kuiper Belt is composed of 4 distinct dynamical groups: resonant objects, scattered disk objects, detached objects, and classical KBOs. I will also discuss the special sub-class of the Haumea collisional family.

- **Resonant Objects:** KBOs in mean motion resonance (MMR) with Neptune, meaning that the object and Neptune return to the initial configuration after both completing an integer number of orbits, are an important class of objects: The relative populations of the different resonances may be indicative of the rate of planet migration in the early Solar System (Chiang and Jordan, 2002; Hahn and Malhotra, 2005). Additionally, KBOs in resonance can survive for the age of the Solar System (~4.5 Gyr) in large eccentricity orbits (Gladman et al., 2008) and are protected from close encounters with Neptune (Morbidelli et al., 2008). I adopt the notation of Gladman et al. (2008) for defining resonances as *A*:*B*, where *A* and *B* are the number of orbits completed by the inner (Neptune) and outer (KBO) objects, respectively. The order of the resonance is *A*-*B*, with higher order resonances being less stable unless $e>>1$. The largest resonant population is the Plutinos, named for the most famous member, Pluto. These KBOs are in a 3:2 resonance with Neptune and nominally mark the inner boundary of the classically defined Kuiper Belt. Other notable Plutinos are Orcus, Ixion, and 2003 AZ_{84}. At the outer edge of the classically defined Kuiper Belt are KBOs in the 2:1

resonance with Neptune, sometimes called "twotinos." Other resonant populations with relatively large membership are the 5:3, 7:4, and 5:2 resonances; populated higher-order resonances include 19:9 and 27:4 (Gladman et al., 2008). Fig. 3 shows the distribution and classification of KBOs from 30-73 AU, including those in resonant populations.

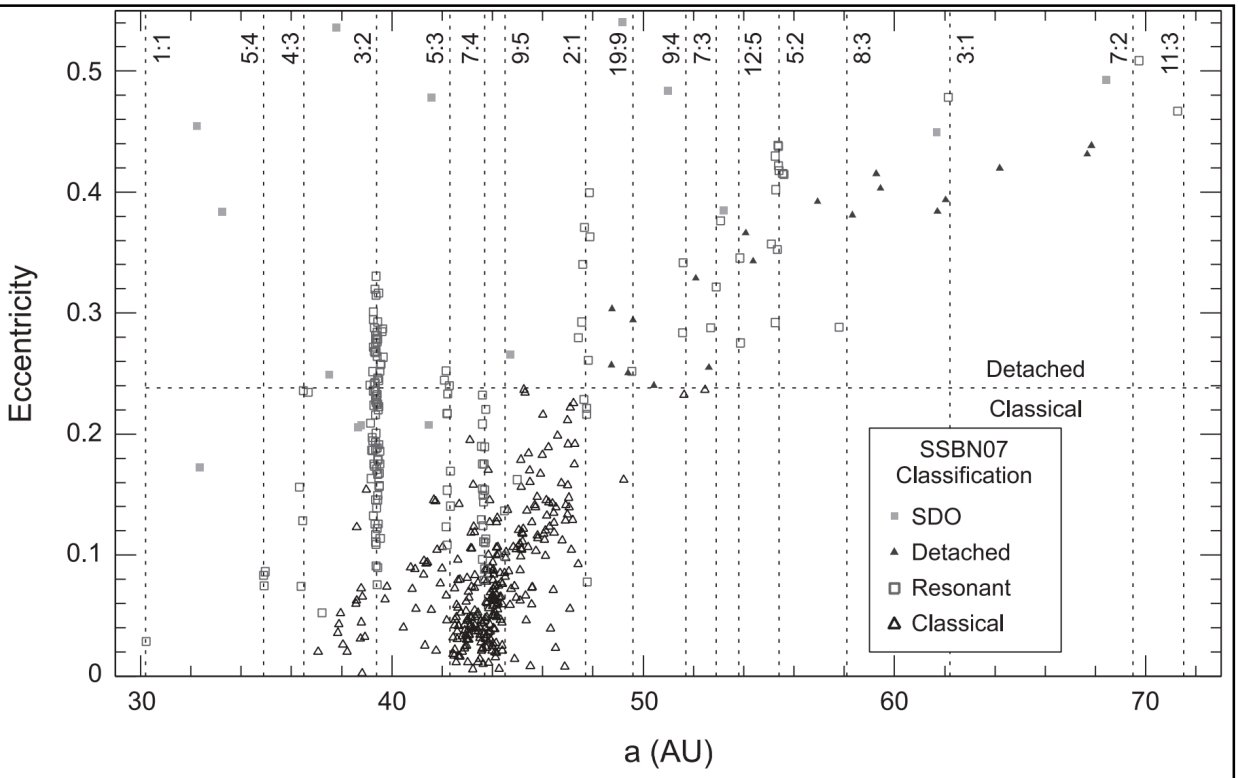

Figure 3: Eccentricity as a function of semi-major axis (a) for all KBOs with semi-major axes between ~30 and ~73 AU known in 2007. The classical definition of the Kuiper Belt is between the 3:2 and 2:1 Neptune resonances (note the higher concentration of objects). Detached objects have semi-major axes beyond the 2:1 resonance and eccentricities greater than 0.24. (From Gladman et al. (2008))

- **Scattered Disk Objects (SDOs):** The SDOs are defined as KBOs that are currently interacting gravitationally with Neptune; in other words, they are currently "scattering" off Neptune. Any KBO with $\Delta a \geq 1.5$ AU in a 10 Myr

orbital integration is considered an SDO (Gladman et al., 2008). These objects are essentially in transition from one population of minor bodies to another: SDOs may be a source population for Centaurs and Oort Cloud objects.

- **Detached Objects:** KBOs with $e \geq 0.24$ and a semi-major axis outside the 2:1 Neptune resonance but still within 2000 AU, beyond which forces external to the Solar System are non-negligible, are considered detached objects (Gladman et al., 2008). The word "detached" refers to Neptune's negligible influence on these objects, and it is uncertain whether this population is composed of former SDOs. Notable examples of detached objects are Eris, and the sednoids Sedna and 2012 VP_{113}. (A sednoid is a KBO with q>50 AU and a>150 AU.) Current theories that explain the existence of this population are the new planet theory of Batygin and Brown (2016) (see *Further Discovery in the Outer Solar System*, pp. 5) and disruption of the outer Kuiper Belt by a passing star (Delsanti and Jewitt, 2006). Detached objects, with their higher eccentricities, experience very different amounts of solar insolation over just one orbit, possibly providing the opportunity to study the formation and collapse of KBO atmospheres.

- **Classical KBOs:** Any KBOs not included in the previous 3 categories are considered to be part of the classical Kuiper Belt. These objects make up the

largest fraction of the 1532 known KBOs and due to their large numbers sub-classes have been identified. The classical belt can be divided into three regions based on semi-major axis (Gladman et al., 2008): the inner belt (30 AU<a<39.4 AU), main belt (39.4 AU<a<48.4 AU), and the outer belt (48.4 AU<a<2000 AU). All classical KBOs have eccentricities less than 0.24. The semi-major axes of KBOs in the 3:2 and 2:1 resonances are 39.4 AU and 48.4 AU, respectively. As seen in Fig. 3, a majority of the classical KBOs reside in the main belt and are sometimes referred to as "cubewanos" after the first classical KBO discovered, 1992 QB_1.

A separate division of the classical KBOs is based on orbital inclination. Dynamically hot classicals have inclinations greater than 5°, while cold classicals have inclinations below 5° (Gladman et al., 2008). The exact value of the transition is still somewhat arbitrary, but the two populations established are nevertheless remarkably distinct. A rich literature exists on the colors of classical KBOs with the consensus being that all cold classicals are red while hot classicals show a distribution of colors, with no red hot classicals above i=20° (Tegler and Romanishin, 2000; Trujillo and Brown, 2002; Doressoundiram et al., 2002; Tegler et al., 2003; Peixinho et al., 2004; Gulbis et al., 2006; Chiang et al., 2007; Doressoundiram et al., 2008; Morbidelli et al., 2008). Brucker et al. (2009) find that cold classicals have higher geometric albedos. Other observational work suggests that hot classicals are brighter in terms of absolute magnitude than cold classicals

(Levison and Stern, 2001; Morbidelli et al., 2008) while theoretical work refutes this (Pike and Kavelaars, 2013). The absolute magnitude, H, is related to the visible geometric albedo, p_V, and the diameter, D, of the body:

$$H = -5log_{10}\left(\frac{D\sqrt{p_V}}{1329\ km}\right). \quad (2)$$

Combined with the findings of Brucker et al. (2009), hot classicals may be larger than cold classicals, but more observational work is necessary to prove this. Cold classicals also have a higher binary fraction than hot classicals, possibly as high as 100% for intrinsically bright cold classicals (Noll et al., 2008a; Noll et al., 2014).

Cold classicals are redder, brighter, smaller, and more likely to be binaries than hot classicals, pointing to unique origins for both populations and the possibility that cold classicals formed in situ (Brucker et al., 2009). The hot classicals may have formed closer to the Sun and were later perturbed by Neptune into their current high-inclination orbits (Chiang et al., 2007; Levison et al., 2008). The different origins of these two populations and their continued divergence provide valuable clues about the surface processes at work on all KBOs.

- **Haumea Family:** The first collisional family discovered in the Kuiper Belt is related to the dwarf planet Haumea (Brown et al., 2007a). The Haumea family is composed of Haumea, its two satellites Hi'iaka and Namaka, and 10 other KBOs. At some indeterminate time in the past, the proto-Haumea was

struck by a large impactor (Brown et al., 2007a), resulting in the current triple system, Haumea's fast rotation (~3.9 hr; Lacerda et al., 2008), high density (2.6-3.34 g cm-3; Rabinowitz et al., 2006), and its loss of volatile ices (Trujillo et al., 2007). The Haumea family is not a distinct dynamical classification but instead exists in parallel with those described above. For instance, Haumea itself may be in a 12:7 resonance with Neptune while the other members of its family are all cubewanos. These objects are distinguished from the larger KBO population by similar orbital parameters, high albedos, neutral colors, and strong H_2O ice absorption (Brown et al., 2007a; Snodgrass et al., 2010; Trujillo et al., 2011). Water ice has been detected in the spectra of all Haumea family members except Haumea's smaller moon Namaka, possibly due to lack of adequate signal-to-noise observations. The signature of H_2O ice is so strong on these objects that it has even been detected on Haumea's larger satellite Hi'iaka, which is only ~320 km in diameter (Barkume et al., 2006; Ragozzine and Brown, 2009; Dumas et al., 2011). Conversely, the lack of H_2O ice in the spectrum of Salacia, a large KBO with similar orbital parameters, prevents it from being included in the Haumea family (Schaller and Brown, 2008). Other collisional families may exist in the Kuiper Belt, and studying how the individual members have evolved following a common origin would prove vital to comprehending the evolution of KBO surfaces.

Related Dynamical Classifications. Understanding the history and evolution of KBOs does not begin at 30 AU or end at 2000 AU. Other minor bodies interior to the Kuiper Belt and in the Oort Cloud are important to the story as well, since not all objects formed where they currently orbit. The Oort Cloud, a spherical repository of extremely long period comets and objects ejected from the inner parts of the Solar System by Jupiter and Neptune, will not be discussed in any more depth as it is only hypothesized (Oort, 1950) and no object currently orbiting there has been discovered to-date. Instead, I will focus on those objects interior to the Kuiper Belt that are more easily observable, including Centaurs, the Uranus Trojan, Neptune Trojans and Captured KBOs.

- **Centaurs:** The Centaur population is similar to the SDOs in that they are transitioning from one dynamical group to another. These comet-like objects, possibly former KBOs, reach perihelion between 7.35 and 30 AU and are dynamically unstable with an average lifetime on the order of 1 Myr (Tiscareno and Malhotra, 2003; Horner et al., 2004). After leaving the Centaur population, these minor bodies either impact one of the giant planets, get ejected to the Oort Cloud, or evolve into JFCs or Near-Earth Objects (NEOs) (Tegler et al., 2008a). The origin of these objects is still unknown since gravitational interaction with Neptune typically increases the semi-major axes of minor bodies (Levison and Duncan, 1997). Centaurs allow us the chance to observe how a KBO-like body reacts to higher amounts of

solar insolation. In at least one case the results are truly extraordinary: the largest Centaur, Chariklo, has two thin rings of water ice (Braga-Ribas et al., 2014). Indirect evidence suggests that another large Centaur, Chiron, may have rings too (Ortiz et al., 2015). The formation of Chariklo's rings may be due to cometary activity, with the further possibility of shepherd moonlets maintaining their structure (Braga-Ribas et al., 2014). Interior processes that produce ring systems in the present-day may be analogous to those at work earlier in Solar System history when radiogenic heating was the dominant energy source on KBOs.

- **The Uranus Trojan:** The first and only known Uranus Trojan, 2011 QF_{99}, was serendipitously discovered in 2013 at Uranus' L_4 point, 60° ahead of the planet in its orbit (Alexandersen et al., 2013). This object, thought to be a captured Centaur, is in an unstable 70,000-year orbit at the L_4 point, after which it will enter a Uranus co-orbital for ~1 Myr and then become a Centaur once again (Alexandersen et al., 2013). With only one data point, it is hard to say if dynamical instability is the norm for Uranus Trojans. If it is, this would explain the fact that only one has been identified to-date: the population is small due to short residence time.

- **Neptune Trojans:** At present, 18 Neptune Trojans are known across the L_4 and L_5 points with a predicted population 10 times larger than Jupiter's, for

which ~1 million are predicted (Nesvorný and Vokrouhlický, 2009). Unlike the Uranus Trojan, Neptune Trojans are thought to be primordial, and not likely captured Centaurs or KBOs (Sheppard and Trujillo, 2006), though they may contribute to the Centaur population (Horner and Lykawka, 2010). The discovery of a high-inclination Trojan (i=25°) suggests a thick cloud of these minor bodies at both the L_4 and L_5 points and favors a "freeze-in" origin. Following the era of planetary migration and after Neptune had reached a stable orbit, any objects occupying the new L_4 and L_5 points were captured (Sheppard and Trujillo, 2006; Nesvorný and Vokrouhlický, 2009). Because many of these objects have remained in their frozen-in orbits, the Neptune Trojans represent a large reservoir of primordial bodies right on the edge of the Kuiper Belt.

- **Captured KBOs:** At present, there are over 100 irregular satellites known orbiting the giant planets, of which only two are thought to be captured KBOs. These satellites are Phoebe of Saturn (Johnson and Lunine, 2005) and Triton of Neptune (Agnor and Hamilton, 2006). Irregular satellites stand out because their orbits are highly-inclined, eccentric, distant, and/or retrograde. The Cassini spacecraft obtained information used to determine Phoebe's composition, which resembles Triton's and Pluto's, implying that Phoebe originated in the Kuiper Belt region (Johnson and Lunine, 2005). If Phoebe is

truly a captured KBO, that would make it the second ever visited by a spacecraft, with Triton being the first.

The surface compositions of Triton and Pluto are very similar: N_2, CO, CH_4 (methane), C_2H_6 (ethane), and H_2O have been detected on both; Triton's spectrum additionally shows features due to CO_2 absorption. These two objects are also very similar in size and mass (Triton's diameter is larger by ~330 km and it is denser). Triton's retrograde orbit identities it as a captured KBO, as it is easier to capture objects into retrograde, as opposed to prograde, orbits. Theoretical work performed by Agnor and Hamilton (2006) points to Triton as part of a binary KBO that was stripped apart by Neptune; the companion was ejected and Triton entered orbit. Subsequent orbit circularization and tidal heating may be responsible for the smaller amount of volatiles noticed on Triton's surface compared to Pluto (McKinnon et al., 1995). Due to their similarities, studying Triton provides context for understanding Pluto, and vice versa. These valuable connections have resulted in many breakthroughs in KBO science over the years, and will continue to do so in the years to come.

Binaries and Multiple Systems in the Kuiper Belt. The first KBO binary was identified in 1978 with the discovery of Charon (Christy and Harrington, 1978). Determination of Charon's period and semi-major axis enabled the calculation of Pluto's mass using Newton's Version of Kepler's Third Law. It was not until almost

a quarter century later that another KBO binary was identified. As with Charon, a companion around 1998 WW_{31} was serendipitously discovered by Veillet et al. (2002). Since then, nearly 80 KBO binaries have been identified. As mentioned previously, and shown in Fig. 4, a large number of cold classical KBOs are binaries, (Noll et al., 2008a; Noll et al., 2014). All 4 Kuiper Belt dwarf planets have at least one companion, with Makemake's discovered most recently (Parker et al., 2016). Of the 10 largest KBOs known, 8 have at least one companion, with the third largest known KBO, 2007 OR_{10}, recently determined to be a binary (Marton et al., 2016). Two triple systems have been observed, Haumea and 1999 TC_{36} (Benecchi et al., 2010), and one sextuple system, Pluto, with 4 additional small satellites discovered using the Hubble Space Telescope (Weaver et al., 2006; Showalter et al., 2011; Showalter et al., 2012). Due to the richness and diversity of KBO binaries, this field continues to be an area of intense study.

The most important aspect of KBO binaries is that the presence of a satellite allows for a calculation of the total system mass (considered to be the primary mass if the satellite mass is assumed to be negligible). Together with an independent measurement of the diameter from an occultation or radiometric measurements, the density can be calculated. With density in-hand, inferences can be made about the composition, porosity, and likely region of formation. For instance, the density of Eris, a binary and the second largest KBO, is very high (2.5 g cm^{-3}; Brown and Schaller, 2007; Sicardy et al., 2011) compared to the average KBO (<2.0 g cm^{-3}); for comparison, Pluto's density is 1.86 g cm^{-3} (Stern et al., 2015).

Eris is considered a detached object in the scheme of Gladman et al. (2008), but its high density points to formation much closer to the Sun, certainly not at its current orbital distance (a≈68 AU). Fundamental measurements like mass, diameter, and density are incredibly important for understanding the history of the Kuiper Belt.

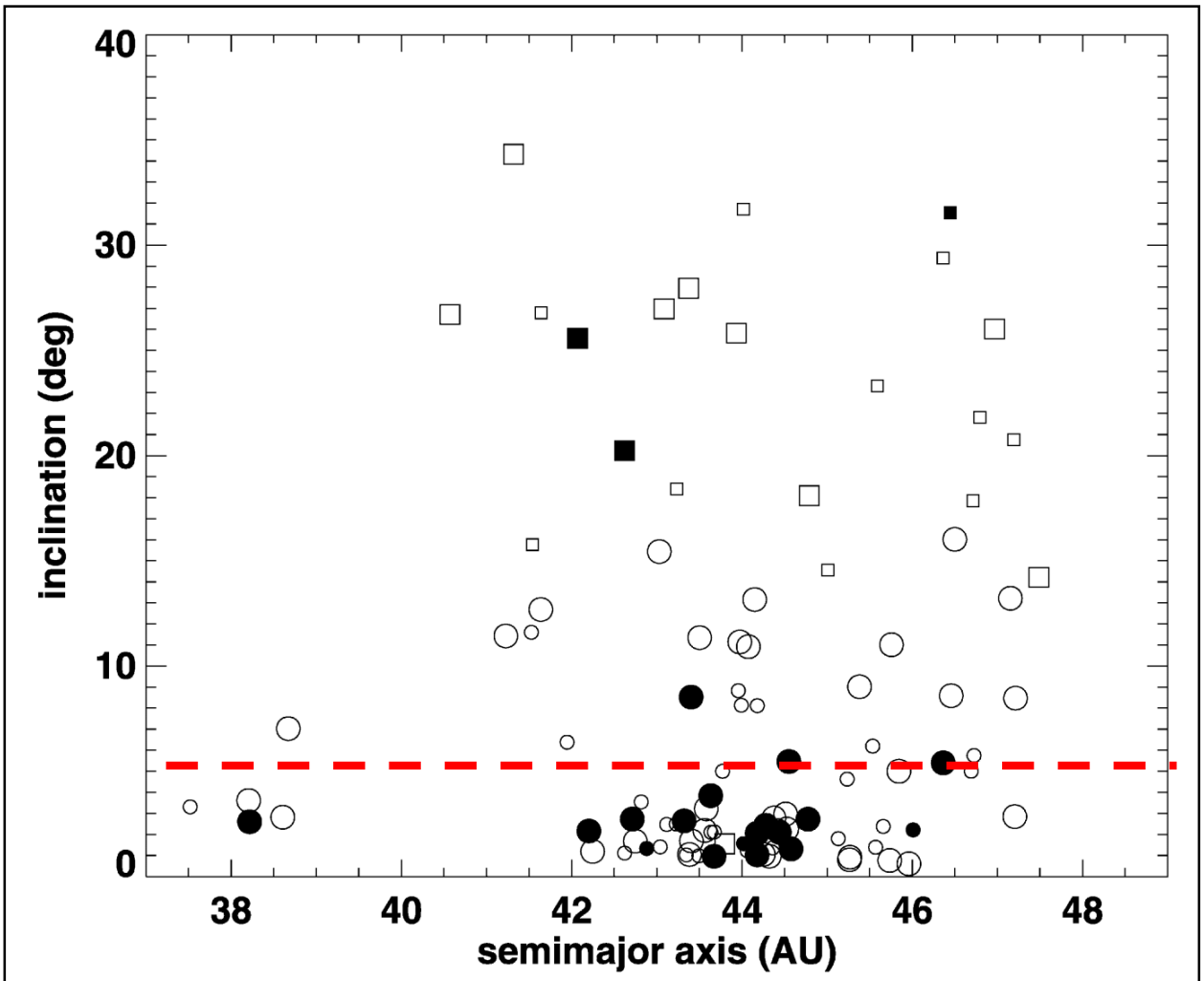

Figure 4: Inclinations of classical KBOs plotted against semi-major axis. The red dashed line has been added at 5° inclination to mark the boundary between dynamically cold (below) and hot (above) classicals. All objects on this plot are considered classical KBOs in the scheme of Gladman et al. (2008); objects shown as circles are those also considered classical in the scheme of Elliot et al. (2005). The main belt runs from 39.4-48.4 AU. Filled shapes denote binary KBOs. Shape sizes refer to binaries observed at different plate scales: larger for 0.025″/pixel and smaller for 0.075″/pixel. Note that a majority of the binaries in this plot are dynamically cold and found in the main belt. (From Noll et al. (2008a))

The formation of KBO binaries provides clues about the early history of the outer Solar System. The three primary formation mechanisms are giant impacts capture, and co-accretion, with capture the most prevalent (Noll et al., 2008b). Giant impacts such as the ones described for the Haumea and Pluto systems (Brown et al., 2007a; Canup, 2011) may actually have been relatively rare occurrences in the early Kuiper Belt. The capture process is thought to conserve the number of KBO binaries because it is a 3-body process. In order for the capture process to work, and be as efficient as models of the number of KBO binaries predict, a binary object must make a close approach to another KBO (Goldreich et al., 2002). One object is captured into orbit by the KBO, and the other is ejected, similar to the process described for the capture of Triton but involving smaller objects (Agnor and Hamilton, 2006). This can result in satellites with very large orbital periods, as is the case for Teharonhiawako's satellite Sawiskera that has an orbital period of almost 829 days (Grundy et al., 2011). In general, both methods of formation agree with a chaotic origin of the Kuiper Belt suggested by the Nice Model (Gomes et al., 2005; Morbidelli et al., 2005; Tsiganis et al., 2005). Co-accretion likely describes the creation of the source population for the capture process and the high number of KBO binaries among the cold classicals (Noll et al., 2014).

Formation of the Kuiper Belt. The formation of the Kuiper Belt we see today is integral to understanding the formation of the entire Solar System and an accurate theory must reproduce various aspects of the current Kuiper Belt,

including (Morbidelli et al., 2008): (1) the observed populations of resonant objects, (2) the existence of detached objects, (3) the distinct populations of cold and hot classical KBOs, (4) the edge of the classical belt at the 2:1 Neptune resonance, and (5) the mass deficit of the current Kuiper Belt. Points (1)-(3) were discussed in "Dynamical Classification of KBOs" on page 7. In regards to (4), there is a marked absence of low eccentricity KBOs (i.e., not classified as SDOs or detached objects) beyond the 2:1 resonance at 48.4 AU that is not easily explained by observational bias (Trujillo and Brown, 2001). Point (5) refers to the apparent loss of ≥99.9% of the Kuiper Belt's mass after formation: about 10-30 M_{Earth} of material is required to produce the population we notice today in a reasonable time span of ~10-100 Myr (Morbidelli et al., 2008). The estimated mass of the present-day Kuiper Belt is 0.01 M_{Earth} (Bernstein et al., 2004) to 0.1 M_{Earth} (Gladman et al., 2001), or 2-3 orders of magnitude lower than the required original mass.

To-date, the most successful theory for explaining the observed structure of the Kuiper Belt is the Nice Model, named for the city in France where the theory was developed, not for the way that researchers of early Solar System history feel about it. Not only does it reproduce the 5 observations outlined in the previous paragraph, it also reproduces the orbital parameters of the giant planets (Tsiganis et al., 2005), explains the inclination distribution of Jupiter's (Morbidelli et al., 2005) and Neptune's (Tsiganis et al., 2005; Sheppard and Trujillo, 2006) Trojan populations, and provides a trigger for the Late Heavy Bombardment (LHB) of the inner Solar System (Gomes et al., 2005).

The Nice Model is a computer simulation that takes as inputs the assumed state of the early Solar System and evolves the system through time. The most successful runs of the simulation, those that best produce the Solar System as we observe it, involve a very compact outer Solar System: the giant planets are found between 5.5 and 14 AU and the primordial disk of planetesimals end at 34 AU (Gomes et al., 2005). For reference, the giant planets today are found at semi-major axes between 5.2 and 30 AU, and the classical Kuiper Belt extends to 48.4 AU. The orbits of the giant planets are initially circular with Uranus found outside of Neptune's orbit and Saturn interior to the 2:1 mean motion resonance with Jupiter. The mass of the disk of planetesimals beyond Uranus' orbit is 35 M_{Earth}. After 650 Myr have elapsed in the simulation, Jupiter's and Saturn's slow migrations move them through a 2:1 resonance (Jupiter completes two orbits for every one of Saturn), exciting their orbital eccentricities. The eccentricities and semi-major axes of Neptune and Uranus increase as a result of this resonance passage, and their orbits become chaotic: they pass very near each other and scatter objects as they travel through the planetesimal disk. At some point, the two planets switch places, resulting in the order observed today. With planetesimals now scattered throughout the orbits of the giant planets, eccentricities are damped through dynamical friction. The giant planets continue their outward migration until they reach their current orbits. The disk of planetesimals is now severely depleted; what remains is the Kuiper Belt, largely as it is today. Snapshots of a Nice Model simulation are shown in Fig. 5.

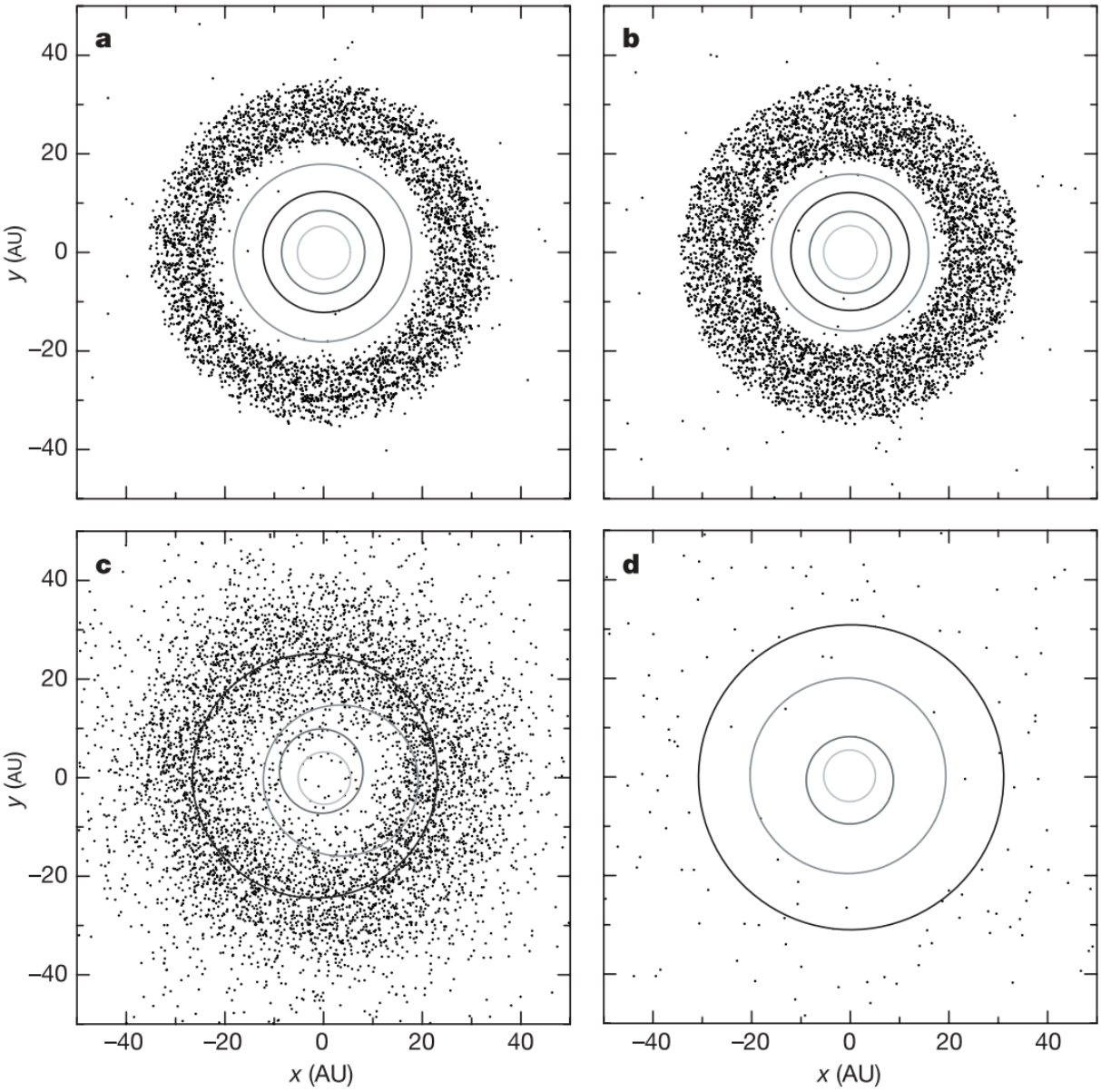

Figure 5: Nice Model simulation snapshots. Initial conditions have the giant planets between 5.5 and 14 AU and a primordial planetesimal disk of mass 35 M_{Earth} extending from 15.5 to 34 AU. The panels show the simulation after (a) 100 Myr, (b) 879 Myr, (c) 882 Myr, and (d) 1082 Myr. Uranus and Neptune switch places in the chaotic 3 Myr span between panels (b) and (c). Panel (d) shows the final orbits of the giant planets and the Kuiper Belt. (From Gomes et al. (2005))

The final orbital parameters of individual planetesimals can be determined by tracing them in the simulation. The runs described above accurately reproduce the population of resonant objects in the final Kuiper Belt. In fact, the Nice Model is the first not to result in an overabundance of low-eccentricity resonant objects, as observed (e.g., Gladman et al., 2008). Additionally, a population of detached objects is produced in the simulations, in agreement with observations. The mass deficit is also explained by the Nice Model: The final mass of the Kuiper Belt in the simulations is between 0.02 and 0.08 M_{Earth}, within the estimated range of 0.01-0.1 M_{Earth}.

The cold classical objects were emplaced during Neptune's high eccentricity phase ($e \geq 0.15$) following its last encounter with Uranus ($a \approx 28$ AU). During this period, regions within the 2:1 mean motion resonance with Neptune were chaotically unstable and objects began to move radially. According to Morbidelli (2002), the mean motion resonances interior to the 2:1 were very wide and overlapped, allowing for free movement of planetesimals. The present-day cold classical KBOs are thought to have formed at the outer edge of the original planetesimal disk and moved inwards during Neptune's high-eccentricity phase. After this phase ended and Neptune's orbit re-circularized, these objects became frozen in place without the ability to freely move through resonances. Thus the cold classical KBO population was formed with a distinct outer edge at the current 2:1 resonance with Neptune. The smaller sizes of these objects (Levison and Stern, 2001; Grundy et al., 2005) can be explained by their migration inwards from a

relatively mass-poor region of the planetesimal disk. This theory does not explain the redder colors of the cold classicals (see "CH_3OH (methanol)," pp. 32) and it is unlikely that inclinations were excited during this period to form the hot classical KBO population.

However, the work of Gomes (2003) provides an origin for the hot classicals. After Neptune's orbit circularization, it began to migrate outwards along with a scattered disk of planetesimals (analogous to today's scattered disk population). Some of these objects decoupled from Neptune (i.e., no longer were being actively scattered) and entered eccentricity-damping resonances with Neptune. As Neptune continued to migrate, so did the resonances and the objects trapped in them in a process known as "resonance sweeping." (Had Neptune remained stationary, the eccentricities of objects would have increased again, resulting in Neptune-crossing orbits and re-coupling with Neptune, making them part of the scattered disk once again (Gomes, 2003).) Some objects then dropped out of resonance and became trapped in the Kuiper Belt. The large majority of these objects had high inclinations and are known today as the hot classical KBOs. When in the scattered disk, orbital inclinations would have been excited and there is a dynamical bias for objects with high inclinations to enter eccentricity-damping resonances. It is then easier for these objects to drop out of resonance because resonances are weaker for lower eccentricities (Gladman et al., 2008). This aspect of the Nice Model explains the hot classical population and their larger sizes (Levison and Stern, 2001; Grundy et al.,

2005): these objects were moved outward from a more mass-rich region of the planetesimal disk by Neptune's migration.

As previously described, the Nice Model explains the 5 important observational aspects of the current Kuiper Belt, but it still has some weaknesses. In particular, it cannot simultaneously produce KBOs at the highest and lowest observed inclinations. However, the Nice Model does accurately and concurrently explain a majority of the observations. Believable initial and final conditions add credence to an in-between that is believable as well. Of particular interest to this thesis, the Nice Model paints the picture of a chaotic environment shortly after planetary formation and provides context for the giant impact origin of the Pluto system and the three-body capture of Triton by Neptune. The work presented in Chapters II, III, and IV aims to describe the surface evolution of Pluto, Charon, and Triton following these formation events.

Extrasolar Kuiper Belts. Our Kuiper Belt is a collection of unique objects, but Kuiper Belts themselves are not unique. Over two-dozen dusty debris disks, analogous to our own Kuiper Belt in formation and structure, have been directly imaged around other stars, including the one presented in Fig. 6. We do not, and may never, have the capability to directly image exo-KBOs, but the dynamical, physical, and chemical processes at work on objects in our Kuiper Belt should be applicable to objects in exo-Kuiper Belts as well. KBOs are likely some of the most numerous planetary bodies in the universe and those in our own Solar System provide the context necessary for understanding this important class of object.

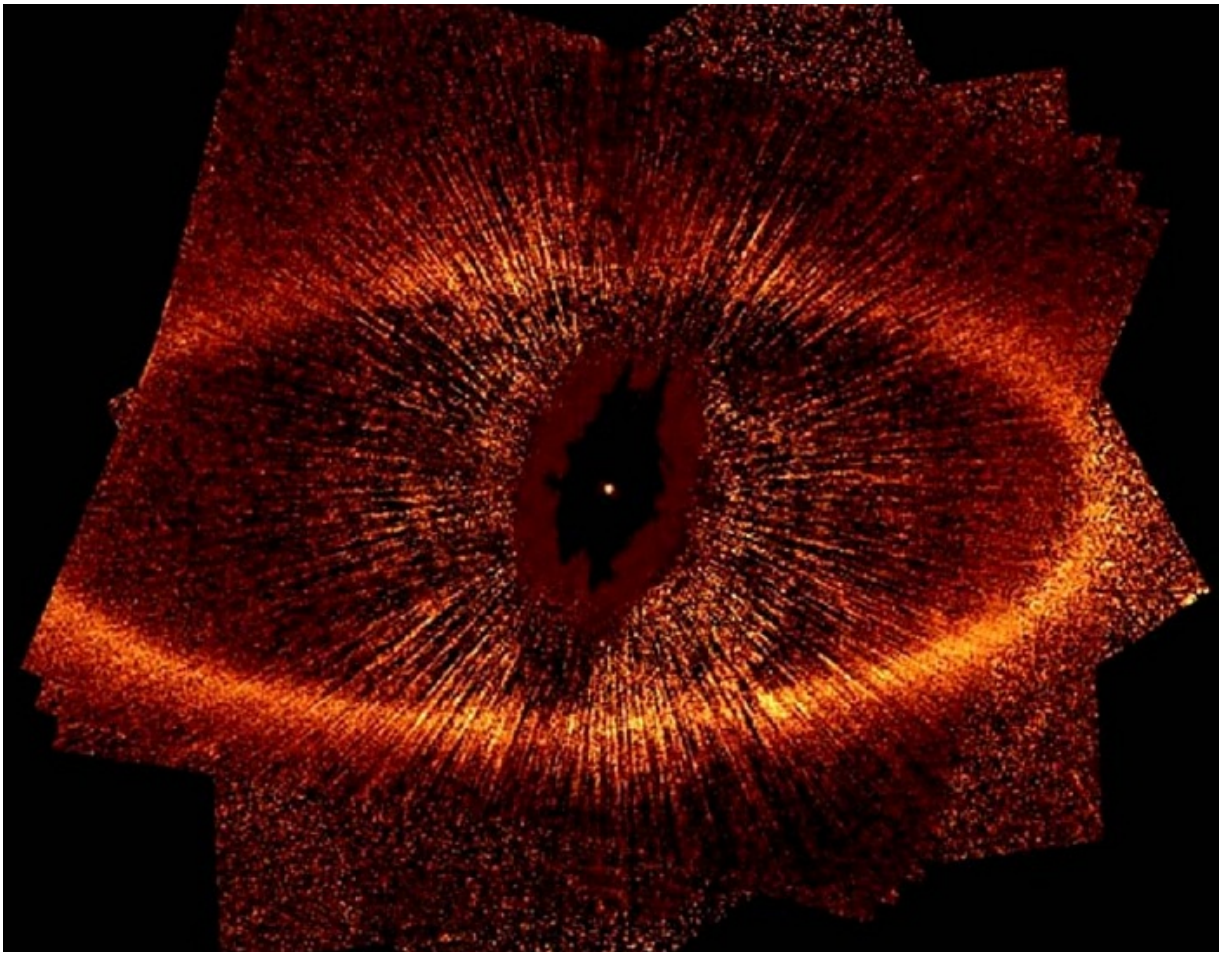

Figure 6: Coronagraphic image from HST of a debris disk surrounding the young (100-300 Myr) A-type star Fomalhaut. The inner edge of the debris disk, analogous to our Kuiper Belt, is at 133 AU and has a thickness of ~25 AU. Light from the center of the image was blocked by the coronagraph spot to prevent washing out the debris disk; the dot in the center is artificial. The inner edge of our Kuiper Belt would fit inside the coronagraph spot. (From Kalas et al. (2008))

Composition and Evolution of KBO Surfaces

The observed surface compositions of KBOs are a direct result of their formation environment, early thermal events, and various physical and chemical processes active over the past few billion years of Solar System history. The previous sections provided context for the importance of formation environment

(e.g., the cold and hot classical KBO populations) and described the thermal events (e.g., Pluto's and Haumea's giant impacts, Triton's capture) that set the stage for further surface evolution. Now I will discuss the specific ices incorporated into KBOs, how those ices are retained or lost, and what processes have altered the surfaces of KBOs up to the present day.

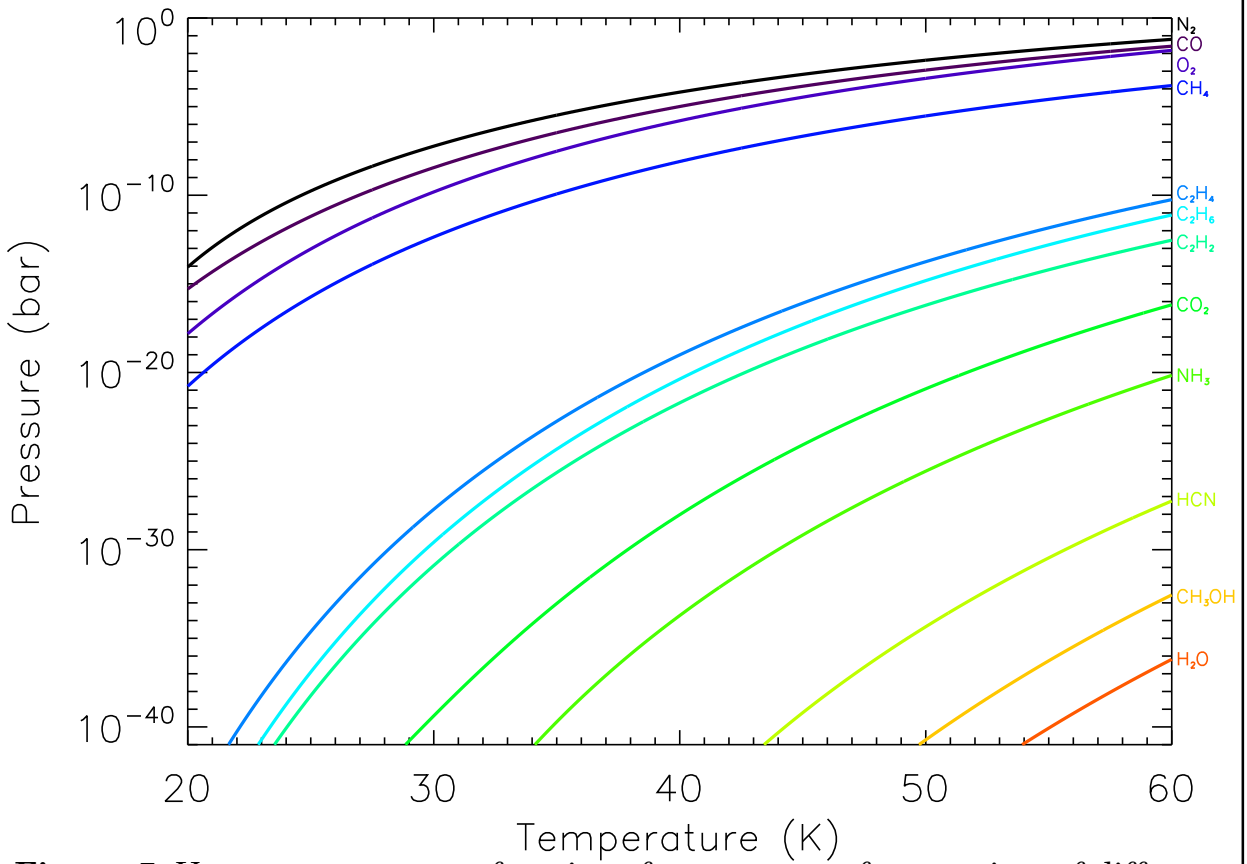

Figure 7: Vapor pressure as a function of temperature for a variety of different ices, all of which are described in more detail in the text. The function and coefficients describing this relationship for each ice were taken from Fray and Schmitt (2009). Typical Kuiper Belt temperatures vary from 30-50 K, so I plot the temperature range 20-60K; the pressure range is 10^{-42} to 1 bar. In terms of ices important to KBO studies, only N_2, CO, O_2, and CH_4 have non-negligible (>1 nbar) vapor pressures at these temperatures. Water, perhaps the most common ice in the outer Solar System, is a relatively non-volatile ice with a negligible vapor pressure, even at higher temperatures. Note the large gap separating the relatively volatile ices and the relatively non-volatile ices.

Volatile and Non-volatile Ices. The bulk composition of KBOs is a combination of rock and ice, with ice fractions anywhere between 0 and 1 (0.3-0.4 may be considered typical values; Brown, 2012). The primary ice component is water, but other trace ices also condensed in the solar nebula and became incorporated into KBOs (Lewis, 1972). These trace ices are typically divided into two groups based on their relative vapor pressures: volatile and non-volatile ices. The relatively volatile ices, those with non-negligible vapor pressures at Kuiper Belt temperatures (~30-50 K, see Fig. 7), are, in decreasing order of volatility, N_2, CO, O_2, and CH_4; the relatively non-volatile ices include H_2O, CO_2, NH_3, CH_3OH, SO_2, HCN, and non-methane hydrocarbons (Fray and Schmitt, 2009). Further information on each ice and the objects on which they have been detected are provided below; a discussion of non-methane hydrocarbons is presented in the "Surface, Atmospheric, and Interior Processes" section (pp. 38).

- **N_2 (molecular nitrogen):** Only the two largest icy objects in the outer Solar System, Triton and Pluto, have N_2 positively identified on their surfaces (e.g., Cruikshank et al., 1993; Owen et al., 1993). The presence of N_2 ice has been inferred on the other large KBOs Eris (Brown et al., 2005b; Tegler et al., 2010), Makemake (Licandro et al., 2006; Tegler et al., 2008b), and Sedna (Barucci et al., 2005; Barucci et al., 2010), though no direct detections have yet been made.

- **CO (carbon monoxide):** Again, only Triton and Pluto are known to have CO ice on their surfaces (Cruikshank et al., 1993; Owen et al., 1993). The vapor pressures of CO and N_2 are at the same order of magnitude, and the two species are typically co-located on KBO surfaces (Grundy et al., 2010; Grundy et al., 2013; Holler et al., 2016a). To date, CO has only been identified on Pluto and Triton, the same two bodies with the only definitive detections of N_2 ice.

- **CH_4 (methane):** The least volatile of the relatively volatile ices, and the easiest to detect spectrally, is CH_4. It has been definitively identified on Triton (Cruikshank et al., 1993), Pluto (e.g., Owen et al., 1993), Eris (Brown et al., 2005b), Makemake (Licandro et al., 2006), and Sedna (Barucci et al., 2005; Barucci et al., 2010); CH_4 was also identified on 2007 OR_{10} (Brown et al., 2011a) and Quaoar (Schaller and Brown, 2007a), but these claims require follow-up observations. Intriguingly, a very tentative CH_4 detection was reported on the intermediate-sized KBO Varuna (Lorenzi et al., 2014); the reason this is unexpected will be discussed in the next section on "Theories of Volatile Retention" (pp. 33).

- **O_2 (molecular oxygen):** The volatile ice O_2 was tentatively reported on dwarf planet Haumea but the detection is not particularly robust and requires further observations (Tegler et al., 2007). O_2 ice was previously

reported on Ganymede (Calvin and Spencer, 1997) but the same formation mechanism (plasma bombardment of surface H_2O ice within Jupiter's magnetosphere) is not applicable to Haumea.

- **H_2O (water):** Water ice is the most common species detected on KBO surfaces. It has been identified on Triton (Cruikshank et al., 2000), Pluto (Stern et al., 2015; Grundy et al., 2016a), Charon (e.g., Buie and Grundy, 2000), the entire Haumea family (Brown et al., 2007a; Snodgrass et al., 2010; Trujillo et al., 2011; Barkume et al., 2006), Quaoar (Jewitt and Luu, 2004), Sedna (Barucci et al., 2010), and Orcus (Barucci et al., 2008), among many others. New Horizons' flyby through the Pluto system was required to identify H_2O in Pluto's spectrum, due to the thick layer of volatile ices that masks the H_2O substrate and confusion with strong absorption features from CH_4. The presence of water ice on so many KBOs is not surprising given that it is an important, if not the dominant, component of the bulk compositions of KBOs. KBOs with featureless spectra, those devoid of any surface ices including water, are too small for differentiation to have occurred in their interiors (Brown, 2012). Outflows of water ice onto the surface following differentiation are likely responsible for the strong water ice signature on Charon (Moore et al., 2016).

- **NH_3 (ammonia):** Ammonia is a non-volatile compound that acts as an anti-freeze, depressing the freezing point of water and allowing it to flow more easily. It is typically associated with KBOs that have a strong water ice signature in their spectra, such as Charon (e.g., Buie and Grundy, 2000) and Orcus (Barucci et al., 2008). Ammonia has also been detected on the large Uranian satellite Miranda (Bauer et al., 2002) and the minor satellites of Pluto (Cook et al., 2016). Surprisingly, NH_3 has not been detected in spectra of Haumea, the KBO with the strongest water ice absorption (Pinilla-Alonso et al., 2009), though higher signal-to-noise spectra may be necessary to make a definitive statement. Haumea's lack of volatile ices is explainable in the context of the giant impact that formed its dynamical family and perhaps this may provide an explanation for its lack of NH_3 as well.

- **CO_2 (carbon dioxide):** CO_2 is a common ice in the outer Solar System, as evidenced by its presence on the icy satellites of Saturn and Uranus (Clark et al., 2005; Brown et al., 2006; Clark et al., 2012; Dalton et al., 2012; Cartwright et al., 2015), and Triton (Cruikshank et al., 1993). The lack of detections on KBOs is likely due to the difficulty in resolving the very narrow absorption features in their spectra.

- **CH_3OH (methanol):** Brown et al. (2011b) propose that methanol ice is responsible for the red colors of the cold classical KBOs. Methanol condensed

beyond 20 AU in the solar nebula and was then incorporated into the planetesimals that would later become the cold classicals. Subsequent irradiation of methanol left behind red by-products, resulting in the red surfaces measured today (Brunetto et al., 2006). Since the hot classicals formed over a larger range of radial distances interior and exterior to 20 AU (compared to the cold classicals), they cover a larger range of colors from neutral to red (the cold classicals are predominantly red). Methanol has been identified in the comae of comets (e.g., Brown 2012) and on the Centaur Pholus (Davies et al., 1993), but no definitive detections have been made on KBOs. However, methanol has been suggested on the surfaces of 1996 GQ_{21} (Barkume et al., 2008), 2002 VE_{95} (Barucci et al., 2006) and Sedna (Barucci et al., 2010). Brown (2012) summed the spectra of 38 KBOs and Centaurs in order to increase the signal-to-noise ratio and search for methanol absorption. He reports a weak signature in the summed spectrum, suggesting the presence of methanol on many of the objects but in such small quantities that it is undetectable in the individual spectra.

- **SO_2 (sulfur dioxide) and HCN (hydrogen cyanide):** These non-volatile ices have not yet been detected on the surfaces of any KBOs, though they could reasonably be expected to be present. SO_2 has been previously detected on the other small bodies Io (i.e., Carlson et al., 2007) and Ceres (Hendrix et al., 2016) and HCN is formed in photolysis processes that take place in the

atmospheres (Lara et al., 1997; Krasnopolsky and Cruikshank, 1999) and on the surfaces (Moore and Hudson, 2003) of volatile-rich bodies.

Theories of Volatile Retention. Volatile ices are particularly important because they may contribute to the formation of an atmosphere around KBOs. Atmospheres, in turn, enable transport of volatile ices across the surface and this movement can be tracked in order to quantify temporal surface changes. Photolysis in the atmosphere also results in the creation of non-methane hydrocarbons and nitriles (molecules with a triple bonded nitrogen and carbon atom), classes of species with astrobiological importance. These processes, and others, will be discussed further in the next section. First, it is important to understand why some KBOs have retained, and others have completely lost, their volatile inventories over the age of the Solar System.

The discovery and spectral characterization of the large KBOs Eris, Makemake, Haumea, Sedna, and Quaoar in the early 21st century opened a new era in KBO studies. Pluto and Triton, the only two large outer Solar System bodies previously known to retain volatile ices on their surfaces, were now no longer alone. The diversity of this subset has enhanced our understanding of the larger KBO population, particularly in the area of volatile retention. All of these objects have retained volatile ices over the age of the Solar System, except Haumea whose lack of volatiles can be explained by a giant impact. However, the composition and amount of volatile ices present on the surface vary across the subset. Any process invoked to

explain these observations must also explain the fact that a majority of KBO surfaces are devoid of volatile ices.

The volatile retention theory of Schaller and Brown (2007b) is elegant in its simplicity. It also accurately predicts which objects should retain volatile ices, which should lose them, and to first order reproduces the relative amounts of volatiles on the largest KBOs. This theory takes advantage of assumptions about atmospheric escape in order to provide a lower limit on the atmospheric loss rate. In general, sublimation of volatile ices will form an atmosphere and result in loss of molecules through the processes of Jeans escape and/or hydrodynamic escape (Stern and Trafton, 2008). Jeans escape refers to atmospheric loss of lighter molecules from the high velocity tail of the Maxwellian distribution. Escape through this process occurs at the exobase (the altitude at which the mean free path of the molecules is equal to the scale height) and provides a lower limit on atmospheric escape. Hydrodynamic escape removes molecules from a large fraction of the Maxwellian distribution through collisions of thermally excited lighter molecules with heavier molecules, causing a large outflow. The regime that a KBO's atmosphere is in, Jeans or hydrodynamic, may vary during a KBO's orbit especially in the case of high eccentricity, and can be determined by spacecraft measurements of atmospheric thermal structures or occultations of bright background stars observed from Earth. Pluto is currently in the Jeans escape regime, as determined by New Horizons.

Considering this information, Schaller and Brown (2007b) make reasonable assumptions for placing lower limits on atmospheric loss from KBOs: (1) model

atmospheric escape in the Jeans regime since it provides a lower limit on the atmospheric escape rate and (2) put the exobase at the surface where the temperature is lower than at its actual altitude. Any object that loses its model atmosphere over the age of the Solar System under these conditions is guaranteed to have lost its real atmosphere if at any point it was in the hydrodynamic regime. The modeled loss rate of atmospheric molecules is represented mathematically as:

$$\frac{dM_{vol}}{dt} = 4\pi R^2 \frac{P_{vap}(T)}{\sqrt{2\pi mkT}} \left(1 + \frac{GMm}{kTR}\right) e^{\frac{-GMm}{kTR}}, \quad (3)$$

where dM_{vol}/dt is the loss rate in molecules/s, R is the radius of the KBO, $P_{vap}(T)$ is the volatile vapor pressure as a function of temperature, m is the molecular mass of the volatile, k is the Boltzmann constant, T is the equilibrium temperature, G is the gravitational constant, and M is the mass of the KBO. Each volatile species (N_2, CH_4, CO) was considered separately in the model to determine the different escape rates for each. (The volatile species O_2 was not considered as it has never been definitively detected as a solid or gas on any KBO.) The initial inventory of each volatile on the surface is an estimate and changing the amount by an order of magnitude does not affect the final results. For each KBO, the mass lost over one orbit is calculated and converted to a "volatile loss equivalent temperature," defined as the equilibrium temperature of a body identical in mass in a circular orbit. This temperature is likely comparable to the perihelion temperature for the KBO's actual orbit, as a majority of atmospheric escape occurs at perihelion. A more complicated model that included more realistic escape rates (rather than lower limits) was developed by Johnson et al. (2015), though they only considered loss of

N_2. This model will not be discussed further since the simpler model of Schaller and Brown (2007b) is sufficient for an understanding of volatile loss and retention on KBOs.

The results of the Schaller and Brown (2007b) model are presented in Fig. 8. The solid curves denote the boundaries of diameter and equivalent temperature that result in complete loss of that volatile from a KBO over the age of the Solar System. Objects to the left of these volatile retention curves have completely lost their initial volatile inventories, while those to the right are expected to retain them (at least for the lower limits on the loss rate). The most important objects are those in the transition zone near the volatile retention curves, such as Quaoar, Haumea (2003 EL_{61}), Makemake (2005 FY_9), and 2007 OR_{10} because they provide valuable tests of the theory's accuracy. A KBO not in the transition zone that may stretch the limits of the theory is Varuna. This object, due to its smaller size, is fully to the left of the volatile retention curves, yet a tentative detection of CH_4 was made in near-infrared spectra (Lorenzi et al., 2014). If this detection is supported by future observations, Varuna could be the smallest KBO known to support volatile ices on its surface. From Schaller and Brown (2007b), it is unlikely that this CH_4 would be primordial, but other theories of its placement on the surface such as an impact that released trapped CH_4 from the interior are not entirely satisfactory (Lorenzi et al., 2014). At present, the volatile retention theory of Schaller and Brown (2007b) is consistent with observations made in the intervening decade. This theory will continue to be tested as more objects are discovered and their surface compositions

are determined. The ultimate result will be a better understanding of the evolution of KBO surfaces, atmospheres, and interiors.

Surface, Atmospheric, and Interior Processes. Frequent allusions have been made in this document to the physical and chemical processes operating on the surfaces, atmospheres, and interiors of KBOs. In this section I will discuss these processes in-depth and explore how they relate and interact with each other.

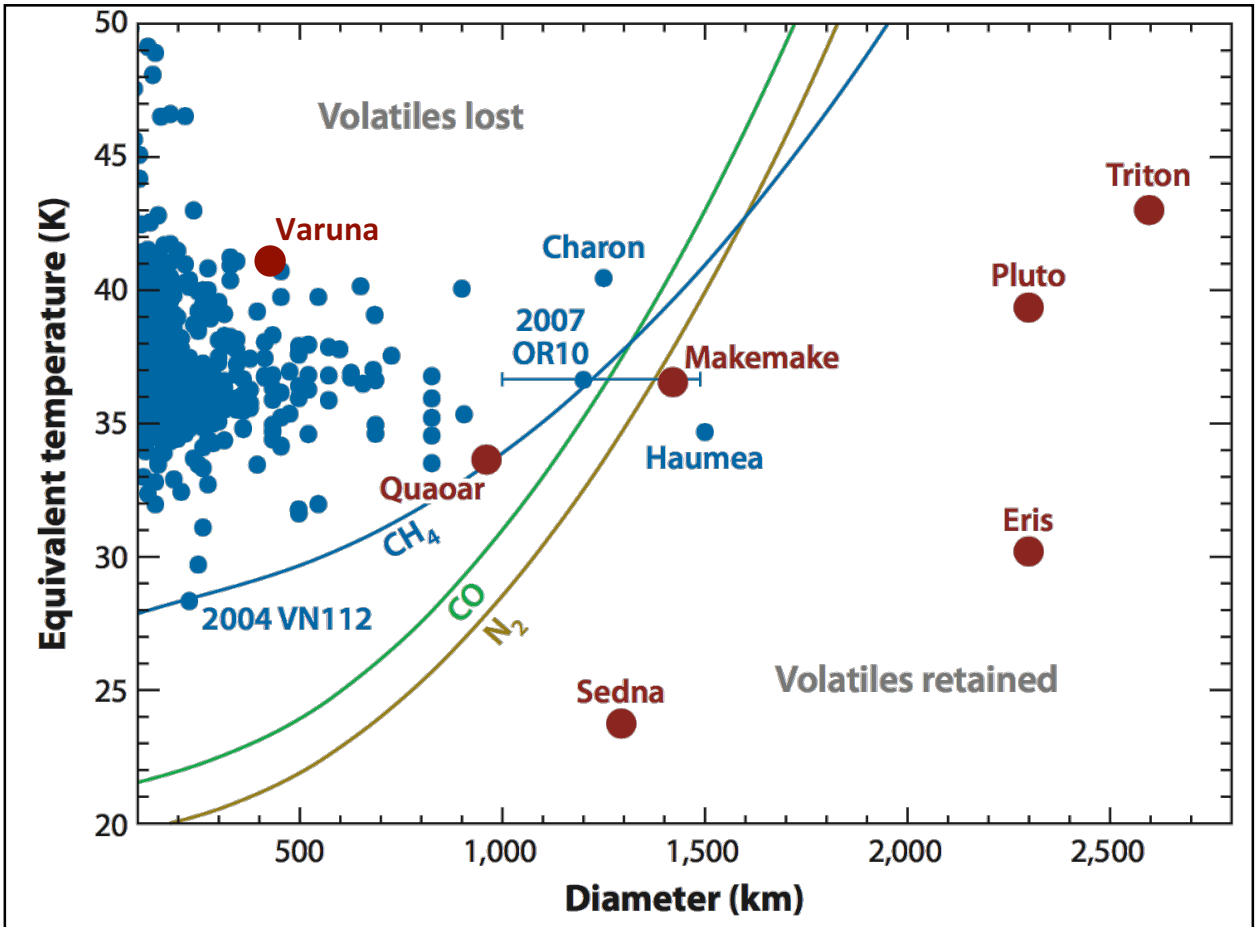

Figure 8: Plot indicating which KBOs should retain volatiles based on a simple atmospheric loss model. The volatile retention curves for N_2, CO, and CH_4 that run through the center of the diagram separate objects that should no longer retain volatiles (left side) from those that should (right side). Objects near the curves may or may not retain volatile ices on their surfaces. 2007 OR_{10} is on the larger end of its error bar based on recently published results (Pál et al., 2016). This model has been successful in explaining observations. (From Brown (2012))

A natural system, on its face, may appear uncomplicated and orderly, easily explained by a handful of independent internal and external processes and inputs. Upon closer examination, this paradigm inevitably breaks down and one finds a complicated web of connections and feedback between seemingly unrelated processes. KBOs are no different. The purpose of the work presented in Chapters II-IV of this thesis is to understand the interplay of these myriad processes on observable aspects of KBOs. I present a collection of identified and potential processes at work on KBOs as a rainbow in Fig. 9. A web diagram might be more appropriate, but those are notoriously convoluted, not to mention that many of the possible connections between processes may exist but are currently not well understood. I represent the processes as a cyclical rainbow to draw attention to the more obvious connections between the processes that affect KBO surfaces, atmospheres, and interiors. However, this analogy is not perfect, especially since interior processes can play significant roles in altering the surfaces and atmospheres of KBOs, but the opposite is not necessarily true. In the following paragraphs I will highlight the connections within smaller groups of processes that may draw from all 3 categories (surface, atmospheric, interior), examine how they affect the observable properties of KBOs, and provide examples.

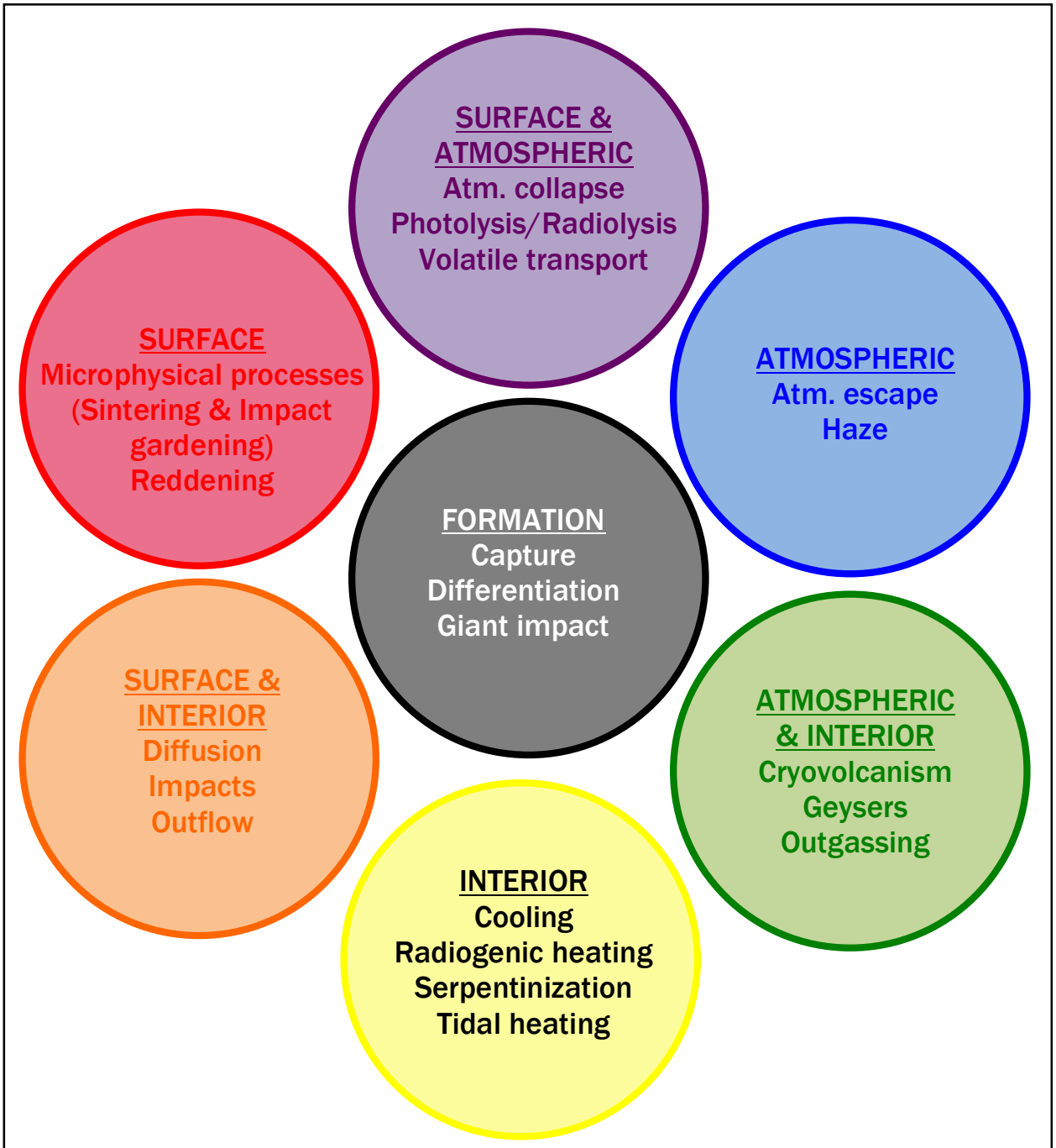

Figure 9: Cartoon representation of the important physical and chemical processes in action on KBOs. Surface (red), atmospheric (blue), and interior (yellow) processes are represented by the primary colors; the secondary colors purple, green, and orange are formed where the appropriate processes overlap. In terms of mixing pigments, black is the combination of all colors and so is found in the center. Formation processes are the most important in determining the future of a KBO and therefore occupy this central black circle. In general, interior processes affect the surfaces and atmospheres of KBOs but the converse is not true, causing the cyclical analogy to break down.

The central circle in Fig. 9, labeled "Formation," is colored black since it is the combination of all colors (I use the analogy of mixing pigments, not light, in Fig. 9). The properties of KBOs that we observe today are due in large part to the radial location where the body formed and the three processes listed in the central circle: differentiation, capture, and giant impacts. These processes are early thermal events in the history of a KBO that significantly contribute to the internal structure and observed surface composition, therefore determining if an atmosphere could exist in the present day. In some cases, the absence of these processes during a KBO's history is fundamental to understanding its current state.

- **Differentiation:** This process is dependent on the mass of the KBO, with differentiation more likely to occur in larger objects. Luu and Jewitt (2002) calculate that objects with radii greater than ~500 km will be able to retain internal heat and at least undergo partial differentiation. An energy source is necessary to initiate differentiation and keep it going, likely leftover heat of formation and/or radiogenic heating. Differentiation ends when the interior cools and solidifies. A more massive KBO will differentiate into a rocky core with an ice-rock mantle. Pure ice has the lowest density and will preferentially move to the surface. Analogous to the eruption of magma onto the surface of the early Earth to form the crust, cryo-magmas (mostly H_2O ice) will erupt onto the surface of the KBO, forming an icy crust. This may explain the featureless spectra of the smaller KBOs: they were not massive

enough for significant differentiation to occur and are likely a mixture of ice and rock throughout their interiors.

- **Capture:** Triton, a former KBO, provides the perfect example of how being captured by a gas giant planet can significantly alter an object's surface, atmospheric, and interior properties. The non-volatile ices H_2O and CO_2 are clearly evident in Triton's spectrum (e.g., Grundy et al., 2010), even though these ices are likely the substrate upon which the volatile ices deposit; these same ices are absent in the spectrum of Pluto (e.g., Grundy et al., 2013) even though Fig. 8 shows Triton further to the right of the volatile retention curves, implying it should retain more of its initial volatile inventory. Triton's capture by Neptune and subsequent orbit circularization can explain this discrepancy since it would have resulted in significant tidal heating and loss of volatile ices by hydrodynamic escape (McKinnon et al., 1995).

- **Giant impacts:** These events are also external to KBOs and can influence the evolution of their surfaces, atmospheres, and interiors. Giant impacts are responsible for the creation of the Haumea family (Brown et al., 2007a) and the Pluto system (Canup, 2011), including Charon. Haumea and its family members exhibit strong H_2O ice absorption in their spectra, indicating a progenitor body large enough to undergo differentiation. The giant impact resulted in the destruction and dispersal of this body throughout the Kuiper

Belt and the heat of impact was also high enough to remove volatile ices completely from the largest remaining member, Haumea. Fig. 8 shows Haumea in the transition zone for retaining volatiles and no volatile ices are observed on its surface. However, Quaoar and Makemake (2005 FY_9), two other transition zone KBOs, are observed to retain CH_4 ice. The giant impact that formed Pluto, Charon, and its 4 minor satellites was also the beginning of Pluto and Charon's divergent evolutionary paths. Charon was massive enough for differentiation and outflow of H_2O ice onto the surface (Moore et al., 2016), but not massive enough to retain volatiles. Pluto, unlike Haumea, retained its volatile ices after the giant impact and up to the present day. The reason for this is unknown, though it may have to do with formation environment and/or severity of the impact. Canup (2011) models Pluto's giant impact as a glancing collision between the proto-Pluto and proto-Charon while the event that created the Haumea family must have been more severe in order for it to disperse debris throughout the Kuiper Belt.

In general, I will try to progress through the different post-formation processes starting on the inside and working outward. As mentioned previously, surface and atmospheric processes have negligible effects on the interior, but the interior can significantly influence the other two. The interior processes to consider on KBOs are similar to those on other terrestrial bodies: radiogenic heating, tidal heating, cooling, and serpentinization.

- **Radiogenic heating:** This internal heating process was likely important shortly after formation because the radionuclide in highest abundance, ^{26}Al, has a half-life of 7.4×10^5 years. Decay of this radionuclide may have resulted in internal temperatures of 180 K; the long-lived radionuclides ^{40}K, ^{235}U, ^{238}U, and ^{232}Th may have also contributed, but not as significantly or as early as ^{26}Al due to their lower abundances and longer half-lives (Choi et al., 2002; McKinnon et al., 2008). The magnitude of interior heating due to radioactive decay can be probed by the presence of water ice on KBO surfaces. Radiogenic heating is a driver of differentiation and significant differentiation likely results in outflow of water onto the surface, as noticed on Charon (Moore et al., 2016). Larger objects, and those KBOs with higher rock fractions (lower water fractions), had higher radiogenic heat flux and therefore should exhibit strong water ice absorption in their spectra (unless covered by a veneer of volatile ices).

- **Tidal heating:** One such process is tidal heating. This process may be necessary to describe loss of volatile ices on Triton and Charon and could also explain the potential presence of water ice on the surfaces of small KBO satellites. As described previously, Neptune's capture of Triton and Triton's subsequent orbital evolution generated significant amounts of internal heat. Triton is currently in a synchronous, circular orbit around Neptune with the eccentricity damped through dissipation of energy within Triton itself. Tidal

forces due to Neptune distorted the shape of Triton through a gravitational gradient, elongating it along the imaginary line connecting the two bodies. When Triton was not synchronously orbiting Neptune (rotation and orbital periods not equal), the orientation of this stretching changed over the course of an orbit. This spatially varying tidal distortion generated internal heat through friction that was then dissipated through conduction to the surface. The time for Trion's orbital circularization, τ_{circ}, can be written as:

$$\tau_{circ} = \frac{4}{63} Q_2 \left(\frac{a^3}{G(m_1+m_2)}\right)^{1/2} \left(\frac{m_2}{m_1}\right) \left(\frac{a}{R_2}\right)^5, \quad (4)$$

where Q is the tidal quality factor (a measure of an object's response to tidal distortion, a higher value represents a more rigid object), a is the semi-major axis, m is mass, and R is radius (Goldreich and Soter, 1966). The subscripts denote Neptune (1) and Triton (2) in this situation and the timescale for the circularization of Triton's orbit is approximately 4 Myr.

This same process circularized and synchronized Charon's orbit around Pluto and it is likely that the heat generated increased the rate of volatile loss on Charon. The heat created during tidal circularization may also be enough to partially differentiate a small satellite and cause outflows of H_2O onto the surface. Water ice was detected on Hi'iaka, the largest moon of Haumea (Barkume et al., 2006), and on the minor moons of Pluto: Styx, Nix, Kerberos, and Hydra (Cook et al., 2016). Whether the presence of water ice on these objects is due to heat generated by tidal circularization or by the material they formed from after the respective giant impacts is a matter of

debate. This idea of tidally induced outflows would be supported if H_2O ice were detected on any of the satellites of the larger KBOs, such as Dysnomia (Eris), S/2015 (136472) 1 (Makemake), Weywot (Quaoar), or Vanth (Orcus). However, spectra of small satellites are difficult to obtain due to low flux from these objects and small angular separation from their primaries. Improvements to currently existing facilities, as well as the commissioning of next generation telescopes in space and on the ground, will enable these observations in the relatively near future.

- **Cooling:** KBOs began to cool and contract following the loss of their internal heat sources such as the residual heat of accretion, radiogenic heating, and tidal heating. Significant contraction or expansion of a body results in distinct topographical features on the surface, and both may explain the transition region between highlands and lowlands on Charon (Fig. 10; Malamud et al., 2016). Of the two KBOs (and one former KBO) visited by spacecraft, only Charon shows these features, and they suggest alternating periods of expansion and contraction due to freezing and thawing of a low-volume sub-surface ocean (Malamud et al., 2016) or simply expansion of a high-volume ocean (Moore et al., 2016). Malamud et al. (2016) propose that other KBOs in Charon's size range (e.g., Haumea, Quaoar, Sedna, and Orcus) may have similar features on their surfaces. Smaller bodies are expected to show similar features while larger bodies like Triton, Pluto, Eris, 2007 OR_{10},

and Makemake would relax faster and the warmer interior directly beneath the surface would work to erase these features.

Figure 10: Image of Charon, Pluto's largest satellite, from the New Horizons flyby in July 2015. The areas highlighted in light blue are possible extensional features on Charon. This region is the geological transition from the highlands (above the light blue region) and the lowlands (below) and may have been formed following two periods of expansion and contraction. (From Malamud et al. (2016))

- **Serpentinization:** This chemical process is important for understanding the early thermal histories of KBOs because it is a highly exothermic reaction. Serpentinization is the process of converting ultramafic rock (high magnesium and iron content) into rocks of the serpentine group in the presence of liquid water. To geologists, this is a low temperature reaction, but

in the context of the Kuiper Belt it is a very high temperature reaction because it requires water in the liquid phase. Serpentinization is therefore only likely to occur early in a KBO's history when interior conditions can support liquid water. Since serpentinization releases energy, it may have been an important driver of differentiation in larger bodies. It also likely contributed to the creation of CH_4 on many KBOs. Some serpentinization reactions produce H_2, which then interacts with CO or CO_2 to produce CH_4 and H_2O (e.g., Neal and Stanger, 1983). CO in particular was an abundant molecule in the solar nebula (Mousis et al., 2015) and is still found on the surfaces of Pluto and Triton in the present-day.

Serpentinization may be an important part of the story of Varuna, the intermediate-sized KBO with a tentative detection of CH_4 on its surface (Lorenzi et al., 2014). If CH_4 is currently present on Varuna, it cannot be explained by the volatile retention theory of Schaller and Brown (2007b). Comparison to the dwarf planet Haumea provides a possible answer. Both Varuna and Haumea are triaxial ellipsoids (the dimensions of the object along the *x*-, *y*-, and *z*-axis are different; imagine a football with smoother ends (similar to a rugby ball); Lacerda and Jewitt, 2007; Sicardy et al., 2010) with very fast rotation periods of ~6.3 hours (Sheppard and Jewitt, 2002) and ~3.9 hours (Lacarda et al., 2008), respectively. Varuna also has a low density (0.992 g cm^{-3}; Lacerda and Jewitt, 2007) and porosity possibly as high as 50% (McKinnon et al., 2008). Considering this information together suggests

Varuna suffered from a giant impact similar to Haumea's. Such an event would not only result in the physical and rotational properties observed, but also would have heated the interior. This heating may have driven differentiation and resulted in liquid water in the interior, enabling serpentinization. Outflow and solidification of H_2O followed, since H_2O is detected on the surface today (Licandro et al., 2001; Lorenzi et al., 2014). Outgassing of CH_4 may also have occurred at this time. The water ice on the surface, having cooled from a higher temperature, was therefore in the crystalline phase with an orderly lattice structure (the converse is H_2O molecules in random orientations as in amorphous water ice). Water ice can trap "guest" molecules within cages in the lattice, stabilizing the water ice and forming a clathrate (Mousis et al., 2015). Methane gas can be trapped in this way, forming methane clathrate. Destabilization of methane clathrate only occurs with a temperature increase, allowing it to exist for long periods in cold environments such as KBO surfaces (Mousis et al., 2015). With present technology and laboratory data, methane clathrate is impossible to discern from a mixture of CH_4 and H_2O in a KBO's spectrum (Mousis et al., 2015). Thus, impact-induced serpentinization and subsequent creation of methane clathrate may explain the observed surface composition of Varuna.

These next few processes are those that bring material from below the surface up onto the surface where it can be observed by Earth-based telescopes and

spacecraft. Some of these processes occurred long ago, like outflow and outgassing, or were more probable in the past, such as impacts. Others may be ongoing, like diffusion, cryovolcanism, and geyser activity.

- **Outflow/outgassing:** These processes will be discussed together since they both brought material from deeper within KBO interiors and likely occurred simultaneously. As discussed previously, outflow onto the surface as a result of differentiation is the most likely reason that H_2O is observed on many KBOs. Separation of rocks and liquid water, with rock sinking to the center and water rising towards the surface, followed by the freezing and expansion of the water caused eruptions onto the surface (Moore et al., 2016). This appears to be the best explanation for the fact that the entirety of Charon's surface is covered in H_2O ice (Grundy et al., 2016a). Differentiation also worked to bring the even less dense volatile species from the interior to the surface. These volatiles were likely outgassed at approximately the same time, forming primordial atmospheres around KBOs and also depositing onto the surface. Atmospheric escape then stripped away the primordial atmospheres from all but the largest KBOs (Schaller and Brown, 2007b). After sufficient cooling on the larger KBOs, volatiles increased their deposition rate onto the surface, covering up the underlying H_2O ice substrate.

- **Geysers/cryovolcanism:** Compared to outflow and outgassing, these processes act on a smaller scale and may currently be moving material from the interiors to the surfaces of KBOs. The two terms refer to similar processes, but cryovolcanism pertains to the creation of a structure analogous to a volcano on Earth. Geysers are simply the eruption of material without formation of a volcano-like structure. Geysers were observed by Voyager 2 during its flyby past Triton in August 1989 (Smith et al., 1989; Soderblom et al., 1990). Fig. 11 shows dark plumes created as a result of the geysers, and some work has suggested they are due to the destabilization of clathrates (Croft et al., 1995). The dark color is surprising given that the plumes should be made of high-albedo volatile ices. Geysers affect a localized area on Triton, indicate the presence of winds, and provide information on atmospheric structure (some plumes are seen to level out at an atmospheric boundary about 8 km above the surface; Soderblom et al., 1990). Geysers were not observed on either Pluto or Charon, but some features on Pluto are thought to be dormant cryovolcanoes (Fig. 12; Moore et al., 2016). Ongoing large-scale resurfacing from cryovolcanism has been invoked to explain the high abundance of crystalline water ice compared to amorphous water ice on Haumea (Dumas et al., 2011), Orcus (de Bergh et al., 2005), Quaoar (Jewitt and Luu, 2004), and Charon (Cook et al., 2007). This seems unlikely given that ongoing activity requires internal heat sources and these are probably negligible in the present day (see Chapter V for a more detailed discussion of

the likelihood of cryovolcanism on KBOs). Cryovolcanism at one point was likely responsible for resurfacing on KBOs, but is unlikely to be an important process now.

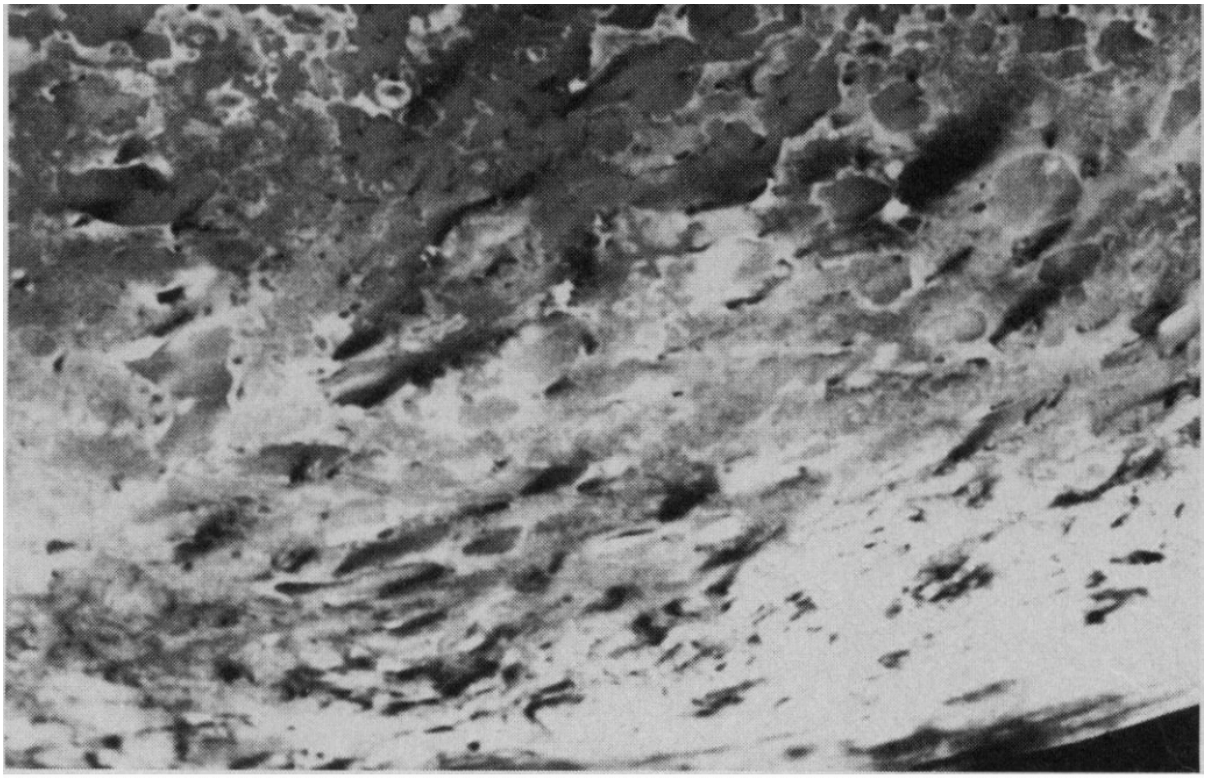

Figure 11: Image of Triton's southern hemisphere from the Voyager 2 flyby in August 1989. The dark streaks seen across the image, and most prominently in the top right, are interpreted as geysers of dark material. The direction of the dark streaks indicates the wind directions and the geysers level out at about 8 km, providing information on atmospheric structure. The origin of the geysers is unknown, though they could be due to the release of trapped gases from clathrates as temperature increases. (From Smith et al. (1989))

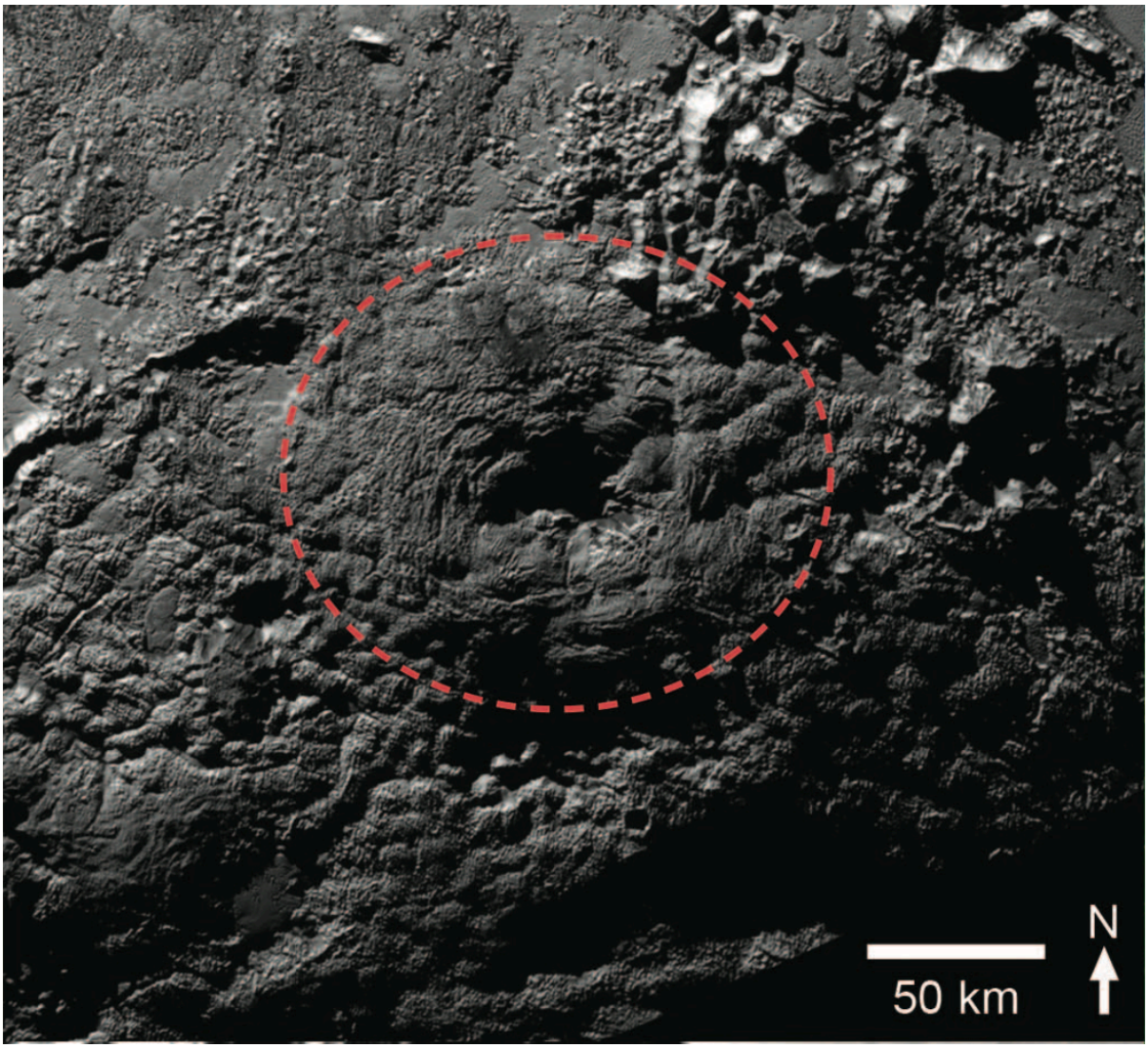

Figure 12: Possible dormant cryovolcano on the surface of Pluto from the New Horizons flyby in July 2015. This feature, unofficially named Wright Mons, is ~150 km across, ~3-4 km high, and the central depression is ~5 km deep. (From Moore et al. (2016))

- **Diffusion:** The slow diffusion of trace molecules through an overlying layer of ice can actually contribute to observed compositions of KBOs. The best example is on Charon, where NH_3 molecules may be diffusing through the upper layer of H_2O ice. This replenishes NH_3 in the upper surface layers, counteracting its destruction by radiation and cosmic rays. The process of

NH_3 diffusion also produces NH_3 hydrate (Uras and Devlin, 2000; Livingston et al., 2002), which is observed in the spectrum of Charon (e.g., Cook et al., 2007). Ammonia hydrate is easily identifiable in ground-based spectra of Charon indicating that it is prevalent across Charon's surface. Livingston et al. (2002) report that the diffusion rate of NH_3 through H_2O ice is higher than the self-diffusion rate of H_2O at 140 K (the lowest temperature they considered in the laboratory was 100 K). Diffusion of NH_3 is a relatively quick process; additionally, a higher thermal gradient exists for KBOs than for this laboratory set-up. Other KBOs with a definitive detection of NH_3 are Orcus, an object also covered in a thick layer of H_2O ice (Barucci et al., 2008), and the minor moons of Pluto (Cook et al., 2016). It is possible that diffusion is at work on these objects as well.

- **Impacts:** Material just beneath the surface can be excavated by impacts and localized heating of the surface can occur around an impact, increasing the rate of diffusion. One, possibly both, of these processes may be responsible for the increased abundance of NH_3 in a bright rayed crater observed on Charon (Grundy et al., 2016a). The presence of such a high concentration of NH_3 suggests that the impact was recent, within the past 20 Myr, since NH_3 within the first few millimeters of the surface (the depth probed by near-infrared spectra) is destroyed on these timescales (Cooper et al., 2003). According to theoretical work by Zahnle et al., (2003), the current flux of

impactors larger than 1.5 km is 2.6×10^{-6} yr^{-1} on Pluto, comparable to the rates on Triton and Europa. Taking into account gravitational focusing, the impact rate on Charon is 16% of the rate on Pluto and Triton, or 4.2×10^{-7} yr^{-1}. Over 20 Myr, the expected number of impacts on Charon is ~8, so the "fresh" impact observed by New Horizons (crater size ~5 km) is rather common. Impact rates for all sizes of impactors were likely higher in the distant past. Impact craters are also likely deposition sites for volatile ices due to their temperature being lower, on average, over a diurnal cycle due to shadowing. The unofficially named Sputnik Planitia on Pluto is a possible ancient impact basin and reservoir for volatile ices (Schenk et al., 2015). Convection of the N_2 ice in Sputnik Planitia replenishes the surface of this region on timescales of half a million years, explaining the high albedo (Buratti et al., 2016) and lack of craters (McKinnon et al., 2016). Other KBOs with high albedos and large-variation light curves could exhibit a similar surface feature.

Microphysical processes work on a small scale but can have significant consequences for observations of KBOs. In particular, they can affect the surface texture of KBOs, which in turn affects spectral and photometric observations (see "Hapke Modeling," pp. 69). Two such processes are sintering and solar gardening.

- **Sintering:** Deposition of volatiles onto a KBO's surface will form small grains, resulting in a highly reflective surface. Over time, these grains combine to form larger grains and the albedo decreases in a process known as sintering. Earthly examples of sintering include the fusing of ice cubes in a glass of water or the creation of a glacier from compaction of years of snowfall. Sintering is the compaction of ice grains by the growth of the neck between two grains by heat and/or pressure without melting the grains (Eluszkiewicz, 1991). This process reduces the porosity of the ice (defined as the ratio between the volume of voids and the total volume) and reduces the surface albedo. The smooth surface of Triton observed by Voyager 2 may be a result of sintering occurring on seasonal (~100 year) timescales (Eluszkiewicz, 1991).

- **Solar gardening:** Grundy and Stansberry (2000) provide a scenario for surface texture and albedo changes on objects (i.e., Pluto, Triton, and possibly Eris, Makemake, and Sedna) with a thick layer of N_2 ice that they refer to as "solar gardening." This process works because of a thermal imbalance between ice at depth and ice nearer the surface, but not in the way one would naïvely expect. Nitrogen ice is a better absorber in the thermal infrared (~70 μm) than at visible wavelengths, meaning that absorption of visible light primarily occurs at greater depths than the depth of thermal emission. (Shorter wavelength visible light can penetrate greater depths than thermal

infrared radiation.) In other words, N_2 ice is heating up at greater depths and cooling down at shallower depths. This results in sublimation of N_2 at depth and deposition at the surface. Grundy and Stansberry (2000) assume that the N_2 gas freely escapes from the ice; they also prefer a scenario where deposition of small N_2 grains occurs on the surface, increasing the albedo. This process, which works on sub-seasonal timescales (<100 years), can result in deposition of ice during summer, when solar insolation is highest, and could explain Triton's observed plume activity through the sudden release of built up N_2 gas below the surface.

Surface-atmosphere interactions are naturally easier to observe than surface-interior interactions, and therefore are of great interest. Some of these processes are observable from the Earth, including volatile transport and atmospheric collapse.

- **Volatile transport:** Bulk movement of volatile ices on the surfaces of KBOs are a seasonal process and requires data sets with long time-baselines to be observed. Typically, an increase in solar insolation, due to a change in the sub-solar latitude, causes volatile ices to sublimate into the atmosphere where they are transported and deposited on cooler regions. Winter and summer hemispheres are referred to on KBOs due to the long seasons and slow rate of change in the sub-solar latitude (the latitude at which the Sun is

directly overhead at local noon). Volatile transport moves material predominantly from the summer hemisphere (the region of the surface that receives sunlight during part of a diurnal cycle) to the winter hemisphere (the region of the surface in darkness for a full diurnal cycle, similar to the South polar region on Earth during northern hemisphere summer). In general, volatile transport is a radiative process that can significantly alter the albedo distribution on KBOs. Sublimation of volatile ices may reveal the underlying non-volatile substrate and/or the darker radiation processed materials such as non-methane hydrocarbons and tholins. Deposition will act to increase the albedo. Evidence for volatile transport over the timescale of a decade has been inferred from changes in volatile ice absorption in near-infrared spectra of Triton and Pluto; this will be discussed in more detail in Chapters II and III, respectively. Photometric observations (color, albedo, light curve) also suggest volatile transport on Triton (Smith et al., 1989; Buratti et al., 1994; Brown et al., 1995) and Pluto (Buratti et al., 2015). The data sets necessary to detect evidence of volatile transport on other bodies over these timescales do not exist. Triton and Pluto are the brightest objects at visible wavelengths in the considered population, and so high signal-to-noise spectra can be obtained at various sub-observer longitudes (the longitude directly "below" the observer). This is not achievable for most KBOs. Additionally, some of the brighter objects like Makemake and Eris have not been known for long enough periods to check for volatile transport on their surfaces. The orbital

periods of KBOs are hundreds of years, so the seasons are also quite long, even on Triton and Pluto, so observations must be made as close to summer solstice or perihelion as possible (as was done for Triton and Pluto, respectively).

- **Atmospheric collapse:** KBO albedos can also be affected by atmospheric collapse, as on Eris. The visible geometric albedo of Eris is ~0.96, making it one of the most reflective objects in the Solar System (Sicardy et al., 2011). This could be due to Eris' large heliocentric distance (~98 AU), causing the primarily N_2 atmosphere to deposit onto the surface. Assuming that Eris had an N_2-dominated atmosphere with a surface pressure of 15 μbar (comparable to Pluto's at its peak pressure), collapse of the atmosphere would result in N_2 ice with a uniform thickness on the order of 10 mm across the surface. This calculation assumes Eris' radius is 1163 km (Sicardy et al., 2011), Eris' mass is 1.66×10^{22} kg (Brown and Schaller, 2007), and the density of N_2 ice is 250 kg m^{-3} (Satorre et al., 2004). While this is not a very thick layer of ice, it may be enough to explain Eris' high visible geometric albedo and the lack of a definitive detection of N_2 in its spectrum. The same may be true for Makemake, a large KBO near aphelion at ~52 AU with a visible albedo of ~0.77 (Ortiz et al., 2012). However, just being far from the Sun may not be enough for atmospheric collapse, and predicting when collapse will occur is difficult, as illustrated by Pluto. Olkin et al. (2015) extrapolate occultation

data from 1988-2013 and predict that Pluto's atmosphere does not collapse at any point during its orbit (Pluto reaches aphelion at 49 AU). Theoretical work by Young (2013) was unable to rule out the collapse of the atmosphere prior to 2015 (Pluto's atmosphere has yet to collapse), an event that obviously did not occur. Continued observations will be key to a better understanding of the process of atmospheric collapse, and Pluto provides an ideal laboratory to follow events as they happen.

The diversity of ice species increased following KBO formation due to radiation processing. Interaction of molecules with gamma, X-ray, and UV radiation (photolysis) or cosmic rays, charged particles, and the solar wind (radiolysis) initiates chemical reactions. These reactions create non-methane hydrocarbons, tholins, and nitriles. Radiation processing of surface material results in surface reddening, while photolysis and radiolysis in the atmosphere can produce haze. I will discuss the combined effects of the processes of photolysis and radiolysis in the atmospheres and on the surfaces of KBOs separately.

- **Photolysis/radiolysis in the atmosphere:** Species created as a result of photolysis and/or radiolysis will henceforth be referred to as "photochemical products." For the atmospheres of Pluto and Triton, reactions can proceed with any of the dominant atmospheric species: N_2, CH_4, and CO. The photochemical products produced are predominantly non-methane

hydrocarbons and some nitriles. Different models produce different photochemical product abundances, however. Lara et al. (1997) report the most abundant species are, in order: C_2H_6 (ethane), C_2H_2 (acetylene), HCN (hydrogen cyanide), and C_2H_4 (ethylene). Krasnopolsky and Cruikshank (1999) report a very different list: C_2H_2, C_4H_2 (diacetylene), HCN, H_2, C_2H_4, HC_3N (cyanoacetylene), C_2H_6, C_3H_2 (cyclopropenylidene), and C_3H_4 (propyne). They further report that the highest precipitation rates from the atmosphere (these are non-volatile species) is, in order: C_2H_2, C_4H_2, HC_3N, HCN, C_2H_6, and C_2H_4. Wong et al. (2017) present photochemical models based on data from New Horizons and find that the top three precipitating species are C_2H_2 (179 g cm^{-2} s^{-1}), C_2H_4 (95 g cm^{-2} s^{-1}), and C_2H_6 (62 g cm^{-2} s^{-1}). Lara et al. (1997) did not calculate precipitation rates and the results of Krasnopolsky and Cruikshank (1999) and Wong et al. (2017) do not agree with observations of surface composition. It is possible that absorption from some of the species with predicted higher abundances is not easily observable (overlapping with a CH_4 absorption feature, perhaps) or laboratory data are not available, thus preventing a definitive detection.

- **Photolysis/radiolysis on the surface:** The observations tend to favor Lara et al. (1997) because the only non-methane hydrocarbons detected on KBO surfaces are C_2H_6 on Triton (DeMeo et al., 2010; Holler et al., 2016a (Chapter II)), Pluto (DeMeo et al., 2010; Holler et al., 2014 (Chapter III)), and

Makemake (Brown et al., 2007b) and C_2H_4 on Makemake (Brown et al., 2015). These detections were of surface ices since these species precipitate and accumulate on the surface; concentrations in the atmosphere are not high enough to observe absorption in spectra. In the presence of a shielding atmosphere, these species will remain largely unaltered except by cosmic rays. Even with the low column densities of CH_4 in the atmospheres of Pluto and Triton, UV radiation (specifically Lyman-α photons) cannot reach the surface, preventing further photolysis (Holler et al., 2014; Holler et al., 2016a). Without an atmosphere, radiation is free to bombard the surface and initiate further photochemical reactions. The end result of these reactions is tholins that darken and redden the surface (Sagan and Khare, 1979). Large regions of tholins were observed on Pluto (Stern et al., 2015) and Charon's red North Pole is thought to be where molecules captured from Pluto's escaping atmosphere (Bagenal et al., 2016; Gladstone et al., 2016) accumulated over time and underwent radiation processing (Grundy et al., 2016b). The presence of tholins on Pluto suggest periods in the past when the atmosphere was thinner or had collapsed to the surface or that cosmic rays play a large role in the production of tholins.

Laboratory work provides information on the intermediate species between N_2, CH_4, and CO and tholins. For surface compositions similar to Pluto's and Triton's (primarily N_2 with trace CH_4 and CO), HCN can be created in photochemical reactions (Moore and Hudson, 2003). Irradiation of

C_2H_6 ice, a species previously identified on Triton, Pluto, and Makemake, results in CH_4, C_2H_2, C_2H_4, C_3H_4, C_3H_6 (propene), C_3H_8 (propane), and C_4H_{10} (butane) (Hudson et al., 2009). The trend towards longer-chain hydrocarbons, and ultimately tholins, is clearly evident. Sasaki et al. (2005) undertook a search to identify C_2H_2, C_2H_4, C_2H_6, and C_3H_8 in near-infrared spectra of Pluto, but they were unsuccessful due to low spectral resolution. Non-methane hydrocarbon species absorb more strongly in the mid-infrared and should be more easily identifiable due to fewer wavelengths of CH_4 absorption (the species that dominates the near-infrared).

Smaller objects that did not retain CH_4 on their surfaces for long can still exhibit red surfaces. By smaller objects I am referring to objects smaller than Charon, a relatively large KBO without significant tholin coverage across the surface. In particular, KBOs that formed in the cold, mass-starved outer reaches of the primordial trans-Neptunian disk appear very red. As discussed previously, these cold classical KBOs are possibly red because CH_3OH (methanol) could condense on their surfaces at these heliocentric distances (Brown et al., 2011b). Methanol was then converted to red photochemical products through photolysis and radiolysis (Brunetto et al., 2006) since there were no atmospheres protecting these objects' surfaces.

Studying KBOs

Everything you have read to this point is merely an overview of what is known about Kuiper Belt Objects, their formation and current environments, and the processes that continue to drive the evolution of their surfaces. The information presented thus far is by no means exhaustive and future work will continue to create more questions than answers. Many allusions were made in the previous pages to the techniques used to study the surface compositions of KBOs, and in this section I will go more in-depth into the techniques important to this thesis.

Near-infrared Reflectance Spectra. The surface compositions of KBOs are best studied through analysis of near-infrared reflectance spectra. The near-infrared (~0.8-2.5 μm) is the ideal wavelength regime for studying vibrational transitions of surface ices because many important molecules (i.e., N_2, CH_4, CO, CO_2, H_2O, NH_3, C_2H_6, CH_3OH) absorb at these wavelengths, flux from the Sun is adequate, and this spectral region is not dominated by absorption from water vapor in Earth's atmosphere (telluric absorption). The mid-infrared (~2.5-5 μm) is more ideal for studying ice absorption bands, but solar flux is lower at these wavelengths and significantly more telluric absorption is present. Important absorption features of N_2, nitriles, and non-methane hydrocarbons are present in this spectral region. The atmospheric transmission window covers the near-UV to the near-IR, and this is why most optical Earth-based observatories also offer near-infrared instrumentation. Observations in the mid-infrared are extremely difficult, but not impossible, from Earth. Space-based observatories, such as the James Webb Space

Telescope (JWST), which is set to launch in October 2018, are ideal platforms for mid-infrared observations.

Emission from KBOs can be approximated as a blackbody with a peak in the thermal (~70 μm), so the Sun must be relied on to provide the photons for near-infrared reflectance spectra. The majority of solar near-infrared flux incident on the surface of a KBO is reflected back into space with some photons at particular wavelengths absorbed by surface ices. (Since the Sun is not a perfect blackbody, observations of a solar-type star are interspersed between observations of the KBO during an observing run. This spectrum is later divided out to remove the solar spectral slope and absorption features, leaving behind the reflectance spectrum of the KBO.) The absorbed photons are those with energies corresponding to the difference in vibrational energy levels of the surface ice species, represented by (Tennyson, 2011):

$$E_V = \hbar\omega\left(v + \frac{1}{2}\right), \tag{5}$$

where E_V is the vibrational energy, $\hbar$ is the reduced Planck's constant ($h/2\pi$), ω is the fundamental frequency, and v is the vibrational quantum number (an integer). Since exact values of the energy levels are impossible to determine, the change in energy for a vibrational transition, ΔE_V, is calculated instead (simply replace E_V with ΔE_V and v+1/2 with Δv in the above equation). The fundamental (strongest) vibrational transition occurs for Δv=1, resulting in $\Delta E_V = \hbar\omega$. Any positive value of Δv is allowed for absorption, but larger numbers generally correspond to weaker absorption features (these are referred to as overtones).

The absorption of a photon that excites a vibrational transition causes a change in the vibrational state of the molecule itself, hence the name. Picture a CO molecule as two different-sized spheres connected by a spring, with the carbon and oxygen atoms initially stationary with respect to each other. Absorption of the correct amount of energy will cause the molecule to stretch at the appropriate frequency and the "spring," in this case the chemical bond holding the molecule together, provides the restoring force. This vibrational mode is the simplest to consider and other more complicated vibrational modes exist, as is the case for CH_4, which is a tetrahedral molecule rather than a linear molecule like CO. The magnitude of the stretching, or other vibrational mode, depends on Δv. The different energy states are represented with an anharmonic oscillator potential, as shown in Fig. 13.

Vibrational transitions not only require a change in the vibrational quantum number, but also the presence of dipole moment in the molecule. In order for the molecule to interact with electromagnetic radiation there must be an internal electric field. Molecules are naturally vibrating (because T>0 K) and those with non-uniform charge distributions (e.g., CH_4) will generate an internal electric field due to the movement of charges. Diatomic homonuclear molecules (e.g., N_2) have uniform charge distributions and therefore no internal electric field. Yet N_2 ice has a vibrational spectrum, due either to asymmetries in the crystal lattice in pure N_2 ice, random thermal motions (collision-induced absorption), or because it is in solution with other species such as CH_4. N_2 is in solution with CH_4 on the surfaces

of Triton and Pluto and this contributes to the near-infrared absorption bands noticed in their spectra. Within the crystal lattice, each N_2 molecule may be surrounded by other N_2 molecules and by CH_4 molecules. This asymmetry within the lattice contributes to a dipole moment in the N_2 molecule, allowing for it to undergo vibrational transitions. These transitions are weak, however, and N_2 absorption is only identifiable in the spectra of Triton and Pluto because it is the dominant surface ice (>95%).

Additional complications must be considered when determining some

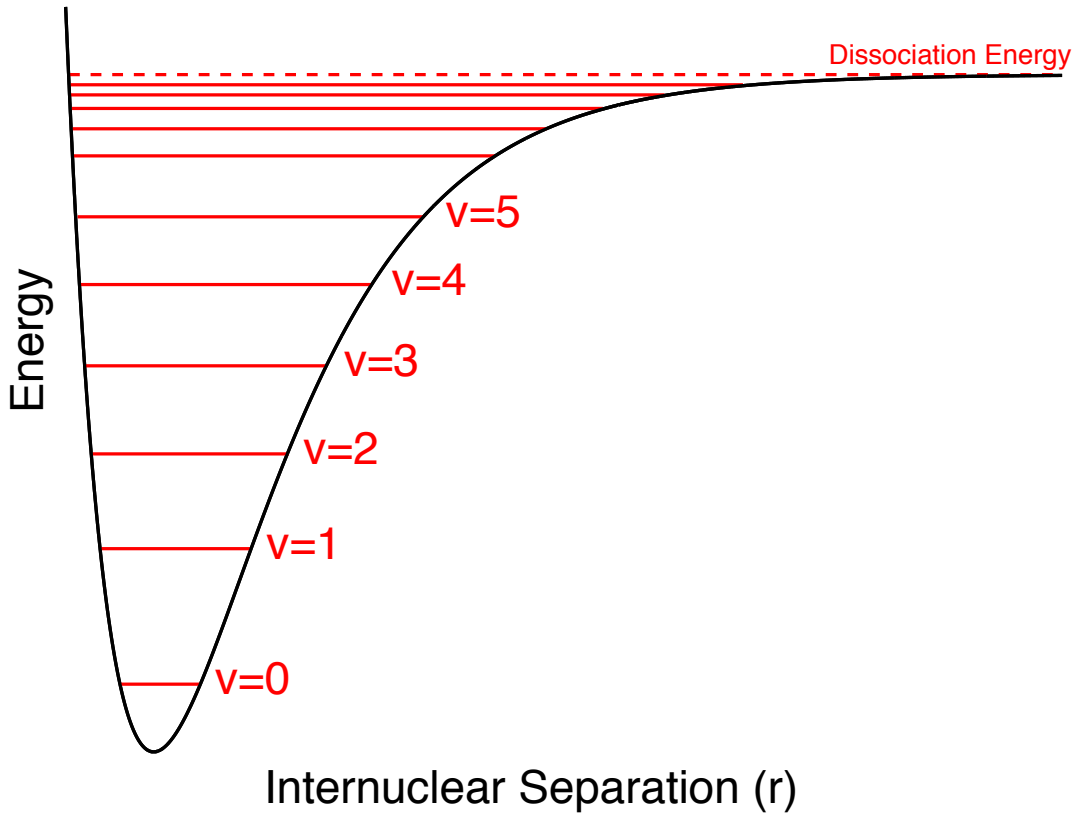

Figure 13: Cartoon of an anharmonic potential, also known as a Morse potential. The form of the potential is $V(r)=d(1-e^{-w(r-r_0)})^2$, where d is the depth of the potential, w is a width parameter, r is the internuclear separation, and r_0 is the initial internuclear separation. The anharmonic potential is not symmetric like the harmonic potential due to the presence of a dissociation energy; this also results in different energy increments between vibrational transitions. The values of the vibrational quantum number, v, are presented on the right side.

molecules' vibrational spectra. For instance, some molecules of the same species may include different isotopes of the constituent atoms; just as atoms with different numbers of neutrons are known as isotopes, molecules composed of different isotopes are known as isotopologues. Take CO for example: The most common isotopologue is $^{12}C^{16}O$ because ^{12}C and ^{16}O are the most common isotopes of carbon and oxygen, respectively. One other stable isotope of carbon exists, ^{13}C, and two other stable isotopes of oxygen exist, ^{17}O and ^{18}O. Isotopologues of CO may therefore include any combination of carbon and oxygen isotopes and each isotopologue has a unique vibrational spectrum.

Another complication to consider is the lattice structure of ices. Two important ices in the Kuiper Belt, N_2 and H_2O, have different lattice structures based on temperature and radiation dosage, respectively. N_2 has two phases at low pressure: the α and β phases. The α phase exists at temperatures below 35.61 K and the β phase exists at higher temperatures (Scott, 1976). N_2 in the α phase has a more orderly structure that results in weaker and narrower near-infrared absorption features compared to the β phase. The transition temperature is in the range of Kuiper Belt temperatures, so it is possible that some objects with very low surface temperatures, like Eris, have N_2 on their surfaces but it cannot be easily observed because it is in the α phase. For objects like Eris, the presence of N_2 can be inferred by measuring shifts in the central wavelengths of CH_4 absorption bands (e.g., Brown et al., 2005b; Tegler et al., 2010).

Water ice also exists in two phases on the surfaces of KBOs: crystalline and amorphous. Crystalline water ice is the dominant form of water ice on Earth and a variant is found on KBOs. (The variations are due to the exact geometry of the lattice structure.) This variant forms when crystalline water ice cools below 140 K (Leto and Baratta, 2003). Conversion of crystalline water ice to amorphous water ice occurs over time as it is bombarded by high-energy radiation and cosmic rays. The orientation of an individual water molecule in amorphous water ice is random with respect to its neighbors. The 1.65 μm absorption feature is unique to crystalline water ice and is used to identify this phase on the surfaces of KBOs (Grundy and Schmitt, 1998). Over a few million years, all crystalline water ice to a depth of ~100 m should be converted to the amorphous phase by photolysis and radiolysis (Cooper et al., 2003; Cook et al., 2007), yet it is still observed today on many KBOs. Many authors have invoked active cryovolcanism as a means of replenishing crystalline water ice on the surface. However, this explanation is neither feasible nor necessary. Most KBO interiors are probably not at temperatures above 140 K in the present-day and cryovolcanism must be prevalent across the surface to maintain such high crystalline water ice percentages at all rotational phases; for example, the percentage of crystalline water ice on Charon's surface is measured to be in excess of 90% (Verbiscer et al., 2006; Cook et al., 2007; Merlin et al., 2010). Additionally, Zheng et al. (2009), among others, present results from the laboratory that show amorphous water ice can be converted back into the crystalline phase by thermal recrystallization. The processes of irradiation

amorphization and thermal recrystallization reach equilibrium ~1 Gyr after crystalline ice is emplaced on the surface, even at temperatures as low as 30 K. The balance of the two phases of water ice and their co-existence on KBOs such as Charon will be discussed in more detail in Chapter V.

An underrated (and underfunded) aspect of KBO studies is the analysis of ices in the laboratory. Our understanding of KBO surface compositions comes from near-infrared spectra, and our understanding of those spectra comes from laboratory experiments. I previously discussed the theory behind near-infrared reflectance spectra, then provided examples of special cases, like N_2, where the theory is not the complete picture. Laboratory experiments fill in the gaps, enabling identification of ices on the surfaces of KBOs. A few groups are at work studying ices in the laboratory, with new spectra recently published for N_2:CH_4 solutions (Protopapa et al., 2015) and non-methane hydrocarbons (Hudson et al., 2014a; Hudson et al., 2014b). The process begins in a vacuum chamber where a molecular gas is deposited onto a thin substrate at a desired temperature (Hudson et al., 2008). The sample can be studied as is by shining near- or mid-infrared light on it and observing the reflectance spectrum, or bombarded with ions or high-energy photons to create by-products whose spectra are then obtained and analyzed. Absorption coefficients and indices of refraction (real and complex components) are also provided and used primarily for modeling purposes. Nature can produce more complex ices and ice mixtures in conditions not easily replicated in the laboratory, so previously unidentified absorption features in KBO spectra are important for

developing future experiments. Understanding of KBO surface compositions, and particularly the presence of trace species, will continue advance at the rate of laboratory studies.

Hapke Modeling. A powerful tool for analyzing near-infrared spectra of KBOs, and one that makes heavy use of laboratory data, is known as Hapke modeling (Hapke, 2012). This technique uses a radiative transfer model that accounts for scattering and absorption of light from a surface with non-zero roughness (i.e., composed of grains). When implemented, Hapke modeling constructs synthetic spectra based on assumed surface composition for comparison to observations. The free parameters when modeling a surface are grain size and areal fraction of each ice. Due to degeneracies between grain size and areal fraction, the output values should not be accepted as truly representative of the actual surface properties. Hapke modeling is ideal for characterizing the surface compositions of KBOs but is less useful for determining grain sizes and absolute amounts of a species on the surface. Other parameters discussed below, including the angular width of the opposition effect, compaction parameter, phase function, surface roughness, and asymmetry factor, are assigned values for a given surface; different surfaces may have different values for these fixed parameters.

The theory behind Hapke modeling has a lot of moving parts with the ultimate result being an equation for the bidirectional reflectance, the reflectance from a non-specular surface where the angles of incidence (i) and emission (e) are not necessarily equal (Hapke, 2012):

$$r(i,e,g) = \frac{w}{4\pi}\frac{\mu_{0e}}{\mu_{0e}+\mu_e}\left[\left(1+B(g)\right)P(g) + H(\mu_{0e})H(\mu_e) - 1\right]S(i,e,g)\,. \quad (6)$$

The variable w represents the single scattering albedo, $B(g)$ is the backscatter function, $P(g)$ is the phase function, $H(x)$ is typically the Ambartsumian-Chandrasekhar H-function, and $S(i, e, g)$ is the shadowing function. In cases where shadowing is not considered ($S(i, e, g)=1$), μ_{0e} and μ_e are reduced to $\mu_0=\cos(i)$ and $\mu=\cos(e)$, respectively, these functions are more complicated when considering shadowing, as shown later. The phase angle (the angle between the incident and emitted light) is represented by g. The incidence and emission angles are measured with respect to surface normal and vary across different parts of the surface visible to the observer because g is constant over the integration time of a spectrum. The incidence angle can also be interpreted as the zenith angle of the incoming sunlight and the emission angle as the observer viewing angle. For disk-integrated spectra (most long-slit spectra of KBOs), one can set up a grid across the projection of the KBO on the sky to calculate the incidence and emission angles on a smaller scale, as was done by Olkin et al. (2007). For spacecraft data, i and e can be determined on a pixel-by-pixel basis (Protopapa et al., 2016). The equation presented above for the bidirectional reflectance is for one surface component; as is the case for many KBOs whose surface compositions are known, more than one ice species is present. For an areal mixture (a patchy distribution also sometimes referred to as a "checkerboard" mixture), the total bidirectional reflectance is:

$$r_{total} = \sum_i F_i\, r_i\,, \quad (7)$$

where the sum of the F_is, the fractions of the individual surface components, is equal to 1. Some researchers take advantage of a Levenberg-Marquardt χ^2 minimization algorithm to expedite the search for a best fit to the data (Press et al., 2007).

I will now describe the components of the bidirectional reflectance equation, starting with w, the single scattering albedo. This function, in its simplest form, is the ratio of the light scattered (S) to the light incident (E) on an individual particle. To obtain the volume-average single scattering albedo for a collection of particles, one must consider the effects of multiple types of grains:

$$S = \sum_i N_i \, \sigma_i Q_{S_i} \tag{8}$$

$$E = \sum_i N_i \, \sigma_i \, , \tag{9}$$

N_i in the above equations is the number of particles per unit volume of type i, σ_i is the geometric cross-section for each type of particle, and Q_{Si} is the unitless scattering efficiency of each type of particle. For a given species it is convenient to consider identical particles, in which case w=Q_s, where Q_s is:

$$Q_S = S_e + (1 - S_e)\frac{(1-S_i)\Theta}{1-S_i\Theta}, \tag{10}$$

where S_e and S_i are the external and internal scattering coefficients, respectively, and Θ is the thermal transmission factor. These three quantities are calculated using the equivalent slab approximation, a key assumption in Hapke modeling. In this approximation, the size of the individual ice grains is assumed to be much larger than the wavelength of the incident, unpolarized light (D>>λ). These assumptions allow spherical grains to be considered as a slab with thickness D for

the purposes of calculating the transmitted and reflected light at the grain boundaries. Hapke (2012) provides empirical formulae for S_e and S_i:

$$S_e = 0.0587 + 0.8543R(0) + 0.0870R(0)^2 \quad (11)$$

$$S_i = 1 - \frac{1}{n}[0.9413 - 0.8543R(0) - 0.0870R(0)^2], \quad (12)$$

where

$$R(0) = \frac{(n-1)^2+k^2}{(n+1)^2+k^2}. \quad (13)$$

$R(0)$ is the coefficient of normal specular (mirror-like) reflection and n and k are the real and imaginary components of the complex index of refraction ($m=n+ik$), respectively. Values for n and k are obtained from laboratory work and are a key input for Hapke modeling. The internal transmission factor is approximately $\Theta=e^{-\alpha D}$, where α is the absorption coefficient (equal to $4\pi k/\lambda$) and D is the grain diameter (one of the two free parameters in Hapke modeling).

The backscatter function, $B(g)$, is an approximate mathematical expression for the opposition effect. This effect is important at small phase angles when the Sun, observer, and target surface are nearly lined up. Reflection by the surface is enhanced due to coherent backscatter (more scattering in direction of incident radiation when the size of the scattering particles is comparable to the wavelength; between phase angles of 0° and 2°) and shadow-hiding (increase in surface brightness due to disappearance of shadows behind grains and/or illumination of holes; important between phase angles of 0° and 20°). (The opposition effect is partially responsible for some objects in the Solar System having geometric albedos larger than 1. The geometric albedo is calculated as the ratio of reflected light from

the object to the theoretical reflection from a diffusively scattering disk of the same radius, known as a Lambertian disk. Thus, if an object is a strongly coherent scatterer rather than a diffusive scatterer, the geometric albedo can exceed 1.) The backscatter function is represented by:

$$B(g) = \frac{B_0}{1+(1/h)tan(g/2)}, \quad (14)$$

where B_0 is an empirical factor for the angular width of the opposition effect and h is the compaction parameter. B_0 is the ratio of light scattered from the illuminated portion of the ice grain to the total light scattered by the particle (both for g=0°). Light can be internally scattered within the grain so this value is not necessarily 1, though many make this assumption due to lack of information. If B_0=1, the particle is opaque and all the light reflected by the particle is reflected from the outer surface. The compaction parameter accounts for the strength of the opposition effect as the phase angle decreases (the slope of the non-linear increase) and is related to the surface porosity. Coherent backscatter and shadow-hiding each have their own independent values for B_0 and h.

The phase function, $P(g)$, describes the angular distribution of light scattered by a particle. Below I present the form of the Henyey-Greenstein phase function, a common choice for $P(g)$, which is a function of a single parameter, ξ, known as the asymmetry factor:

$$P(g) = \frac{1-\xi^2}{(1+2\xi cos\,(g)+\xi^2)^{3/2}}. \quad (15)$$

The asymmetry factor varies between -1 and 1 for backscattering and forward scattering, respectively (this parameter is assigned a value and is not a free parameter).

The Ambartsumian-Chandrasekhar H-function does not appear to have physical meaning and is purely a mathematical necessity. The integral form of the H-function is:

$$H(x) = 1 + \frac{wx}{2} H(x) \int_0^1 \frac{H(x')}{x+x'} dx'. \quad (16)$$

Hapke (2012) provides an analytical expression for the H-function that is accurate to 1% (compared to the integral form) for all values of x:

$$H(x) = \left\{1 - wx\left[r_0 + \frac{1-2r_0x}{2} ln\left(\frac{1+x}{x}\right)\right]\right\}^{-1}. \quad (17)$$

The variable x takes on the values of μ_{0e} and μ_e in the bidirectional reflectance and w is again the single scattering albedo. The diffusive reflectance (ratio of scattered to transmitted light) is $r_0=(1-\gamma)/(1+\gamma)$, where $\gamma = \sqrt{1-w}$ is the albedo factor. Values can be computed for the H-function using the analytical expression or numerically from the integral form, as in Hiroi (1994).

For completeness I include the mathematical expressions for the shadowing function, $S(i, e, g)$, though I recommend the interested reader refer to Chapter 12 of Hapke (2012) for a more thorough description. The shadowing function accounts for the effects of shadows cast by parts of the surface on others, tilted surfaces, and surface roughness. For an incidence angle less than or equal to the emission angle ($i \leq e$), Hapke (2012) presents the following expressions for $S(i, e, g)$, μ_{0e}, and μ_e:

$$S(i,e,g) = \frac{\mu_e}{\eta_e(e)} \frac{\mu_0}{\eta_{0e}(i)} \frac{\chi(\bar{\theta})}{1-f(g)+f(g)\chi(\bar{\theta})\left[\frac{\mu_0}{\eta_{0e}(i)}\right]} \tag{18}$$

$$\mu_{0e} = \chi(\bar{\theta})\left[cos(i) + sin(i)\, tan\,(\bar{\theta}) \frac{cos(g)E_2(e)+sin^2(g/2)E_2(i)}{2-E_1(e)-(g/\pi)E_1(i)}\right] \tag{19}$$

$$\mu_e = \chi(\bar{\theta})\left[cos(e) + sin(e)\, tan(\bar{\theta}) \frac{E_2(e)-sin^2(g/2)E_2(i)}{2-E_1(e)-(g/\pi)E_1(i)}\right]. \tag{20}$$

For $i>e$ the equations become:

$$S(i,e,g) = \frac{\mu_e}{\eta_e(e)} \frac{\mu_0}{\eta_{0e}(i)} \frac{\chi(\bar{\theta})}{1-f(g)+f(g)\chi(\bar{\theta})\left[\frac{\mu}{\eta_e(e)}\right]} \tag{21}$$

$$\mu_{0e} = \chi(\bar{\theta})\left[cos(i) + sin(i)\, tan\,(\bar{\theta}) \frac{E_2(i)-sin^2(g/2)E_2(e)}{2-E_1(i)-(g/\pi)E_2(e)}\right] \tag{22}$$

$$\mu_e = \chi(\bar{\theta})\left[cos(e) + sin(e)\, tan(\bar{\theta}) \frac{cos\,(g)E_2(i)+sin^2(g/2)E_2(e)}{2-E_1(i)-(g/\pi)E_1(e)}\right]. \tag{23}$$

In the above equations, $\bar{\theta}$ is known as the mean slope angle (a measure of surface roughness) and is another fixed value in Hapke modeling. The other functions $f(g)$, $\eta_{0e}(i)$, $\eta_e(e)$, $\chi(\bar{\theta})$, $E_1(x)$, and $E_2(x)$ are defined below:

$$f(g) = e^{-2tan\,(g/2)} \tag{24}$$

$$\eta_{0e}(i) = \chi(\bar{\theta})\left[cos(i) + sin(i)\, tan\,(\bar{\theta}) \frac{E_2(i)}{2-E_1(i)}\right] \tag{25}$$

$$\eta_e(e) = \chi(\bar{\theta})\left[cos(e) + sin(e)\, tan\,(\bar{\theta}) \frac{E_2(e)}{2-E_1(e)}\right] \tag{26}$$

$$\chi(\bar{\theta}) = \frac{1}{\sqrt{1+\pi tan^2(\bar{\theta})}} \tag{27}$$

$$E_1(x) = e^{-\frac{2}{\pi}cot\,(\bar{\theta})cot\,(x)} \tag{28}$$

$$E_2(x) = e^{-\frac{1}{\pi}cot^2\,(\bar{\theta})cot^2(x)}. \tag{29}$$

A simplification can be made where shadowing is ignored: $S(i, e, g)=1$, $\mu_{0e}=\mu_0=\cos(i)$, and $\mu_e=\mu=\cos(e)$.

Additional terms may be added to the equation for bidirectional reflectance to account for further aspects of the physics of real-life surfaces. The terms heretofore described are deemed adequate for modeling KBO surfaces and were used to model Pluto's surface composition in Chapter III.

Geologic vs. Astronomical KBOs

Of the thousands of KBOs and their satellites (as well as Triton and Phoebe) currently known, only three have ever been visited up-close by spacecraft: Triton by Voyager 2 and Pluto and Charon by New Horizons. Voyager 2 flew through the Neptune system and made a close approach to Triton on August 25, 1989, and for the next quarter century those views of Triton provided our only look at these icy minor bodies. Disappointingly, Voyager 2 did not carry a near-infrared spectrograph onboard so a "ground truth" surface composition was not obtained. Pluto, one of only two KBOs known at the time (the other being Charon), was often referred to as "the other Triton," and preparations were made for the New Horizons mission assuming many similarities between the two (not a bad assumption). The New Horizons spacecraft flew by Pluto and Charon on July 14, 2015, providing our best-ever view of these two KBOs. A few mysteries were solved, like the reason for Pluto's large light curve amplitude and the absence of a ring system, but many more questions were generated.

In a broader context, there are 3 big questions pertaining to KBO atmospheres, surfaces, and interiors that will continue to drive KBO studies forward in the coming decades:

- ***How are KBO surfaces altered by atmospheric interaction?***
- ***What are the important physical and chemical processes on KBO surfaces?***
- ***What are the likely replenishment mechanisms on KBOs?***

The combination of data from Voyager 2 and New Horizons with Earth-based data will help to answer the above questions. In particular, further understanding of the processes at work on the "geologic" bodies Triton, Pluto, and Charon will enhance our understanding of the "astronomical" bodies that have not been visited by spacecraft (and may never be). Aspects of astronomical KBOs not easily studied from Earth, but that will benefit from continued studies of the geologic bodies, include atmospheric dynamics, production of non-methane hydrocarbons and tholins, nitriles and haze production, atmospheric collapse, interpretation of color data, interpretation of light curves, volatile transport, diffusion of trace species, and evaluation of the potential for interior processes such as cryovolcanism. Additionally, building up a larger collection of bodies where surface processes are better understood will enable trends and patterns to become evident, as is the case for KBO dynamical classes. It will also help answer the question of how unique, or

ordinary, Triton, Pluto, and Charon are in the context of the icy bodies of the outer Solar System.

The next 3 chapters cover different aspects of the surface compositions of the geologic bodies Triton, Pluto, and Charon, and what can be learned from this information about active, recent, or ancient surface processes. In Chapter II, I discuss the areal distributions of volatile and non-volatile ices on Triton, and describe how these distributions have changed since the Voyager 2 flyby in 1989. Chapter III is an investigation into the distribution of ethane ice on Pluto's surface, and how this was used to make predictions about volatile transport on Pluto. Chapter IV makes use of Charon-only spectra from the OSIRIS instrument on Keck to calculate the surface temperature and NH_3 abundance at 6 different sub-observer latitudes; a discussion of the likelihood of cryovolcanism on Charon and other large KBOs is also presented. Chapter V ties Chapters II, III, and IV together in the context of comparative KBOlogy.

CHAPTER II

ON THE SURFACE COMPOSITION OF TRITON'S SOUTHERN LATITUDES[1]

Abstract

We present the results of an investigation to determine the longitudinal (zonal) distributions and temporal evolution of ices on the surface of Triton. Between 2002 and 2014, we obtained 63 nights of near-infrared (0.67-2.55 μm) spectra using the SpeX instrument at NASA's Infrared Telescope Facility (IRTF). Triton has spectral features in this wavelength region from N_2, CO, CH_4, CO_2, and H_2O. Absorption features of ethane (C_2H_6) and ^{13}CO are coincident at 2.405 μm, a feature that we detect in our spectra. We calculated the integrated band area (or fractional band depth in the case of H_2O) in each nightly average spectrum, constructed longitudinal distributions, and quantified temporal evolution for each of the chosen absorption bands. The volatile ices (N_2, CO, CH_4) show significant variability over one Triton rotation and have well-constrained longitudes of peak absorption. The non-volatile ices (CO_2, H_2O) show poorly-constrained peak longitudes and little variability. The longitudinal distribution of the 2.405 μm band shows little variability over one Triton rotation and is 97±44° and 92±44° out of phase with the 1.58 μm and 2.35 μm CO bands, respectively. This evidence indicates

[1] This paper was originally published in Icarus and was reformatted in this document to satisfy the CU Graduate School thesis formatting requirements. Citation: Holler, B.J., Young, L.A., Grundy, W.M., Olkin, C.B., 2016a. On the surface composition of Triton's southern latitudes. Icarus 267, 255-266.

that the 2.405 μm band is due to absorption from non-volatile ethane. CH_4 absorption increased over the period of the observations while absorption from all other ices showed no statistically significant change. We conclude from these results that the southern latitudes of Triton are currently dominated by non-volatile ices and as the sub-solar latitude migrates northwards, a larger quantity of volatile ice is coming into view.

Introduction

The images of Triton taken during the Voyager 2 flyby in August 1989 provided a tantalizing view of a diverse and dynamic surface. Two adjacent terrains on the imaged hemisphere appear drastically different in both color and texture, hinting that these two distinct surface units may have different surface ice compositions (Stone and Miner, 1989). Triton is frequently compared to Pluto, and with good reason. Triton and Pluto are comparable in size and may have come from the same initial population; it is believed that Triton is a captured Kuiper Belt Object (Agnor and Hamilton, 2006). However, Triton has a more diverse collection of surface ices, with N_2, CO, CH_4, CO_2, and H_2O ices definitively identified in ground-based spectra (Cruikshank et al., 1993; Cruikshank et al., 2000). Spectral signatures, possibly due to C_2H_6 (ethane), are present as well (DeMeo et al., 2010). Two independent investigations suggest that Triton's surface temperature is about 38 K (Broadfoot et al., 1989; Tryka et al, 1993). At this temperature, the sublimation pressures of N_2 (22 μbar), CO (3 μbar), and CH_4 (0.002 μbar) are non-

negligible, while the sublimation pressures of CO_2 (10^{-24} μbar), H_2O (0 μbar), and ethane (2×10^{-16} μbar) are negligible (Fray and Schmitt, 2009). Henceforth, we will refer to N_2, CO, and CH_4 as volatile ices due to their relatively higher sublimation pressures compared to the non-volatile ices: CO_2, H_2O, and ethane. CO_2 and H_2O are less mobile and presumably constitute the substrate upon which the volatile ices (N_2, CO, CH_4) deposit. The presence of volatile ices on the surface, though predicted for an object with the surface temperature and diameter of Triton (Schaller and Brown, 2007; Johnson et al., 2015), is surprising. The capture process and subsequent circularization of Triton's orbit through tidal interactions heated Triton significantly, resulting in the production of a thick atmosphere and blowoff of volatile species (McKinnon et al., 1995). Present-day surface composition is puzzling in light of the dynamical history of Triton.

The continued presence of volatile ices allows for an atmosphere around Triton. Despite its low surface temperature and high geometric albedo (0.719; Hicks and Buratti, 2004), the surface pressure on Triton was measured at 14±1 μbar by Voyager 2 in 1989 (Gurrola, 1995). Stellar occultations in the 1990s (through 1997) showed a surprising increase in both temperature and pressure (Elliot et al., 1998). The next occultation was observed in 2008 but the data have yet to be reduced and analyzed, so the current state of Triton's atmosphere is unknown (Sicardy et al., 2008). Triton's atmosphere is dominated by N_2 with traces of CO and CH_4 (Tyler et al., 1989; Lellouch et al., 2010). Volatile transport, driven by migration of the sub-solar point, is responsible for the observed spatial distributions and temporal

evolution of surface ices on Triton (Buratti et al., 1994; Bauer et al., 2010). Previously published papers describe in more detail the significant seasonal variations on Triton due to migration of the sub-solar point (e.g., Trafton, 1984; Hansen and Paige, 1992; Moore and Spencer, 1990). Fig. 1 shows the change in the sub-solar latitude over the period 1000-3000 C.E. A subset of that figure covering 1980-2020 C.E. is presented in Fig. 2. After reaching its maximum southern extent in 2000 (-50°), the sub-solar point[2] has turned northward, reaching -42° at the time of this writing in mid-2015. Images obtained by Voyager 2 were taken during this extended period of southern illumination. A higher albedo in the southern hemisphere led some to argue for a south polar region covered in volatile ices (e.g., Stone and Miner, 1989; Moore and Spencer, 1990). With limited spectral information in the near-infrared from Voyager 2, the composition of various regions of Triton's surface from the flyby epoch are unknown.

As measured by Voyager 2, the mixing ratio of CH_4 to N_2 in Triton's atmosphere is on the order of ~10^{-4} (Broadfoot et al., 1989; Herbert and Sandel, 1991). The presence of CH_4, even at these levels, drives ongoing photochemistry (Lara et al., 1997; Krasnopolsky and Cruikshank, 1995). Indeed, photochemical haze was seen in Triton's atmosphere by Voyager 2 (Herbert and Sandel, 1991; Rages and Pollack, 1992). The most common photochemical products of the interaction between CH_4 and extreme-UV photons, cosmic rays, and charged

[2] Triton is in a synchronous, retrograde orbit about Neptune. Its rotation is also retrograde with sunrise in the west. The sub-Neptune point is at 0° longitude. The south pole is the current summer pole.

particles from Neptune's magnetosphere are acetylene (C_2H_2), ethylene (C_2H_4), and ethane (Krasnopolsky and Cruikshank, 1995; Moore and Hudson, 2003). Higher order hydrocarbons may also be created in much smaller quantities. Photochemistry occurs primarily in Triton's atmosphere, as demonstrated by a calculation of the flux of Lyman-α photons reaching the surface. The optical depth for Lyman-α photons in Triton's atmosphere, τ, is the product of the UV cross-section of CH_4 at 120 nm (1.8×10^{-17} cm^2; Chen and Wu, 2004) and the column density of CH_4 (2.15×10^{18} cm^{-2}; Lellouch et al., 2010). This results in τ=38.7 and means that the flux of Lyman-α photons reaching Triton's surface is so exceedingly small as to be negligible. Photochemical reactions involving CH_4 occur exclusively in Triton's atmosphere.

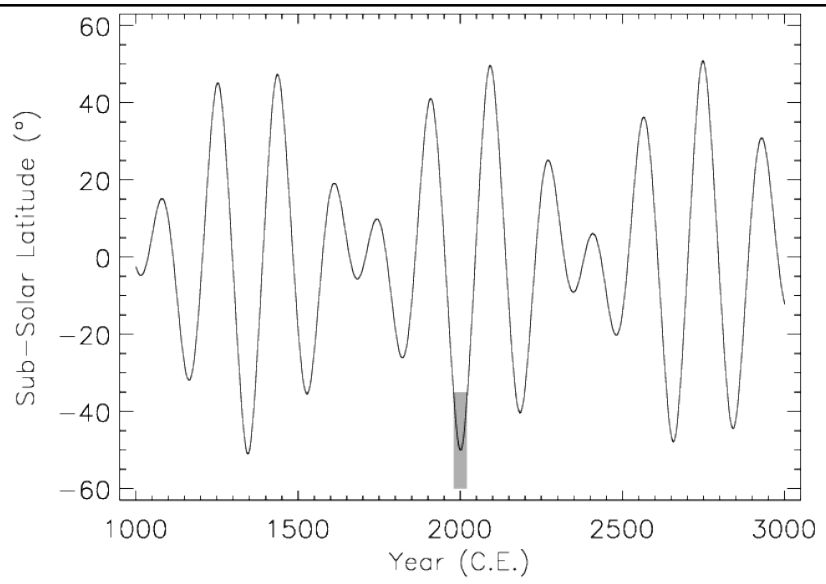

Figure 1: Sub-solar latitude on Triton between 1000 and 3000 C.E. (data from JPL HORIZONS). The combination of Neptune's obliquity (30°), the inclination of Triton's orbit (20°), and the rapid precession of Triton's orbital node (637±40 years) contribute to Triton's unique seasons (Trafton, 1984). This results in a beat pattern between the precession period and the 165-year orbit of Neptune. The shaded region covers the years 1980-2020 and is presented in more detail in Fig. 2.

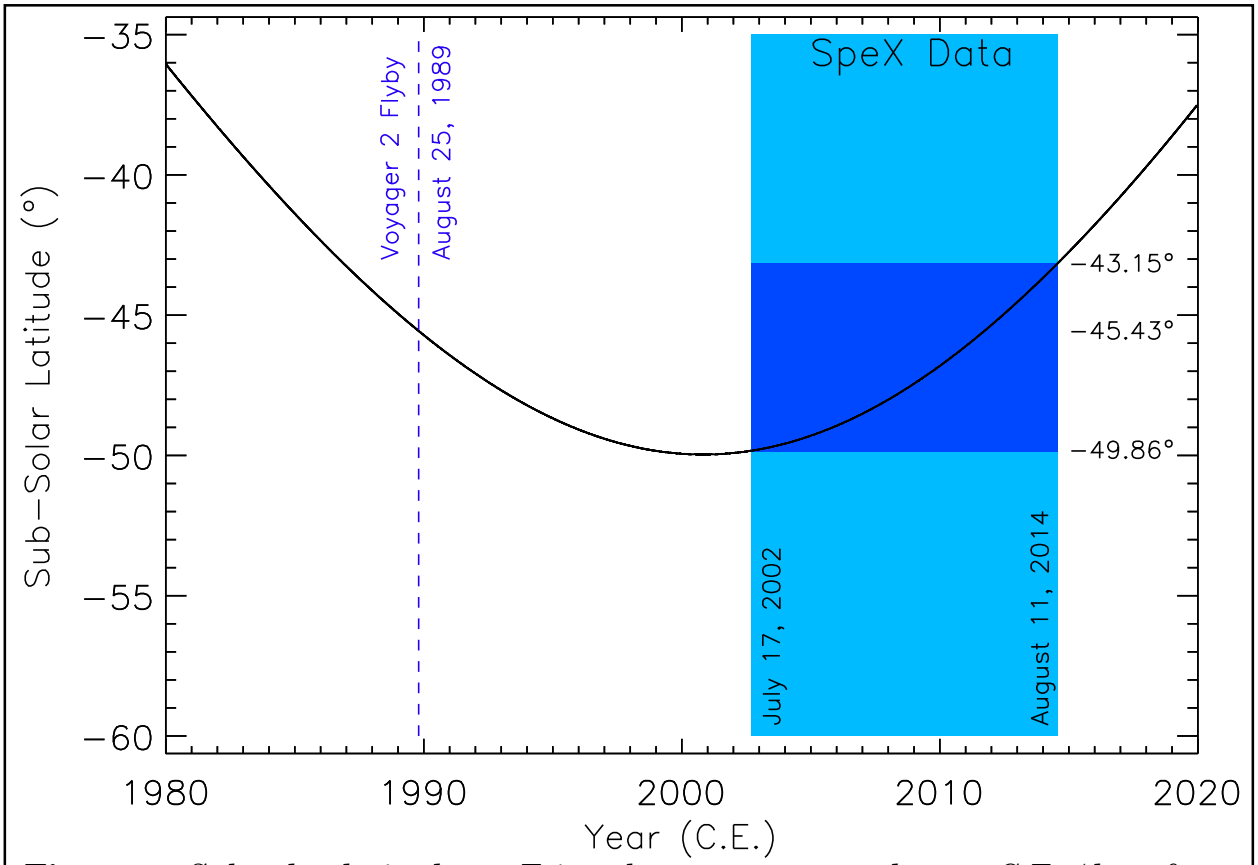

Figure 2: Sub-solar latitude on Triton between 1980 and 2020 C.E. (data from JPL HORIZONS). The maximum southern excursion of the sub-solar latitude was approximately -50° and occurred in 2000. The Voyager 2 flyby took place when the sub-solar latitude was -45.43°. The lighter region denotes the time baseline of the IRTF/SpeX observations analyzed in this paper. The darker region denotes the range of sub-solar latitudes observed. The sub-solar latitude has monotonically increased over the period of our observations.

Ethane, a photochemical product produced in large quantities (Krasnopolsky and Cruikshank, 1995), was cited as a possible constituent ice on Triton's surface by DeMeo et al. (2010). Theoretically, after forming in the atmosphere, non-volatile ethane would precipitate onto Triton's surface and accumulate over time. Once a 1 μm spherical grain forms, it precipitates out of the atmosphere at the Stokes' velocity (Mark Bullock, private communication):

$$v = \frac{2gR^2(\rho - \rho_{atm})}{9\mu}, \quad (1)$$

where g is the gravitational acceleration on Triton (77.9 cm s^{-2}), R is the radius of the ethane grains, ρ is the density of ethane (0.713 g cm^{-3}; Barth and Toon, 2003), ρ_{atm} is the density of the atmosphere, and μ is the dynamic viscosity of the atmosphere. The number density of the dominant component of Triton's atmosphere, N_2, is 10^{16} cm^{-3} at the surface (Herbert and Sandel, 1991), and we used this to calculate a mass density of 4.65×10^{-7} g cm^{-3}. This value is negligible compared to the density of solid ethane, so it was ignored in the calculation. We calculate the dynamic viscosity using Sutherland's formula (Eq. (2)). This gives a lower limit on the viscosity and therefore an upper limit to the Stokes' velocity since the effects of turbulence and eddies are ignored. The dynamic viscosity (μ) of an N_2 atmosphere at T=50 K (temperature of Triton's troposphere; Tyler et al., 1989) is:

$$\mu = \mu_0 \frac{T_0 + C}{T + C} \left(\frac{T}{T_0}\right)^{3/2}, \quad (2)$$

where T_0 is a reference temperature (300.55 K for N_2), μ_0 is the dynamic viscosity at the reference temperature (0.0002 g cm^{-1} s^{-1} for N_2), and C is Sutherland's constant for the gas in question (111 K for N_2). We calculate μ=0.00003 g cm^{-1} s^{-1}. Combining all this information yielded a descent velocity of ~0.004 cm s^{-1} for a 1 μm ethane grain. Ethane more than likely does not form perfectly spherical grains, but instead takes the form of fractal aggregates; we assume spheres for ease of calculation, so the descent velocity quoted is an upper limit. Horizontal winds at altitudes below 8 km on Triton are ~500 cm s^{-1} (Ingersoll, 1990). This means that within one equatorial circumnavigation of Triton, an ethane grain would descend, at most, on

the order of 100 m from its altitude of origin. Based on this calculation, we would expect ethane to precipitate uniformly onto Triton's surface independent of where it formed in the atmosphere. With an accumulation rate of 28 g cm^{-2} Gyr^{-1} (Krasnopolsky and Cruikshank, 1995), we calculate that a total of 180 cm of ethane has precipitated uniformly onto the surface of Triton over the age of the solar system. This assumes that Triton's atmosphere was in a steady state for the past 4.56 Gyr, so the calculated value is a rough upper limit.

Ethane ice was previously detected on Pluto, an icy, outer solar system body similar in size to Triton (DeMeo et al., 2010; Holler et al., 2014). DeMeo et al. (2010) also made a tentative detection of ethane on Triton. In this work we study the longitudinal variability of the 2.405 μm absorption feature and test whether ^{13}CO or ethane is responsible for its presence. The 2.405 μm feature is interesting because it could be due to ethane, ^{13}CO, or both (Cruikshank et al., 2006). DeMeo et al. (2010) find that the 2.405 μm feature in Triton's spectrum is too strong to be due to ethane absorption alone; ^{13}CO is therefore partially responsible for the observed depth. They also suggest the same for Pluto, presenting the possibility of a systematic error such as inaccurate optical constants. Work by Cruikshank et al. (2006) suggests that the 2.405 μm band in the spectra of Pluto and Triton is due to ethane and not ^{13}CO.

Sufficient solar illumination and the presence of strong vibrational transitions of N_2, CH_4, CO, CO_2, and H_2O make the near-infrared (0.7-2.5 μm) ideal for determining longitudinal distributions and for quantifying temporal evolution of

these ices on the surface of Triton. We obtained reflectance spectra of Triton between 2002-2014 using the same telescope and instrument, allowing for easy comparison and combination of data in an effort to describe the effects of volatile transport on Triton's surface in both space and time. We also investigated the spatial and temporal variability of the absorption feature at 2.405 μm using this large data set.

Observations & reduction

Triton was observed from 2002-2014 using the SpeX infrared spectrograph at NASA's 3-meter Infrared Telescope Facility (IRTF) atop Mauna Kea (Rayner et al., 1998, 2003). During this period, 63 nights of usable reflectance spectra were obtained with observational circumstances found in Table 1 (information for 2002/07/17 to 2009/07/21 adapted from Grundy et al., 2010). Text files including the spectra for all good nights can be found at *www2.lowell.edu/users/grundy/abstracts/2010.Triton.html* and as supplementary material online. Spectra were obtained in the short cross-dispersed mode using a 0.3" × 15" slit. We aimed for a rotation angle close to the parallactic angle while avoiding angles within 15° of the imaginary line connecting Neptune and Triton. Following this procedure significantly reduced flux contamination from Neptune. All spectra obtained prior to 2014 were resampled onto a consistent wavelength grid covering 0.67-2.55 μm at $\lambda/\Delta\lambda$~2000 to match observations made with SpeX following its 2014 upgrade.

Triton spectra were obtained using an ABBA slit dither pattern, with 2-minute integrations at each A and B position. Observations of Triton were interspersed with observations of a nearby solar analog star roughly once an hour. Solar analog spectra were also obtained following an ABBA dither pattern, with integration times dependent on the star. A solar analog requiring a large slew away from Neptune's position would potentially result in a less-than-optimal airmass correction and cause instrumental flexure, so three different stars were used between 2002 and 2014. New solar analogs were found when Neptune's motion across the sky produced too large a separation from the previous solar analog. From 2002-2007, HD 202282 (spectral type G3 V; Houk and Smith-Moore, 1988) was used as the solar analog. From 2007-2014, BS 8283 (binary with spectral types G0 V and G1 IV; Neckel, 1986; Pourbaix et al., 2004) was used as the solar analog. This binary star was checked against HD 202282 in 2007 to ensure that it could serve as the solar analog. Starting in 2014, HD 215295 (spectral type G2/3 V; Houk and Swift, 1999) was used as the solar analog.

An optimal extraction algorithm was used to reduce the Triton spectra (Horne, 1986). Wavelength calibration was performed using spectra of argon lamps contained within the SpeX instrument as well as sky emission lines in the Triton spectra themselves. The use of AB pairs eliminated sky emission lines. Airmass-corrected solar analog spectra were matched to Triton spectra with similar airmasses from the same night. Dividing the Triton spectra by the matching solar analog spectra removed solar absorption lines and corrected for telluric absorption.

Some telluric absorption persisted because it is not possible for the Triton and solar analog spectra to be obtained simultaneously at the same airmass. All spectra were then normalized. A grand average spectrum of all 63 individual nightly spectra was constructed by performing a weighted average within each wavelength bin (Fig. 3). Geometric albedos were not obtainable because the slit did not admit all light from the target object.

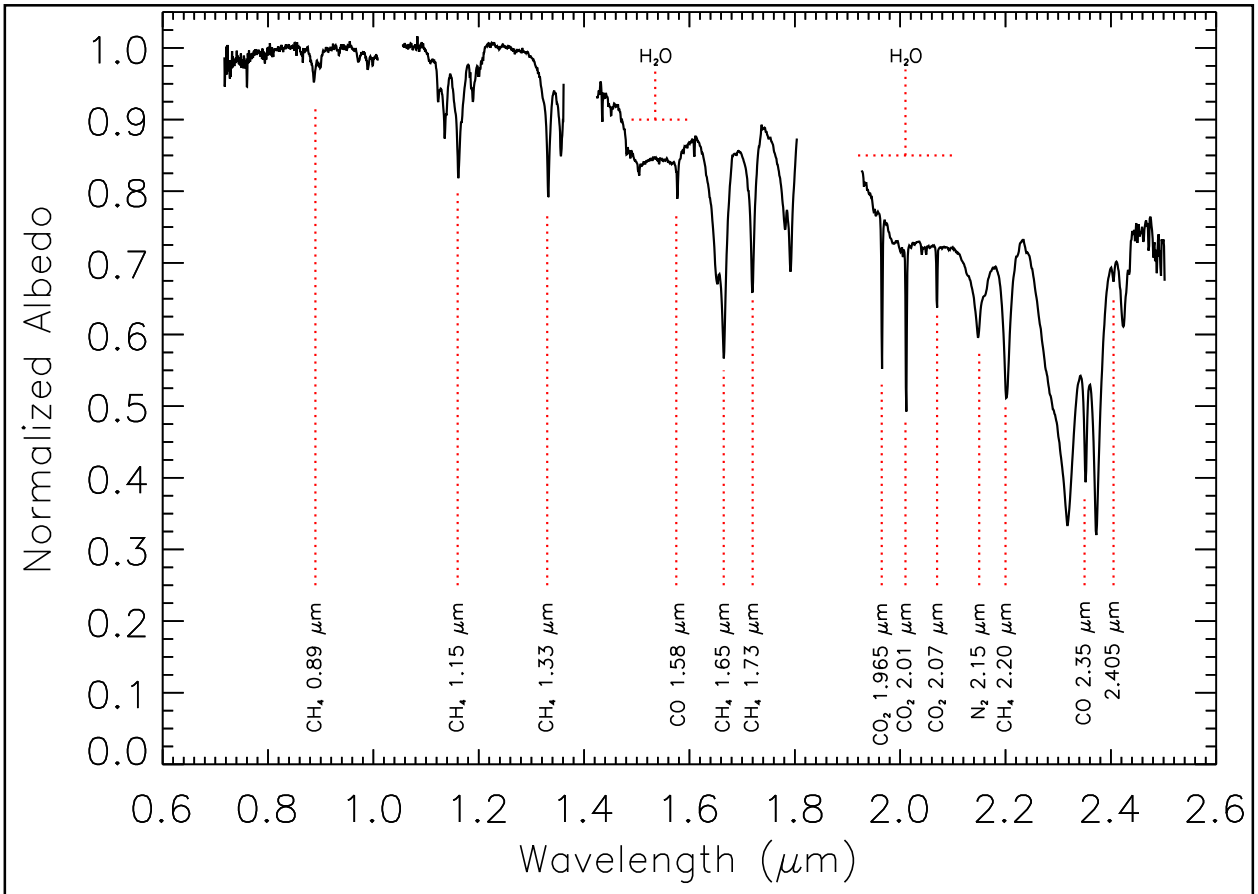

Figure 3: Combined Triton grand average spectrum of the 63 individual spectra obtained between 2002 and 2014. Regions affected by significant telluric absorption were removed. The SpeX instrument currently covers 0.67-2.55 μm at a spectral resolution of ~2000. All 63 spectra were resampled onto a consistent wavelength grid before being combined. The absorption bands considered in the analysis are identified and marked with dotted lines.

Table 1: Observational Circumstances

UT date mean-time	Weather and *H*-band seeing	Sub-Earth lon. (°E)	Sub-Earth lat. (°S)	Phase angle (°)	Total exp. time (min)
2002/07/17 09:53	Cirrus 0.8″	124.3	49.8	0.52	84
2002/07/18 09:36	Thin cirrus 0.8″	184.8	49.8	0.49	64
2002/07/19 09:31	Thin cirrus 0.7″	245.8	49.8	0.46	68
2002/07/20 09:27	Thin cirrus 0.8″	306.9	49.8	0.42	68
2002/07/21 09:29	Thin cirrus 0.6″	8.2	49.8	0.39	68
2002/07/22 09:21	Clear 0.7″	69.1	49.8	0.36	84
2002/09/16 06:19	Cirrus 0.5″	249.5	49.9	1.34	84
2002/10/03 06:32	N/A 0.6″	211.0	49.9	1.67	48
2003/07/04 13:58	Clear 0.5″	101.0	49.6	0.98	64
2003/08/10 10:09	Some clouds 0.5″	196.4	49.7	0.19	58
2003/09/10 09:32	Clear 0.6″	292.6	49.8	1.13	40
2003/10/16 05:51	Patchy clouds 0.5″	327.5	49.8	1.80	88
2004/06/28 13:07	Cirrus 0.5″	194.9	49.3	1.19	152
2004/08/12 12:19	Clear 0.7″	67.7	49.5	0.21	52
2004/09/12 10:51	Clear 1.0″	161.7	49.6	1.15	48
2004/10/21 06:13	Partly cloudy 0.8″	18.0	49.6	1.84	52
2005/07/04 13:06	Clear 0.7″	244.6	48.9	1.10	146
2005/09/19 08:02	Clear 0.5″	265.2	49.3	1.26	68
2006/05/26 14:52	Clear 0.4″	62.3	48.4	1.86	40

Table 1 (cont.)

UT date mean-time	Weather and *H*-band seeing	Sub-Earth lon. (°E)	Sub-Earth lat. (°S)	Phase angle (°)	Total exp. time (min)
2006/06/26 13:39	Cirrus 0.4″	157.9	48.5	1.37	128
2006/07/26 11:01	Clear 0.9″	188.0	48.6	0.53	72
2006/08/30 09:14	Clear 0.7″	166.0	48.8	0.62	48
2006/10/28 05:59	Thin cirrus 0.6″	170.3	49.0	1.85	68
2007/06/21 13:15	Clear 0.8″	252.6	47.9	1.53	136
2007/06/22 13:10	Thin cirrus 0.6″	313.7	47.9	1.51	160
2007/06/23 13:18	Clear 0.6″	15.2	47.9	1.49	128
2007/06/24 14:06	Clear 0.7″	78.5	47.9	1.47	88
2007/06/25 13:13	Clear 0.5″	137.5	47.9	1.45	132
2008/07/14 10:57	Clear 0.5″	318.3	47.4	1.01	72
2008/09/01 07:02	Clear 0.6″	68.1	47.8	0.55	56
2008/09/28 09:55	Partly cloudy 0.5″	288.5	48.0	1.32	60
2009/06/22 14:35	Clear 0.7″	102.2	46.6	1.59	32
2009/06/24 14:25	Clear 0.6″	224.3	46.6	1.56	80
2009/07/21 12:07	Clear 0.5″	71.7	46.8	0.88	64
2009/08/13 12:07	Mostly clear 0.6″	39.8	47.0	0.15	56
2009/08/31 11:07	N/A 0.5″	60.0	47.2	0.44	42
2010/08/07 11:08	N/A 0.7″	71.9	46.3	0.43	56
2010/08/30 09:55	Clear 0.9″	36.9	46.5	0.33	80

Table 1 (cont.)

UT date mean-time	Weather and *H*-band seeing	Sub-Earth lon. (°E)	Sub-Earth lat. (°S)	Phase angle (°)	Total exp. time (min)
2011/06/11 15:01	Clear 0.5″	233.0	45.1	1.83	28
2011/06/12 14:23	Cirrus 0.4″	292.7	45.1	1.82	86
2011/06/20 14:40	Clear 1.0″	63.4	45.1	1.72	50
2011/06/28 14:31	Cirrus 0.7″	193.0	45.2	1.58	60
2011/08/06 12:04	N/A 0.6″	54.8	45.5	0.55	60
2011/08/23 09:08	N/A 0.5″	8.1	45.6	0.02	64
2011/09/18 09:42	N/A 0.5″	161.3	45.9	0.84	56
2011/11/13 06:07	Mostly clear 0.9″	341.4	46.2	1.87	144
2012/06/25 14:19	Clear 0.7″	111.6	44.3	1.66	80
2012/07/18 14:43	Clear 0.7″	81.1	44.5	1.15	66
2012/09/02 07:01	N/A 0.7″	357.9	44.9	0.29	72
2012/09/05 09:44	Cirrus 0.7″	188.5	45.0	0.39	284
2012/09/08 08:41	Cirrus 0.7″	9.5	45.0	0.49	200
2012/09/09 09:52	Clear 0.7″	73.7	45.0	0.52	224
2012/09/10 09:51	Clear 0.6″	134.9	45.0	0.55	228
2012/09/12 10:03	Clear 0.7″	257.9	45.1	0.61	232
2012/09/13 08:54	Clear 0.7″	316.1	45.1	0.64	248
2013/07/23 15:11	N/A 0.7″	70.1	43.6	1.09	36
2013/07/25 14:55	Clear 0.9″	191.9	43.6	1.03	48

Table 1 (cont.)

UT date mean-time	Weather and *H*-band seeing	Sub-Earth lon. (°E)	Sub-Earth lat. (°S)	Phase angle (°)	Total exp. time (min)
2013/07/28 14:57	N/A 0.6″	15.7	43.6	0.95	56
2014/08/04 13:49	Mostly clear 1.0″	122.9	42.8	0.82	135
2014/08/05 13:19	Clear 0.7″	182.9	42.8	0.79	155
2014/08/06 13:10	Clear 0.5″	243.7	42.8	0.76	175
2014/08/10 12:57	Clear 0.7″	128.1	42.8	0.63	167
2014/08/11 12:59	Clear 0.3″	189.4	42.9	0.60	171

Analysis

N_2, CO, CH_4, CO_2, and the 2.405 μm band. We calculated the integrated band areas (identical to an equivalent width calculation for a normalized spectrum) of the absorption bands presented in Table 2 in order to quantify N_2, CO, CH_4, CO_2, and 2.405 μm band variations with longitude and time on the surface of Triton. As a first step, we determined the wavelength range of three separate regions around each feature: pre-absorption continuum, band, and post-absorption continuum. These wavelength ranges are presented for each absorption band in Table 2. A least squares linear fit was performed across the band on the points within the pre- and post-continuum regions (in this context, continuum does not refer to a region completely devoid of absorption). After the spectrum was normalized by the best-fit line, the integrated band area was calculated via numerical integration. The errors

on the integrated band areas were computed in an identical manner to those in Grundy et al. (2010).

The integrated band area of each night-averaged spectrum was plotted against its corresponding sub-observer longitude. A sinusoid of the form $y=A\sin(x+B)+C$, where y is integrated band area (in μm) and x is longitude, was robustly fit to the longitudinal (zonal) distribution using a non-linear least squares algorithm. The data were initially fit to a sinusoid and the residuals and standard deviation of the residuals were calculated; data points with residuals greater than 3-σ were removed and another sinusoidal fit performed (Buie and Bus, 1992). This robust-fitting process was repeated a total of three times. The period was fixed at 2π, representing one rotation of Triton. The reduced χ^2 was calculated for the sinusoidal fit and a horizontal line placed at the mean value of C (to model zero variability over one Triton rotation). The number of degrees of freedom was 60 for the sinusoidal fit and 62 for the no-variability model. The longitude of peak absorption, peak-to-peak amplitude (twice the amplitude divided by the minimum), mean (C), and reduced χ^2 values of the sinusoidal and no-variability models for each absorption band are presented in Table 3.

To quantify temporal change, the integrated band area for each night-averaged spectrum was plotted against the corresponding Julian date. The observations from each night were made over a small range of sub-observer longitudes, so to disentangle the effects of longitudinal and temporal variability the value of the sinusoidal fit at the mean longitude for each night was subtracted off.

The mean was added back on to maintain a similar mean value as the longitudinal fit. We plotted these values against phase angle for each absorption band to determine if the resulting distributions had a slope or followed a non-linear functional form. When plotted against phase angle, all distributions were essentially reasonable scatter about a mean, so phase angle effects were not considered any further in the analysis. A robust linear least squares fit was performed to determine if a particular ice species saw an increase or decrease in absorption between 2002 and 2014. The slope (m), slope detection level (m/σ_m), and y-intercept (b) for each absorption band are found in Table 4.

We also investigated how combinations of CH_4 bands varied with longitude and time. In particular, we combined the weak CH_4 bands (0.89, 1.15, and 1.33 μm), strong CH_4 bands (1.65, 1.73, and 2.20 μm), and all CH_4 bands. Combination involved addition of the integrated band areas for the appropriate CH_4 bands on each night and propagation of errors. A combination of the bands comprising the CO_2 triplet (1.965, 2.01, and 2.07 μm) was constructed in an identical manner. A combination of the 1.58 and 2.35 μm CO bands was performed but the results did not add any new information. Results for the sinusoidal fit to longitude and the linear fit to time for each combination are found in Tables 3 and 4, respectively.

H_2O. Analysis of the longitudinal distribution and temporal evolution of H_2O ice on Triton proceeded differently than for the other ices. As seen in Fig. 3, absorption due to H_2O is very broad and overlaps with absorption bands of CH_4, CO, and CO_2. This prevented the calculation of an integrated band area, so instead we

calculated fractional band depth for H_2O. The fractional band depth was computed for each individual spectrum by dividing the mean value of the points in a relatively flat region of H_2O absorption (1.5099-1.5694 μm) by the mean value of the points in a suitable continuum region (1.2195-1.2693 μm), and subtracting this quantity from one. While the fractional band depth is an even cruder estimation of abundance than the integrated band area, it still provides information on how H_2O abundance differs with longitude and time. We aimed to determine differences and not absolute amounts of any species in this paper. The procedures described in the previous section were used to determine the longitudinal distribution and temporal evolution of H_2O ice on the surface of Triton. Information on the sinusoidal fit to longitude and the linear fit to time are found in Tables 3 and 4, respectively.

Table 2: Continuum and Band Regions

Absorption band	Pre-absorption (μm)	Band (μm)	Post-absorption (μm)
N_2 (2.15 μm)	2.0925-2.1164	2.1164-2.1739	2.1739-2.1838
CO (1.58 μm)	1.5510-1.5701	1.5701-1.5859	1.5859-1.6047
CO (2.35 μm)	2.3336-2.3453	2.3453-2.3592	2.3592-2.3678
CO_2 (1.965 μm)	1.9564-1.9608	1.9608-1.9707	1.9707-1.9850
CO_2 (2.01 μm)	1.9995-2.0068	2.0068-2.0178	2.0178-2.0381
CO_2 (2.07 μm)	2.0539-2.0651	2.0651-2.0736	2.0736-2.0963
2.405 μm	2.3970-2.4014	2.4014-2.4090	2.4090-2.4134
Weak CH_4 bands			
CH_4 (0.89 μm)	0.8595-0.8776	0.8776-0.9085	0.9085-0.9298
CH_4 (1.15 μm)	1.0694-1.0995	1.0995-1.2096	1.2096-1.2296
CH_4 (1.33 μm)	1.2402-1.2920	1.2920-1.3423	1.3423-1.3435
Strong CH_4 bands			
CH_4 (1.65 μm)	1.6040-1.6194	1.6194-1.6839	1.6839-1.6985
CH_4 (1.73 μm)	1.6855-1.6970	1.6970-1.7368	1.7368-1.7439
CH_4 (2.20 μm)	2.1739-2.1838	2.1838-2.2279	2.2279-2.2360

Table 3: Rotational Sinusoidal Fits

Absorption band	Peak long. (°)	Peak-to-peak amp. (%)	Mean (10^{-6} μm)	Reduced χ^2 Line	Reduced χ^2 Sine
N_2 (2.15 μm)	35±1	68±1	3371.6±8.8	2.8	45
CO (1.58 μm)	60±3	33±1	342.6±1.5	1.3	2.1
CO (2.35 μm)	55±4	90±6	1016±13	0.9	3.7
CO_2 (1.965 μm)	97±54	8±8	732±20	0.1	0.1
CO_2 (2.01 μm)	124±83	4±7	846±20	0.3	0.3
CO_2 (2.07 μm)	236±12	15±3	297.6±2.9	0.2	0.2
CO_2 (All)	128±61	4±5	1877±31	0.3	0.3
H_2O[3]	228±100	1±1	0.15938±0.00085	1.5	1.5
2.405 μm	152±44	30±25	95.3±7.1	1.1	1.1
CH_4 (All avg.)	296±1	22±1	24144.8±3.2	6.3	48
Weak CH_4 bands					
CH_4 (Weak avg.)	285±1	36±1	8620.4±1.7	15	58
CH_4 (0.89 μm)	304±1	37±1	566.3±1.7	3.2	5.0
CH_4 (1.15 μm)	284±1	37±1	6140.2±4.3	19	54
CH_4 (1.33 μm)	284±2	32±1	1901.9±5.6	5.4	14
Strong CH_4 bands					
CH_4 (Strong avg.)	307±2	16±1	15514±28	3.2	16.6
CH_4 (1.65 μm)	313±2	15±1	8068±14	2.4	14
CH_4 (1.73 μm)	315±4	19±1	3050±13	1.4	4.5
CH_4 (2.20 μm)	289±1	17±1	4397.70±0.60	1.9	4.3

[3] The fractional band depth was calculated for the H_2O absorption instead of the integrated band area. Therefore, the mean value and uncertainty on the mean value are reported as unitless fractions.

Table 4: Secular Linear Fits

Absorption band	$m \pm \sigma_m$ (10^{-6} μm yr^{-1})	m/σ_m	$b \pm \sigma_b$ (10^{-6} μm)	Reduced χ^2 $\lvert m \rvert > 0$	Reduced χ^2 $m = 0$
N_2 (2.15 μm)	11.4±3.2	3.6	3373±12	2.6	2.8
CO (1.58 μm)	4.6±1.2	4.0	342.0±4.8	1.0	1.3
CO (2.35 μm)	-1.4±4.5	0.3	1015±18	0.9	0.9
CO_2 (1.965 μm)	2.6±4.6	0.6	732±19	0.1	0.1
CO_2 (2.01 μm)	6.1±5.0	1.2	848±21	0.3	0.3
CO_2 (2.07 μm)	1.0±2.4	0.4	297.5±9.7	0.2	0.2
CO_2 (All)	9.6±7.2	1.3	1879±30	2.0	2.1
H_2O[4]	0.0±0.0	0.2	0.15938±0.00084	1.5	1.5
2.405 μm	-2.4±1.8	1.4	94.4±7.3	1.1	1.1
CH_4 (All avg.)	30.3±7.9	3.8	24154±32	6.0	6.1
Weak CH_4 bands					
CH_4 (Weak avg.)	-32.1±4.3	7.5	8607±18	14	15
CH_4 (0.89 μm)	-3.4±1.3	2.6	566.1±5.5	3.0	3.3
CH_4 (1.15 μm)	-25.4±3.5	7.3	6131±14	18	19
CH_4 (1.33 μm)	-3.7±2.0	1.9	1899.5±8.0	5.3	5.3
Strong CH_4 bands					
CH_4 (Strong avg.)	63.7±6.6	9.7	15529±27	1.7	3.1
CH_4 (1.65 μm)	23.1±3.4	6.8	8072±14	1.6	2.3
CH_4 (1.73 μm)	14.8±3.1	4.7	3053±23	1.0	1.4
CH_4 (2.20 μm)	26.4±4.7	5.6	4407±19	1.3	1.8

Results & discussion

The longitudinal (zonal) distributions of N_2, CO, CH_4 (all bands), CO_2 (all bands), H_2O, and the 2.405 μm band are presented in Fig. 4-7 and 9-11. A discussion of temporal variability is found later in this section. Plots presenting absorption as a function of time are provided for CH_4 (strong), N_2, CO (2.35 μm), and the CO_2 triplet in Fig. 13-16.

[4] The fractional band depth was calculated for the H_2O absorption instead of the integrated band area. The slope and the uncertainty on the slope are instead reported in units of fractional band depth per year. The *y*-intercept and the uncertainty on the *y*-intercept are instead reported as unitless fractions.

The two species with the largest peak-to-peak amplitudes are the volatiles N_2 (Fig. 4) and CO (1.58 μm, Fig. 5; 2.35 μm, Fig. 6), with values of 68±1%, 33±1%, and 90±6%, respectively. The longitudes of peak absorption are 35±1°, 60±1°, and 55±4°, respectively. The phase difference between N_2 and the 1.58 μm CO band is 25±1°; between N_2 and the 2.35 μm CO band it is 20±4°; and between the two CO bands it is 5±5°. The longitudinal distributions of N_2 and CO are nearly in-phase, suggesting these species migrate together across the surface of Triton. The large peak-to-peak amplitude as well as the relative and absolute longitudes of peak absorption of these species agree with previous work performed on a smaller SpeX data set in Grundy et al. (2010). Both ices have similar, non-negligible sublimation pressures (Fray and Schmitt, 2009) and are fully miscible in one another (Vetter et al., 2007). However, note that the distributions are not completely in-phase, even when accounting for the uncertainty. The 1.58 μm CO band is found within a region of H_2O absorption, but as described below, H_2O ice shows negligible variability over one Triton rotation. The 2.35 μm CO band is in between two strong CH_4 bands at 2.32 and 2.38 μm. However, the fact that the two CO bands are fully in-phase suggests that our choices of continua regions for each band eliminated any effect from the surrounding bands. Therefore, the peak longitudes of the CO bands are accurate and the shift with respect to N_2 is real. An explanation for this phenomenon is not immediately evident.

Triton's spectrum is dominated by CH_4 absorption bands. We present here only the longitudinal variation of the sum of all CH_4 bands (Fig. 7) since the

individual CH_4 bands all have roughly the same distribution. CH_4 shows moderate variability over one Triton rotation with a peak-to-peak amplitude of 22±1%. The individual CH_4 bands, and thus the groupings of bands, all have peak longitudes in the region between ~285-315° (Fig. 8), which is in agreement with the results from Grundy et al. (2010). These peak longitudes are found on the opposite side of the sub-Neptune hemisphere from those of N_2 and the two CO bands (phase differences of 99±1° from N_2, 124±3° from the 1.58 μm CO band, and 115±4° from the 2.35 μm CO band). While only small amounts of CH_4 can be diluted in N_2, and vice versa (Prokhvatilov and Yantsevich, 1983), there is no reason to believe that the N_2 and CH_4 distributions should be so far out of phase. In fact, it is possible for N_2:CH_4 and CH_4:N_2 mixtures to spatially coexist (Tegler et al., 2012; Protopapa et al., 2015). The fact that the two distributions are so far out of phase is unexpected. A similar pattern for the N_2, CO, and CH_4 distributions are seen on Pluto (Grundy et al., 2013). This similarity may imply more than mere coincidence and requires further study.

The non-volatile ices CO_2 and H_2O show very little variation over one Triton rotation and have highly uncertain longitudes of peak absorption. We present the longitudinal variation of the sum of the CO_2 triplet (Fig. 9) rather than the individual CO_2 bands because the distributions are similar and the sum has smaller error bars. The peak longitude for the combination of CO_2 bands is 128±61° and the peak-to-peak amplitude is 4±5%. We calculated the sinusoidal fit to the H_2O fractional band depths (Fig. 10) and obtained a peak longitude of 228±100° and a

peak-to-peak amplitude of 1±1%. The longitudinal distributions for both species cannot be distinguished between a sinusoid and a horizontal line (Table 3), meaning that their distributions across the surface of Triton are uniform. This is the same conclusion reached by Grundy et al. (2010) for the non-volatile ices. We note that the peak longitude (152±44°), low amplitude, and reduced χ^2 values for the 2.405 μm band suggest a uniform surface distribution as well.

We investigated what effects, if any, the two CH_4 absorption bands at 2.38 and 2.43 μm had on the longitudinal distribution of the 2.405 μm band. The effect of CH_4 absorption must be negligible since the 2.405 μm band distribution has such a low mean (0.0000953±0.0000071 μm) and a negligible amplitude (0.000012±0.000010 μm). The peak-to-peak amplitude for the 2.405 μm band is potentially large (30±25%, rivaling the N_2 band), but this is misleading. The mean of the sinusoidal fit is very small and the amplitude is therefore large in comparison. However, the amplitude itself is low in an absolute sense. Contamination from more strongly variable CH_4 would be noticeable from its effects on both the mean and the amplitude of the sinusoidal fit. From this we conclude that our choice of continuum regions on either side of the 2.405 μm band effectively removed contamination from the adjacent CH_4 bands. The species responsible for the 2.405 μm band is distributed nearly uniformly across the surface of Triton.

From the grand average spectrum (Fig. 3) we detect the 2.405 μm absorption band at the 4.5-σ level. We compared the longitudinal distributions of CO (Fig. 5 & 6) and the 2.405 μm band (Fig. 11) to determine the origin of the latter.

The phase difference between the 2.405 μm band and the 1.58 μm CO band is 92±44°. The phase difference between the 2.405 μm band and the 2.35 μm CO band is 97±44°. Even if fractionation of CO were a factor on the surface of Triton, we would not expect the longitudinal distributions of ^{12}CO and ^{13}CO to be this far out of phase. Perhaps the quantity of ^{13}CO present on Triton is too low to detect in reflectance spectra. Assuming that carbon on Triton matches solar composition, 1% of all CO on Triton should be in the form of ^{13}CO (Scott et al., 2006). Even if ^{13}CO absorption at 2.405 μm were 1% as strong as ^{12}CO absorption at 2.35 μm (Fig. 3), the feature would be indistinguishable from noise. The longitudinal distribution of the 2.405 μm band also shares features with the distributions of non-volatile CO_2 and H_2O (Table 3): a poorly constrained peak longitude and low amplitude. This provides additional circumstantial evidence that the species responsible for the 2.405 μm band is also relatively non-volatile. Both ^{12}CO and ^{13}CO are volatile whereas ethane is non-volatile. This supports the interpretation that ethane is responsible for the absorption feature at 2.405 μm.

A summary of the longitudinal distributions across Triton's surface is presented in Fig. 12. From this figure we note the large uncertainties on the peak longitudes for the non-volatile ices (CO_2, H_2O, ethane) and the smaller uncertainties on the peak longitudes for the volatile ices (N_2, CO, CH_4). The volatile ices also show larger variability across the surface of Triton, with the longitude of peak absorption likely corresponding to a large patch of a particular ice species. CO_2 and H_2O are uniformly distributed across the surface and act as the substrate upon which the

volatile ices non-uniformly deposit (with ethane as a contaminant). One would expect the deposition of volatile ices to induce variability in the non-volatile ices, especially in regions of thick volatile coverage, yet non-volatile variability is negligible. The viewing geometry of Triton provides an explanation: Any latitude less than 90° minus the sub-solar latitude will be visible at all times. The simplest explanation for the observed variability of non-volatile ices is that they dominate the always visible south polar region. Therefore, the south polar region is relatively devoid of volatile ices. The volatile ices should be found farther north where parts of the surface rotate into and out of view.

We support this claim with our analysis of the temporal evolution of the volatile and non-volatile ices. Statistically significant slopes (≥3-σ) were found for the strong CH_4 band grouping, N_2, CO (1.58 μm), and CH_4 (all, weak band grouping, 1.15 μm, 1.65 μm, 1.73 μm, 2.20 μm). However, for all but the strong CH_4 band grouping (Fig. 13), the reduced χ^2 values do not favor a sloped line over a horizontal line (Table 4). We find that a positively sloped line is statistically preferred for the strong CH_4 band grouping, meaning the quantity of CH_4 present on the visible portion of Triton increased over time. Figures 14-16 present the temporal distributions for N_2, CO (2.35 μm), and the CO_2 triplet. N_2 and CO are volatile ices that might be expected to show a similar change in time to volatile CH_4; the two CO bands show similar changes in time, so only one is presented. From our analysis, we conclude that the signal-to-noise ratios of the nightly spectra are not high enough to distinguish between a flat and non-zero slope for any ices other than CH_4. Grundy

et al. (2010) found that the N_2 ice integrated band area showed a small decrease between 2000 and 2009 by considering two subsets of their data: 2000-2004 and 2005-2009 (see Fig. 11 of that paper). A slight downward shift in the longitudinal distribution was detected over this time period that they interpret as a change in the texture of the N_2 ice, not a change in areal coverage. A negligible change in N_2 absorption, as reported by Grundy et al. (2010), is consistent with the results of this work. Analysis of temporal variation for other species was not provided in their work.

We considered the possibility that the observed increase in CH_4 absorption was due to volatile transport. Evidence for volatile transport on Triton dates to the 1950s, with conclusive evidence for surface color change between 1979 and the Voyager 2 flyby in 1989 (Smith et al., 1989; Buratti et al., 1994; Brown et al., 1995). The disk-averaged visible spectrum (0.3-0.8 μm) of Triton became significantly less red between 1979 and 1989 as the sub-solar latitude moved 10° south. This color change was interpreted as deposition of volatile ices onto older, redder regions of the surface. Bauer et al. (2010) present evidence for significant albedo changes across the surface of Triton between the Voyager 2 flyby in 1989 and 2005. The albedo of the equatorial regions and the sub-Neptune hemisphere increased and the albedo decreased in the anti-Neptune hemisphere over this period. We note that volatile ice absorptions peak on the sub-Neptune hemisphere (Fig. 12, this work). Fig. 2 from Bauer et al. (2010) shows the 2005 visible albedo map compared to the Voyager 2 albedo map. Shortly after the Voyager 2 flyby in 1989, many argued that volatile

ices were found in the southern hemisphere due to the higher albedo (e.g., Stone and Miner, 1989; Moore and Spencer, 1990). This remains unconfirmed due to limited spectral information from Voyager 2.

The increase in CH_4 absorption may instead be due to a change in viewing geometry. Our findings suggest that the southern latitudes are primarily denuded of volatile ices, revealing the underlying non-volatile substrate. We propose that volatile ices migrated during the southern summer to the northern hemisphere where they deposited in the region near the summer/winter terminator. As the sub-solar (and thus, the sub-observer) latitude moves northwards, we receive more direct reflection from these northern latitudes and less from the region surrounding the south pole. We define the south polar region to be the entire southern hemisphere due to its visual characteristics (Moore and Spencer, 1990). The northern temperate region is defined between 0° and the most northerly observable latitude. Imagine the sub-observer point at Triton's equator; the north pole and south pole are 90° away from the equator and just visible on the edge of the disk. For other values of the sub-observer latitude, the visible region will be bounded by the nearest pole at one extreme and the latitude 90° away on the other.

At the start of the observations described in this work (July 2002), the sub-observer latitude was -49.86°; on the night of the last observation in August 2014, it was -43.15°. In both cases, the most southerly observable latitude was -90°. In 2002, the most northerly observable latitude was 40.14°; in 2014 it was 46.85°. We developed code that calculated the projected solid angle of each small area of

Triton's surface to determine the total projected area of a chosen range of latitudes. Then we divided this value by the total projected area (equal to π) to obtain the percentage of Triton's visible disk due to the chosen region. Due to longitudinal symmetry, this percentage applies at all rotational phases. See the "Calculation of Projected Solid Angle" section (pp. 116) for a more detailed mathematical description. The south polar region was responsible for 88.2% of the projected area in 2002 and 84.2% in 2014, a fractional decrease of 0.05. The northern temperate region was responsible for 11.8% of the projected area in 2002 and 15.8% in 2014, a fractional increase of 0.34.

A significant increase in albedo near the longitude of peak absorption for CH_4 is seen in the 2005 map from Bauer et al. (2010). No such brightening is noticed at the longitudes of peak N_2 or CO absorption and the latitudes of increased albedo were visible in both 1989 and 2005 (this region was visible for the entire duration of our observations). These facts cannot be explained by a change in viewing geometry and a volatile transport explanation is not immediately evident. A variety of future observations and modeling of volatile transport on Triton will be necessary to explain the observed temporal changes.

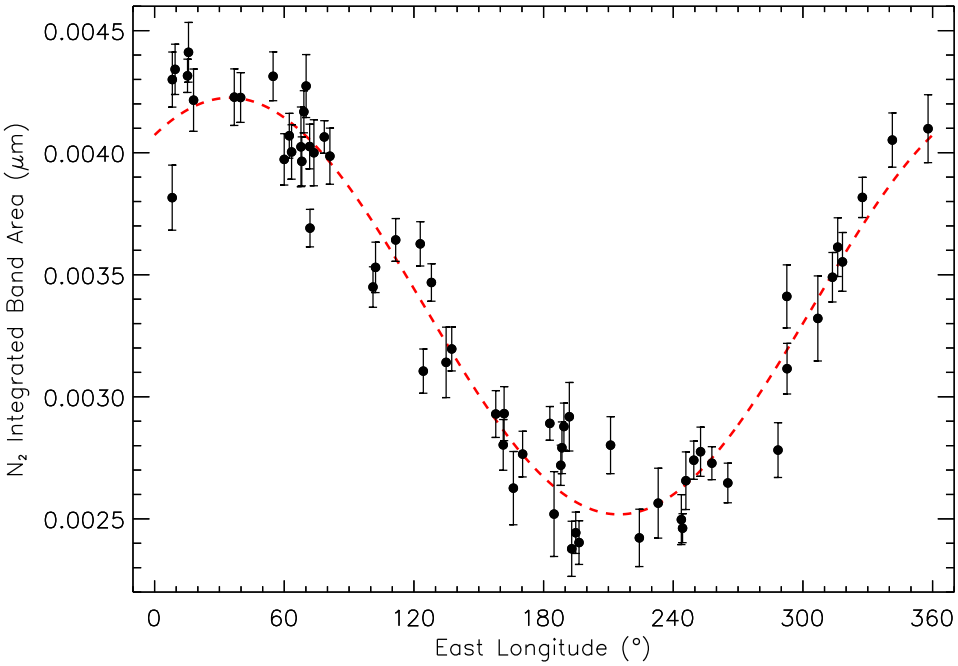

Figure 4: Integrated band area of the 2.15 μm N_2 band plotted against sub-observer longitude. The dashed line is a robust sinusoidal fit to the points. N_2 ice shows significant variation over one Triton rotation.

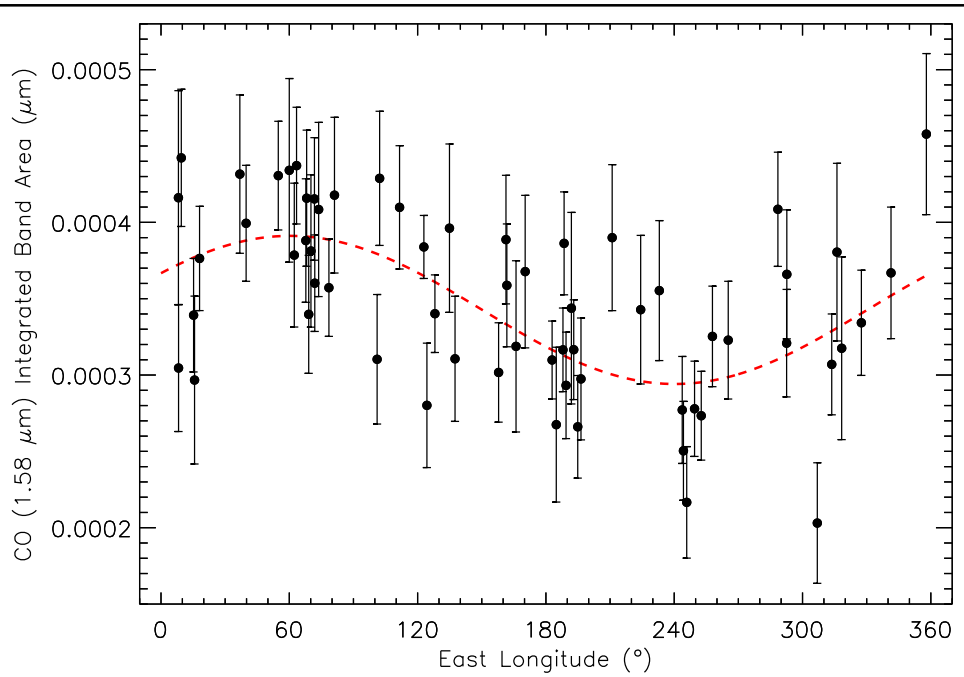

Figure 5: Integrated band area of the 1.58 μm CO band plotted against sub-observer longitude. The dashed line is a robust sinusoidal fit to the points. The phase difference between the 1.58 μm and 2.35 μm CO bands is 5±5°.

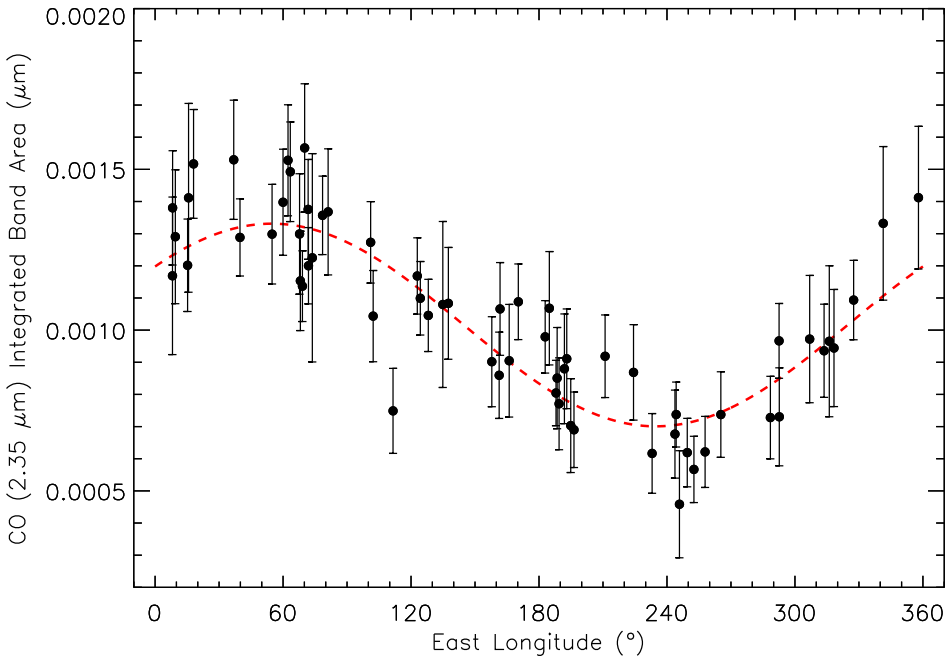

Figure 6: Integrated band area of the 2.35 μm CO band plotted against sub-observer longitude. The dashed line is a robust sinusoidal fit to the points. CO ice shows significant variation over one Triton rotation with a peak longitude similar to that of N_2 ice. This suggests that N_2 and CO migrate together as Triton's seasons change. The phase difference between the two CO bands is 5±5°.

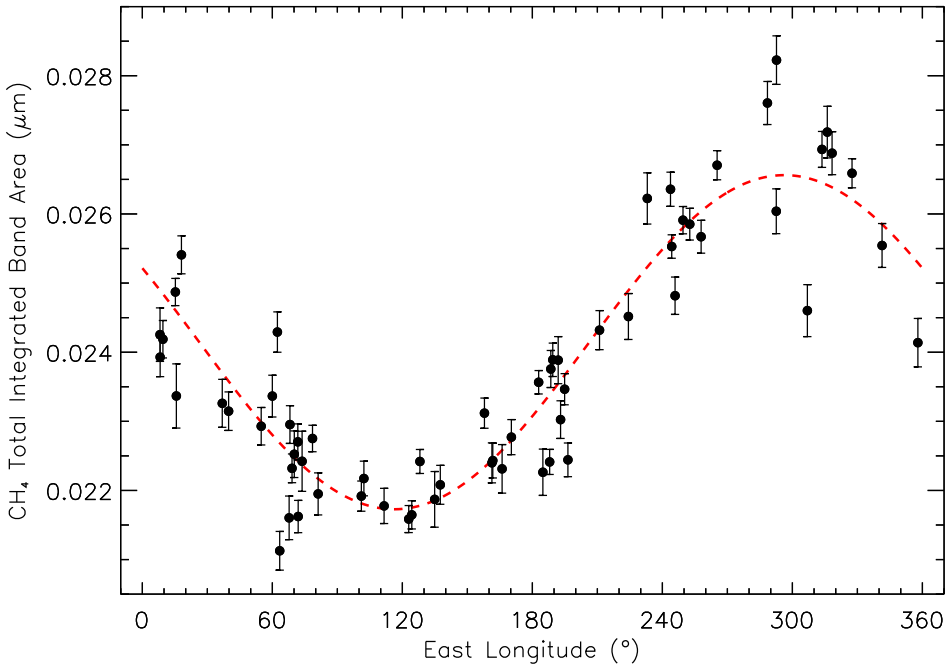

Figure 7: Total integrated band area of all CH_4 bands plotted against sub-observer longitude. The dashed line is a robust sinusoidal fit to the points. CH_4 ice shows moderate variation over one Triton rotation.

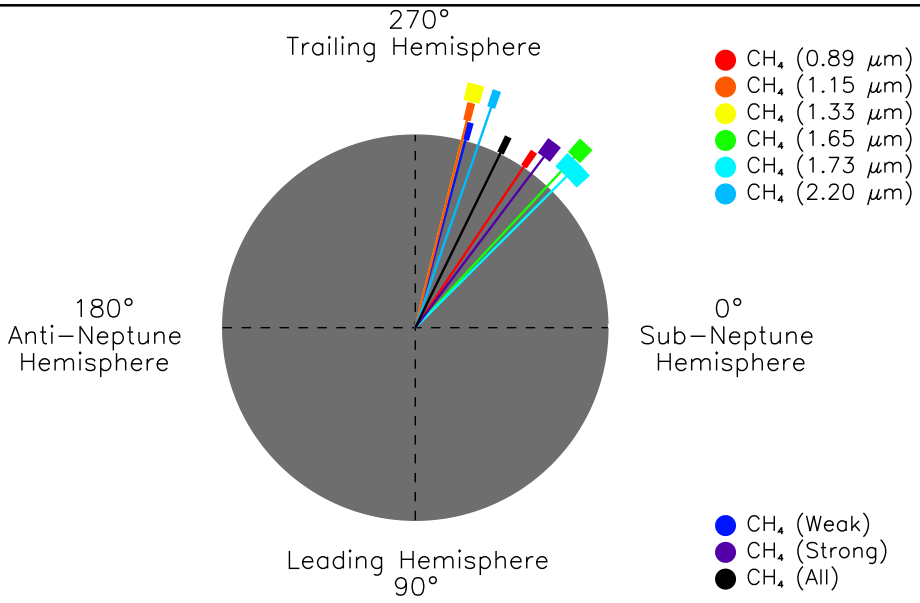

Figure 8: Range of longitude of peak absorption (longitude ± uncertainty) for all CH_4 bands and combination of CH_4 bands. Bar sizes do not represent the extent of the ices but instead show the possible location of the peak longitude for that species. The 0.89, 1.15, and 1.33 μm bands comprise the weak CH_4 grouping. The 1.65, 1.73, and 2.20 μm bands comprise the strong CH_4 grouping. Triton is viewed looking down on the south pole, with rotation and orbital motion counterclockwise.

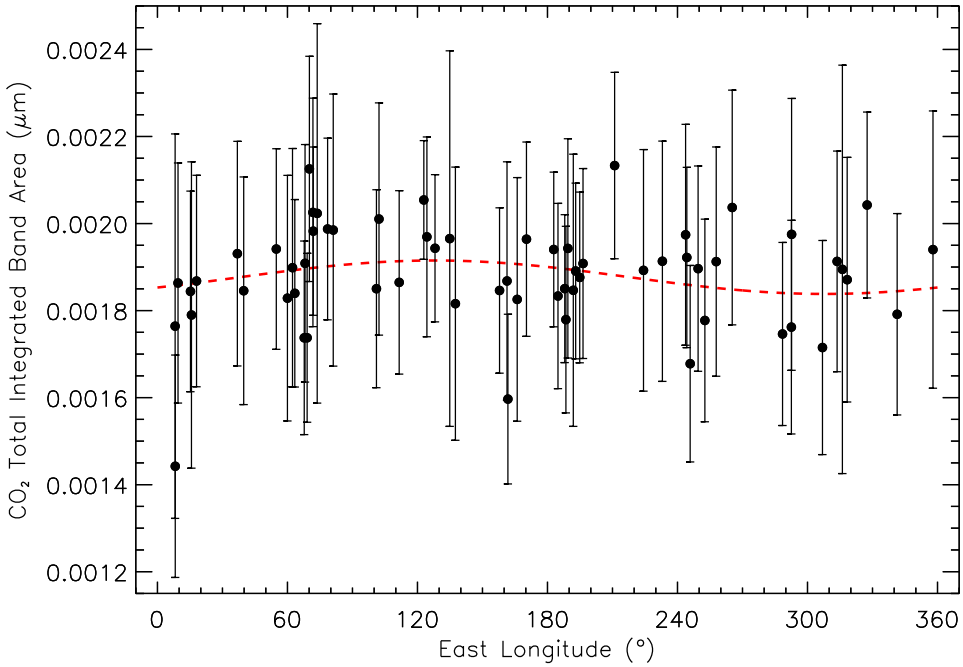

Figure 9: Total integrated band area of all CO_2 bands plotted against sub-observer longitude. The dashed line is a robust sinusoidal fit to the points. CO_2 ice shows negligible variation over one Triton rotation. Additionally, the longitude of peak absorption for CO_2 is uncertain (Table 3).

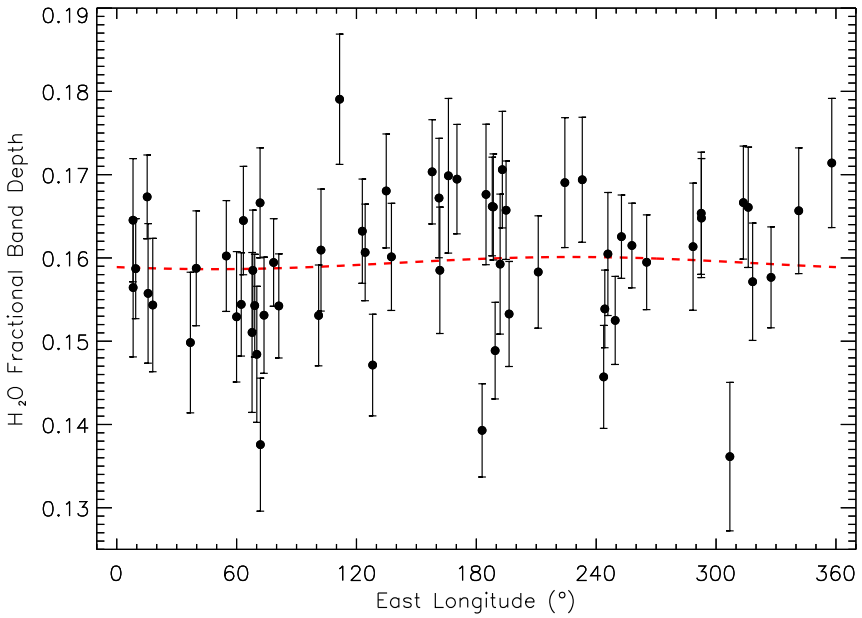

Figure 10: Fractional band depth of H_2O ice absorption plotted against sub-observer longitude. The dashed line is a robust sinusoidal fit to the points. H_2O ice shows negligible variation over one Triton rotation with a large uncertainty in the longitude of peak absorption (Table 3).

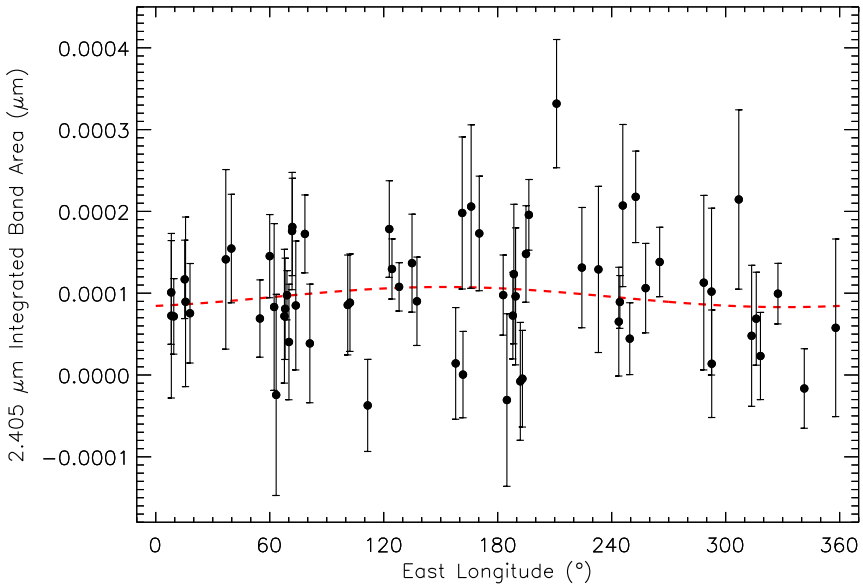

Figure 11: Integrated band area of the 2.405 μm band plotted against sub-observer longitude. The dashed line is a robust sinusoidal fit to the points. The 2.405 μm band shows negligible variation over one Triton rotation with large uncertainties in both the longitude of peak absorption and peak-to-peak amplitude (Table 3). The 2.405 μm band is consistent with ethane absorption. Negative values of integrated band area correspond to individual nightly spectra with lower signal-to-noise ratios and have no physical meaning.

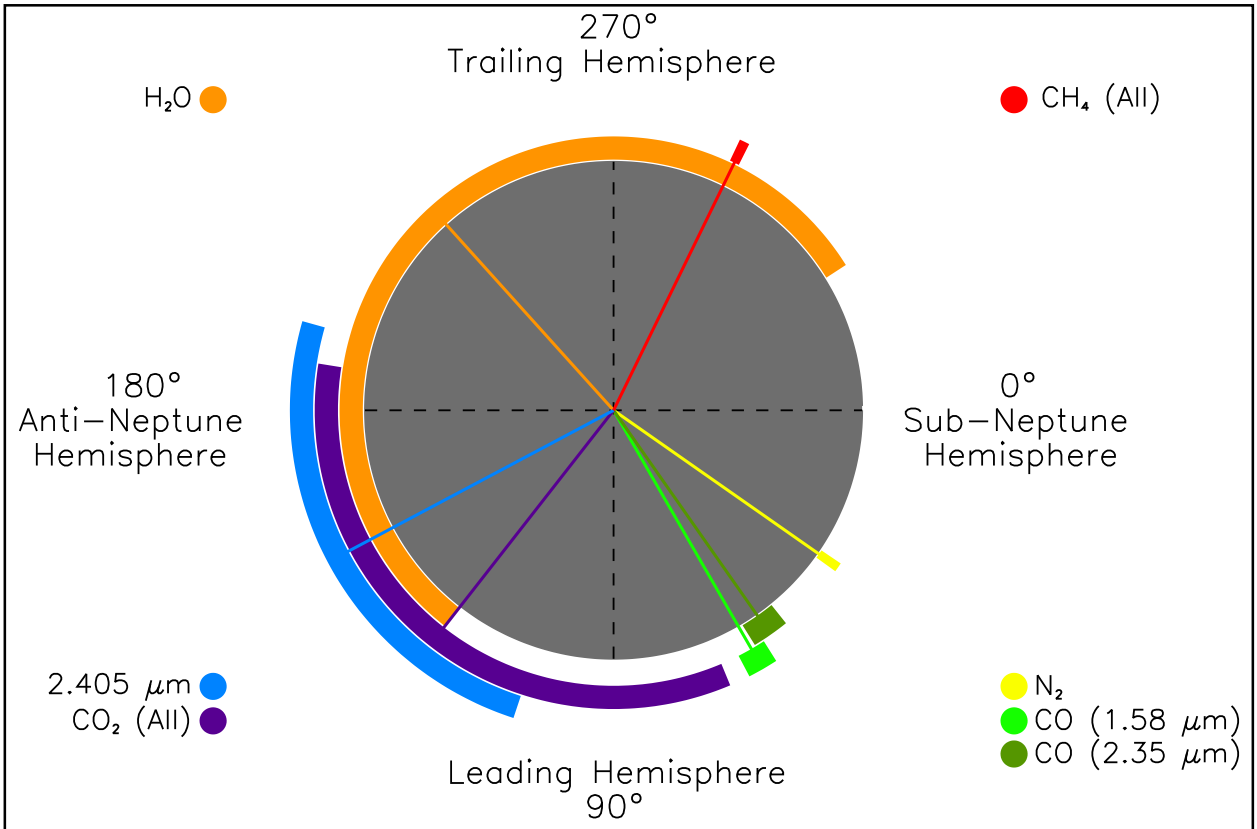

Figure 12: Range of longitude of peak absorption (longitude ± uncertainty) for all ice species found on Triton's surface. The peaks from the longitudinal distributions of the combined CH_4 bands and the combined CO_2 bands are presented for those species (denoted by "All"). Bar sizes do not represent the extent of the ices but instead show the possible location of the peak longitude for that species. Legends are in the quadrant of their respective distributions. Triton is viewed looking down on the south pole, with rotation and orbital motion counterclockwise.

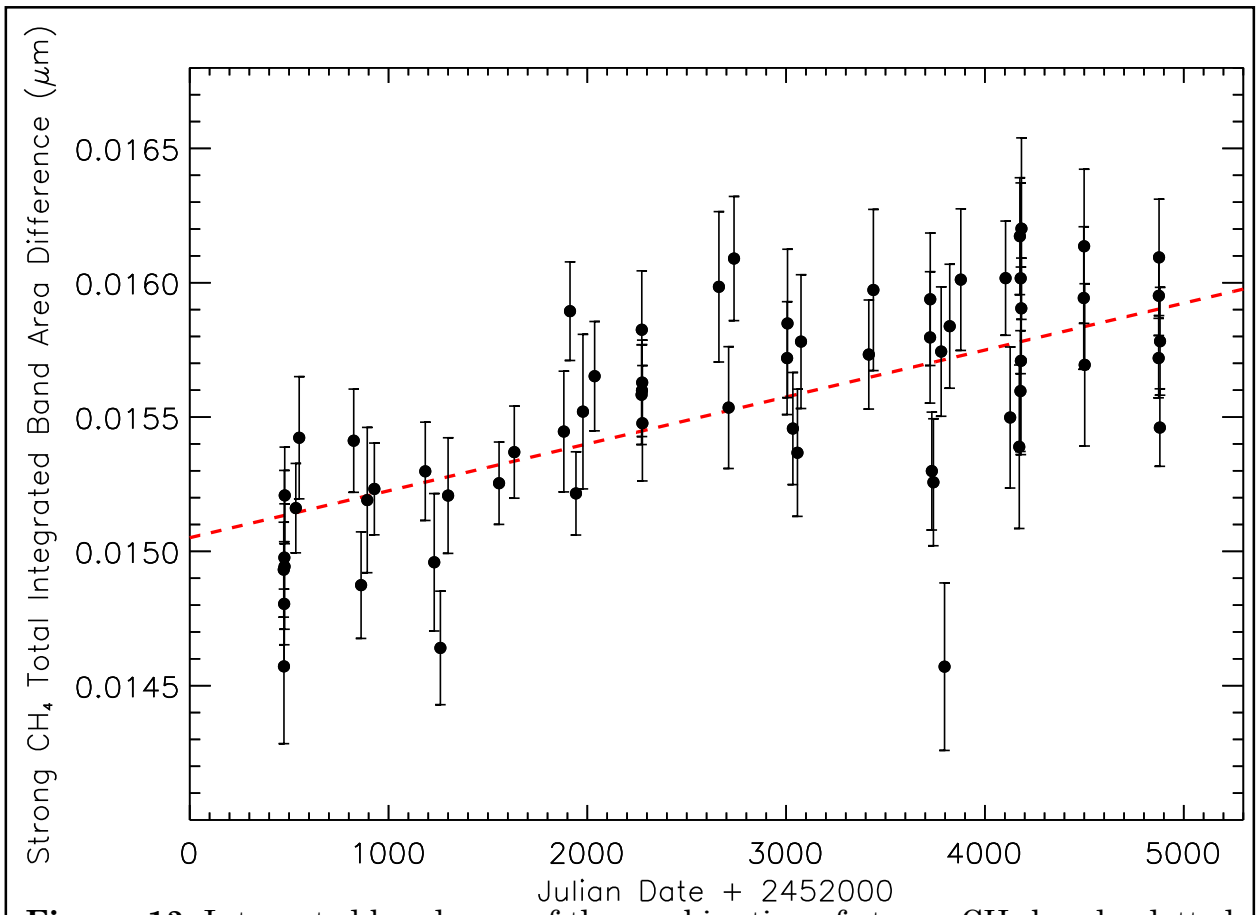

Figure 13: Integrated band area of the combination of strong CH_4 bands plotted against Julian date. The dashed line is the robust linear fit to the points. We found an increase in absorption for the combination of strong CH_4 bands over the period of our observations at the 9.7-σ level. Reduced χ^2 values (Table 4) favor a sloped line over a horizontal line. The integrated band area difference was calculated by subtracting the value of the sinusoidal fit at the proper phase from the integrated band area; the mean was added to maintain the same offset as the longitudinal distribution.

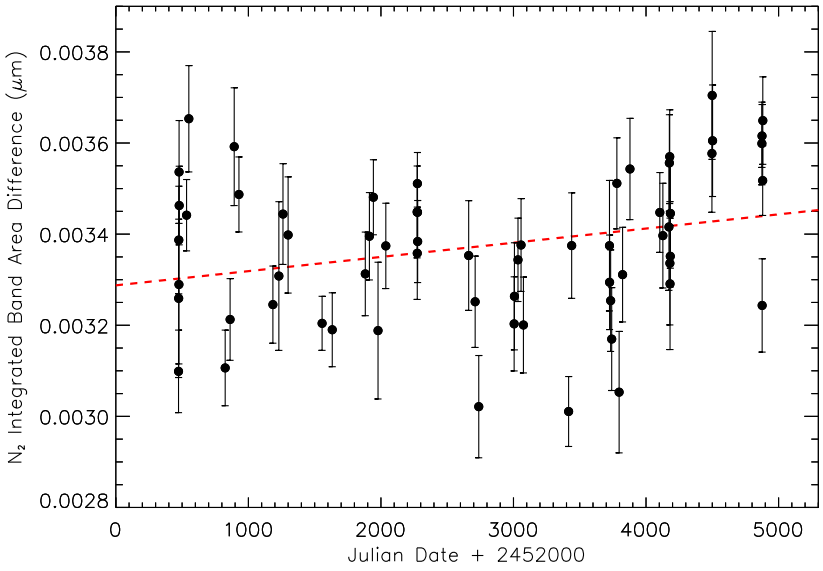

Figure 14: Integrated band area of the N_2 band plotted against Julian date. The dashed line is the robust linear fit to the points. We found a positive slope at the 3.6-σ level but the reduced χ^2 values (Table 4) do not favor a sloped line over a horizontal line. The integrated band area difference was calculated by subtracting the value of the sinusoidal fit at the proper phase from the integrated band area; the mean was added to maintain the same offset as the longitudinal distribution.

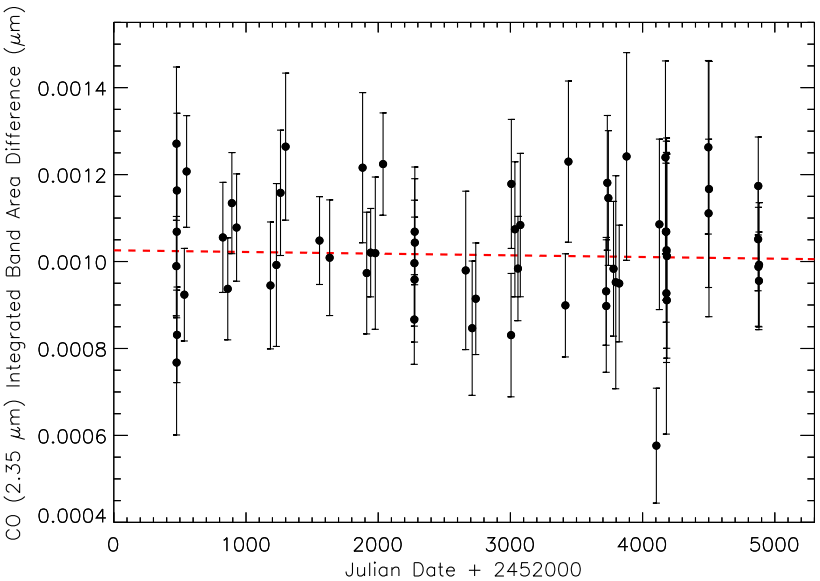

Figure 15: Integrated band area of the 2.35 μm CO band plotted against Julian date. The dashed line is the robust linear fit to the points. We found a negative slope at the 0.3-σ level and the reduced χ^2 values (Table 4) do not favor a sloped line over a horizontal line. The integrated band area difference was calculated by subtracting the value of the sinusoidal fit at the proper phase from the integrated band area; the mean was added to maintain the same offset as the longitudinal distribution.

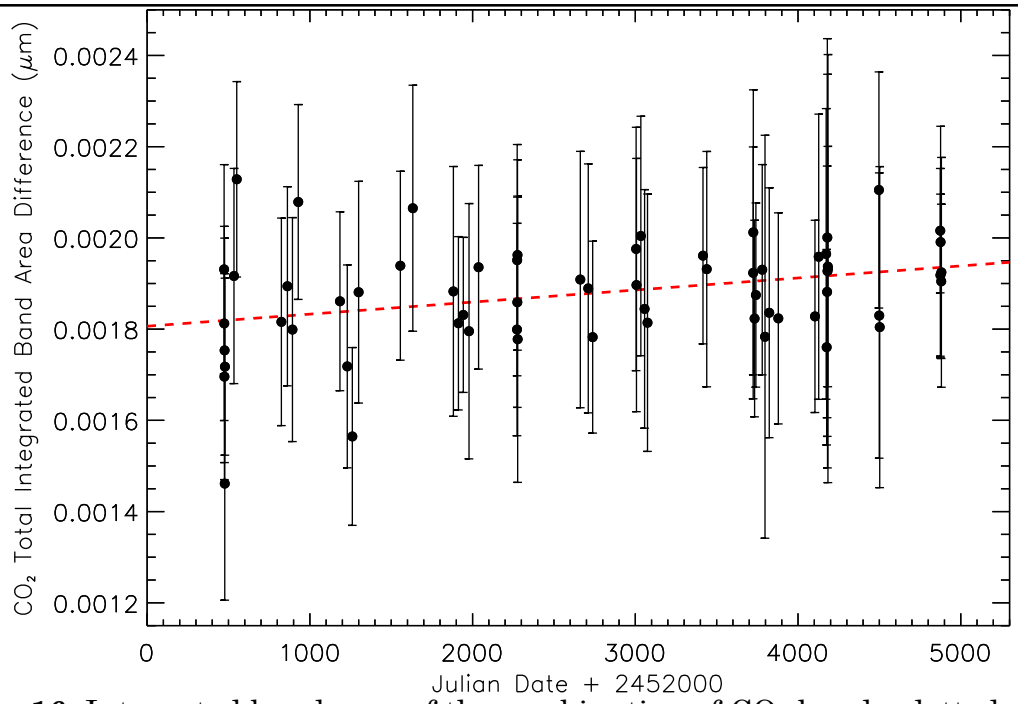

Figure 16: Integrated band area of the combination of CO_2 bands plotted against Julian date. The dashed line is the robust linear fit to the points. We found a positive slope at the 1.3-σ level and the reduced χ^2 values (Table 4) do not favor a sloped line over a horizontal line. The integrated band area difference was calculated by subtracting the value of the sinusoidal fit at the proper phase from the integrated band area; the mean was added to maintain the same offset as the longitudinal distribution.

Summary

Between 2002 and 2014, 63 near-infrared spectra were obtained with the SpeX instrument at NASA's IRTF. Analysis of the longitudinal (zonal) and temporal distributions of various ices indicate compositional changes in the 25 years since the Voyager 2 flyby. The findings of this work are summarized below:

- The volatile ices, N_2, CO, and CH_4, show significant variability over one Triton rotation. N_2 and CO have similar longitudes of peak absorption, with CH_4 offset by about 90°.

- The non-volatile ices, CO_2 and H_2O, show little variability over one Triton rotation. In fact, the longitudinal distributions for these ices are consistent with horizontal lines, suggesting a uniform distribution across the visible surface of Triton.

- The 2.405 μm band was detected at the 4.5-σ level in the grand average spectrum. Both non-volatile ethane (C_2H_6) and volatile ^{13}CO absorb at 2.405 μm. The longitudinal distribution of the 2.405 μm band is 92±44° and 97±44° out of phase with the distributions for the 1.58 μm and 2.35 μm CO bands, respectively. If there is negligible fractionation of CO, this implies that the band cannot be due to ^{13}CO. Additionally, the longitudinal distribution of the band cannot be distinguished between a sinusoid and a horizontal line, suggesting a uniform distribution across the surface, similar to the other non-volatile ices CO_2 and H_2O. This evidence is consistent with ethane absorption at 2.405 μm.

- Over the period of the observations, absorption from the combination of strong CH_4 bands (1.65, 1.73, and 2.20 μm) increased. While slopes were detected above the 3.0-σ level for N_2, CO (1.58 μm), and CH_4 (all, weak, 1.15 μm, 1.65 μm, 1.73 μm, 2.20 μm), the reduced χ^2 values for these bands do not favor a sloped line over a horizontal line. The increase in CH_4 absorption

between 2002 and 2014 may be due to volatile transport or a change in viewing geometry. Slopes for all other absorption bands were detected below the 3.0-σ level and are therefore consistent with the null hypothesis of no temporal change.

- The Voyager 2 flyby provided images of Triton's southern latitudes, but no spectra. The high albedo of the southern hemisphere in 1989 suggested coverage by volatile ices. The combination of volatile and non-volatile ice distributions implies a southern hemisphere currently denuded of volatile ices. Revealing the full extent of temporal changes since the Voyager 2 flyby will be the subject of future work.

IRTF/SpeX observations of Triton are ongoing, with five nights of spectra obtained in 2015 and a proposal submitted to continue the program in 2016. New observations are required to fully understand the processes that are altering Triton's surface. Spatially-resolved spectra of Triton would allow us to determine the latitudes of volatile and non-volatile ices. An albedo map of Triton, for comparison to previous maps made in 1989 and 2005, would be useful for quantifying the movement of ices across the surface. Information from occultations would indicate whether the surface pressure increased or decreased since the last observed occultation in 1997. Together, this information would allow us to

understand Triton's surface evolution since the Voyager 2 flyby in 1989 and to predict future changes.

Calculation of Projected Solid Angle

We derive here an equation for the calculation of the projected solid angle of a portion of a sphere. An infinitesimal solid angle (dΩ) on the surface of a sphere can be calculated from the product of the infinitesimal latitude (dθ) and longitude (dϕ), and the cosine of the latitude:

$$d\Omega = d\theta d\phi cos\theta. \quad (3)$$

The cosθ term is necessary since the solid angle of the poles themselves is zero. Integrating Eq. (3) over the entire surface of the sphere (ϕ from 0 to 2π and θ from -π/2 to π/2) results in a solid angle of 4π, as expected.

For an observer, the emission angle (χ) from each dΩ affects the calculation of the surface area visible at any given time. The projected solid angle (Ω_{proj}) is the integral of the product of the solid angle and the cosine of the emission angle:

$$\Omega_{proj} = \int_{\phi_1}^{\phi_2} \int_{\theta_1}^{\theta_2} cos\chi cos\theta d\theta d\phi \, . \quad (4)$$

The total projected solid angle has a value of π and can be visualized as an arbitrary hemisphere projected onto a circular disk of the same radius.

Now consider two vectors, $\bar{r}$ and $\overline{r_0}$, that represent the direction from the center of the sphere to a surface element dΩ and the direction from the center of the sphere to the observer, respectively. The x, y, and z components of $\bar{r}$ and $\overline{r_0}$ are

measured from the center of the sphere as seen by the observer. In vector notation, we have:

$$\bar{r} = (cos\theta cos\phi, cos\theta sin\phi, sin\theta) \quad (5)$$

and

$$\overline{r_0} = (cos\theta_0 cos\phi_0, cos\theta_0 sin\phi_0, sin\theta_0). \quad (6)$$

The emission angle is defined by the dot product of Eq. (5) and (6):

$$\bar{r} \cdot \overline{r_0} = |\bar{r}||\overline{r_0}|cos\chi \Longrightarrow cos\chi = \frac{\bar{r}\cdot\overline{r_0}}{|\bar{r}||\overline{r_0}|}. \quad (7)$$

Since of $\bar{r}$ and $\overline{r_0}$ are unit vectors, their moduli are 1. Therefore, cosχ is equal to the dot product of the two unit vectors:

$$cos\chi = \bar{r} \cdot \overline{r_0} = cos\theta cos\phi cos\theta_0 cos\phi_0 + cos\theta sin\phi cos\theta_0 sin\phi_0 + sin\theta sin\theta_0 . \quad (8)$$

The sub-observer longitude is chosen to be zero by rotational symmetry, simplifying the expression for cosχ:

$$cos\chi = cos\theta cos\phi cos\theta_0 + sin\theta sin\theta_0 . \quad (9)$$

Plugging Eq. (8) into Eq. (4) yields the projected area in terms of latitude, longitude, sub-observer latitude, and sub-observer longitude:

$$\Omega_{proj} = \int_{\phi_1}^{\phi_2}\int_{\theta_1}^{\theta_2} cos\theta[cos\theta cos\phi cos\theta_0 + sin\theta sin\theta_0]d\theta d\phi . \quad (10)$$

In this work we implemented a numerical calculation of Eq. (5) in IDL. We started by considered all longitudes (ϕ_1=0 and ϕ_2=2π) for a chosen range of latitudes, then ignored any infinitesimal surface areas with a corresponding value of cosχ that was negative. By dividing the resulting projected area by π, the value of the total projected area, we obtained a percentage of the projected area due to the region in question.

CHAPTER III

EVIDENCE FOR LONGITUDINAL VARIABILITY OF ETHANE ICE ON THE SURFACE OF PLUTO[5]

Abstract

We present the results of an investigation using near-infrared spectra of Pluto taken on 72 separate nights using SpeX/IRTF. These data were obtained between 2001 and 2013 at various sub-observer longitudes. The aim of this work was to confirm the presence of ethane ice and to determine any longitudinal trends on the surface of Pluto. We computed models of the continuum near the 2.405 μm band using Hapke theory and calculated an equivalent width of the ethane absorption feature for six evenly spaced longitude bins and a grand average spectrum. The 2.405 μm band on Pluto was detected at the 7.5-σ level from the grand average spectrum. Additionally, the band was found to vary longitudinally with the highest absorption occurring in the N_2-rich region and the lowest absorption occurring in the visibly dark region. The longitudinal variability of ^{12}CO does not match that of the 2.405 μm band, suggesting a minimal contribution to the band by ^{13}CO. We argue for ethane production in the atmosphere and present a theory of volatile transport to explain the observed longitudinal trend.

---

[5] This paper was originally published in Icarus and was reformatted in this document to satisfy the CU Graduate School thesis formatting requirements. Citation: Holler, B.J., Young, L.A., Grundy, W.M., Olkin, C.B., Cook, J.C., 2014. Evidence for longitudinal variability of ethane ice on the surface of Pluto. Icarus 243, 104-110.

Introduction

Almost 85 years have passed since the discovery of Pluto, yet its surface characteristics are still not fully understood. The primary surface ice components are N_2, CH_4, and CO (Cruikshank et al., 1997). The presence of these volatile ices is elegantly explained by comparing Pluto's surface temperature (~40 K; Tryka et al., 1994; Lellouch et al., 2000; Lellouch et al., 2011) and diameter (~2368 km; Lellouch et al., 2014) to the volatile loss curves of N_2, CH_4, and CO (Schaller and Brown, 2007). Pluto is sufficiently large and cold to retain these species over the age of the Solar System and is able to support an atmosphere of N_2, CH_4, and CO (e.g., Elliot et al., 2007). However, these volatile ices vary both with Pluto longitude and time (Grundy et al., 2013, hereafter referred to as G13; Grundy et al., 2014, hereafter referred to as G14). These variations are most likely due to changes in illumination across Pluto's surface as it orbits the Sun, allowing for sublimation of volatiles and subsequent transport, or to changes in viewing geometry.

In addition to Pluto's changing axial orientation with respect to the Sun and Earth, chemical processes are altering the composition of the surface. Extreme-UV photons and cosmic rays interact with molecules in the atmosphere, on the surface, and in some cases can penetrate deeper into the ice. In particular, CH_4 molecules may undergo photolysis or radiolysis to be converted into other hydrocarbon products such as acetylene (C_2H_2), ethylene (C_2H_4), ethane (C_2H_6), and propane (C_3H_8) (Lara et al., 1997; Krasnopolsky and Cruikshank, 1999; Moore and Hudson, 2003). From Figure 32 in Fray and Schmitt (2009), the sublimation pressures (at 40

K) of N_2 (~100 μbar), CO (~10 μbar), and CH_4 (~0.01 μbar) are much higher than those of acetylene, ethylene, and ethane (<<0.001 μbar). Non-methane hydrocarbon species shall henceforth be referred to as non-volatiles since their sublimation pressures are negligible at 40 K.

A simple calculation of the flux of Lyman-α photons reaching the surface of Pluto can answer the question of where photochemistry takes place: On the surface or in the atmosphere? The flux of photons ($F=F_0e^{-\sigma N}$) hitting Pluto's surface depends on the photon flux at Pluto's orbital distance of 30 AU (F_0=3x10^8 cm^{-2} s^{-1}; Madey et al., 2002), the UV cross-section of CH_4 at 120 nm (σ=1.8x10^{-17} cm^2; Chen and Wu, 2004), and the column density of CH_4 (N=1.75x10^{19} cm^{-2}; Lellouch et al., 2009). This calculation yields a flux of Lyman-α photons on the order of 10^{-129} cm^{-2} s^{-1}, a number that is effectively zero. If Pluto's atmosphere collapses, this calculation is no longer valid. Thus we assume photochemical products such as ethane are mainly formed in the atmosphere (Lara et al., 1997; Krasnopolsky and Cruikshank, 1999) and the descent time is long enough that horizontal winds may transport the products a great distance away from the region of origin before precipitating onto the surface (Mark Bullock, private communication). This will result in a uniform surface distribution of photochemical products regardless of whether the atmospheric CH_4 is uniform (Lellouch et al., 2015) or not (Cook et al., 2013). These non-volatile ices may subsequently be covered over time by deposition of volatiles onto the surface.

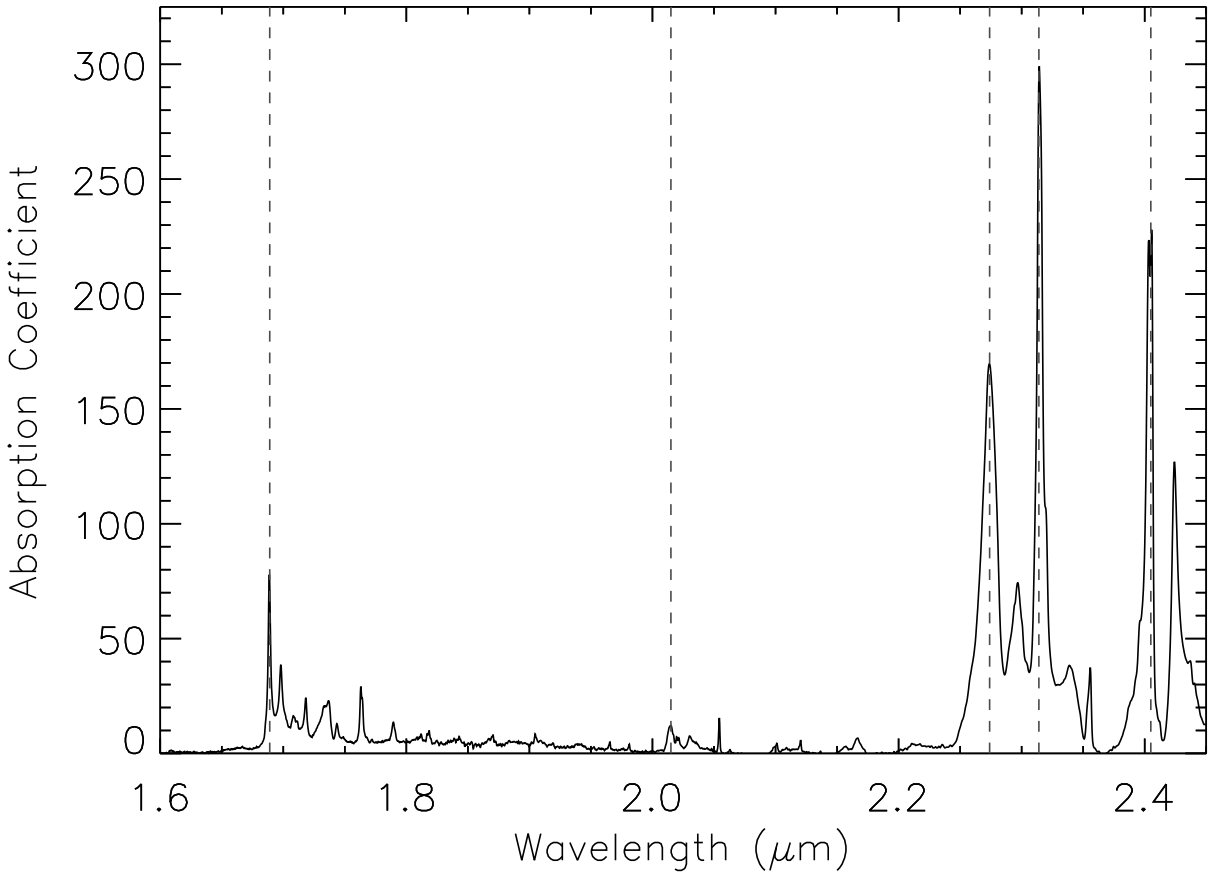

Figure 1: Absorption coefficients for pure ethane (C_2H_6) at 21 K (adapted from Quirico and Schmitt, 1997a). Dashed gray lines mark the positions of ethane lines of interest in the range 1.6-2.45 μm. From left to right: 1.689, 2.015, 2.274, 2.314, and 2.405 μm. The spectral range of IRTF/SpeX is 0.8-2.43 μm.

Sasaki et al. (2005) performed a search for acetylene, ethylene, ethane, and propane ices on Pluto in the *L* band (3.0-4.0 μm) but the results were inconclusive. DeMeo et al. (2010) identified weak ethane absorption bands at 2.274, 2.405, 2.457, and 2.461 μm in the *K* band and constrained pure ethane to <10%. The 2.405 μm band coincides with an absorption band of ^{13}CO, an isotopologue of the more abundant ^{12}CO (Cruikshank et al., 2006). DeMeo et al. (2010) argue that the 2.405 μm band is too deep compared to the 2.457 and 2.461 μm bands, and therefore ^{13}CO must contribute to the depth of the 2.405 μm band. However, individual bands of a

species may not reach maximum depth at the same longitude (as is the case for CH_4 on Pluto and Triton from G13 and Grundy et al. (2010), respectively). Conversely, Cruikshank et al. (2006) argue, based on currently unpublished CO laboratory data, that the contribution of ^{13}CO is negligible and that the 2.405 μm feature is almost entirely due to ethane absorption. This issue will be addressed more thoroughly in the Discussion section. In the same manner as DeMeo et al. (2010), Merlin et al. (2010) find less pure ethane ice on Pluto's surface (5%) in favor of more heavily radiation-processed tholins (20%). They also present an ethane life cycle theory where the surface of Pluto is effectively shielded from radiation and cosmic rays by the atmosphere during perihelion and covered in N_2 ice during aphelion. They indicate a preference for ethane creation either on methane-rich surface ice patches during aphelion or within the atmosphere during perihelion. See Figure 1 for ethane bands relevant to this work and Table 1 in Hudson et al. (2009) for a full description of ethane absorption bands seen in the infrared.

Observations

The combined Pluto/Charon spectra analyzed in this investigation were obtained on 72 nights from 2001 to 2013 using the SpeX infrared spectrograph on the 3-meter Infrared Telescope Facility (IRTF) (Rayner et al., 1998; Rayner et al., 2003). The reader is referred to Table 1 in G13 for observational circumstances of the first 65 nights (2001-2012), and Table 1 in G14 for the observational circumstances of the later seven nights (2013). The observed wavelength range

covered 0.8 to 2.43 μm using slit widths of 0.3″ ($\lambda/\Delta\lambda$~1600-1900) and 0.5″ ($\lambda/\Delta\lambda$~1200); the slit is 15″ in length. Pluto itself subtends 0.1″ while the maximum separation between Pluto and Charon is 1″, too small for SpeX to routinely spatially resolve the two bodies. Charon accounts for 20.8% of the total reflecting area in the Pluto system. However, Charon contributes less than 20.8% of the light in a combined Pluto/Charon spectrum since Charon's albedo is wavelength-dependent and generally lower than Pluto's between 0.8 and 2.43 μm (Douté et al., 1999). Spectra were obtained with the slit rotation parallel to the imaginary line connecting Pluto and Charon so that the fraction of light from Charon was independent of slit width, seeing, or guiding accuracy. This eliminated the need to quantify Charon's contribution for each individual spectrum taken throughout a given night. We included Charon's contribution when performing spectral modeling. Pluto's minor satellites Nix, Styx, Kerberos, and Hydra are so small as to be negligible in this analysis (Weaver et al., 2006; Showalter et al., 2011; Showalter et al., 2012). For a more thorough description of our observing process, the reader is again referred to G13 and G14.

Analysis

The raw spectra were reduced as described in G13. The reduced spectra analyzed in this investigation can be found as supplementary material accompanying this paper and at *http://www2.lowell.edu/users/grundy/abstracts/2014.IRTF-Pluto.html*. A weighted average was performed on the albedo values

within each wavelength interval; each value was weighted according to its uncertainty, with more accurate measurements given larger weighting factors. The resulting grand average spectrum, calculated from 72 individual spectra and covering 0.8-2.43 μm, has a spectral resolution of ~1100 and a signal-to-noise ratio (SNR) of 155 and is seen in Figure 2. The SNR was calculated by fitting a portion of the spectrum (2.38-2.40 μm) to a cubic polynomial and evaluating the scatter of the data points with respect to the fit. This region was chosen to calculate the SNR because it not only was a good fit to a cubic but also comprised a large portion of the region included in the later analysis. The 72 spectra were then sorted into six longitude bins covering the 60° intervals described in Table 1. The spectra in each longitude bin were averaged in the same manner as the grand average. The bin ranges were chosen based on the spectral characteristics described in Figure 3. Bins 1 and 2 roughly match the section observed to be dark in Pluto's visible light curve (Buie et al., 2010a; Buie et al., 2010b); this region is most likely dominated by low-albedo tholins, but this has yet to be confirmed. Bins 3 and 4 roughly correspond to a region of Pluto dominated by N_2 ice with a peak in absorption of CO, two species found to be spatially concurrent on Pluto (G13); the visible light curve also peaks in this region (Buie et al., 2010a; Buie et al., 2010b). Bins 5 and 6 cover the third of Pluto dominated by CH_4 ice.

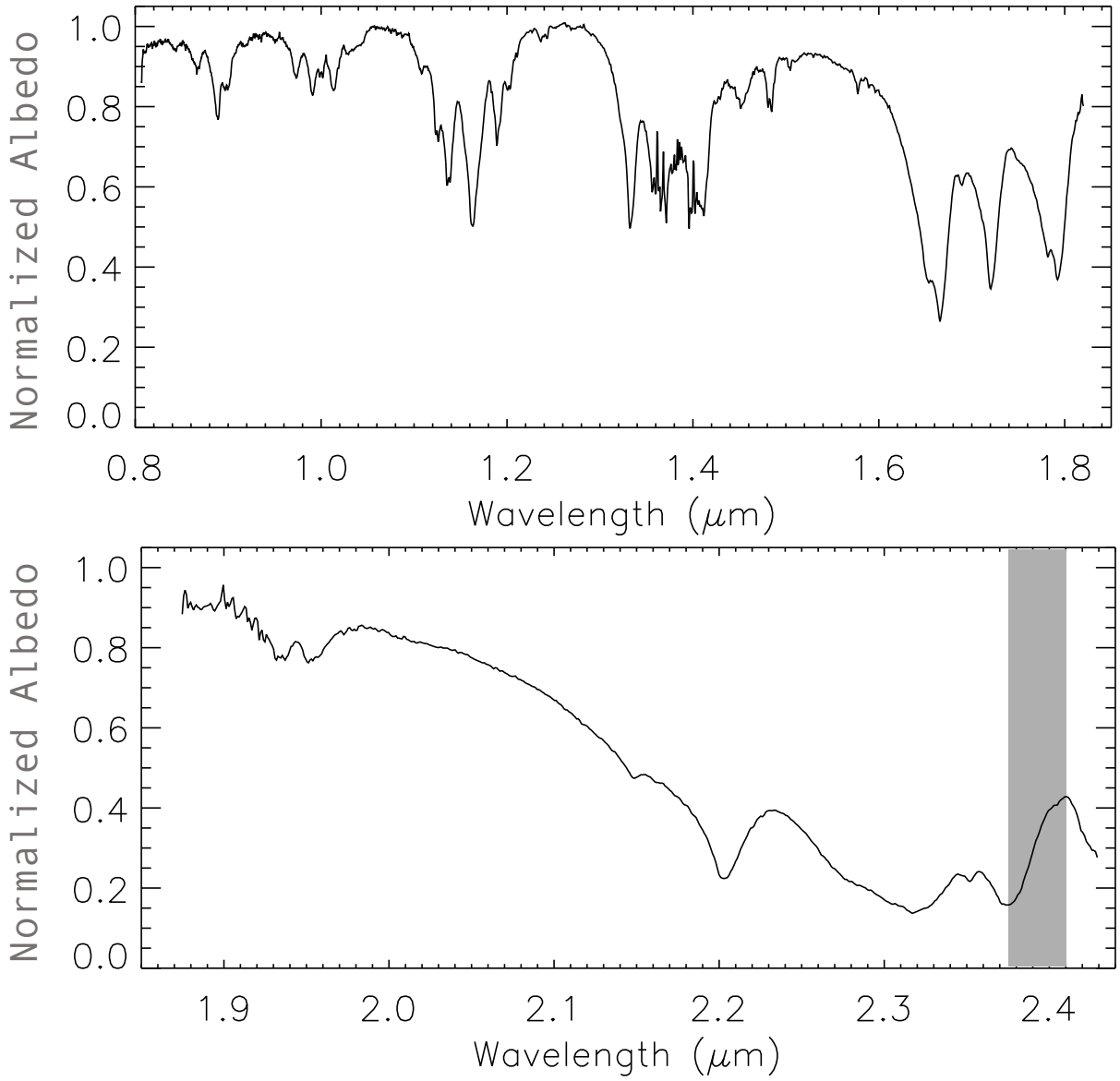

Figure 2: Combined Pluto/Charon grand average spectrum of the 72 individual spectra covering 0.8-1.85 μm (top panel) and 1.85-2.43 μm (bottom panel). Telluric absorption is present near 1.85 μm, therefore this region has been removed from the spectrum. The gray shaded region denotes the analysis region used in this investigation (described in the Analysis section). The signal-to-noise ratio of the grand average spectrum is 155.

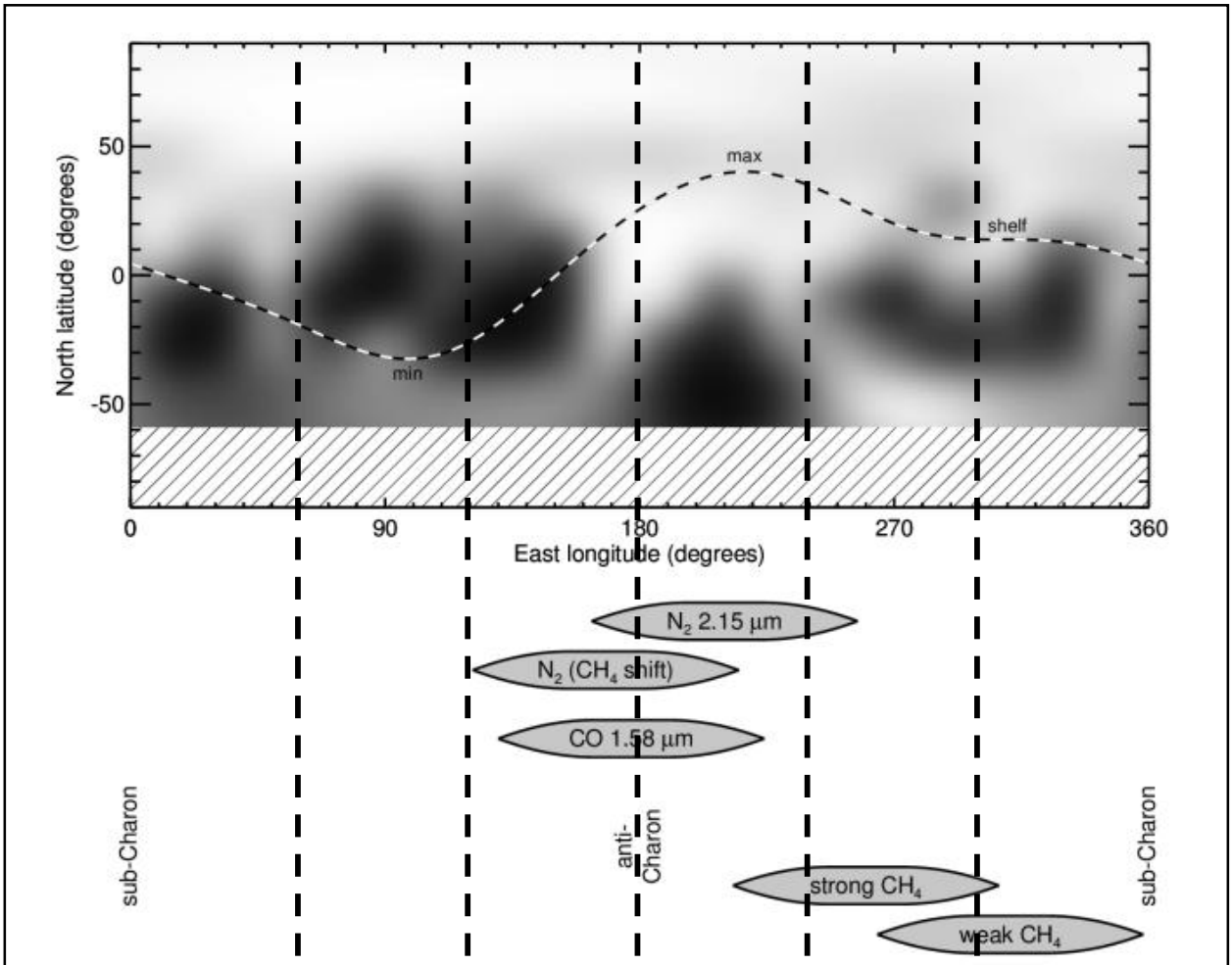

Figure 3: Pluto albedo map and visible light curve (Buie et al., 2010a; Buie et al., 2010b) with approximate longitude regions of peak absorption marked for various species by gray "battleships." This plot is adapted from Figure 25 in GR13 with dashed lines added to show the regions covered by the six 60° longitude bins. The hash marks denote the region of Pluto not currently observable at the time of the Buie et al. data acquisition (2002-2003). The region from 0°-90° is dark and does not show a peak absorption of any particular species. Strong and weak refer to strength of the CH_4 bands. The strong CH_4 bands have a peak absorption offset spatially from the weak CH_4 bands. See G13 for descriptions of the strong and weak CH_4 bands.

Table 1: Longitude Bins

Bin #	Terrain Description	Longitude Range[6]	# of Spectra	SNR	*W* (10^{-4} μm)
GA	Grand Average	2.8°-355.4°	72	155	1.57±0.21
1	Dark 1	0°-60°	9	55	2.14±0.57
2	Dark 2	60°-120°	13	108	0.72±0.38
3	N_2-dominated 1	120°-180°	13	51	2.18±0.52
4	N_2-dominated 2	180°-240°	15	68	1.71±0.42
5	CH_4-dominated 1	240°-300°	10	66	1.27±0.63
6	CH_4-dominated 2	300°-360°	12	91	1.11±0.50

The goal of this investigation was to determine how ethane abundance varies as a function of longitude across Pluto's surface. Our analysis focused on the 2.405 μm band. Other potential ethane bands within the range of the data (0.8-2.43 μm) at 1.689, 2.015, 2.274, and 2.314 μm suffered from confusion by strong CH_4 absorption bands or telluric absorption. More bands exist at 2.457 and 2.461 μm but fell outside of the data range. We made use of code based on Hapke theory (e.g., Hapke, 2012) to construct synthetic spectra that modeled the region near the 2.405 μm band. For convenience, these models will be referred to henceforth as ethane-absent continuum models. They are not spectrally flat, but instead are models assuming no ethane present on Pluto's surface. This was a more appropriate method than simply fitting the continuum to a polynomial because the surface ice components and their characteristics were taken into account. Additionally, the polynomial fits did not appear adequate even to the eye. The equivalent width of an absorption band provides a reasonable stand-in for the abundance of a substance present so we

[6] These longitudes correspond to the right-hand-rule coordinate system where 0° longitude is the sub-Charon point, north is aligned parallel to Pluto's spin axis, and sunrise is to the east.

calculated the equivalent width of the 2.405 μm band for each longitude bin and the grand average using the normalized residual.

Our analysis spanned the 2.376-2.410 μm region (gray shaded region in Figure 2); more points were present at shorter and longer wavelengths but were never adequately fit by the synthetic spectra, resulting in a visibly worse model for the continuum in the region of interest near the 2.405 μm band. Decreasing the number of points also decreased the computation time significantly. The points within the band (2.399-2.409 μm; ~10 nm in width) were excluded from the ethane-absent continuum models so that discrepancies between the model and data would not influence the χ^2 value and the behavior of the code. Failing to remove these points usually resulted in a model with parameters for the other materials altered in an attempt to fit the shape of the band.

We followed the procedure used in Cook et al. (2007) using modeling techniques described by Roush (1994) for computing the ethane-absent continuum models. The code used a simplex method (e.g., Press et al., 2007) to search the multi-dimensional parameter space for the combination of mass fractions and grain sizes that minimized χ^2. Individual materials were placed in intimate mixtures (also called "salt-and-pepper" mixtures) making up separate spatial components. We considered four spatial components in our ethane-absent continuum models: pure CH_4, Triton tholin, an N_2/N_2:CO/shifted CH_4 intimate mixture, and an H_2O/amorphous carbon intimate mixture (to model Charon). The areal coverage of the Charon spatial component was set to a constant value of 20.8% throughout this

investigation based on the ratio of Charon's reflecting area to Pluto's. The areal coverage of the other three spatial components was allowed to vary.

The sources of the optical constants of the materials considered in this investigation can be found in Table 2. Optical constants are temperature-dependent and affect the absorptive and reflective properties of a given material. The temperature of the N_2 and CH_4 ices could be chosen manually, resulting in a re-calculation of the optical constants; these are the temperature values shown in Table 2. The N_2 and CH_4 temperatures (40 K) were chosen based on estimates of Pluto's surface temperature (~40 K; Tryka et al., 1994; Lellouch et al., 2000; Lellouch et al., 2011). Additionally, CH_4 could be given an arbitrary spectral blueshift to account for being dissolved in solution with N_2. By manually choosing a blueshift, optical constants for pure CH_4 were used instead of those for an N_2:CH_4 solution. A constant blueshift of 6 nm was chosen for the shifted CH_4 throughout this investigation for the purpose of consistency.

Table 2: Optical Constants

Material	Temperature (K)	Reference
CH_4	40	Grundy et al. (2002)
Triton tholin	N/A	Khare et al. (1994)
N_2	40	Grundy et al. (1993)
N_2:CO	36.5	Quirico and Schmitt (1997b)
Amorphous carbon	N/A	Rouleau and Martin (1991)
H_2O	50	Grundy and Schmitt (1998)

Because no N_2 or CO bands were present in the small region analyzed, the 2.15 μm N_2 and 2.35 μm CO bands were analyzed independently to determine the

best-fit mass fractions and grain sizes. For N_2, the best-fit values were 99.17% and 103.6 mm, respectively. The best-fit values for CO were 0.1048% and 0.2585 mm, respectively. The errors on these values play no role from this point forward so are not reported here. Both DeMeo et al. (2010) and Merlin et al. (2010) chose an N_2 mass fraction of 99.54% and a CO mass fraction of 0.1%. DeMeo et al. (2010) chose an N_2 and CO grain size of 95 mm. The N_2 and CO grain sizes are identical since they do not consider an intimate mixture but instead have CO dissolved in solution with N_2. This investigation also used an N_2:CO solution, and the different grain sizes are interpreted as due to the separation of CO reflecting centers within the larger N_2 matrix. Similarly, Merlin et al. (2010) use an N_2 and CO solution and take the grain size to be 20 cm. This large grain size is most likely due to individual particles of sub-millimeter size behaving as an aggregate (Grundy and Buie, 2001). The mass fractions and grain sizes of N_2 and CO were then set as constants throughout the analysis of the selected region. The mass fractions and grain sizes of the other materials remained free parameters.

Synthetic spectra created using Hapke theory are not unique: Degeneracies exist between the mass fraction and grain size of a particular material and those of the other materials. No special significance should be given to the values output by the Hapke code beyond the fact that the values result in a reasonable fit to the data. Areal coverage for the spatial components, mass fractions, and grain sizes were computed for the materials described above but have limited scientific value since they are based only on an analysis of the region from 2.376-2.410 μm; they are not

quoted here. We do not perform a full analysis of the spectra from 0.8-2.43 μm as it is beyond the scope of this paper.

After obtaining the ethane-absent continuum model for a particular longitude bin, the residuals (model minus data) within the region of the ethane band were calculated. The residuals were then normalized by the ethane-absent continuum for consistency and easier comparison of results with G13 and G14. The equivalent width of the 2.405 μm band and associated errors were computed by performing a simple Riemann sum over the extent of the band (2.399-2.409 μm): $W=\Sigma\Delta_i R_i$, where Δ_i is the wavelength separation between data points i-1 and i and R_i is the normalized residual at data point i.

Results

We report a 7.5-σ detection of the 2.405 μm band from modeling the continuum of the grand average spectrum. The equivalent width of the band was calculated to be (1.57±0.21) x 10^{-4} μm. The dashed line in Figure 4 denotes the grand average equivalent width value with the gray shaded regions representing the uncertainty. These SpeX data suggest the presence of ethane ice on the surface of Pluto.

Equivalent widths for the 2.405 μm band from the six longitude bins can be found in Table 1 and are presented graphically in Figure 4. Nominally, peak absorption occurs between 120°-180°, but due to the uncertainties on the equivalent width calculations, the peak may actually occur in either the 0°-60° (Dark 1) or

180°-240° (N_2-dominated 2) bins instead. The minimum could occur in either the 60°-120° (Dark 2), 240°-300° (CH_4-dominated 1), or 300°-360° (CH_4-dominated 2) bins. Pluto's visible light curve is at a minimum between 60° and 120° (Buie et al., 2010a; Buie et al., 2010b), a potentially tholin-dominated region that almost exactly coincides with the full extent of the darkest area of Pluto as seen in Figure 3. Absorption is not clearly evident in the bin 2 spectrum (Figure 5, Figure 6) and the equivalent width value is 1.9-σ above zero; a definitive statement about absorption in this region cannot be confidently made based on the statistics. Additionally, the difference between the equivalent width in this region and those of the adjacent regions is statistically significant. In terms of equivalent width of the 2.405 μm band, the 60°-120° region is unique on this half of Pluto and appears to have more in common with the CH_4-dominated regions (240°-300° and 300°-360°). The ethane-absent continuum models for all six longitude bins and the grand average plotted against the data are found in Figure 5 with normalized residuals found in Figure 6.

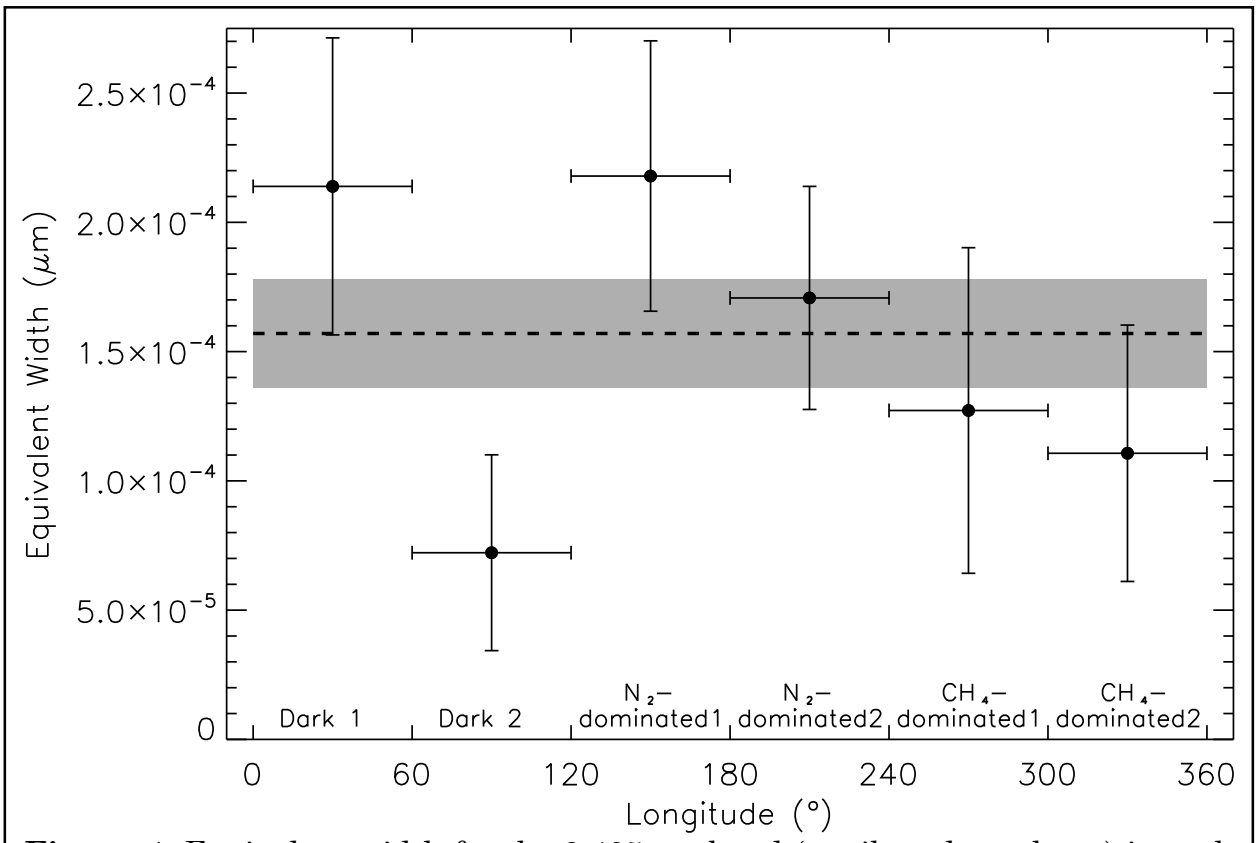

Figure 4: Equivalent width for the 2.405 μm band (attributed to ethane) in each of the 60° longitude bins. Vertical error bars are 1-σ errors computed on the equivalent width. Horizontal bars mark the longitude range covered by each bin. The black dashed line is the value of the equivalent width from the grand average and the gray area represents the error on that calculation.

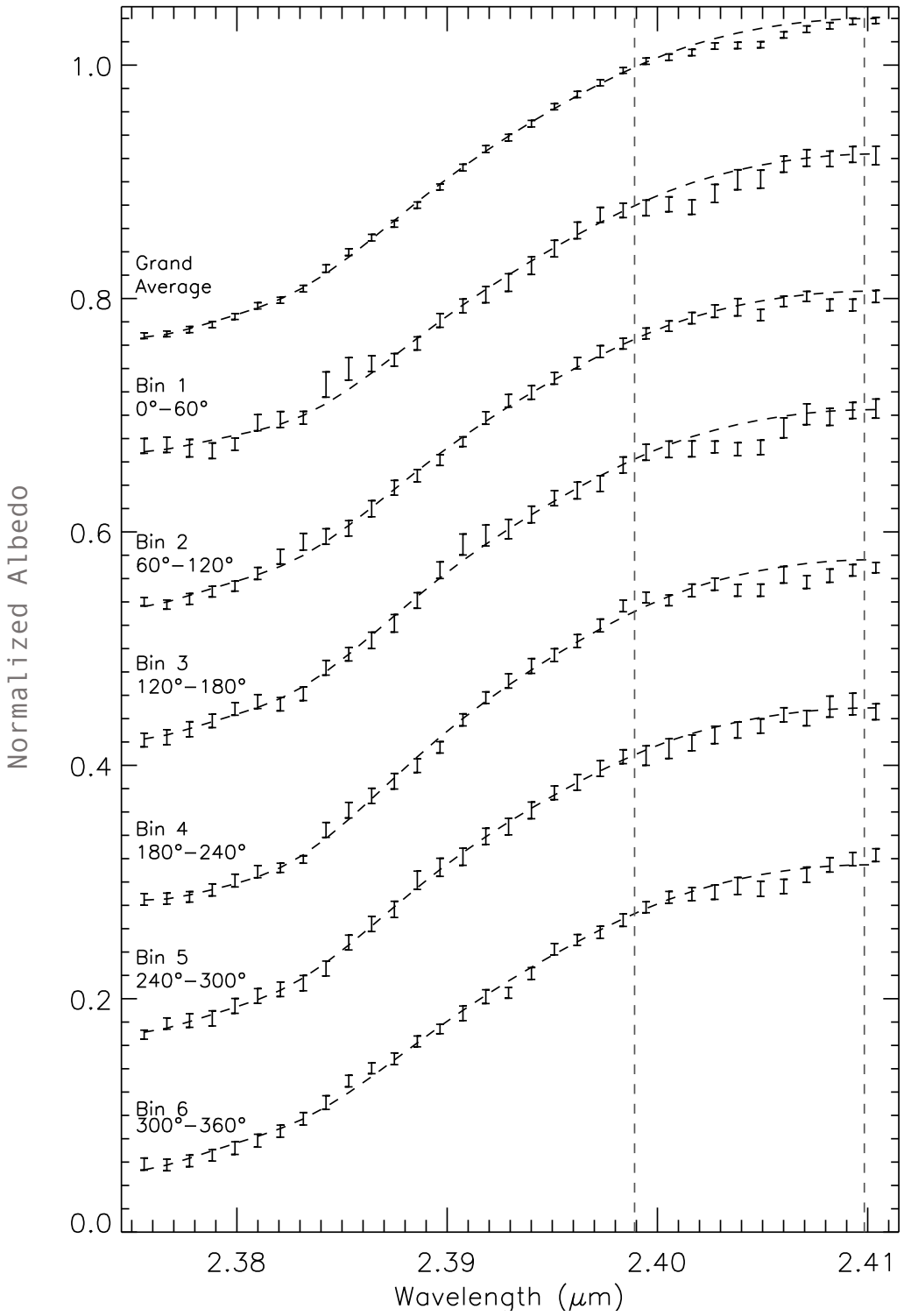

Figure 5: Stacked spectra of the grand and longitude bin averages from 2.376 to 2.410 μm. All spectra are offset from zero for clarity and do not represent the true normalized albedo values. Ethane-absent models are represented by the dashed lines and are unique for each longitude bin. Labels on the left-hand side refer to the curve directly below. Vertical dashed lines denote the extent of the 2.405 μm band (2.399-2.409 μm).

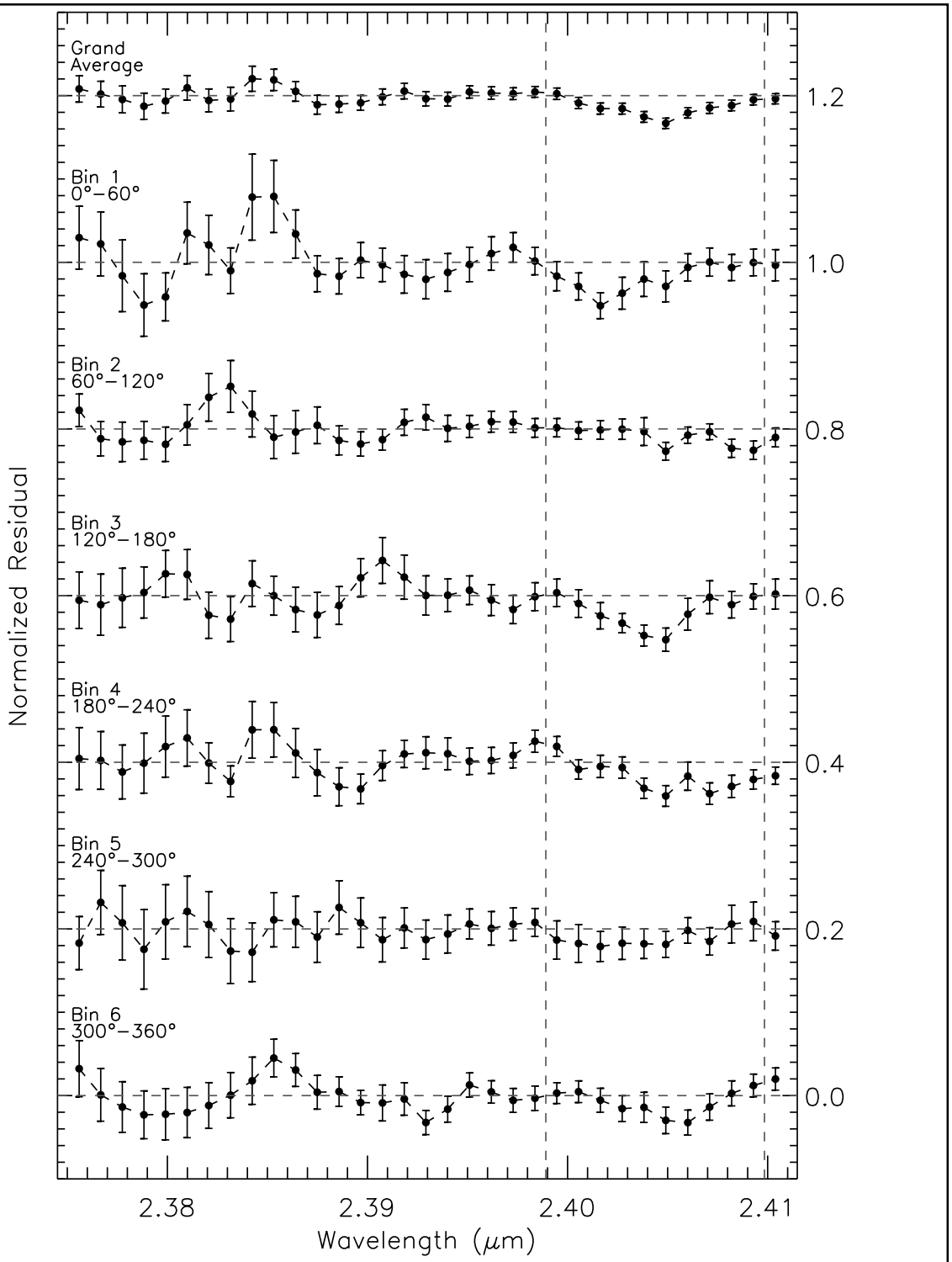

Figure 6: Stacked normalized residuals of the grand and longitude bin averages from 2.376 to 2.410 μm. Horizontal dashed lines show the zero value for each bin. Labels on the left-hand side refer to the curve directly below. Vertical dashed lines denote the extent of the 2.405 μm band (2.399-2.409 μm). Bins 3 (4.2-σ) and 4 (4.1-σ) show a definite detection of the band, while Bins 2 (1.9-σ) and 5 (2.0-σ) show a less certain detection of the band.

Discussion

As discussed briefly in the Introduction, ^{13}CO and ethane both have absorption features at 2.405 μm, the band of interest in this investigation. Disentangling the contributions of these two species presents a problem. No other ethane bands were identified in our spectra to corroborate a detection of ethane ice on the surface of Pluto, either due to confusion by CH_4 absorption or because the bands are found beyond the spectral range of the SpeX instrument. To solve this problem, we chose to look into the longitudinal distribution of ^{12}CO from the equivalent widths of the 1.58 μm ^{12}CO absorption feature. The 2.35 μm feature is not useful due to its location between two strong CH_4 bands. Without a way to confidently quantify the fractionation of ^{13}CO and ^{12}CO ices on the surface of Pluto, we assumed that these two isotopologues have identical spatial distributions. Determining the spatial distribution of ^{12}CO therefore indirectly provides a spatial distribution for ^{13}CO.

Figure 3 from G13 shows the longitudinal distribution of ^{12}CO from calculations of the equivalent widths of the 1.58 μm feature in nightly spectra. The distribution could be described as "triangular" with a peak near 180° longitude. Compare this to the pattern of equivalent widths for the 2.405 μm band in Figure 4 of this work. The two distributions do not match, so we conclude that the contribution of ^{13}CO to the observed depth of the 2.405 μm band is minimal. Due to the scarcity of ^{13}CO laboratory optical constants and absorption coefficients, we are unable to calculate a ratio of ethane to ^{13}CO for the 2.405 μm band. We are also

unable to evaluate the accuracy of our assumptions about the identical spatial distributions of the CO isotopologues. That being said, we will move forward with the interpretation of our results assuming that the 2.405 μm band is due almost entirely to ethane absorption.

The 2.405 μm band is not likely due to CH_4 absorption either. New absorption coefficients for CH_4:N_2 and N_2:CH_4 (Protopapa et al., 2013) do not show a band at 2.405 μm. However, CH_4 absorption occurs at shorter and longer wavelengths on either side of the 2.405 μm feature. The CH_4 absorption vs. longitude distribution is not anti-correlated to that of ethane (compare Figure 4 of this work to Figure 4 in G13). Anti-correlation would imply that the variations in the 2.405 μm equivalent width are artificial and due to variation in nearby CH_4 band depths with longitude. The two distributions are not anti-correlated, suggesting that the variation seen in the 2.405 μm band is due to variations in ethane absorption across Pluto's surface.

Ethane is a non-volatile species at outer Solar System temperatures, so any ethane created in the atmosphere should remain on Pluto until converted to other hydrocarbon compounds. The longitudinal variations detected in this investigation suggest that volatile transport plays a key role in making Pluto's surface a dynamic milieu. Compare the nominal peak of ethane absorption (120°-180°) to the peak of the visible light curve (180°-240°) (Buie et al., 2010a; Buie et al., 2010b) in Figure 7. The maximum ethane absorption is shifted one longitude bin to the west of the light curve peak, whereas the other bins approximately follow the same pattern as the light curve. Note also that the data used to construct the albedo map and the visible

light curve of Pluto were obtained between 2002 and 2003, and that a majority of our SpeX data were obtained after this period. As described in the Introduction, we would expect to see a uniform distribution of ethane on the surface if formed in the atmosphere. However, this does not describe the observation of a non-uniform longitudinal distribution with a peak in the N_2-dominated 1 (120°-180°) region. This does not mean that ethane is not formed in the atmosphere, but instead that we must develop a more sophisticated explanation.

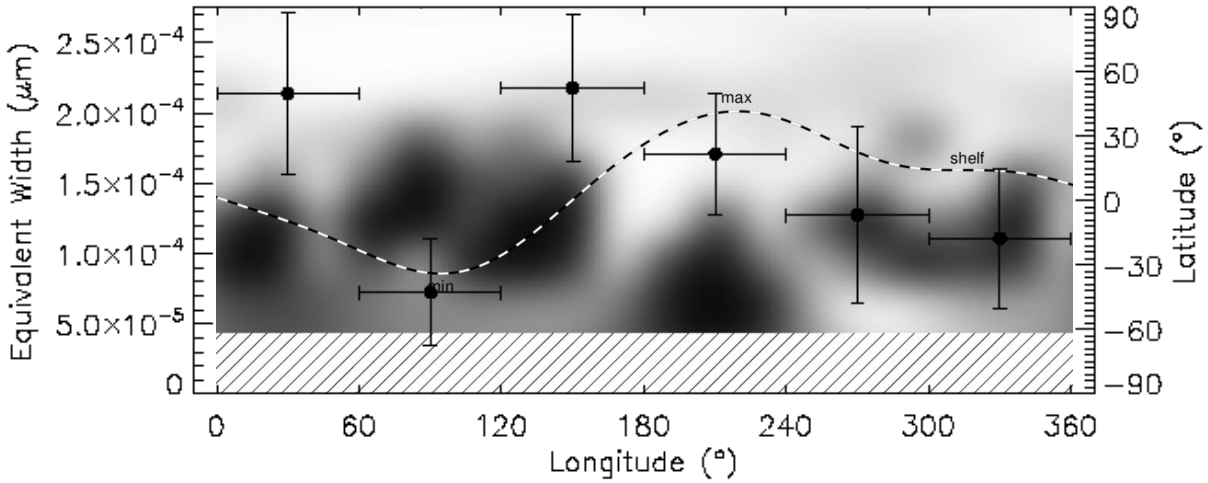

Figure 7: Equivalent width values from Table 1/Figure 4 super-imposed on the Pluto albedo map and visible light curve of Buie et al. (2010a). The visible light curve albedo is arbitrarily scaled. Refer to Figure 3 for more description of the albedo map and Figure 4 for more description of the equivalent widths.

We suggest that, as Pluto's North Pole continues to rotate into view following perihelion in 1989, the northern latitudes are receiving an increasing amount of solar insolation. These northern latitudes are home to the majority of the high-albedo volatile ices on Pluto, as seen in the global albedo map (Buie et al., 2010a; Buie et al., 2010b). As these latitudes receive more energy, the deposited volatiles (predominantly N_2 between 120° and 240° longitude) sublimate and either reside in

the atmosphere or are transported and re-deposited in other regions. The sublimation rate has increased faster than the deposition rate as revealed by Pluto's monotonically increasing atmospheric pressure between 1989 and 2013 (Olkin et al., 2015). As the volatile ices sublimate from the northern latitudes, the underlying non-volatile ethane is revealed. In this scenario, the shift between the absorption and light curve peaks is due to the original amount of volatiles present in these regions. We expect the brighter areas to be correlated with more volatile ice content and to absorb less sunlight, therefore sublimation in this region proceeds more slowly. A greater quantity of volatiles should remain in the region marked by a peak in visible albedo. This means the region directly to the west may have undergone significant uncovering of the underlying ethane. Conversely, the regions dominated by CH_4 show less ethane absorption because CH_4 is less volatile than both N_2 and CO. What we are indirectly seeing is evidence for changes in Pluto's regional albedos and volatile distribution since the albedo map data were obtained.

The CH_4-dominated regions (240°-300° and 300°-360°) are not likely candidates as regions of peak ethane absorption. The difference between the equivalent widths of these bins and that of the N_2-dominated 1 bin (120°-180°) are at the 1.1-σ and 1.5-σ levels, respectively. This is further evidence that ethane forms primarily in Pluto's atmosphere instead of on the surface. Ethane formation in the surface ice is not impossible, but it should make a negligible contribution to the total ethane abundance due to atmospheric shielding, as seen from the calculation performed in the Introduction. Again, if Pluto's atmosphere collapses, the previous

statement is no longer accurate and ethane formation in the surface ice would be the dominant production mechanism. Ethane formation will occur when CH_4 is present in the atmosphere and may be ongoing throughout a full Pluto orbit at different rates. Maximum ethane production in the atmosphere would be expected to peak post-perihelion at maximum atmospheric pressure. Pluto's atmospheric pressure continues to monotonically increase (Olkin et al., 2015) as it moves away from perihelion, so it is possible that the peak ethane formation period has not yet occurred.

The Ralph/LEISA instrument on New Horizons has the spectral range (1.25-2.50 μm) and spectral resolution (250) to resolve the 2.405 μm band on Pluto (Figure 6 in Young et al., 2008). Ralph/LEISA will be able to confirm longitudinal variability of ethane with spatial resolution upwards of 5-7 km pixel^{-1} near closest approach to Pluto (Young et al., 2008). The Ralph/MVIC (four filters: blue (400-550 nm), red (540-700 nm), near-IR (780-975 nm), CH_4 filter (860-910 nm)) and LORRI (wavelength range of 350-850 nm) instruments onboard New Horizons will make available color and albedo information (Young et al., 2008; Cheng et al., 2008) useful for testing our theory of volatile transport on Pluto. The albedo data will be useful for constructing an updated global albedo map for comparison to that of Buie et al. (2010b). Color data from these instruments will suggest potential sublimation and deposition sites on Pluto (Moore et al., 1999; Howard and Moore, 2008). Bluer regions might be considered sites of recent deposition, with redder regions potentially marking sites of recent sublimation as noticed on Triton from Voyager 2

data (Eluszkiewicz, 1991). The Alice instrument will be useful for determining the height at which formation occurs by obtaining a vertical profile of gaseous ethane and CH_4 mixing ratios.

Conclusion

Using near-infrared spectra of Pluto taken with the SpeX instrument at the IRTF over 72 nights, our investigation has made an independent confirmation of the 2.405 μm band at the 7.5-σ level, hinting heavily at the presence of ethane ice on Pluto's surface. We detect longitudinal variability of ethane by breaking the surface into six 60° longitude bins approximately matching previously noticed surface ice distributions. The longitudinal variability observed for the equivalent width of the 2.405 μm band does not match that of ^{12}CO and ^{13}CO, suggesting that the band is due entirely to ethane absorption. Peak ethane absorption nominally occurs in the N_2-dominated region between 120° and 180° longitude, with a nominal minimum in the Dark 2 region between 60° and 120° longitude. Decreased ethane absorption in the methane-dominated regions (240°-300° and 300°-360°) suggests ethane formation in the atmosphere and a uniform distribution of ethane across Pluto's surface. The non-uniformity of the ethane distribution points to coverage of non-volatile ethane by volatile ices, with transport of these volatiles as seasons on Pluto change. We predict that New Horizons will find evidence for recent sublimation on Pluto between the longitudes of 120° and 180°.

Our IRTF/SpeX data set currently constitutes a long time baseline of Pluto data taken at many sub-observer longitudes. We very eagerly anticipate the flyby of the New Horizons spacecraft through the Pluto system in July 2015. New Horizons will provide a much needed "ground truth" comparison for post-flyby data obtained through our IRTF/SpeX program and with other ground-based instruments.

CHAPTER IV

MEASURING TEMPERATURE AND AMMONIA HYDRATE ICE ON CHARON IN 2015 FROM KECK/OSIRIS SPECTRA[7]

Abstract

In this work we investigated the longitudinal (zonal) variability of H_2O and ammonia (NH_3) hydrate ices on the surface of Charon through analysis of the 1.65 μm and 2.21 μm absorption features, respectively. Near-infrared spectra presented here were obtained between 2015-07-14 and 2015-08-30 UT with the OSIRIS integral field spectrograph on Keck I. Spectra centered on six different sub-observer longitudes were obtained through the Hbb (1.473-1.803 μm) and Kbb (1.965-2.381 μm) filters. Gaussian functions were fit to the aforementioned bands to obtain information on band center, band depth, full width at half maximum, and band area. The shift in the band center of the temperature-dependent 1.65 μm feature was used to calculate the H_2O ice temperature. The mean temperature of the ice on the observable portion of Charon's surface is 45±14 K and we report no statistically significant variations in temperature across the surface. We hypothesize that the crystalline and amorphous phases of water ice reached equilibrium over 3.5 Gyr ago, with thermal recrystallization balancing the effects of irradiation amorphization. We do not believe that cryovolcanism is necessary to explain the presence of crystalline water ice on the surface of Charon. Absorption from

[7] This paper is currently in-review at Icarus. Citation: Holler, B.J., Young, L.A., Buie, M.W., Grundy, W.M., Lyke, J.E., Young, E.F., Roe, H.G., 2016b. Measuring temperature and ammonia hydrate ice on Charon in 2015 from Keck/OSIRIS spectra. Icarus, submitted.

ammonia species is detected between 12° and 290° which agrees with results from New Horizons. Ongoing diffusion of ammonia through the rocky mantle and upper layer of water ice is one possible mechanism for maintaining its presence in Charon's surface ice. Reduced Charon spectra corrected for telluric and solar absorption are available as supplementary online material.

Introduction

Charon, the largest moon of Pluto, was serendipitously discovered in 1978 as an unresolved extension to Pluto's disk that predictably changed position (Christy and Harrington, 1978). In the nearly four decades since its discovery, and especially since the mutual events in the late 1980s (Buie et al., 1987; Marcialis et al., 1987), studies focused solely on Charon remain sparse due largely to the difficulty in isolating Charon from Pluto from most ground-based observatories. Charon orbits the system barycenter at a distance of 19,750 km, or ~17 R_{Pluto} (Tholen et al., 2008; Brozović et al., 2015); this translates to a maximum angular separation of less than 1″ at Pluto and Charon's geocentric distance in 2015 (~32 AU). Spectral observations of Charon were once best suited for space-based facilities, however, ground-based facilities with large-class telescopes and adaptive optics systems can now effectively obtain unblended spectra of Pluto and Charon at these small separations. Observations of Charon from the New Horizons flyby provide spatially resolved "ground truth" context for previous and future Earth-based observations.

The near-infrared spectrum of Charon is dominated by absorption features of water ice (Brown and Calvin, 2000; Buie and Grundy, 2000; Dumas et al., 2001), with over 90% thought to be in the crystalline phase (Cook et al., 2007; Merlin et al., 2010). The only other confirmed ice species detected on Charon is ammonia (NH_3) hydrate, with an absorption feature at 2.21 μm (Brown and Calvin, 2000; Buie and Grundy, 2000; Dumas et al., 2001; Cook et al., 2007; Verbiscer et al., 2007; Merlin et al., 2010). Both crystalline water ice (Buie and Grundy, 2000; Dumas et al., 2001) and ammonia hydrate (DeMeo et al., 2015) may show evidence for differences in absorption between the leading and trailing hemispheres. A difference in surface ice temperature of over 10 K between the sub-Pluto and anti-Pluto hemispheres was calculated by Cook et al. (2007); however, they assigned uncertainties of 5-10 K to the temperature measurements, so the calculated difference may not be real.

The lack of volatile ices (N_2, CH_4, and CO) on Charon is consistent with theories of volatile loss and retention on small outer solar system objects (Schaller and Brown, 2007a; Johnson et al., 2015). At 45 K (this work), the partial pressures of N_2 (~0.6 mbar), CH_4 (~0.2 μbar), and CO (~0.1 mbar) are high enough to form an atmosphere (Fray and Schmitt, 2009). New Horizons observations of a solar occultation in the UV place 3-σ upper limits on Charon's surface pressure at 4.2, 0.3, and 1.2 picobar for atmospheres composed solely of N_2, CH_4, and CO, respectively (Stern et al., 2016). This means Charon's volatiles escaped from its atmosphere and surface over the age of the solar system; small quantities may exist on the surface, but if so, are well below the threshold for detectability. In contrast, the non-volatile

ices H_2O and NH_3 are detected on Charon; due to their negligible partial pressures (Fray and Schmitt, 2009), these ices are retained.

Cook et al. (2007) define the *e*-folding time for the conversion of crystalline water ice to amorphous water ice as the time necessary to reduce the crystalline fraction (ratio of crystalline water ice to total water ice) from 1 to 1/*e*. The crystalline fraction is an exponential function and decreases with increasing radiation dosage, which is a function of heliocentric distance and time (Cooper et al., 2003). The *e*-folding time for crystalline water ice to be converted to amorphous water ice in a radiation environment of 1 eV-10 GeV protons, without considering recrystallization processes, is 1.5 Myr; this is down to the depth probed by near-infrared *H* and *K* band observations (~350 μm; Cook et al., 2007). The destruction of ammonia hydrate down to this same depth in the same radiation environment is 20 Myr (Cooper et al., 2003; Cook et al., 2007). The amorphous phase, which only makes up ~10% of the water ice content on Charon (Cook et al., 2007; Merlin et al., 2010), should dominate in high-radiation environments since crystalline water ice requires a formation temperature greater than 140 K (Leto and Baratta, 2003), well above the surface temperature of Charon. However, laboratory work suggests that thermal recrystallization achieves an equilibrium with irradiation amorphization after a period of time that depends on temperature (Leto and Baratta, 2003; Mastrapa and Brown, 2006; Zheng et al., 2009). The observed fractions of crystalline and amorphous water ice on Charon may be real and potentially

explainable without invoking a replenishment mechanism (see Results & discussion).

Crystalline water ice is formed in an orderly lattice structure while amorphous water ice is a random organization of water molecules. This structural difference results in distinctive absorption features between the spectra of the two phases. In particular, an absorption feature at 1.65 μm is present only in the spectrum of crystalline water ice and is absent in the spectrum of amorphous water ice (Grundy and Schmitt, 1998). This absorption feature is of special interest because it is temperature-dependent: The shift of the band with respect to a reference value provides a means of measuring the temperature and was used in previous work to calculate the surface temperature of Charon (e.g., Cook et al., 2007). Verbiscer et al. (2006) modeled areal mixtures of ammonia hydrate and water ice and found that ammonia hydrate suppresses the 1.65 μm crystalline H_2O band. It is possible that the presence of ammonia hydrate in an intimate mixture with water ice could shift the 1.65 μm band center, but optical constants for such a mixture are not currently available to test this. Lacking definite information, we performed this work under the assumption that ammonia hydrate does not shift the 1.65 μm band center.

Observations

Pluto and Charon were observed on 6 nights in Summer 2015 using the OH-Suppressing Infra-Red Imaging Spectrograph (OSIRIS) on Keck I (Larkin et al.,

2006; Mieda et al., 2014). The motivation and design of these observations was to obtain marginally resolved spectral cubes of Pluto at spectral resolutions 10 times higher than that from New Horizons. We present analysis of Charon here. Pluto will be addressed in a later paper. Observational circumstances for each night are found in Table 1 and the hemisphere of Charon visible on each night is shown in Fig. 1. Over the 6 nights, a total of 240 minutes of *H* band observations and 260 minutes of *K* band observations were obtained. Spectra of Pluto and Charon were also obtained in 2010, 2012, and 2013 but were not included in this work because we wished to focus on those data taken during the New Horizons flyby epoch for direct comparison to New Horizons results. This direct comparison places ground-based observations in the context of the "ground truth" provided by New Horizons and will enhance the results of later analysis of previous years' data.

The OSIRIS instrument. The OSIRIS instrument is a spectrograph equipped with an integral field unit (IFU), so it obtains spectra at multiple spatial locations within the field of view. We used OSIRIS in conjunction with the adaptive optics (AO) system on Keck I to reduce the size of the point spread function (PSF) for Pluto and Charon. The AO system was operated in laser guide star (LGS) mode on one night (2015-07-14 UT) and in natural guide star (NGS) mode for the other five nights. NGS mode was preferred and used more frequently than LGS mode due to above-average seeing (~0.3″ in *H*) and because LGS required a 45-60 minute laser check-out period. After passing through the AO system, light from a rectangular region of sky passes through an array of lenslets and onto a grating, producing

overlapping spectra on the detector. Each lenslet roughly corresponds to one pixel on the detector.

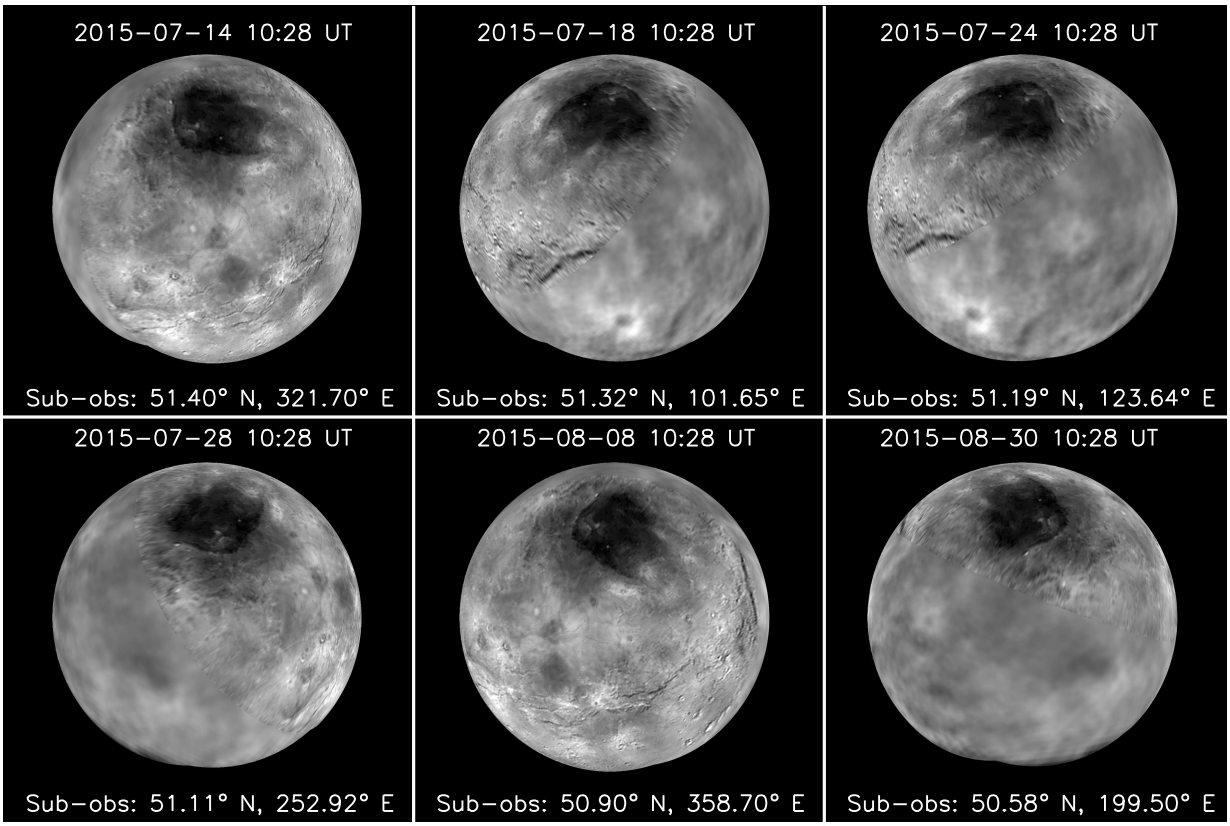

Figure 1: Spherical projections of Charon showing the hemisphere visible from Earth at the UT date and time specified above each image. The sub-observer latitude and longitude, specified beneath each image, marks the point directly "below" the observer and therefore the center of each map. These spherical maps were constructed from a visible light Charon albedo map obtained by the New Horizons spacecraft and available from the JPL Photojournal (PIA19866: Global Map of Pluto's Moon Charon; *http://photojournal.jpl.nasa.gov/catalog/PIA19866*).

We observed Pluto and Charon in the near-infrared through the broadband Hbb (*H* band, 1.473-1.803 μm) and Kbb (*K* band, 1.965-2.381 μm) filters that use a 16 × 64 lenslet array, for a total of 1,019 overlapping spectra (five spectra fall off the edge of the detector). The dispersion of the Hbb and Kbb filters is 0.000200 and

0.000250 μm/pixel, respectively, and the average spectral resolution is ~3800. For comparison, the spectral resolution of the Linear Etalon Imaging Spectral Array (LEISA) on the New Horizons spacecraft is 250 between 1.25 and 2.50 μm, with a special region of higher resolution ($\lambda/\Delta\lambda$~560) between 2.10 and 2.25 μm (Reuter et al., 2008; Young et al., 2008). OSIRIS therefore provides a spectral resolving power over 15× higher than LEISA over the full spectral range, and almost 7× higher over LEISA's special region.

Observing strategy. Our observations were made using the finest plate scale of 0.020″ per lenslet, resulting in a 0.32″ × 1.28″ field of view. This field of view was aligned along the imaginary line connecting Pluto and Charon, with Charon always at the top of the field and Pluto always at the bottom (Fig. 2); consistent alignment helped simplify the reduction process. In Summer 2015, Pluto and Charon were ~32 AU from the Earth, resulting in a spatial resolution of ~500 km/pixel. At this resolution, Charon was over two pixels in diameter and the centers of the two bodies were separated by >30 pixels on the chip (Fig. 2). Adaptive optics and the large separation between Pluto and Charon significantly reduced cross-contamination so separate spectra of each object could be extracted. The range of angular separations during the observing period for Styx (1.47-1.82″), Nix (1.60-2.19″), Kerberos (1.98-2.54″), and Hydra (2.21-2.85″) placed them outside the field of view; additionally, they are too faint to be detected by OSIRIS.

An A-B-A-sky dither pattern was used to ensure that Pluto and Charon did not fall on the same pixels throughout the night. The magnitude of the dither was

small enough that both Pluto and Charon were in the field of view in every image, even at larger angular separations. The sky image from each set was used in the reduction to remove sky background; AB subtraction was not performed, hence the use of a small dither. The integration time for each component of the dither sequence was 8 min in the Hbb filter and 5 min in the Kbb filter. The integration time for the Kbb filter was shorter due to higher levels of sky background in the *K* band.

These observations provided near-complete longitudinal coverage of Charon over a 1.5 month span (Table 1). Six sets of observations separated in sub-observer longitude by 60° provide ideal coverage, but this is difficult to perform in a short time frame due to the 6.4-day rotation of Charon. Due to an unanticipated failure of an important component of the OSIRIS instrument in late June 2015, we were unable to observe on our preferred (and originally scheduled) dates in early July. However, because it was crucial that these observations be made around the time of the New Horizons flyby through the Pluto system, our lost nights were rescheduled. This resulted in some regions of Charon being oversampled while others were undersampled. The longitudinal coverage was still adequate for the purposes of quantifying variability across the surface of Charon.

A solar analog was observed at the beginning of each night in both the Hbb and Kbb filters to correct the Charon spectra for solar absorption lines. Spectra of the solar analog HD 159662 (G2/G3 V spectral type; Houk and Smith-Moore, 1988) were used for this purpose. Additionally, *H* and *K* spectra of stars at similar

airmasses to Pluto and Charon, and with comparable R and brighter H and K magnitudes, were obtained at the beginning, middle, and end of the night. It is planned for these PSF stars to be used in future work to help extract spectral information from specific regions of Pluto, since Pluto is partially spatially resolved

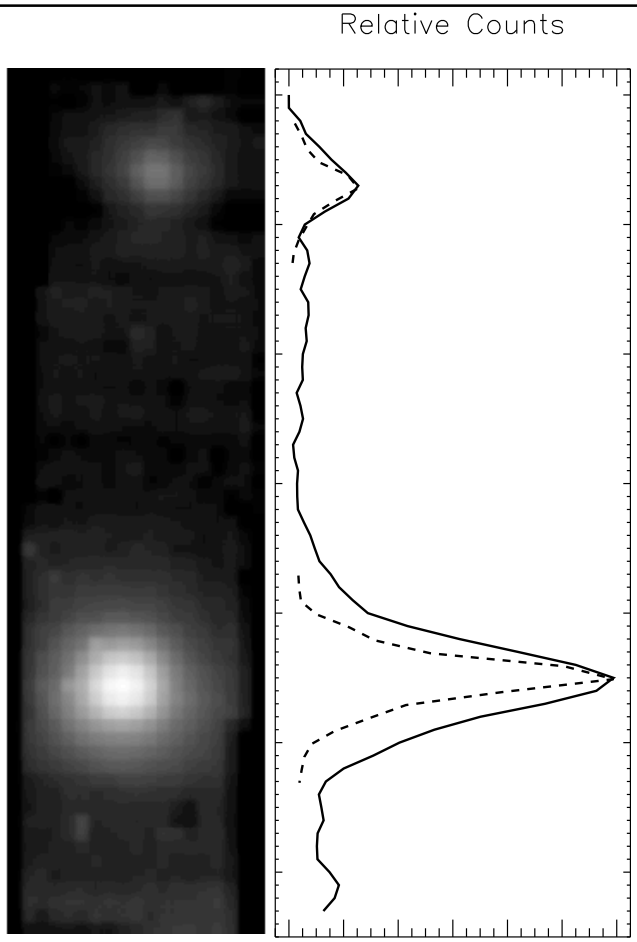

Figure 2: *Left*: Spectrally-averaged image of a 3D data cube obtained on the night of 2015-07-14 UT with the Kbb filter (1.965-2.381 μm). These data were taken in the B dither position with an exposure time of 300 seconds at an airmass of 1.50. Pluto is at the bottom of the image and Charon is near the top. The two are clearly separated on the detector even at an angular separation of 0.74″. This image is representative of the data obtained in Summer 2015. *Right*: One-dimensional profile of the average image shown on the left. The horizontal axis (relative counts) is linear. The dashed curves are the one-dimensional profile of a PSF star taken on the same night (scaled on the horizontal axis to fit on the plot) for comparison to the widths of Pluto and Charon. Pluto is about 2 PSFs across and so is partially spatially resolved. Charon is only slightly wider than the PSF width and is effectively unresolved.

by OSIRIS. The spectra of these stars were not used in this work and will not be discussed further.

Table 1: Observational Circumstances

UT date mean-time	Weather conditions	Sub-Earth Lon. (°E)[8]	Pluto-Charon sep. (″)	Phase angle (°)	Total exp. time (min)	
					H band	*K* band
2015-07-14 10:28	Clear	322	0.74	0.24	24	30
2015-07-18 08:12	Some cirrus	102	0.84	0.36	48	30
2015-07-24 08:11	Some cirrus	124	0.80	0.53	48	45
2015-07-28 10:28	Clear	253	0.83	0.64	24	65
2015-08-08 08:06	Clear	359	0.65	0.94	48	45
2015-08-30 07:55	Clear	200	0.67	1.41	48	45

Reduction

A more detailed description of the reduction strategy is presented in the "Additional Information on Reduction and Analysis" section (pp. 179); reduced Charon spectra corrected for solar and telluric absorption are available as supplementary material online. Fig. 3 is a flowchart that details the steps in the reduction. The raw data were first processed through the OSIRIS Data Reduction Pipeline (DRP; Krabbe et al., 2004) to produce 3D data cubes (1 spectral and 2 spatial dimensions). We created 2 sets of data cubes: dark- and sky-subtracted. The

[8] The rotation periods of Charon and Pluto and Charon's orbital period are equal (~6.4 days). We use the preferred coordinate system where the sub-Pluto point on Charon is at 0° longitude and the anti-Pluto point is at 180° longitude (Zangari, 2015). The sub-observer longitude decreases with time and differs by180° between Pluto and Charon.

master dark of the appropriate exposure time was subtracted from all 4 images in a set (3 science, 1 sky) to produce the dark-subtracted data cubes. The sky-subtracted data cubes were constructed by subtracting the sky image of each set from the other images in the set; dark subtraction was not explicitly performed because sky subtraction implicitly includes dark subtraction. The rest of the reduction was handled using in-house IDL routines. The trace and aperture radii were determined in each data cube from the mean (spectrally-averaged) image; different aperture radii were used for Pluto, Charon, and the solar analog to minimize the addition of noise. One-dimensional spectra were extracted from the sky-subtracted data cubes by summing the values in each pixel of the circular apertures surrounding Pluto, Charon, and the solar analog star. We constructed a wavelength solution from the measured positions of OH emission lines in the dark-subtracted data cubes and published vacuum wavelength values (Rousselot et al., 2000); our wavelength solution was nearly identical to the one output by the DRP, so we used our wavelength solution. Telluric absorption was corrected for by dividing the science spectra by ATRAN models of atmospheric transmission (Lord, 1992). The telluric-corrected Charon spectra were divided by the telluric-corrected solar analog spectrum in the appropriate band from that night to remove solar absorption features, yielding units of arbitrary albedo. This was converted to geometric albedo by scaling to the Charon spectrum in Fig. 3 of Buie and Grundy (2000). An adjustment to the geometric albedo was applied to correct for differences in radii:

Buie and Grundy (2000) used 593 km, while Stern et al. (2015) report a value of 606 km from New Horizons.

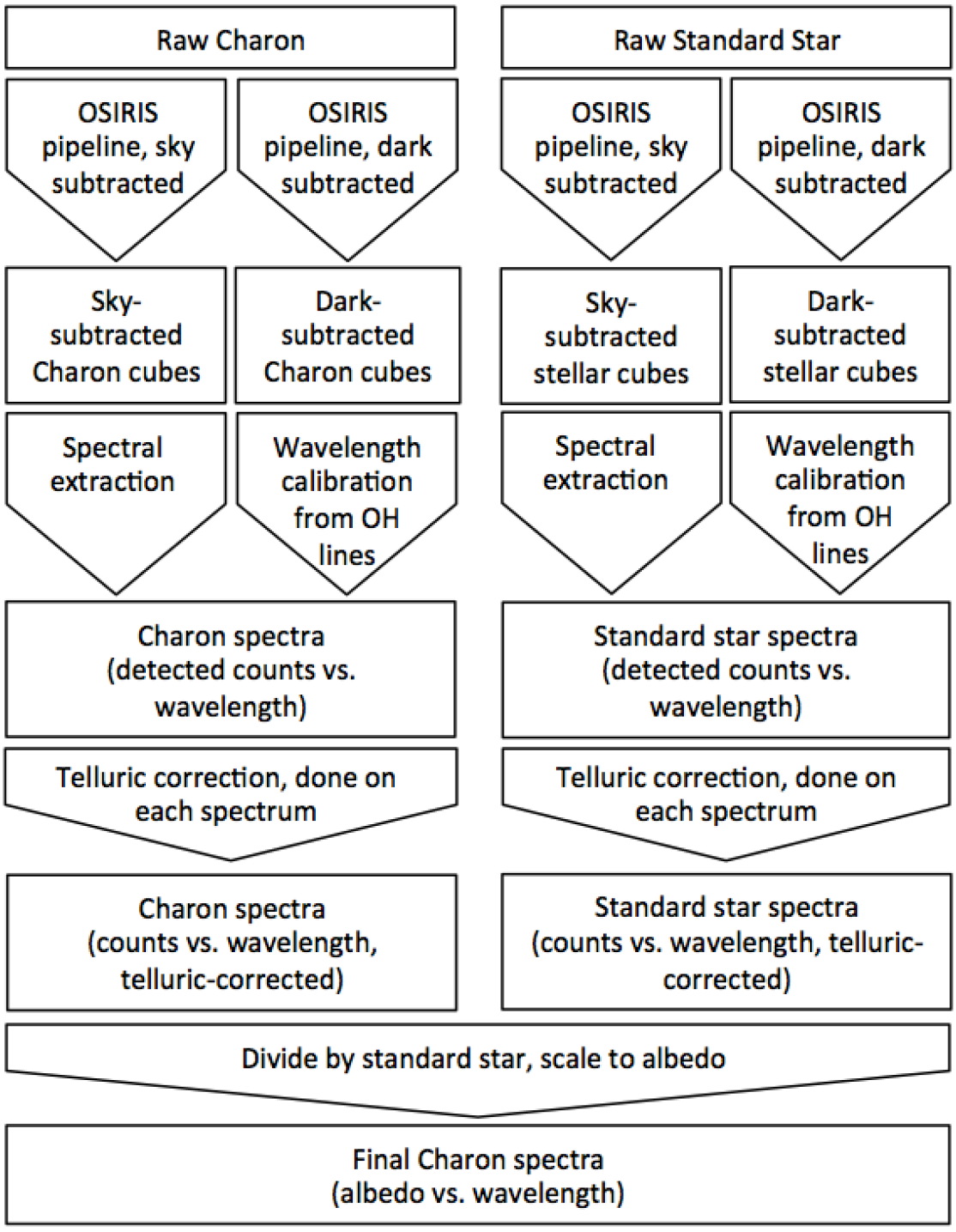

Figure 3: Flowchart detailing the reduction strategy.

Analysis

Charon night averaged spectra were calculated as weighted averages of the individual *H* and individual *K* spectra from a given night. Gaussian functions of the form $y=a*\exp(-(\lambda-\mu)^2/2w^2)$, where a is the amplitude of the Gaussian, λ is wavelength (the independent variable), μ is the band center, and w is the 1/*e* half width, were fit to the 1.65 μm and 2.21 μm absorption features in each individual *H* and *K* spectrum, respectively. The fit regions covered 1.610-1.714 μm for *H* and 2.165-2.270 μm for *K*. These models were then compared to the data and the standard deviation of the residual (data minus model) was taken as the uncertainty on the albedo value in each wavelength bin. Gaussian weighting ($1/\sigma^2$) was used to compute the weighted night averaged spectra. For the night averaged spectra, the standard deviation of the mean for each wavelength bin was taken to be the uncertainty on the albedo in that bin. The night averaged spectra are presented in Fig. 4. The Charon grand average spectrum (Fig. 5) was computed as a weighted average of the night averaged spectra, again using Gaussian weighting. We then analyzed the 1.65 μm crystalline H_2O band and the 2.21 μm ammonia hydrate band in the night averaged and grand average spectra in order to quantify longitudinal (zonal) variability in surface temperature and ammonia hydrate ice.

We modeled the absorption bands and surrounding continuum regions as (Gaussian + 1) × polynomial. From this we extracted fit values for the amplitude, band center, and 1/*e* half width of the absorption bands. We modeled the continuum regions (the adjacent regions on either side of the absorption features) differently

for the 1.65 μm and 2.21 μm bands. We performed a linear fit to the relatively linear regions on either side of the 1.65 μm band; to avoid influencing the fit, points in the band itself were not considered. The continuum wavelength regions were 1.610-1.624 μm and 1.684-1.714 μm. For the 2.21 μm band, we fit a third order polynomial to the wavelength regions between 2.115-2.190 μm and 2.230-2.320 μm. The entire spectrum was then divided by the best-fit polynomial, setting the continuum regions to an average value of +1. This offset was removed so that the continuum was at an average value of zero, thus removing a parameter from the Gaussian fit to the band. Using the IDL routine *mpfitpeak*[9], a Gaussian of the form $y=a*\exp(-(\lambda-\mu)^2/2w^2)$ was fit from 1.610-1.714 μm for the 1.65 μm band and from 2.190-2.230 μm for the 2.21 μm band. The band depth (amplitude), a, band center, μ, and 1/e half width, w, were the fit parameters. We fit for the 1/e half width rather than the full width at half maximum (FWHM) because the existing well-tested routine *mpfitpeak* fits for the 1/e half width and changing variables could introduce the risk of software error. The FWHM can be calculated from the 1/e half width: $\text{FWHM}=2w\sqrt{2ln2}$. The band area, a quantity related to equivalent width, provides a measure of the amount of an absorbing species on the surface and is proportional to the product of the band depth and the 1/e half width ($aw\sqrt{2\pi}$). The band center was used to calculate the ice temperature from the 1.65 μm crystalline water ice band, as described later in this

[9] The IDL routine *mpfitpeak* fits a Gaussian, Lorentzian, or Moffat function to data. Documentation for *mpfitpeak* can be found at *http://hesperia.gsfc.nasa.gov/ssw/gen/idl/fitting/mpfit/mpfitpeak.pro*.

section. Uncertainties on the fit parameters were determined using standard methods for least squares fitting (e.g., Section 15.4 of Press et al., 2007).

As a side note, we initially performed a full 5-parameter sloped Gaussian fit to both absorption bands, as was done in DeMeo et al. (2015) for the 2.21 μm band. The resulting fits poorly matched the data and were accompanied by large uncertainties on the parameters. Fitting so many parameters at once was likely the cause of the poor fits. The two-step process described above was significantly more effective at modeling the absorption features. Additionally, we found that a third order polynomial was a better fit to the continuum on either side of the 2.21 μm feature, and used that as our model instead of a line.

Fig. 6 and 7 show the Gaussian fits to the data and residuals (data minus model) for the 1.65 μm and 2.21 μm bands, respectively. In Tables 2 and 3, the values reported in parentheses are uncertainties on the last two significant figures of the parameter value. Additionally, Table 2 provides values and uncertainties for the wavenumber of the band center, $\bar{\nu}=1/\lambda$. Table 3 also presents the FWHM and the band area. Values from the grand average spectrum (Fig. 5) are also found in Tables 2 and 3 (see "Grand avg." rows); values and uncertainties from the grand average are presented in Fig. 8 and 10 as solid and dashed lines, respectively. The values from the grand average spectrum are in agreement with the averages of all the nightly values, within the uncertainties. Charon was observed at sufficiently large solar phase angles that the opposition effect was not a factor and we could ignore solar phase angle effects. We also ignored the temporal evolution of surface ice

distributions on Charon due to the short duration over which the observations were obtained (~1.5 months).

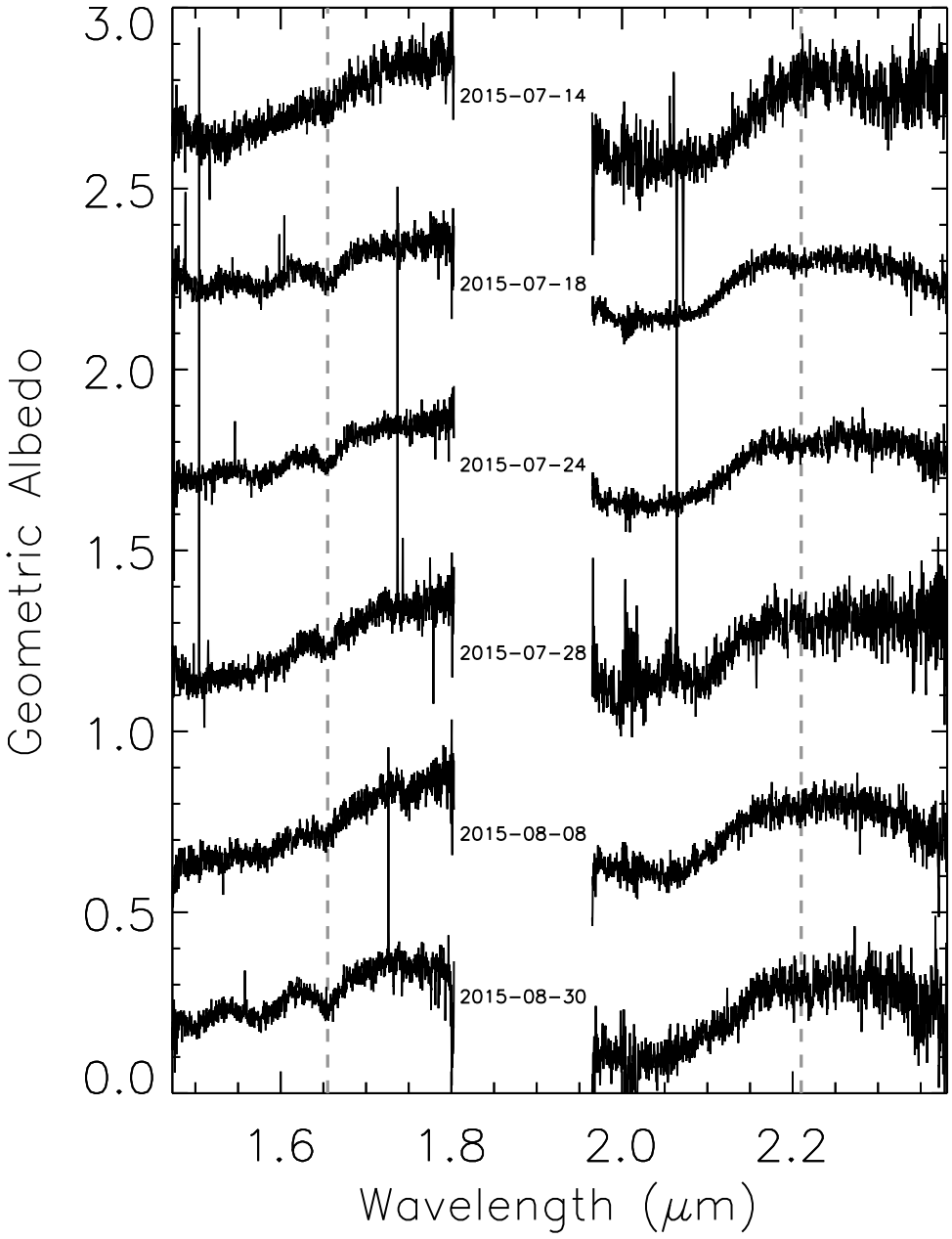

Figure 4: Charon night averaged spectra computed as robust averages (3-σ) of the reduced spectra from each given night (dates are marked between each *H* and *K* pair). The spectra are offset in intervals of 0.5 in geometric albedo for clarity. Vertical dashed lines mark the approximate centers of the 1.65 μm crystalline water ice band and the 2.21 μm ammonia hydrate band. The highest signal-to-noise spectra were obtained on 2015-07-18 and 2015-07-24, and these two nights dominate the grand average (calculated using a weighted average).

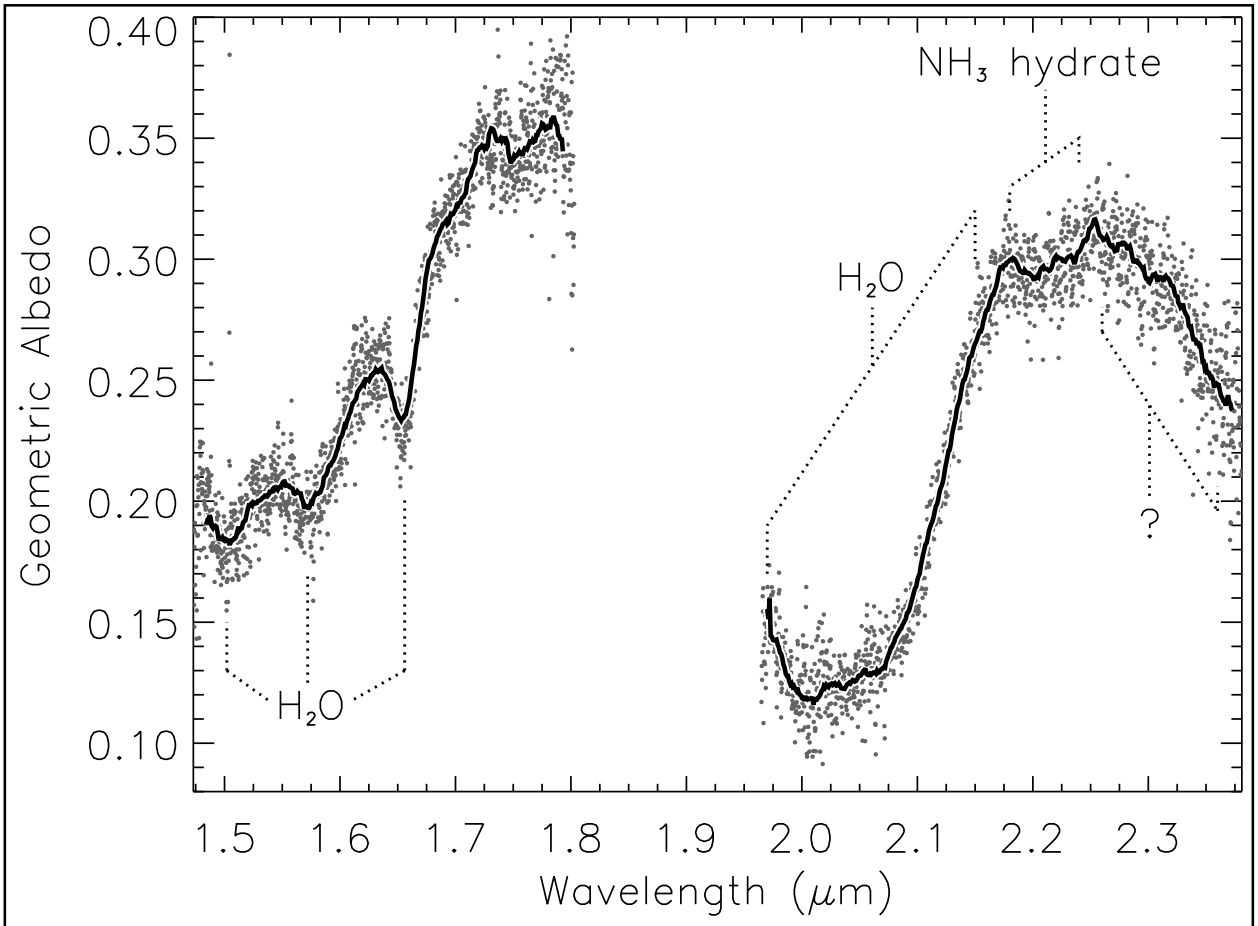

Figure 5: Charon grand average spectrum computed as a weighted average of the night averaged spectra. This spectrum was scaled to the Charon spectrum from Fig. 3 of Buie and Grundy (2000), with an additional correction for differences in Charon radii: Buie and Grundy (2000) used 593 km and we used 606 km from Stern et al. (2015). Exceptionally strong telluric absorption is present in the blank central portion; for this reason, no OSIRIS filter covers this wavelength region. The strong crystalline H_2O feature at 1.65 μm and the weaker ammonia hydrate feature at 2.21 μm are the focus of this work. Other absorption features at 1.5 and 2.0 μm are due to a combination of amorphous and crystalline water ice; another crystalline band is present at 1.56 μm (Mastrapa et al., 2008). The source of absorption at wavelengths >2.25 μm is unknown (Buie and Grundy, 2000).

A look-up table, created using the IDL routine *alpha_h2o*[10] and data from Grundy and Schmitt (1998), was used to determine the temperatures that

[10] *http://www2.lowell.edu/~grundy/abstracts/ice/alpha_H2O.pro*

correspond to the calculated 1.65 μm band centers. The *alpha_h2o* routine computes the absorption coefficients, α, of crystalline water ice as a function of wavelength between 20 and 270 K over a wavelength range of the user's choice. We used *alpha_h2o* to compute the absorption coefficients for temperatures between 20 and 100 K in steps of 1 K from 1.6102-1.7142 μm. The location of the 1.65 μm band center at each temperature value was obtained (to a precision of 0.0001 μm) by determining the wavelength corresponding to the maximum absorption coefficient in the modeled wavelength range (a larger absorption coefficient results in a deeper absorption band in the near-infrared spectrum). These temperature-wavelength pairs were placed in our look-up table and used to determine the surface ice temperatures and uncertainties presented in Table 2.

Table 2: Gaussian Fit Parameters: 1.65 μm H_2O Band

UT date	a	μ (μm)	w (μm)	$\bar{\nu}$ (cm^{-1})	T (K)
2015-07-14	-0.117(67)	1.6562(48)	0.0073(52)	6038±18	28^{+60}_{-28}
2015-07-18	-0.207(23)	1.6555(18)	0.0132(21)	6040.3±6.4	37±24
2015-07-24	-0.194(25)	1.6543(16)	0.0105(18)	6044.9±5.7	53±21
2015-07-28	-0.167(53)	1.6555(22)	0.0061(23)	6040.5±8.0	37±29
2015-08-08	-0.177(45)	1.6526(29)	0.0096(32)	6051±10	74±37
2015-08-30	-0.230(25)	1.6541(16)	0.0120(18)	6045.4±5.7	56±21
Grand avg.	-0.190(17)	1.6549(11)	0.0105(12)	604.62±4.0	45±14

Table 3: Gaussian Fit Parameters: 2.21 μm Ammonia Hydrate Band

UT date	a	μ (μm)	w (μm)	FWHM (μm)	Band Area (μm)
2015-07-14[11]	0.031(91)	2.207(34)	0.011 (+0.039, -0.011)	0.025 (+0.091, -0.025)	0.0008 (+0.0039, -0.0008)
2015-07-18	-0.059(26)	2.2099(64)	0.0133(77)	0.031(18)	0.0020(14)
2015-07-24	-0.074(34)	2.2118(83)	0.018(11)	0.042(25)	0.0033(25)
2015-07-28	-0.086(64)	2.2261(83)	0.0101(96)	0.024(23)	0.0022 (+0.0026, -0.0022)
2015-08-08	-0.030(63)	2.190(28)	0.018 (+0.043, -0.018)	0.04 (+0.10, -0.04)	0.0013 (+0.0043, -0.0013)
2015-08-30	-0.097(54)	2.2167(92)	0.015(11)	0.036(27)	0.0038(35)
Grand avg.	-0.055(18)	2.2125(56)	0.0164(71)	0.039(17)	0.0023(12)

[11] The low SNR of the night averaged spectrum for 2015-07-14 UT is likely responsible for the positive amplitude of the Gaussian fit to the 2.21 μm band on this night (Fig. 7).

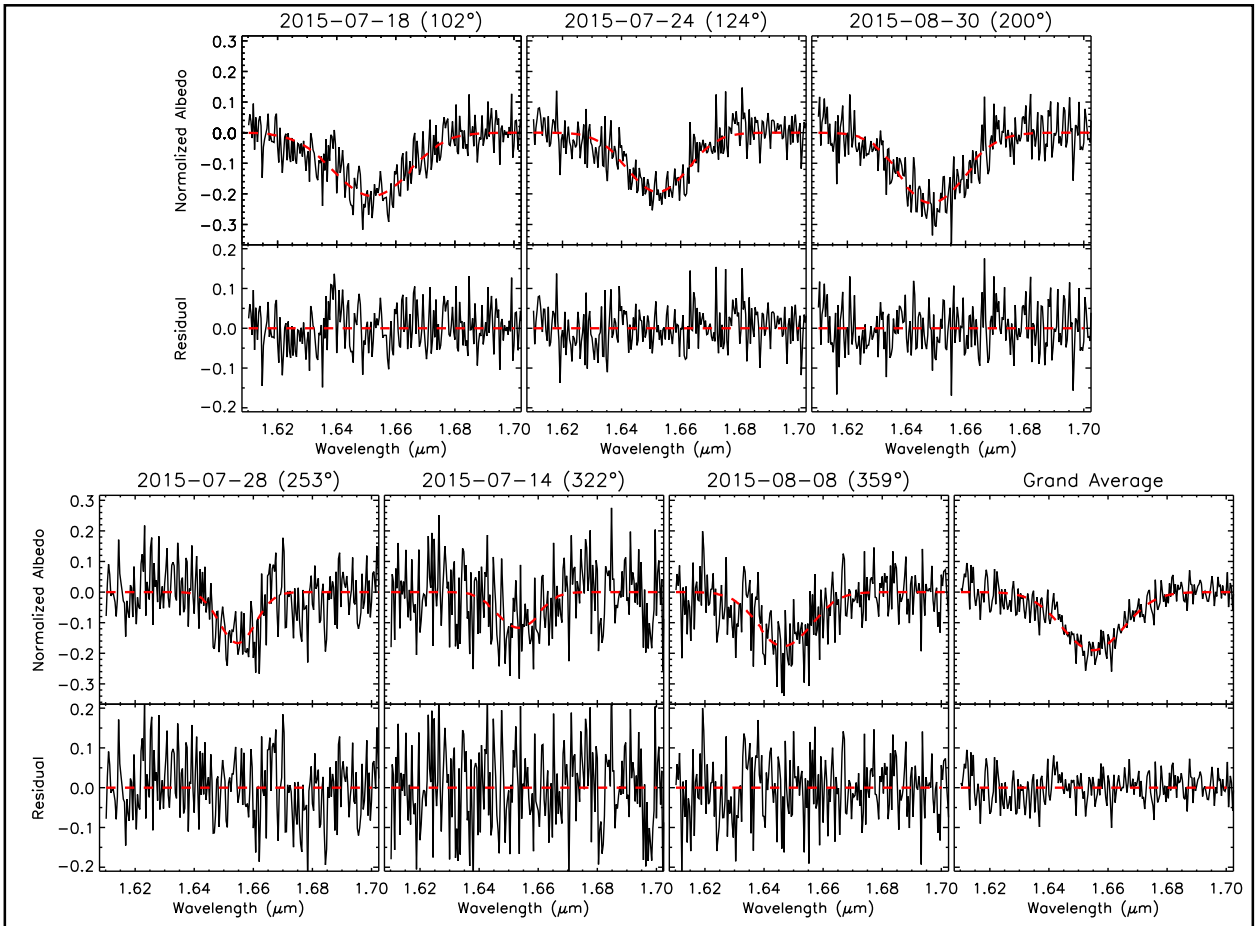

Figure 6: *Top panels in each row*: Gaussian fits (dashed line) to the data for the 1.65 μm crystalline H_2O band. The continuum on either side of the band is centered at zero (see text for explanation). *Bottom panels in each row*: Residuals (data minus model) scattered about zero (dashed line).

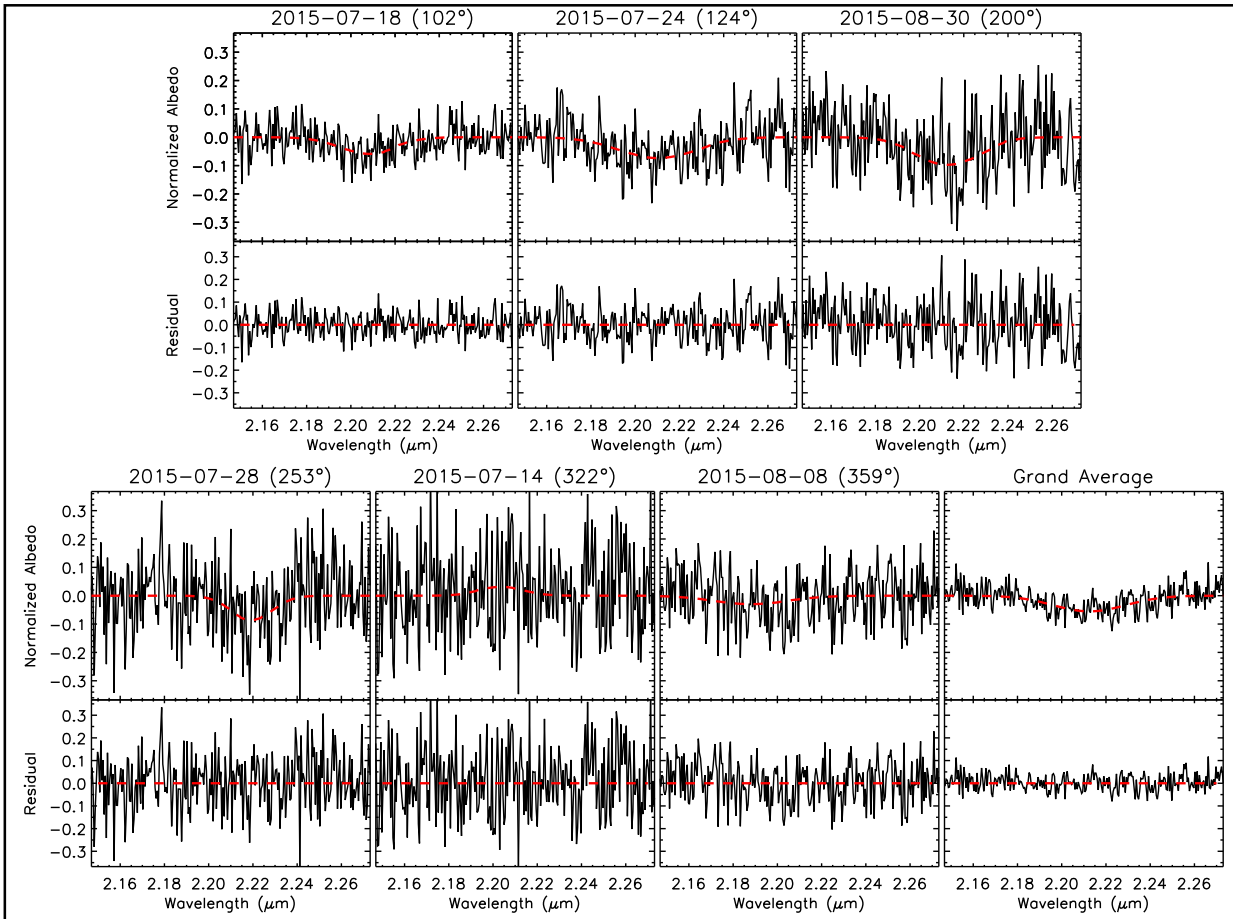

Figure 7: *Top panels in each row*: Gaussian fits (dashed line) to the data for the 2.21 μm ammonia hydrate band. The continuum on either side of the band is centered at zero (see text for explanation). *Bottom panels in each row*: Residuals (data minus model) scattered about zero (dashed line).

Results & discussion

Water ice temperature. The results of the ice temperature calculation from the shift of the 1.65 μm crystalline H_2O band are presented in Fig. 8. The mean surface ice temperature on the observable portion of Charon and its uncertainty, 45±14 K, are represented by horizontal lines. No longitudinal temperature variations were detected on Charon and all temperature measurements are consistent with the grand average value, as expected. The large uncertainties on temperature in this

work are due to a combination of modeling uncertainties in Grundy and Schmitt (1998) and the SNR of the 1D spectra in this work. Summing all the pixels of the Charon aperture within each wavelength bin introduces read noise from each pixel (the Charon aperture was typically 16 pixels in area). Our observations are read noise limited so this is a significant contributor to the noise in the final 1D spectra.

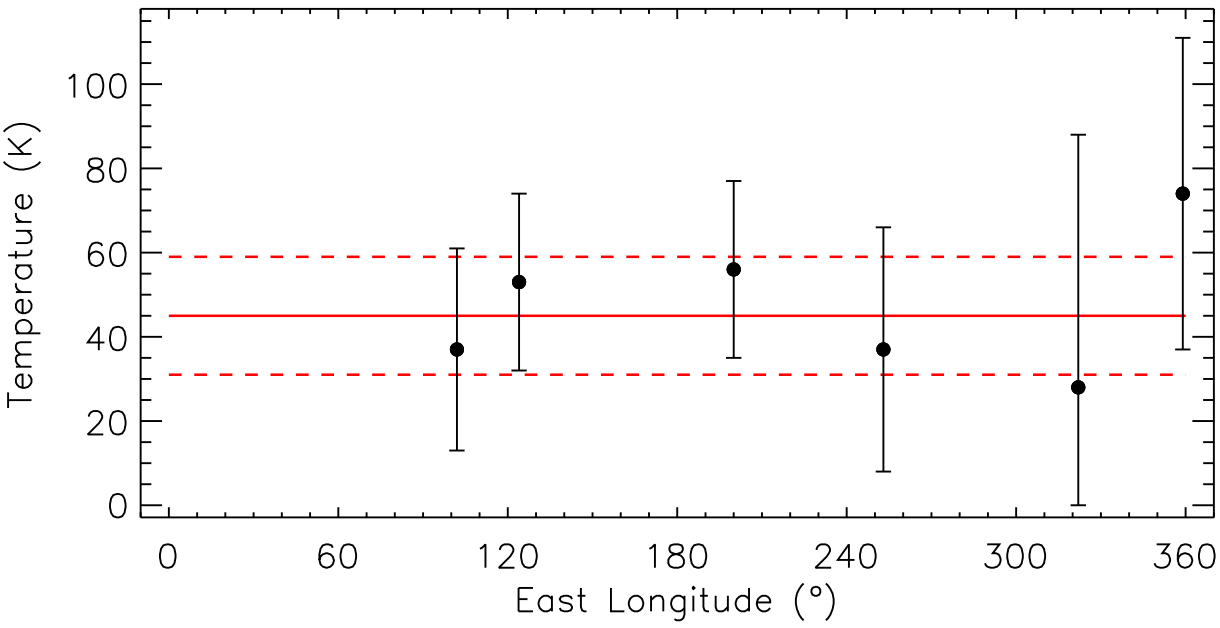

Figure 8: Variation of ice temperature with sub-observer longitude. The solid line represents the mean surface ice temperature on the observable portion of Charon calculated from the grand average spectrum. The dashed lines and error bars are 1-σ uncertainties. Temperature values are truncated at 0 K, resulting in asymmetric error bars for the point at 322° longitude. All night averaged temperature values are consistent with the globally-averaged temperature of 45±14 K.

Our temperature distribution agrees with the results of Cook et al. (2007), who report values of 42.5±10 K on the sub-Pluto hemisphere (270°-90°) and 52.7±10 K on the anti-Pluto hemisphere (90°-270°). Averaging the values from Cook et al. (2007) yields a mean temperature of 47.6±7.1 K, which is in good agreement with

our value of 45±14 K. Our mean ice temperature also agrees with the mean surface temperature of 55.4±2.6 K from Spitzer reported by Lellouch et al. (2011). Comparing our mean ice temperature to thermal measurements and thermophysical modeling, we note that long-wavelength thermal emission is proportional to temperature (Rayleigh-Jeans approximation) so the brightness temperature of 43.7±0.2 K from ALMA (Bryan Butler, personal communication) is directly comparable to, and in good agreement with, our measurement of 45±14 K. Pluto and Charon were unresolved in the Spitzer observations but fully separated in the ALMA observations.

We investigated if this temperature distribution was consistent with the observed visible geometric albedo (p_V) variations across Charon (Buie et al., 2010). For this calculation, we assumed that the ice temperature was proportional to $(1-A)^{1/4}$, where the bolometric Bond albedo, A, is the product of p_V and the phase integral, q. Taking the global geometric albedo to be 0.41 (Buratti et al., submitted) and using a reasonable assumption for the form of the phase integral (q=0.336p_V+0.479; Brucker et al., 2009), we calculate a Bond albedo of 0.25, matching the value reported by Buratti et al. The 8% variation in geometric albedo produces a temperature variation of <1 K across the surface of Charon. From this work, the level of precision on the temperature measurements is not sufficient to rule out these small temperature variations.

Water ice phase. The presence of crystalline water ice on Charon is not in doubt since the 1.65 μm band, unique to the crystalline phase, is clearly detected in

spectra. What is less obvious is the reason why crystalline water ice is present at all, not to mention that it is present in such large quantities (~90%; Cook et al., 2007; Merlin et al., 2010). Conversion of water ice from the crystalline phase to the amorphous phase should take ~1.5 Myr (Cooper et al., 2003), assuming a radiation environment of 1 eV-10 GeV protons and no recrystallization processes. Other authors have suggested that the large quantity of crystalline water ice is due to surface replenishment processes such as cryovolcanism or solid state convection (e.g.: Cook et al., 2007; DeMeo et al., 2015). Due to Charon's small diameter, low density (~1.7 g cm^{-3}), highly circular orbit (e=0.00005), and ancient surface (≥4 Gyr), the most likely sources that would drive these processes, internal and tidal heating, are probably negligible in the present day (Stern et al., 2015). Indeed, no signs of present-day cryovolcanic or solid state convection were noted on Charon's encounter hemisphere (Moore et al., 2016).

Laboratory studies of water ice in its various phases provide a less complicated explanation. Conversion of water ice from the crystalline to the amorphous phase is a reversible process that depends on temperature (Leto and Baratta, 2003; Mastrapa and Brown, 2006; Zheng et al., 2009). These studies used different particles (Lyman-α photons, ions, and electrons, respectively) to bombard samples of crystalline water ice, but the results are comparable since the secondary processes (interactions with electrons and ions produced during previous reactions) are independent of the primary particle and are more important than the identity of the primary particle in altering the state of the water ice (Zheng et al., 2009). The

take away from these experiments is that thermal recrystallization provides a non-negligible balance to irradiation amorphization at temperatures greater than 30 K. After an appropriate amount of time has elapsed (dependent on the temperature) an equilibrium is reached between these two processes and the crystalline-to-amorphous ratio remains constant. Fig. 9 shows that the time needed to reach this equilibrium is less than 1 Gyr for temperatures between 30 and 50 K. Also, the equilibrium ratio of crystalline-to-amorphous water ice is higher at higher temperatures. Zheng et al. (2009) did not quantify the crystalline-to-amorphous ratio explicitly, but instead measured a related quantity, δ, the ratio of the 1.65 μm band depth after irradiation to the band depth prior to irradiation. (This quantity is represented by α in Zheng et al. (2009), but we use δ instead to prevent confusion with other quantities represented by α, such as absorption coefficients. Additionally, we replaced A with B to avoid confusion with bolometric Bond albedo.) We used Eq. 1 from Zheng et al. (2009), $\delta(t)=1-B(1-\exp(-t/k_1))$, where the constants B and k_1 are amplitude and e-folding time, respectively, to construct the curves in Fig. 9. We took the values for B and k_1 at 30 K (B=0.79±0.06, k_1=0.109±0.018 Gyr) and 50 K (B=0.39±0.06, k_1=0.087±0.018 Gyr) from Table 1 of Zheng et al. (2009). The scale factor between irradiation time in the laboratory and actual time on the surface of a KBO is 44 hours per 1.6 Gyr (Cooper et al., 2003; Zheng et al., 2009).

Since thermal recrystallization rates increase with temperature (Zheng et al., 2009), the equilibrium state between crystalline and amorphous water ice will be weighted more toward the maximum temperature reached. We consider Charon as

a fast and slow rotator to calculate the range of maximum temperatures. A fast rotator is an object with a high thermal inertia, meaning that the surface will maintain an elevated temperature for a considerable period following the time of maximum solar insolation (local noon). A slow rotator has a low thermal inertia, resulting in the entirety of the surface in instantaneous equilibrium with incoming solar radiation. For a fast rotator, (e.g., Sicardy et al., 2011), this is near 50-53 K assuming A~0.25 as before, and a beaming parameter of 0.9-0.7. (The beaming parameter takes into account the increased flux from an object at small phase angles, a phenomenon known as the opposition effect.) For Charon as a slow rotator, the maximum temperature would be much higher, 67-71 K, beyond the range of temperatures probed by Zheng et al. (2009). Lellouch et al. (2011) find that Charon is not in instantaneous equilibrium with incoming solar radiation and is therefore not a slow rotator.

Moore et al. (2016) indicate that the youngest surface age on Charon is ~4 Gyr, suggesting that placement of crystalline water ice occurred at this time. It is likely that Charon underwent differentiation following the giant impact that created the system (Canup, 2011) and that water, in some form, was brought to the surface afterwards. Extensional features observed on Charon may be due to a sub-surface ocean that froze, resulting in the eruption of ice onto the surface (Moore et al., 2016). This cryovolcanic period ~4 Gyr ago was likely global in extent since water ice absorption is observed at every longitude on Charon (Grundy et al., 2016).

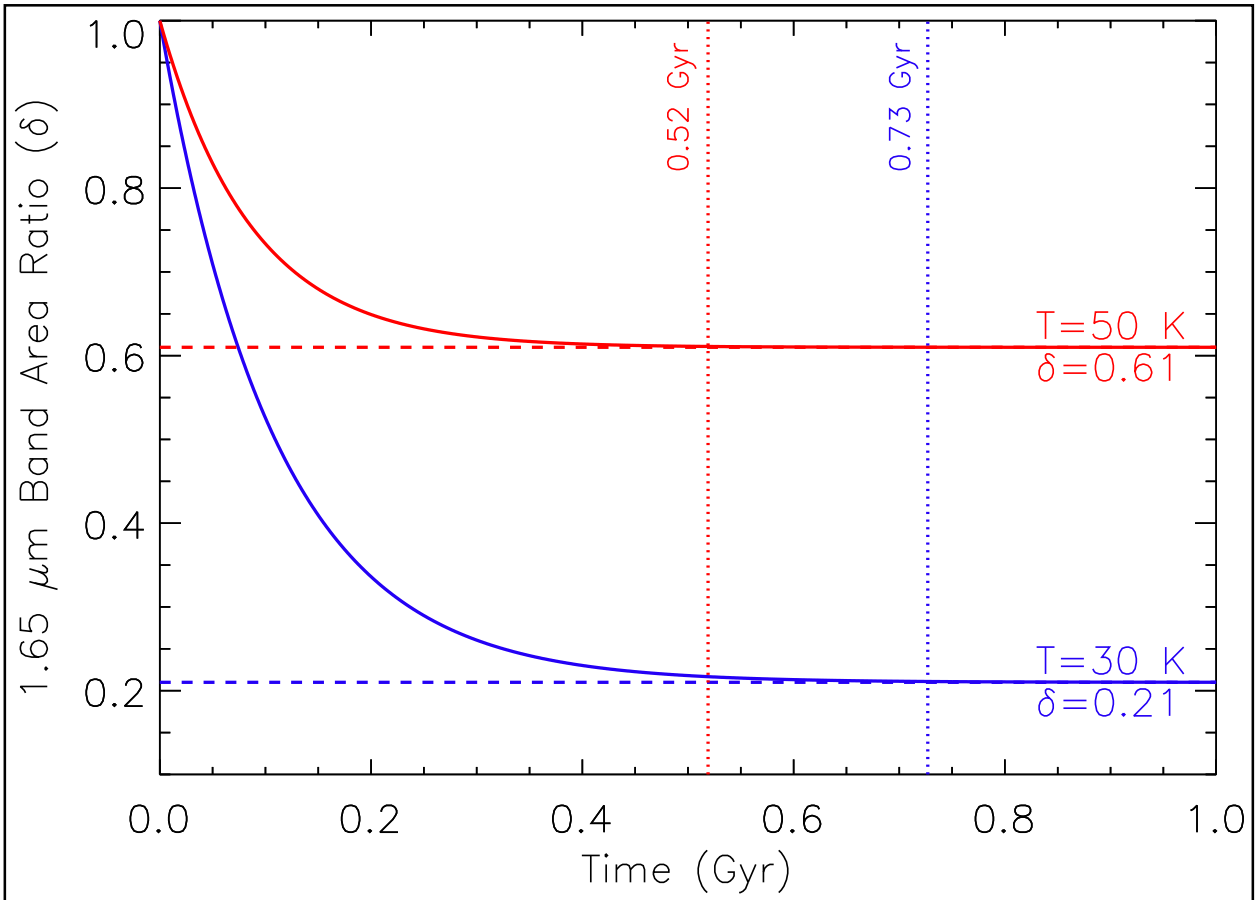

Figure 9: Ratio of the band area after irradiation to the original band area of the 1.65 μm crystalline water ice absorption feature plotted against time (see text for the equation for δ; constants taken from Table 1 of Zheng et al. (2009)). The values of δ presented on the right are the asymptotic values that the curves approach. The vertical dotted lines mark the point in time when the slope has effectively flattened out, corresponding to approximately $6.5k_1$, where k_1 is the *e*-folding time of δ (time required for δ to decrease to $1/e$ of its original value when the sample is exposed to radiation).

Crystalline water ice was detected on the other large KBOs Haumea (Trujillo et al., 2007; Dumas et al., 2011), Orcus (de Bergh et al., 2005), and Quaoar (Fornasier et al., 2004; Jewitt and Luu, 2004). A replenishment mechanism has been invoked to explain the presence of crystalline water ice on each of these bodies. The surface temperatures of these objects are: ≤40 K for Haumea (Merlin et al.,

2007), ≤44 K for Orcus (Barucci et al., 2008), and 44 K for Quaoar (Fraser et al., 2013). It is conceivable that thermal recrystallization is an important process on these KBOs as well. Improved temperature estimates for these bodies would provide vital tests of this theory. Firm detections of crystalline water ice on smaller KBOs, where surface replenishment is unlikely, would further support this theory.

Ammonia hydrate ice. The results of the band-fitting analysis for the 2.21 μm ammonia hydrate absorption band are presented in Fig. 10. Four separate plots are presented: band center, band depth, band FWHM, and band area ($aw\sqrt{2\pi}$) as functions of sub-observer longitude. Grand average values are again presented as horizontal lines in each plot. All quantities are consistent with their respective grand average values, as expected. Note that the plotted points indicate the sub-observer longitude at the time of the observations but the entire visible hemisphere of Charon (sub-observer longitude ± 90°) contributes flux to the spectra. We report the detection of ammonia hydrate on the visible hemispheres centered on the sub-observer longitudes 102°, 124°, and 200°, corresponding to a total detection range of 12° to 290° longitude. Non-detections of ammonia hydrate are reported at the visible hemispheres centered on the sub-observer longitudes 253°, 322°, and 359° (the error bars on the band areas at these sub-observer longitudes, shown in the bottom plot of Fig. 10, extend to 0 μm, suggesting the possibility of no absorption due to ammonia hydrate).

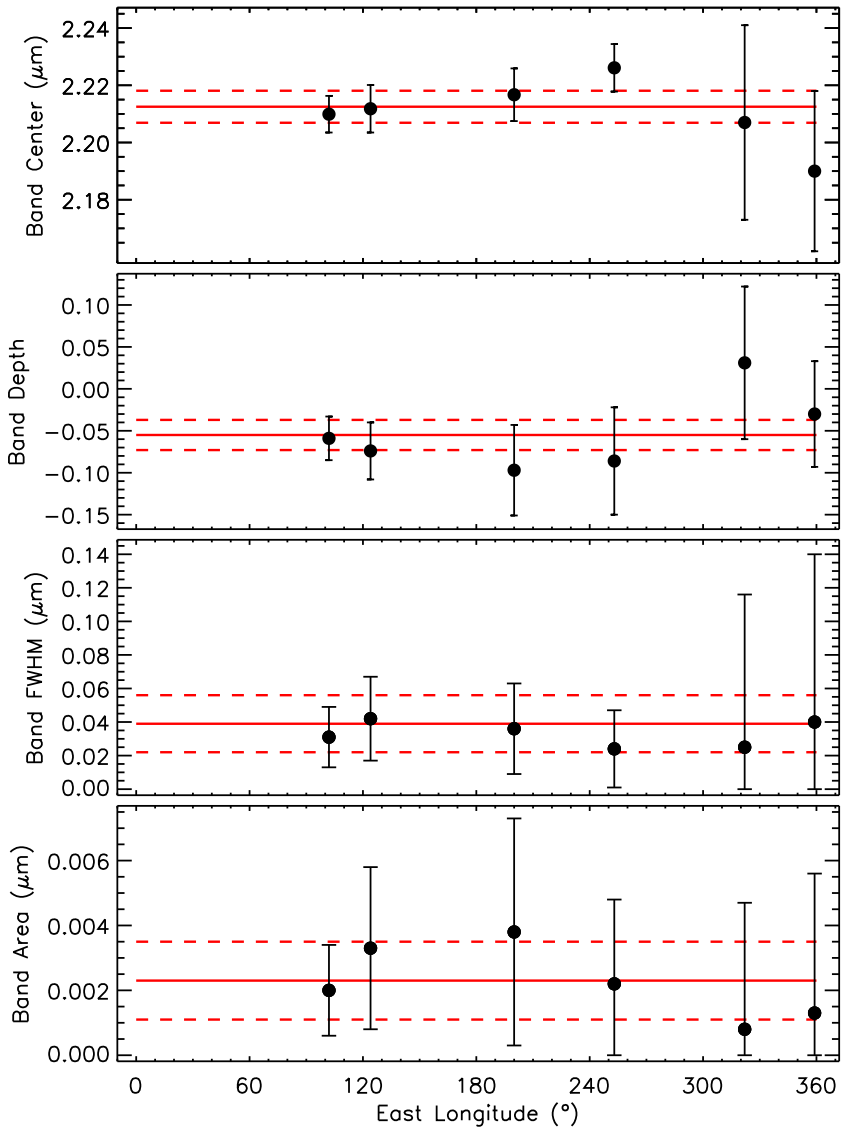

Figure 10: In all panels, the value obtained from fitting the 2.21 μm ammonia hydrate band from the grand average spectrum (Fig. 7) is shown as a solid horizontal line. The dashed lines and error bars represent 1-σ uncertainties. The values for FWHM and band area are truncated at 0 μm, resulting in asymmetric error bars for some points (Table 3). All quantities are consistent with their respective grand average values. *Top panel*: Variation of the 2.21 μm band center with sub-observer longitude. *Top middle panel*: Variation of the 2.21 μm band depth (measured in normalized albedo) with sub-observer longitude. This band depth is measured as the difference between zero and the minimum of the Gaussian, resulting in a negative number. Positive values simply mean that the spectrum was noisy enough to increase the uncertainty on the fit parameters or prevent detection of the absorption feature altogether. *Bottom middle panel*: Variation of the 2.21 μm band full width at half maximum (FWHM) with sub-observer longitude. *Bottom panel*: Variation of the 2.21 μm band area with sub-observer longitude. The band area was calculated as $aw\sqrt{2\pi}$, yielding units of μm.

Fig. 3 from DeMeo et al. (2015) presents the same ammonia hydrate band properties plotted against longitude (except that our band area includes an extra factor of $\sqrt{2\pi}$), and they report statistically significant variations in band center and band depth. We report no statistically significant variations in any of the ammonia hydrate band properties; the higher SNR of their data may be responsible for the discrepancy. Grundy et al. (2016) reported a low level of ammonia at every longitude of the New Horizons encounter hemisphere (~270-60°), with higher concentrations in bright-rayed craters (see Fig. 8c of that paper). Dalle Ore et al. (2016) report uniform distribution and composition of ammonia species across the equatorial region of the encounter hemisphere from New Horizons data. In terms of longitudinal coverage, our results complement the ammonia distribution from New Horizons (Dalle Ore et al., 2016; Grundy et al., 2016), and together they suggest that ammonia is uniformly distributed across the surface of Charon.

The ratio of pure ammonia to its various hydrated states is unknown and we provide no additional constraints because of the difficulty in separating the effects of these different species on the shape of the 2.21 μm band. Ammonia and its various hydrated states absorb at this wavelength, with the hydrates broadening the band (Strazzulla and Palumbo, 1998; Moore et al., 2007); the grand average and most night averaged spectra show a broad absorption feature, requiring the presence of hydrated ammonia (Fig. 4, 5, and 7). The 2.21 μm band depth and band area distributions show no variability, within the error bars, indicating a uniform concentration and/or grain size. Statistically significant differences in band center

across Charon's surface would suggest regional differences in the mixture of ammonia and ammonia hydrates (Strazzulla and Palumbo, 1998; Moore et al., 2007). Since no variation in band center was detected at the spatial resolution of this work, the mixture of ammonia species is assumed to be uniform as well.

The presence of ammonia on Charon is unexpected at first given that a majority of ammonia in the upper ice layers should be destroyed within 20 Myr in a 1 eV-10 GeV proton radiation environment (Cooper et al., 2003; Cook et al., 2007). For crystalline water ice, radiation breaks and reforms the bonds between molecules, thus converting water ice from the crystalline to the amorphous phase. For ammonia ice, the individual molecules are dissociated by radiation and cosmic rays, not undergoing a phase conversion. Although ammonia can also exist in crystalline and amorphous phases, absorption at 2.21 μm is not unique to one phase (Moore et al., 2007). In pure ammonia ice, reforming dissociated ammonia molecules is possible, however, the presence of water molecules hinders this process, and is likely the case on Charon's water ice dominated surface (Moore et al., 2007). Some process is likely renewing ammonia in the surface layers by drawing on a reservoir that is protected from radiation and cosmic rays.

One possibility is the diffusion of ammonia through a thick layer of water ice, a process that also results in the hydration of ammonia (Uras and Devlin, 2000; Livingston et al., 2002). The ammonia may be primordial, contained in the progenitor bodies that collided to form Pluto and Charon (Canup, 2011). Ammonia depresses the freezing point of water and potentially played a role in the

cryovolcanic episode ~4 Gyr ago (Moore et al., 2016). The ammonia in the upper layers would then have been quickly destroyed, but the ammonia further from the surface would have survived. Ammonia on Charon's surface in the present day can be explained by the slow diffusion rate through the upper layers of water ice and by impact gardening. This idea is supported by Fig. 8c from Grundy et al. (2016), which shows a high concentration of ammonia ice correlated with the bright rays of an impact crater, suggesting that sub-surface ammonia was excavated by the impact. Additionally, the heat of the impact may have increased the diffusion rate of ammonia in this localized region. Not all craters with bright rays have higher concentrations of ammonia though, likely because of their different times of formation and the relatively fast dissociation of ammonia molecules. The bright rays would not have enough time to darken prior to the destruction of the ammonia.

Ammonia was positively identified on one other KBO, Orcus (Barucci et al., 2008). Observations of Orcus at different sub-observer longitudes would provide information on the distribution of ammonia across the surface of the KBO. Barucci et al. (2008) only observed Orcus for 100 minutes, or about 8% of its rotation period (Rabinowitz et al., 2007), so the spectra are only from one hemisphere. Ammonia has not been identified on Quaoar, though an absorption feature at 2.21 μm was tentatively associated with CH_4 (Schaller and Brown, 2007b). More extensive observations of Quaoar in the *K* band (~1.9-2.5 μm) are needed to confirm that the 2.21 μm absorption feature is due to CH_4 and not ammonia. Ammonia may be present on Haumea, a KBO with very strong water ice absorption bands, and its

largest moon, Hi'iaka (Barkume et al., 2006). Others argue that ammonia is absent on Haumea (Trujillo et al., 2007; Pinilla-Alonso et al., 2009). Higher SNR spectral observations of Haumea are necessary to determine if ammonia is present at any sub-observer longitude. Haumea also underwent a giant impact at some point in its history, one large enough to remove ice, spin-up the body into an ellipsoid, form two satellites, and create a collisional family in the Kuiper Belt (Brown et al., 2007). Since they all have similar origins, comparison of the surface compositions of Charon, Haumea, and its family members may therefore provide insight into the origin of ammonia on KBOs. In general, spectral observations of small to intermediate-sized KBOs, even if ammonia is not detected, would improve our understanding of the surface processes at work on these bodies.

Summary

Six nights of near-infrared spectral observations of Pluto and Charon were obtained at different sub-observer longitudes between July 14 and August 30, 2015 UT, with the OSIRIS instrument on Keck I. These ground-based spectra have a higher spectral resolution than the LEISA instrument on New Horizons (Reuter et al., 2008; Young et al., 2008), which complements the high spatial resolution data obtained by New Horizons. Charon spectra, uncontaminated by reflected light from Pluto, were extracted from our data. We analyzed the 1.65 μm crystalline water ice and the 2.21 μm ammonia hydrate ice absorption features with the results summarized below:

- The ice temperature on Charon was calculated from the band center shift of the temperature-dependent 1.65 μm crystalline H_2O band (Grundy and Schmitt, 1998). The mean surface ice temperature on the observable portion of Charon, calculated from the grand average spectrum, is 45±14 K. This is consistent with the results of previous work (Cook et al., 2007; Lellouch et al., 2011; Bryan Butler, personal communication). The temperature as a function of longitude shows negligible variation across the surface of Charon and small temperature variations (<1 K) due purely to albedo variations cannot be ruled out at our precision.

- At temperatures ≥30 K, complete amorphization of crystalline water ice does not occur (Leto and Baratta, 2003; Mastrapa and Brown, 2006; Zheng et al., 2009). An equilibrium is reached between irradiation amorphization and thermal recrystallization, and therefore between the crystalline and amorphous water ice phases, between 0.52 and 0.73 Gyr for a surface temperature between 30 and 50 K (Zheng et al., 2009). The maximum surface temperature is likely higher, about 50-53 K for a fast-rotating Charon at its current distance from the Sun. The placement of crystalline water ice on the surface of Charon likely occurred ~4 Gyr ago (Moore et al., 2016), meaning that equilibrium was reached over ~3.5 Gyr ago. We do not believe that cryovolcanism is necessary to explain the presence of crystalline water ice on the surface of Charon.

- Ammonia hydrate was detected between 12° and 290° longitude in this work. Combined with results from New Horizons (Grundy et al., 2016; Dalle Ore et al., 2016), we find that ammonia species on Charon are globally distributed. The longitudinal distributions of the band center, band depth, FWHM, and band area of the 2.21 μm ammonia hydrate absorption feature were found to be uniform. The lack of variability of the band center points to a uniform composition of ammonia species across the surface.

- The presence of ammonia ice everywhere on Charon's surface requires a means of replenishment since it is dissociated on ~20 Myr timescales (Cooper et al., 2003; Cook et al., 2007). Ammonia was likely a primordial component of the progenitor bodies that collided to form Pluto and Charon, and may have played a role in the global cryovolcanic episode ~4 Gyr ago (Moore et al., 2016). Since that time, ammonia has been slowly diffusing its way through the thick overlying layer of water ice and may occasionally be brought to the surface in larger quantities by impacts. This explains the presence of hydrated ammonia and its ubiquity across the surface.

Next-generation telescopes coming online in the 2020s will provide significant improvements in spectral resolution and signal-to-noise, allowing for spectral studies of smaller KBOs. Characterization of the surface compositions of small to intermediate-sized KBOs will further enhance our understanding of how the

various physical and chemical processes shape the surfaces of objects in the Kuiper Belt.

Additional Information on Reduction and Analysis

Data reduction. This section provides a more detailed description of the reduction process for the OSIRIS data. The raw OSIRIS data consisted of 1,019 overlapping spectra on the detector. The first step in the reduction process was to run the data through the OSIRIS Data Reduction Pipeline (Krabbe et al., 2004). The pipeline performs many tasks, including removing cosmic rays, subtracting a bias offset, and correcting dispersion. There is also an option for subtraction of another image, such as a dark frame, prior to image rectification. The primary purpose of the pipeline is to separate the overlapping spectra using a process similar to a Lucy-Richardson deconvolution (Richardson, 1972; Lucy, 1974). This is achieved using rectification matrices, maps of the point spread function of each lenslet at every wavelength, and each combination of filter and plate scale has a unique rectification matrix. The final product of the pipeline is a 3D data cube with two spatial and one spectral dimension. Each 2D image in the data cube corresponds to a different wavelength. We produced two data cubes from each raw file: one by subtracting a master dark frame (the median of 5 individual dark frames) of suitable integration time (dark-subtracted) and one by subtracting the sky image of that set (sky-subtracted).

Following the pipeline reduction, we further reduced the data using an in-house IDL routine to extract 1D Pluto, Charon, and solar analog spectra. All data cubes were reduced following the process outlined below. The first step was to compute the mean of the sky-subtracted 3D data cube in the spectral direction. This collapsed the data cube into a 2D image (Fig. 2, left-hand side). In order to simplify the reduction process, we chose to use the full width at half maximum (FWHM) and centroid positions of Pluto and Charon from the 2D average image. The centroid position was set as the position of the trace and the FWHM as the aperture radius in every image of the data cube. To ensure that this was acceptable, we examined the centroid position of the solar analog in a few Hbb and Kbb data cubes; the maximum deviation of the centroid position from the average within any given cube was about 0.1 pixel. The aperture radii for Pluto, Charon, and the solar analog were different; using the same aperture size for Pluto and Charon would have introduced additional noise into the Charon spectrum. Any pixels not at least partially included in the circular apertures of Pluto or Charon were considered background pixels. The median value of the background pixels in each image was then subtracted from every pixel in the image. The Pluto and Charon fluxes at each wavelength were extracted using the IDL routine *basphote*[12], resulting in a 1D spectrum. The same procedure was followed to extract the 1D spectrum of the solar analog.

[12] The *basphote* IDL routine was written by Marc Buie and performs circular aperture photometry to obtain a flux value for an object in a 2D image. Documentation for *basphote* can be found at *http://www.boulder.swri.edu/~buie/idl/pro/basphote.html*.

We performed our own wavelength calibration using the dark-subtracted sky frames from each set of data cubes. These cubes were collapsed into a 1D spectrum by summing the pixels along both spatial dimensions. A third order polynomial was robustly fit to the 1D spectrum to model the increase in sky glow with increasing wavelength, especially in the *K* band. The polynomial was then subtracted from the spectrum, yielding a flat continuum between the emission lines. The average and standard deviation of the continuum were robustly determined (by removing outliers as in Buie and Bus, 1992) in order to prevent the emission lines from skewing the values. To identify the OH emission lines, a threshold was set at the average of the continuum plus 5 standard deviations. We fit a Lorentzian profile to each group of points above the threshold to determine the centroid of the peak. These values were matched to tabulated vacuum wavelengths of OH emission from Rousselot et al. (2000) to construct a wavelength solution. This procedure was identical for the Pluto/Charon and solar analog data cubes. We used the wavelength solutions from this procedure, as they were nearly identical to the solutions provided by the Data Reduction Pipeline.

Telluric correction. Telluric absorption from water vapor in Earth's atmosphere was corrected for in both *H* and *K* spectra using an iterative method developed in-house and written in IDL. The basic process was to determine the water vapor overburden that best corrected for telluric absorption in the separate Hbb and Kbb solar analog spectra on a nightly basis; we then calculated the transmission spectra at the various airmasses of the individual Charon spectra for

that water vapor overburden. ATRAN models (Lord, 1992) were generated using a web-based input form[13]. These models are synthetic atmospheric transmission spectra that take into account atmospheric absorption primarily from water vapor, but also from trace species such as ozone and methane. The parameters that go into creating the ATRAN models are observatory altitude, observatory latitude, water vapor overburden, number of atmospheric layers, zenith angle, wavelength range, and smoothing resolution. The observatory altitude (13,600 feet for Keck Observatory), observatory latitude (39°, as recommended), number of atmospheric layers (2, as recommended), wavelength range (1.473-2.382 μm), and smoothing resolution (3800) were the same for all ATRAN models. Even though Keck is actually at a latitude of 20°, the instructions recommended setting the latitude to 39°. This value determines the quantity of ozone included in the model and ozone dependence with latitude is negligible compared to diurnal and seasonal variations. ATRAN models were generated by varying the water vapor overburden from 250 μm to 10,000 μm in steps of 250 μm for each value of the zenith angle. The zenith angles (z=cos^{-1}(1/X)) used were those of the solar analog spectra and were calculated from the specified airmass value (X) provided in the data cube FITS headers. The ATRAN atmospheric absorption models were then resampled onto the H and K wavelength grids. Our iterative method, *btellcor*, takes an uncorrected 1D spectrum as an input. From there, it determines the wavelength range of the spectrum and its airmass, then selects the appropriate set (H or K) of resampled ATRAN models.

[13] *http://atran.sofia.usra.edu/cgi-bin/atran/atran.cgi*

The uncorrected spectrum is divided by each model in the set. A line is fit across a region of strong telluric absorption (1.753-1.803 μm for *H* and 2.315-2.377 μm for *K*), with the model that best eliminates telluric absorption determined by calculating the standard deviation of the residuals (data minus model). Because the original ATRAN models were created at a relatively coarse interval of water vapor overburdens (250 μm), the true best fit model may lie in the gaps between ATRAN models. To more accurately determine the best fit water vapor overburden, new ATRAN models are constructed at 10 μm intervals between the ATRAN models bracketing the minimum standard deviation model. The model that best eliminates telluric absorption is then determined in the same manner as described previously.

We assumed a minimal variation in water vapor overburden throughout each 4-5 hour observing session. This assumption was backed up by optical depth measurements from the Caltech Submillimeter Observatory (CSO)[14]; mm of H_2O was calculated by multiplying the optical depth obtained at 225 GHz by 20. Of the 6 observing sessions, the water vapor overburden changed by less than 1 mm for 4 sessions (2015-07-24, 2015-07-28, 2015-08-08, and 2015-08-30 UT), about 1 mm for 1 session (2015-07-18 UT), and 1 night did not have data available (2015-07-14 UT).

Using *btellcor*, the water vapor overburden that best eliminated telluric absorption for each filter/night combination was determined from the average of the 2 A and 1 B spectra of the solar analog obtained at the beginning of the night; the airmass was taken from the B spectrum. We did not aim to determine the true

[14] *http://cso. caltech.edu/tau/*

value of the water vapor overburden, just the value that best corrected the spectrum. ATRAN models were generated using the web-based interface at the determined water vapor overburden and the zenith angle of each Charon spectrum. Each telluric-corrected Charon spectrum was then divided by the appropriate corrected solar analog spectrum to eliminate solar absorption bands.

Geometric albedo scaling. Conversion of relative reflectance to geometric albedo required scaling to a previously published Charon spectrum due to light losses from the Keck AO system. The maximum Strehl ratios for the *H* and *K* bands with NGS are 0.45 and 0.65, respectively[15]; for LGS, the maximum Strehl ratio is 0.39[16]. We used the HST/NICMOS Charon spectrum from Fig. 3 of Buie and Grundy (2000) to anchor our geometric albedo calculation. The average in the relatively flat regions 1.72-1.80 μm (*H* band) and 2.23-2.26 μm (*K* band) were calculated in our grand average spectrum. The *H* spectrum was then multiplied by 0.365 and divided by the *H* average; the *K* spectrum was multiplied by 0.32 and divided by the *K* average. Buie and Grundy (2000) calculated the geometric albedo using a Charon radius of 593 km; Stern et al. (2015) provide a more accurate value of 606 km from New Horizons observations. The *H* and *K* spectra were both scaled by (593 km/606 km)^2 to correct the geometric albedo for the difference in radii (albedo is proportional to the inverse of the square of the radius).

[15] *http://www2.keck.hawaii.edu/optics/ngsao*
[16] *http://www2.keck.hawaii.edu/optics/lgsao/performance.html*

CHAPTER V

CONCLUSIONS AND FUTURE WORK

This thesis examines the surface distributions and temporal evolution of ices on Triton, the distribution of the non-methane hydrocarbon ethane on Pluto, and the temperature and NH_3 distributions on Charon. To do so, near-infrared spectra of Pluto and Triton were obtained over 10+ years with the SpeX instrument on the IRTF and of Charon with the OSIRIS instrument on Keck in the summer of 2015. I wrote a reduction program from scratch to perform spectrophotometry and telluric correction on the Pluto/Charon OSIRIS data. Various techniques were used in the analysis, including longitudinal binning, Hapke modeling, absorption band fitting, and linear and non-linear least squares fitting. I now summarize the results and conclusions of Chapters II, III, and IV in terms of the questions posed on pp. 76.

- ***How are KBO surfaces altered by atmospheric interaction?***
    - Ethane ice is present on both Pluto and Triton in measurable quantities. Because UV photons are primarily absorbed by CH_4 in their atmospheres, creation of ethane is an atmospheric process. By measuring the strength of the 2.405 μm band in both spectra (determined to be due to ethane and not ^{13}CO), the longitudinal distribution of ethane ice was constructed for each body. Ethane is a non-volatile ice and by identifying areas of increased absorption over the time period of years, one can use it as a tracer of volatile transport.

The areas of increased absorption indicate regions of recent volatile sublimation, revealing the underlying non-volatile substrate.

- On Pluto, the longitudes of peak ethane absorption occur in a region noticed to be bright and rich in volatiles in 2002. Formation of ethane in the atmosphere and its slow precipitation should result in a uniform surface distribution in the absence of other factors. The non-uniform distribution that is observed suggests sublimation in these northerly, volatile-rich latitudes between 2002 and 2013 due to the northward migration of the sub-solar point, revealing more of the underlying non-volatile substrate. The inferred albedo change in these regions agrees with the changes observed by comparing older albedo maps of Pluto to the one produced by New Horizons (Buratti et al., 2016).
- On Triton, the low longitudinal variability of ethane and the other non-volatile ices H_2O and CO_2 point to a southern hemisphere significantly depleted in volatile ices. Again, migration of the sub-solar point was invoked to explain these distributions: The sub-solar point reached its most southerly latitude in 2000 after ~50 years in the southern hemisphere. Increased, in some cases constant, solar illumination across the southern hemisphere during this period caused major sublimation of volatile ices, volatile transport, and deposition on colder regions in the northern hemisphere (winter hemisphere). Although Voyager 2 did not carry a near-infrared spectrograph on board, this

result suggests surface changes on Triton over the intervening 3 decades.

- The statistically significant increase in CH_4 ice noticed between 2002 and 2014 on Triton is likely due to changing viewing geometry. The northward migration of the sub-solar point is revealing regions previously in permanent darkness where volatiles were transported and deposited during the long southern summer.

- ***What are the important physical and chemical processes on KBO surfaces?***
  - The relative positions of peak N_2, CO, and CH_4 absorption are similar on both Pluto and Triton. The small sample size may be misleading or this could be a fundamental result based on the relative volatilities and mixing states of these ices. N_2 and CO are fully miscible in one another while N_2 and CH_4 can only mix in small quantities; N_2 and CO have comparable vapor pressures that are 3-4 orders of magnitude higher than the vapor pressure of CH_4. Observations of other large KBOs with likely inventories of these 3 volatile ices, like Eris, Makemake, and Sedna, are necessary to test this hypothesis.
  - Photolysis and radiolysis of CH_4 in the atmospheres of Pluto and Trion are important for the creation of non-methane hydrocarbons, like ethane, and the eventual production of red, dark tholins. Due to their

low albedo, tholins can significantly impact the evolution of surface ice distributions over seasonal and longer timescales. Ethane ice is detected on both Pluto and Triton through the presence of the 2.405 μm absorption band. An isotopologue of carbon monoxide, ^{13}CO, also absorbs at this wavelength but was ruled out on both objects by comparison of the 2.405 μm band and the 1.58 μm CO band distributions. We assumed no mass fractionation of ^{12}CO and ^{13}CO.

- ***What are the likely replenishment mechanisms on KBOs?***
    - Crystalline H_2O is completely converted to amorphous H_2O on the surface of Charon in ~1.5 Myr and NH_3 is destroyed by radiation and cosmic rays in ~20 Myr (Cooper et al., 2003; Cook et al., 2007). Cook et al. (2007) invoked cryovolcanism to explain the presence of crystalline H_2O and NH_3 on Charon and the calculated temperature difference between the anti- and sub-Pluto hemispheres. We detected no statistically significant difference in temperature or NH_3 across Charon's surface. Additionally, New Horizons detected no ongoing plume or geologic activity on Charon.
    - Laboratory work shows that thermal recrystallization and irradiation amorphization reach an equilibrium ~1 Gyr after placement of crystalline water ice on the surface of Charon (e.g., Zheng et al., 2009). Thus the ratio of crystalline and amorphous H_2O remains the same

after this time. This result, combined with the lack of longitudinal variability in temperature and NH_3 abundance, imply that cryovolcanism is not necessary to describe the surface composition of Charon.

- I propose diffusion as the replenishment mechanism for NH_3 in the surface ice of Charon (Uras and Devlin, 2000; Livingston et al., 2002). The lack of detectable longitudinal variability means this process is global in extent. This makes sense in the context of placement of H_2O ice on the surface of Charon: NH_3 depresses the freezing point of H_2O, allowing it to flow at colder temperatures. As the overlying H_2O layer froze, the NH_3 became trapped and is still slowly diffusing to the surface.

On a more general level, studies of the geologic bodies Triton, Pluto, and Charon provide a jumping-off point for something I refer to as "comparative KBOlogy." The phrase "comparative planetology" refers to the study of planets in the context of the larger population, and comparative KBOlogy is my analogous term for KBOs. A better understanding of the objects visited by spacecraft enhances our understanding of the processes at work on the astronomical bodies that can only be studied from afar. This enables trends to become evident among the larger KBO population and provides an opportunity to explain those objects that buck the trend.

For example, comparison of the three geologic bodies shows one case of divergent evolution (Pluto and Charon) and one case of convergent evolution (Triton and Pluto) in terms of surface composition and presence of an atmosphere. The explanation is simple: Pluto and Triton are large enough to retain volatiles and maintain atmospheres while Charon is not (Schaller and Brown, 2007b). By extension, one would expect that Eris, a KBO similar in size to Pluto, would have the same surface composition and also maintain an atmosphere. However, no atmosphere is detected around Eris and only CH_4 has been definitively identified on the surface. In this case, the difference between expectations and observations drives our understanding forward. Eris' high albedo (~0.96, determined from an occultation; Sicardy et al., 2011) and current orbital distance (~98 AU) suggests that the atmosphere has frozen out onto the surface. The lack of N_2 and CO absorption features may be due to N_2 in the α phase (weaker absorption) and the strength of the CH_4 bands obscuring CO absorption. This synthesis of laboratory data, dynamics, near-infrared observations of other KBOs, and occultation data is just one example of the effectiveness of comparative KBOlogy.

Further examples can be found when considering the work performed in this thesis. The analysis of Triton and Pluto spectra confirmed the presence of ethane ice on both surfaces. The only other KBO with a definitive detection of ethane ice is Makemake, an object with very strong CH_4 absorption features (Brown et al., 2007b). Ethane production is an atmospheric process on both Triton and Pluto, but Makemake currently lacks an atmosphere (Sicardy et al., 2010). This

leads to two possible explanations for the presence of ethane on Makemake: (1) Makemake had an atmosphere that collapsed at some point in its orbit or (2) ethane can be formed on the surface as well. If (1) is correct, and Eris' high albedo is due to a collapsed atmosphere, then one could expect to identify ethane on the surface following the restoration of its atmosphere at closer heliocentric distances. The sublimation of volatile ices would reveal the underlying ethane substrate produced during the previous period when Eris maintained an atmosphere. If (2) is the case, one would expect to find ethane on Eris in the present day.

The explanations for the presence of crystalline water ice and ammonia on the surface of Charon have important implications for KBOs of all sizes. Since ongoing cryovolcanism or other high-temperature interior processes are not needed to explain the presence of crystalline H_2O ice in the present day, this ice should be expected on all KBOs large enough for differentiation to occur. Its existence on objects as small as Haumea's satellite Hi'iaka (Barkume et al., 2006) and the minor moons of Pluto (Cook et al., 2016) is possibly explained by ancient giant impacts. However, the presence or absence of NH_3 on KBOs is not as easily explained. Charon and Orcus, two KBOs with strong H_2O absorption features, are the largest KBOs with a definitive detection of NH_3 on their surfaces (Barucci et al., 2008); surprisingly, NH_3 is absent on Haumea, a large object with the strongest H_2O absorption features in the Kuiper Belt (Pinilla-Alonso et al., 2009). It is possible that the giant impact that formed Haumea and its family is responsible, or maybe a

more complicated explanation is required. Detection of NH_3 on other KBOs with H_2O absorption would support the former hypothesis.

Comparative KBOlogy will get a huge boost from the successful launch of the James Webb Space Telescope (JWST), the Large Synoptic Survey Telescope (LSST), and the commissioning of next-generation 20- to 30-meter telescopes like the Thirty Meter Telescope (TMT) and the Giant Magellan Telescope (GMT). JWST, set to launch in October 2018 and begin science operations in, will provide mid-infrared spectra of KBOs to further the search for trace species like non-methane hydrocarbons and nitriles and possibly confirm N_2 on objects like Eris, Makemake, and Sedna (the fundamental absorption feature of N_2 is at 4.25 μm). LSST should see first light in 2019 and is an 8.4-meter optical telescope dedicated to a survey of the entire sky visible from the southern hemisphere. LSST will survey this entire field of view once every 3-4 days, enabling for comparison of images over short timescales to search for new KBOs and characterize their orbits. Large, currently unidentified KBOs may be uncovered by this survey. Next-generation telescopes 2-3 times the diameter of the current largest telescopes will help characterize the surface compositions of dozens more KBOs. This will result in a statistically significant population of KBOs with known compositions, allowing for even stronger conclusions from the study of comparative KBOlogy.

In addition to advances in Earth-based observing facilities, the next few decades will likely see more spacecraft missions to the outer Solar System. A science definition team was put together in early 2016 in order to develop the

framework for an orbiter to either Uranus or Neptune. Such a spacecraft would not launch until the next decade, at the earliest, but the prospect of revisiting Triton with a modern suite of instruments is a tantalizing one. True ground truth observations would be obtained for comparison to years of ground-based observations of Triton, not to mention closer study of other small satellites that could be hiding secrets of their own. In the more immediate future, New Horizons will fly by the very small (~30-45 km in diameter) KBO 2014 MU_{69} on January 1, 2019. This flyby will add one more object to the geologic KBOs and provide a unique look at an extremely small object in the outer Solar System. I am not sure what to expect from this flyby except many new and exciting questions about surface processes on small KBOs. There are also some rumblings about building interest in the planetary science community for another mission to the Kuiper Belt.

In the immediate future, I have a few ongoing KBO projects related to comparative KBOlogy. In Fall 2015 and Spring 2016, I obtained low-resolution near-infrared spectra of the KBOs 2007 OR_{10}, Salacia, 2003 AZ_{84}, and 2004 NT_{33} with the SpeX instrument on the IRTF (Holler et al., 2016c). These spectra will likely be the highest signal-to-noise spectra of these objects ever published and analysis of 2007 OR_{10}'s spectrum should be particularly interesting. This KBO is the third largest known, behind only Pluto and Eris. A tentative detection of CH_4 was made by Brown et al. (2011), but the spectrum had an extremely low signal-to-noise ratio. I look to test this detection and search for other possible surface components such as H_2O, N_2, and CO. Salacia shares orbital parameters with the

Haumea family but previously published observations indicate a lack of H_2O on its surface, disqualifying it from membership in the Haumea family. Again, I look to test this result with my spectra. The other two KBOs, 2003 AZ_{84} and 2004 NT_{33}, have suggestions of water ice on their surfaces, but the near-infrared spectra used were very low signal-to-noise, requiring follow-up observations for confirmation. Future projects include near-infrared spectra of Varuna with IRTF/SpeX to test the detection of CH_4 absorption and the first near-infrared spectra of another large KBO, 2002 MS_4, with Keck/OSIRIS. The background field of this KBO is very crowded, frustrating previous efforts to obtain long-slit spectra; the combined spectral and imaging capabilities of an IFU may be the only way to observe 2002 MS_4 until it moves out of the crowded field. 2002 MS_4 is large enough for differentiation in the past and could be another interesting case study for H_2O and NH_3 ices on KBOs.

I also plan to continue monitoring campaigns of Pluto and Triton with IRTF/SpeX. The current data sets are some of the most important in the study of these two objects, and increasing the time baseline will allow temporal studies to search for seasonal changes. In addition to the IRTF/SpeX observations, I began a program in June 2014 to use matched pairs to search for short-term (1-3 year) changes on Pluto. These matched pairs, obtained at approximately the same sub-observer latitudes and longitudes 14 months apart, eliminate other factors like viewing geometry and rotational phase when trying to detect changes in Pluto's near-infrared spectrum. I have since passed this project off to my undergraduate

student, Maya Yanez, who will be presenting this work at the 2016 DPS meeting (Yanez et al., 2016). This work is incredibly important at this juncture as Pluto continues to move further from perihelion and seasonal changes may be occurring more rapidly. A future project I would like to tackle is imaging of Triton's surface with the Hubble Space Telescope (HST) or JWST to look for albedo changes (indicative of volatile transport) since the Voyager 2 flyby in 1989 and previous HST observations made in 2005 (Bauer et al., 2010). In terms of comparative KBOlogy, Pluto and Triton are the poster children for seasonal surface changes and interpretation of seasonal changes on all other KBOs will proceed from our evolving understanding of these two.

For me, the path forward for the study of KBOs is clear: Identify more KBOs, study more KBO surface compositions with near- and mid-infrared spectra, and draw more conclusions from the population as a whole. In this way, comparative KBOlogy will continue to enhance our understanding of the formation and evolution of the entire Solar System. The Kuiper Belt is the new frontier and larger telescopes, improved instruments, and state-of-the-art spacecraft will enable major discoveries in the decades to come.

REFERENCES

Agnor, C.B., Hamilton, D.P., 2006. Neptune's capture of its moon Triton in a binary-planet gravitational encounter. Nature 441, 192-194.

Alexandersen, M., Gladman, B., Greenstreet, S., Kavelaars, J.J., Petit, J.-M., Gwyn, S., 2013. A Uranian Trojan and the frequency of temporary giant-planet co-orbitals. Science 341, 994-997.

Bagenal, F., Horányi, M., McComas, D.J., and 155 co-authors, 2016. Pluto's interaction with its space environment: Solar wind, energetic particles, and dust. Science 351, id.aad9045.

Barkume, K.M., Brown, M.E., Schaller, E.L., 2006. Water ice on the satellite of Kuiper Belt Object 2003 EL_{61}. ApJ 640, L87-L89.

Barkume, K.M., Brown, M.E., Schaller, E.L., 2008. Near-infrared spectra of Centaurs and Kuiper Belt Objects. AJ 133, 55-67.

Barth, E.L., Toon, O.B., 2003. Microphysical modeling of ethane ice clouds in Titan's atmosphere. Icarus 162, 94-113.

Barucci, M.A., Cruikshank, D.P., Dotto, E., Merlin, F., Poulet, F., Dalle Ore, C., Fornasier, S., de Bergh, C., 2005. Is Sedna another Triton? A&A 439, L1-L4.

Barucci, M.A., Merlin, F., Dotto, E., Doressoundiram, A., de Bergh, C., 2006. TNO surface ices. Observations of the TNO 55638 (2002 VE_{95}) and analysis of the population's spectral properties. A&A 455, 725-730.

Barucci, M.A., Merlin, F., Guilbert, A., de Bergh, C., Alvarez-Candal, A., Hainaut, O., Doressoundiram, A., Dumas, C., Owen, T., Coradini, A., 2008. Surface composition and temperature of the TNO Orcus. A&A 479, L13-L16.

Barucci, M.A., Dalle Ore, C.M., Alvarez-Candal, A., de Bergh, C., Merlin, F., Dumas, C., Cruikshank, D., 2010. (90377) Sedna: Investigation of surface compositional variation. AJ 140, 2095-2100.

Batygin, K., Brown, M.E., 2016. Evidence for a distant giant planet in the Solar System. AJ 151, 22-33.

Bauer, J.M., Roush, T.L., Geballe, T.R., Meech, K.J., Owen, T.C., Vacca, W.D., Rayner, J.T., Jim, K.T.C., 2002. The near infrared spectrum of Miranda: Evidence for crystalline water ice. Icarus 158, 178-190.

Bauer, J.M., Buratti, B.J., Li, J.-Y., Mosher, J.A., Hicks, M.D., Schmidt, B.E., Goguen, J.D., 2010. Direct detection of seasonal changes on Triton with Hubble Space Telescope. ApJL 723, L49-L52.

Benecchi, S.D., Noll, K.S., Grundy, W.M., Levison, H.F., 2010. (47171) 1999 TC_{36}, a transneptunian triple. Icarus 207, 978-991.

Bernstein, G.M., Trilling, D.E., Allen, R.L., Brown, M.E., Holman, M., Malhotra, R., 2004. The size distribution of trans-Neptunian bodies. AJ 128, 1364-1390.

Braga-Ribas, F., Sicardy, B., Ortiz, J.L., and 61 co-authors, 2014. A ring system detected around the Centaur (10199) Chariklo. Nature 508, 72-75.

Broadfoot, A.L., Atreya, S.K., Bertaux, J.L., and 19 co-authors, 1989. Ultraviolet spectrometer observations of Neptune and Triton. Science 246, 1459-1466.

Brown, M.E., Calvin, W.M., 2000. Evidence for crystalline water and ammonia ices on Pluto's satellite Charon. Science 287, 107-109.

Brown, M.E., Trujillo, C., Rabinowitz, D., 2004. Discovery of a candidate inner Oort Cloud planetoid. ApJ 617, 645-649.

Brown, M.E., Trujillo, C.A., Rabinowitz, D., 2005a. 2003 EL_{61}, 2003 UB_{313}, and 2005 FY_9. IAU Circ., No. 8577, #1.

Brown, M.E., Trujillo, C.A., Rabinowitz, D., 2005b. Discovery of a planetary-sized object in the scattered Kuiper Belt. ApJ 635, L97-L100.

Brown, M.E., Barkume, K.M., Ragozzine, D., Shaller, E.L., 2007a. A collisional family of icy objects in the Kuiper belt. Nature 446, 294-296.

Brown, M.E., Barkume, K.M., Blake, G.A., Schaller, E.L., Rabinowitz, D.L., Roe, H.G., Trujillo, C.A., 2007b. Methane and ethane on the bright Kuiper Belt Object 2005 FY9. AJ 133, 284-289.

Brown, M.E., Schaller, E.L., 2007. The mass of dwarf planet Eris. Science 316, 1585.

Brown, M.E., Burgasser, A.J., Fraser, W.C., 2011a. The surface composition of large Kuiper Belt Object 2007 OR10. ApJL 738, L26.

Brown, M.E., Schaller, E.L., Fraser, W.C., 2011b. A hypothesis for the color diversity of the Kuiper Belt. ApJL 739, L60-L64.

Brown, M.E., 2012. The compositions of Kuiper Belt Objects. Annual Review of Earth and Planetary Sciences 40, 467-494.

Brown, M.E., Schaller, E.L., Blake, G.A., 2015. Irradiation products on dwarf planet Makemake. AJ 149, 105.

Brown, R.H., Cruikshank, D.P., Veverka, J., Helfenstein, P., Eluszkiewicz, J., 1995. Surface composition and photometric properties of Triton. In: Cruikshank, D.P. (Ed.), Neptune and Triton. University of Arizona Press, Tucson, pp. 991-1030.

Brown, R.H., Clark, R.N., Buratti, B.J., and 22 co-authors, 2006. Composition and physical properties of Enceladus' surface. Science 311, 1425-1428.

Brozović, M., Showalter, M.R., Jacobson, R.A., Buie, M.W., 2015. The orbits and masses of satellites of Pluto. Icarus 246, 317-329.

Brucker, M.J., Grundy, W.M., Stansberry, J.A., Spencer, J.R., Sheppard, S.S., Chiang, E.I., Buie, M.W., 2009. High albedos of low inclination Classical Kuiper belt objects. Icarus 201, 284-294.

Brunetto, R., Barucci, M.A., Dotto, E., Strazzulla, G., 2006. Ion irradiation of frozen methanol, methane, and benzene: linking to the colors of Centaurs and trans-Neptunian objects. ApJ 644, 646-650.

Buie, M.W., Cruikshank, D.P., Lebofsky, L.A., Tedesco, E.F., 1987. Water frost on Charon. Nature 329, 522-523.

Buie, M.W., Bus, S.J., 1992. Physical observations of (5145) Pholus. Icarus 100, 288-294.

Buie, M.W., Grundy, W.M., 2000. The distribution and physical state of H_2O on Charon. Icarus 148, 324-339.

Buie, M.W., Grundy, W.M., Young, E.F., Young, L.A., Stern, S.A., 2010a. Pluto and Charon with HST I: Monitoring global change and improved surface properties from light curves. AJ 139, 1117-1127.

Buie, M.W., Grundy, W.M., Young, E.F., Young, L.A., Stern, S.A., 2010b. Pluto and Charon with HST II: Resolving changes on Pluto's surface and a map of Charon. AJ 139, 1128-1143.

Burrati, B.J., Goguen, J.D., Gibson, J., Mosher, J., 1994. Historical photometric evidence for volatile transport on Triton. Icarus 110, 303-314.

Buratti, B.J., Hicks, M.D., Dalba, P.A., Chu, D., O'Neill, A., Hillier, J.K., Masiero, J., Banholzer, S., Rhoades, H., 2015. Photometry of Pluto 2008-2014: Evidence of ongoing seasonal volatile transport and activity. ApJL 804, L6.

Burrati, B.J., Hofgartner, J.D., Hicks, M.D., Weaver, H.A., Stern, S.A., Momary, T., Mosher, J.A., Beyer, R.A., Young, L.A., Ennico, K., Olkin, C.B., 2016. Global albedos of Pluto and Charon from LORRI New Horizons observations. arXiv:1604.06129.

Calvin, W.M., Spencer, J.R., 1997. Latitudinal distribution of O_2 on Ganymede: Observations with the Hubble Space Telescope. Icarus 130, 505-516.

Canup, R.M., 2011. On a giant impact origin of Charon, Nix, and Hydra. AJ 141, 35.

Carlson, R.W., Kargel, J.S., Douté, S., Soderblom, L.A., Dalton, J.B., 2007. Io's surface composition. In: Lopes, R.M.C., Spencer, J.R. (Eds.), Io After Galileo: A New View of Jupiter's Volcanic Moon. Springer Praxis Books/Geophysical Sciences, Berlin, Germany, pp.193.

Cartwright, R.J., Emery, J.P., Rivkin, A.S., Trilling, D.E., Pinilla-Alonso, N., 2015. Distribution of CO_2 ice on the large moons of Uranus and evidence for compositional stratification of their near-surfaces. Icarus 257, 428-456.

Chen, F.Z., Wu, C.Y.R., 2004. Temperature-dependent photoabsorption cross sections in the VUV-UV region. I. Methane and ethane. Journal of Quantitative Spectroscopy & Radiative Transfer 85, 195-209.

Cheng, A.F., Weaver, H.A., Conard, S.J., and 13 co-authors, 2008. Long-range reconnaissance imager on New Horizons. Space Science Reviews 140, 189-215.

Chiang, E., Jordan, A., 2002. On the Plutinos and twotinos of the Kuiper belt. AJ 124, 3430-3444.

Chiang, E., Lithwick, Y., Murray-Clay, R., Buie, M., Grundy, W., Holman, M., 2007. A brief history of trans-neptunian space. In: Reipurth, B., Jewitt, D., Keil, K. (Eds.), Protostars and Planets V. University of Arizona Press, Tucson, pp. 895-911.

Choi, Y.-J., Cohen, M., Merk, R., Prialnik, D., 2002. Long-term evolution of objects in the Kuiper Belt zone—Effects of insolation and radiogenic heating. Icarus 106, 300-312.

Christy, J.W., Harrington, R.S., 1978. The satellite of Pluto. AJ 83, 1005-1008.

Clark, R.N., Brown, R.H., Jaumann, R., and 23 co-authors, 2005. Compositional maps of Saturn's moon Phoebe from imaging spectroscopy. Nature 435, 66-69.

Clark, R.N., Cruikshank, D.P., Jaumann, R., and 11 co-authors, 2012. The surface composition of Iapetus: Mapping results from Cassini VIMS. Icarus 218, 831-860.

Cook, J.C., Desch, S.J., Roush, T.L., Trujillo, C.A., Geballe, T.R., 2007. Near-infrared spectroscopy of Charon: Possible evidence for cryovolcanism on Kuiper Belt Objects. ApJ 663, 1406-1419.

Cook, J.C., Young, L.A., Roe, H.G., Young, E.F., Stern, S.A., 2013. Analysis of high-resolution spectra of Pluto: A search for cold gaseous and spatial variation in CH_4 column abundance. Pluto Science Conference, Laurel, MD, 22-26 July 2013.

Cook, J.C., Cruikshank, D.P., Dalle Ore, C.M., and 10 co-authors, 2016. Spectroscopy of Pluto's small satellites. Joint AAS/Division for Planetary Sciences 48/European Planetary Science Congress 11 Meeting Abstracts, #205.03.

Cooper, J.F., Christian, E.R., Richardson, J.D., Wang, C., 2003. Proton irradiation of Centaur, Kuiper Belt, and Oort Cloud objects at plasma to cosmic ray energy. Earth, Moon, and Planets, 92, 261-277.

Croft, S.K., Kargel, J.S., Kirk, R.L., Moore, J.M., Schenk, P.M., Strom, R.G., 1995. The geology of Triton. In: Cruikshank, D.P. (Ed.), Neptune and Triton. University of Arizona Press, Tucson, pp. 879-947.

Cruikshank, D.P., Roush, T.L., Owen, T.C., Geballe, T.R., de Bergh, C., Schmitt, B., Brown, R.H., Bartholomew, M.J., 1993. Ices on the surface of Triton. Science 261, 742-745.

Cruikshank, D.P., Roush, T.L., Moore, J.M., Sykes, M., Owen, T.C., Bartholomew, M.J., Brown, R.H., Tryka, K.A., 1997. The surfaces of Pluto and Charon. In: Stern, S.A., Tholen, D.J. (Eds.), Pluto and Charon. University of Arizona Press, Tucson, pp. 221-267.

Cruikshank, D.P., Schmitt, B., Roush, T.L., Owen, T.C., Quirico, E., Geballe, T.R., de Bergh, C., Bartholomew, M.J., Dalle Ore, C.M., Douté, S., Meier, R., 2000. Water ice on Triton. Icarus 147, 309-316.

Cruikshank, D.P., Mason, R.E., Dalle Ore, C.M., Bernstein, M.P., Quirico, E., Mastrapa, R.M., Emery, J.P., Owen, T.C., 2006. Ethane on Pluto and Triton. Bulletin of the American Astronomical Society 38, 518.

Dalle Ore, C.M., Cook, J.C., Cruikshank, D.P., and 8 co-authors, 2016. Charon's near IR ice signature as seen by New Horizons. 47th LPSC, No. 1903, p. 2122.

Dalton, J.B., Cruikshank, D.P., Clark, R.N., 2012. Compositional analysis of Hyperion with the Cassini Visual and Infrared Mapping Spectrometer. Icarus 220, 752-776.

Davies, J.K., Sykes, M.V., Cruikshank, D.P., 1993. Near-infrared photometry and spectroscopy of the unusual minor planet 5145 Pholus (1992 AD). Icarus 102, 166-169.

Davies, J.K., McFarland, J., Bailey, M.E., Marsden, B.G., Ip, W.-I., 2008. The Early Development of Ideas Concerning the Transneptunian Region. In: Barucci, M.A., Boehnhardt, H., Cruikshank, D.P., Morbidelli, A. (Eds.), The Solar System Beyond Neptune. University of Arizona Press, Tucson, pp. 11-23.

de Bergh, C., Delsanti, A., Tozzi, G.P., Dotto, E., Doressoundiram, A., Barucci, M.A., 2005. The surface of transneptunian object 90482 Orcus. A&A 437, 1115-1120.

Delsanti, A., Jewitt, D., 2006. The solar system beyond the planets. In: Blondel, P., Mason, J. (Eds.), Solar System Update. Springer-Praxis, Germany, 267-294.

DeMeo, F.E., Dumas, C., de Bergh, C., Protopapa, S., Cruikshank, D.P., Geballe, T.R., Alvarez-Candal, A., Merlin, F., Barucci, M.A., 2010. A search for ethane on Pluto and Triton. Icarus 208, 412-424.

DeMeo, F.E., Dumas, C., Cook, J.C., Carry, B., Merlin, F., Verbiscer, A.J., Binzel, R.P., 2015. Spectral variability of Charon's 2.21-μm feature. Icarus 246, 213-219.

Doressoundiram, A., Peixinho, N., de Bergh, C., Fornasier, S., Thébault, P., Barucci, M.A., Veillet, C., 2002. The color distribution in the Edgeworth-Kuiper belt. AJ 124, 2279-2296.

Doressoundiram, A., Boehnhardt, H., Tegler, S.C., Trujillo, C., 2008. Color properties and trends of the transneptunian objects. In: Barucci, M.A., Boehnhardt, H., Cruikshank, D.P., Morbidelli, A. (Eds.), The Solar System Beyond Neptune. University of Arizona Press, Tucson, pp. 91-104.

Douté, S., Schmitt, B., Quirico, E., Owen, T.C., Cruikshank, D.P., de Bergh, C., Geballe, T.R., Roush, T.L., 1999. Evidence for methane segregation at the surface of Pluto. Icarus 142, 421-444.

Dumas, C., Terrile, R.J., Brown, R.H., Schneider, G., Smith, B.A., 2001. Hubble Space Telescope NICMOS spectroscopy of Charon's leading and trailing hemispheres. AJ 121, 1163-1170.

Dumas, C., Carry, B., Hestroffer, D., Merlin, F., 2011. High-contrast observations of (136108) Haumea. A crystalline water-ice multiple system. A&A 528, A105.

Elliot, J.L., Hammel, H.B., Wasserman, L.H., and 11 co-authors, 1998. Global warming on Triton. Nature 393, 765-767.

Elliot, J.L., Kern, S.D., Clancy, K.B., Gulbis, A.A.S., Millis, R.L., Buie, M.W., Wasserman, L.H., Chiang, E.I., Jordan, A.B., Trilling, D.E., Meech, K.J., 2005. The Deep Ecliptic Survey: A search for Kuiper Belt Objects and Centaurs. II. Dynamical classification, the Kuiper Belt plane, and the core population. AJ 129, 1117-1162.

Elliot, J.L., Person, M.J., Gulbis, A.A.S., and 17 co-authors, 2007. Changes in Pluto's atmosphere: 1988-2006. AJ 134, 1-13.

Eluszkiewicz, J., 1991. On the microphysical state of the surface of Triton. JGRS 96, 217-219.

Fornasier, S., Dotto, E., Barucci, M.A., Barbieri, C., 2004. Water ice on the surface of the large TNO 2004 DW. A&A 422, L43-L46.

Fraser, W.C., Trujillo, C., Stephens, A.W., Gimeno, G., Brown, M.E., Gwyn, S., Kavelaars, J.J., 2013. Limits on Quaoar's atmosphere. ApJL 774, L18-L21.

Fray, N., Schmitt, B., 2009. Sublimation of ices of astrophysical interest: A bibliographic review. P&SS 57, 2053-2080.

Gladman, B., Kavelaars, J.J., Petit, J.M., Morbidelli, A., Holman, M.J., Loredo, Y., 2001. The structure of the Kuiper Belt: Size distribution and radial extent. AJ 122, 1051-1066.

Gladman, B., Marsden, B.G., VanLaerhoven, C., 2008. Nomenclature in the Outer Solar System. In: Barucci, M.A., Boehnhardt, H., Cruikshank, D.P., Morbidelli, A. (Eds.), The Solar System Beyond Neptune. University of Arizona Press, Tucson, pp. 43-57.

Gladstone, G.R., Stern, S.A., Ennico, K., and 157 co-authors, 2016. The atmosphere of Pluto as observed by New Horizons. Science 351, id.aad8866.

Goldreich, P., Soter, S., 1966. Q in the Solar System. Icarus 5, 375-389.

Goldreich, P., Lithwick, Y., Sari, R., 2002. Formation of Kuiper-belt binaries by dynamical friction and three-body encounters. Nature 420, 643-646.

Gomes, R.S., 2003. The origin of the Kuiper Belt high-inclination population. Icarus 161, 404-418.

Gomes, R., Levison, H.F., Tsiganis, K., Morbidelli, A., 2005. Origin of the cataclysmic Late Heavy Bombardment period of the terrestrial planets. Nature 435, 466-469.

Grundy, W.M., Schmitt, B., Quirico, E., 1993. The temperature-dependent spectra of α and β nitrogen ice with application to Triton. Icarus 105, 254-258.

Grundy, W.M., Schmitt, B., 1998. The temperature-dependent near-infrared absorption spectrum of hexagonal H_2O ice. JGR 103, 25809-25822.

Grundy, W.M., Stansberry, J.A., 2000. Solar gardening and the seasonal evolution of nitrogen ice on Triton and Pluto. Icarus 148, 340-346.

Grundy, W.M., Buie, M.W., 2001. Distribution and evolution of CH_4, N_2, and CO ices on Pluto's surface: 1995 to 1998. Icarus 153, 248-263.

Grundy, W.M., Schmitt, B., Quirico, E., 2002. The temperature-dependent spectrum of methane ice between 0.7 and 5 μm and opportunities for near-infrared remote thermometry. Icarus 155, 486-496.

Grundy, W.M., Noll, K.S., Stephens, D.C., 2005. Diverse albedos of small trans-Neptunian objects. Icarus 176, 184-191.

Grundy, W.M., Young, L.A., Stansberry, J.A., Buie, M.W., Olkin, C.B., Young, E.F., 2010. Near-infrared spectral monitoring of Triton with IRTF/SpeX II: Spatial distribution and evolution of ices. Icarus 205, 594-604.

Grundy, W.M., Noll, K.S., Nimmo, F., Roe, H.G., Buie, M.W., Porter, S.B., Benecchi, S.D., Stephens, D.C., Levison, H.F., Stansberry, J.A., 2011. Five new and three improved mutual orbits of transneptunian binaries. Icarus 213, 678-692.

Grundy, W.M., Olkin, C.B., Young, L.A., Buie, M.W., Young, E.F., 2013. Near-infrared spectral monitoring of Pluto's ices: Spatial distribution and secular evolution. Icarus 223, 710-721.

Grundy, W.M., Olkin, C.B., Young, L.A., Holler, B.J., 2014. Near-infrared spectral monitoring of Pluto's ices II: Recent decline of CO and N_2 ice absorptions. Icarus 235, 220-224.

Grundy, W.M., Binzel, R.P., Buratti, B.J., and 31 co-authors, 2016a. Surface compositions across Pluto and Charon. Science 351, aad9189.

Grundy, W.M., Cruikshank, D.P., Gladstone, G.R., and 38 co-authors, 2016b. The formation of Charon's red poles from seasonally cold-trapped volatiles. Nature, doi:10.1038/nature19340.

Gulbis, A.A.S., Elliot, J.L., Kane, J.F., 2006. The color of the Kuiper belt core. Icarus 183, 168-178.

Gurrola, E.M., 1995. Interpretation of Radar Data from the Icy Galilean Satellites and Triton. Ph.D. Thesis, Stanford University.

Hahn, J. Malhotra, R., 2005. Neptune's migration into a stirred-up Kuiper belt: A detailed comparison of simulations to observations. AJ 130, 2392-2414.

Hansen, C.J., Paige, D.A., 1992. A thermal model for the seasonal nitrogen cycle on Triton. Icarus 99, 273-288.

Hapke, Bruce, 2012. Theory of Reflectance and Emittance Spectroscopy, Second Edition. Cambridge University Press.

Hendrix, A.R., Vilas, F., Li, J.-Y., 2016. Ceres: Sulfur deposits and graphitized carbon. GRL 43, 8920-8927.

Herbert, F., Sandel, B.R., 1991. CH_4 and haze in Triton's lower atmosphere. JGR: Space Physics Supplement 96, 19241-19252.

Herschel, J., 1846. Le Verrier's planet. The Athenaeum 977, 1019.

Hicks, M.D., Buratti, B.J., 2004. The spectral variability of Triton from 1997-2000. Icarus 171, 210-218.

Hiroi, T., 1994. Recalculation of the isotropic H functions. Icarus 109, 313-317.

Holler, B.J., Young, L.A., Grundy, W.M., Olkin, C.B., Cook, J.C., 2014. Evidence for longitudinal variability of ethane ice on the surface of Pluto. Icarus 243, 104-110.

Holler, B.J., Young, L.A., Grundy, W.M., Olkin, C.B., 2016a. On the surface composition of Triton's southern latitudes. Icarus 267, 255-266.

Holler, B.J., Young, L.A., Buie, M.W., Grundy, W.M., Lyke, J.E., Young, E.F., Roe, H.G., 2016b. Measuring temperature and ammonia hydrate ice on Charon in 2015 from Keck/OSIRIS spectra. arXiv: 1606.05695.

Holler, B.J., Young, L.A., Bus, S.J., Grundy, W.M., Olkin, C.B., Protopapa, S., 2016c. Exploratory spectra of intermediate-sized KBOs with IRTF/SpeX+MORIS. Joint AAS/Division for Planetary Sciences 48/European Planetary Science Congress 11 Meeting Abstracts, #120.17.

Horne, K., 1986. An optimal extraction algorithm for CCD spectroscopy. Publications of the Astronomical Society of the Pacific 98, 609-617.

Horner, J., Evans, N.W., Bailey, M.E., 2004. Simulations of the population of Centaurs – I. The bulk statistics. MNRAS 354, 798-810.

Horner, J., Lykawka, P.S., 2010. The Neptune Trojans – a new source for the Centaurs? MNRAS 402, 13-20.

Houk, N., Smith-Moore, M., 1988. Michigan catalogue of two-dimensional spectral types for the HD stars. In: Declinations -26°.0 to -12°.0, vol. 4. Department of Astronomy, University of Michigan, Ann Arbor, MI.

Houk, N., Swift, C., 1999. Michigan catalogue of two-dimensional spectral types for the HD stars, vol. 5. Department of Astronomy, University of Michigan, Ann Arbor, MI.

Howard, A.D., Moore, J.M., 2008. Sublimation-driven erosion on Callisto: A landform simulation model test. GRL 35, L03203.

Hoyt, William Graves, 1980. Planets X and Pluto. University of Arizona Press, Tucson.

Hudson, R.L., Palumbo, M.E., Strazzulla, G., Moore, M.H., Cooper, J.F., Sturner, S.J., 2008. Laboratory studies of the chemistry of transneptunian object surface materials. In: Barucci, M.A., Boehnhardt, H., Cruikshank, D.P., Morbidelli, A. (Eds.), The Solar System Beyond Neptune. University of Arizona Press, Tucson, pp. 507-523.

Hudson, R.L., Moore, M.H., Raines, L.L., 2009. Ethane ices in the outer Solar System: Spectroscopy and chemistry. Icarus 203, 677-680.

Hudson, R.L., Ferrante, R.F., Moore, M.H., 2014a. Infrared spectra and optical constants of astronomical ices: I. Amorphous and crystalline acetylene. Icarus 228, 276-287.

Hudson, R.L., Gerakines, P.A., Moore, M.H., 2014b. Infrared spectra and optical constants of astronomical ices: II. Ethane and ethylene. Icarus 243, 148-157.

Ingersoll, A.P., 1990. Dynamics of Triton's atmosphere. Nature 344, 315-317.

Jewitt, D., Luu, J., Marsden, B.G., 1992. 1992 QB1. IAU Circ., No. 5611, #1.

Jewitt, D.C., Luu, J., 2004. Crystalline water ice on the Kuiper Belt Object (50000) Quaoar. Nature 432, 731-733.

Johnson, T.V., Lunine, J.I., 2005. Saturn's moon Phoebe as a captured body from the outer Solar System. Nature 435, 69-71.

Johnson, R.E., Oza, A., Young, L.A., Volkov, A.N., Schmidt, C., 2015. Volatile loss and classification of Kuiper Belt Objects. ApJ 809, 43.

Kalas, P., Graham, J.R., Chiang, E., Fitzgerald, M.P., Clampin, M., Kite, E.S., Stapelfeldt, K., Marois, C., Krist, J., 2008. Optical images of an exosolar planet 25 light-years from Earth. Science 322, 1345-1348.

Khare, B.N., Sagan, C., Heinrich, M., Thompson, W.R., Arakawa, E.T., Tuminello, P.S., Clark, M., 1994. Optical constants of Triton tholin: Preliminary results. Bulletin of the American Astronomical Society 26, 1176.

Krabbe, A., Gasaway, T., Song, I., Iserlohe, C., Weiss, J., Larkin, J.E., Barczys, M., Lafreniere, D., 2004. Data reduction pipeline for OSIRIS, the new NIR diffraction-limited imaging field spectrograph for the Keck adaptive optics system. SPIE 5492, 1403-1410.

Krasnopolsky, V.A., Cruikshank, D.P., 1999. Photochemistry of Pluto's atmosphere and ionosphere near perihelion. JGR 104, 21979-21996.

Lacerda, P., Jewitt, D.C., 2007. Densities of Solar System objects from their rotational light curves. AJ 133, 1393-1408.

Lacerda, P., Jewitt, D., Peixinho, N., 2008. High-precision photometry of extreme KBO 2003 EL_{61}. AJ 135, 1749-1756.

Lara, L.M., Ip, W.-H., Rodrigo, R., 1997. Photochemical models of Pluto's atmosphere. Icarus 130, 16-35.

Larkin, J., Barczys, M., Krabbe, A., and 23 co-authors, 2006. OSIRIS: A diffraction limited integral field spectrograph for Keck. SPIE 6269, 42-46.

Lassell, W., 1846. Discovery of supposed ring and satellite of Neptune. MNRAS 7, 157.

Lawler, S.M., Shankman, C., Kaib, N., Bannister, M.T., Gladman, B., Kavelaars, J.J., 2016. A ninth planet would produce a distinctly different distant Kuiper Belt. arXiv: 1605.06575.

Lellouch, E., Laurejis, R., Schmitt, B., Quirico, E., de Bergh, C., Crovisier, J., Coustenis, A., 2000. Pluto's non-isothermal surface. Icarus 147, 220-250.

Lellouch, E., Sicardy, B., de Bergh, C., Käufl, H.-U., Kassi, S., Campargue, A., 2009. Pluto's lower atmosphere structure and methane abundance from high-resolution spectroscopy and stellar occultations. A&A 495, L17-L21.

Lellouch, E., de Bergh, C., Sicardy, B., Ferron, S., Käufl, H.-U., 2010. Detection of CO in Triton's atmosphere and the nature of surface-atmosphere interactions. A&A 512, L8-L13.

Lellouch, E., Stansberry, J., Emery, J., Grundy, W., Cruikshank, D.P., 2011. Thermal properties of Pluto's and Charon's surfaces from Spitzer observations. Icarus 214, 701-716.

Lellouch, E., de Bergh, C., Sicardy, B., Forget, F., Vangvichith, M., Käufl, H.-U., 2015. Exploring the spatial, temporal, and vertical distribution of methane in Pluto's atmosphere. Icarus 246, 268-278.

Leto, G., Baratt, G.A., 2003. Ly-α photon induced amorphization of Ic water ice at 16 Kelvin. A&A 397, 7-13.

Levison, H.F., Duncan, M.J., 1997. From the Kuiper Belt to Jupiter-family comets: The spatial distribution of ecliptic comets. Icarus 127, 13-32.

Levison, H.F., Stern, S.A., 2001. On the size dependence of the inclination distribution of the main Kuiper belt. AJ 121, 1730-1735.

Levison, H.F., Morbidelli, A., Van Laerhoven, C., Gomes, R., Tsiganis, K., 2008. Origin of the structure of the Kuiper belt during a dynamical instability in the orbits of Uranus and Neptune. Icarus 196, 258-273.

Lewis, J.S., 1972. Low temperature condensation from the Solar Nebula. Icarus 16, 241-252.

Licandro, J., Oliva, E., Di Martino, M., 2001. NICS-TNG infrared spectroscopy of trans-neptunian objects 2000 EB173 and 2000 WR106. A&A 373, L29-L32.

Licandro, J., Pinilla-Alonso, N., Pedani, M., Oliva, E., Tozzi, G.P., Grundy, W.M., 2006. The methane ice rich surface of large TNO 2005 FY_9: A Pluto-twin in the trans-neptunian belt? A&A 445, L35-L38.

Livingston, F.E., Smith, J.A., George, S.M., 2002. General trends for bulk division in ice and surface diffusion on ice. The Journal of Physical Chemistry A 106, 6309-6318.

Lord, S.D., 1992. A new software tool for computing Earth's atmospheric transmission of near- and far-infrared radiation. NASA Technical Memorandum 103957.

Lorenzi, V., Pinilla-Alonso, N., Licandro, J., Dalle Ore, C.M., Emery, J.P., 2014. Rotationally resolved spectroscopy of (20000) Varuna in the near-infrared. A&A 562, A85.

Lucy, L.B., 1974. An iterative technique for the rectification of observed distributions. AJ 79, 745-754.

Luu, J.X., Jewitt, D.C., 2002. Kuiper Belt Objects: Relics from the accretion disk of the Sun. Annual Review of Astronomy and Astrophysics 40, 63-101.

Madey, T.E., Johnson, R.E., Orlando, T.M., 2002. Far-out science: Radiation-induced surface processes in the Solar System. Surface Science 500, 838-858.

Malamud, U., Perets, H.B., Schubert, G., 2016. The contraction/expansion history of Charon with implication for its planetary scale tectonic belt. arXiv:1603.00875.

Marcialis, R.L., Rieke, G.H., Lebofsky, L.A., 1987. The surface composition of Charon—Tentative identification of water ice. Science 237, 1349-1351.

Marton, G., Kiss, C., Mueller, T.G., 2016. The moon of the large Kuiper-belt object 2007 OR_{10}. AAS/Division for Planetary Sciences Meeting Abstracts 48, #120.22.

Mastrapa, R.M.E., Brown, R.H., 2006. Ion irradiation of crystalline H_2O-ice: Effect on the 1.65-μm band. Icarus 183, 207-214.

Mastrapa, R.M., Bernstein, M.P., Sandford, S.A., Roush, T.L., Cruikshank, D.P., Dalle Ore, C.M., 2008. Optical constants of amorphous and crystalline H_2O-ice in the near infrared from 1.1 to 2.6 μm. Icarus 197, 307-320.

McKinnon, W.B., Lunine, J.I., Banfield, D., 1995. Origin and evolution of Triton. In: Cruikshank, D.P. (Ed.), Neptune and Triton. University of Arizona Press, Tucson, pp. 807–877.

McKinnon, W.B., Prialnik, D., Stern, S.A., Coradini, A., 2008. Structure and evolution of Kuiper Belt Objects and dwarf planets. In: Barucci, M.A., Boehnhardt, H., Cruikshank, D.P., Morbidelli, A. (Eds.), The Solar System Beyond Neptune. University of Arizona Press, Tucson, pp. 213-241.

McKinnon, W.B., Nimmo, F., Wong, T., and 62 co-authors, 2016. Convection in a volatile nitrogen-ice-rich layer drives Pluto's geological vigour. Nature 534, 82-85.

Merlin, F., Guilbert, A., Dumas, C., Barucci, M.A., de Bergh, C., Vernazza, P., 2007. Properties of the icy surface of the TNO 136108 (2003 EL61). A&A 466, 1185-1188.

Merlin, F., Barucci, M.A., de Bergh, C., DeMeo, F.E., Alvarez-Candal, A., Dumas, C., Cruikshank, D.P., 2010. Chemical and physical properties of the variegated Pluto and Charon surfaces. Icarus 210, 930-943.

Mieda, E., Wright, S.A., Larkin, J.E., Graham, J.R., Adkins, S.M., Lyke, J.E., Campbell, R.D., Maire, J., Do, T., Gordon, J., 2014. Efficiency measurements and installation of a new grating for the OSIRIS spectrograph at Keck Observatory. Publications of the Astronomical Society of the Pacific 126, 250-263.

Moore, J.M., Spencer, J.R., 1990. Koyaanismuuyaw—The hypothesis of a perennially dichotomous Triton. GRL 17, 1757-1760.

Moore, J.M., Asphaug, E., Morrison, D., and 11 co-authors, 1999. Mass movement and landform degradation on the icy Galilean satellites: Results from the Galileo nominal mission. Icarus 140, 294-312.

Moore, J.M., McKinnon, W.B., Spencer, J.R., and 151 co-authors, 2016. The geology of Pluto and Charon through the eyes of New Horizons. Science 351, 1284-1293.

Moore, M.H., Hudson, R.L., 2003. Infrared study of ion-irradiated N_2-dominated ices relevant to Triton and Pluto: formation of HCN and HNC. Icarus 161, 486-500.

Moore, M.H., Ferrante, R.F., Hudson, R.L., Stone, J.N., 2007. Ammonia water ice laboratory studies relevant to outer Solar System surfaces. Icarus 190, 260-273.

Morbidelli, A., 2002. Modern integrations of Solar System dynamics. Annual Review of Earth and Planetary Sciences 30, 89-112.

Morbidelli, A., Levison, H.F., Tsiganis, K., Gomes, R., 2005. Chaotic capture of Jupiter's Trojan asteroids in the early Solar System. Nature 435, 462-465.

Morbidelli, A., Levison, H.F., Gomes, R., 2008. The dynamical structure of the Kuiper belt and its primordial origin. In: Barucci, M.A., Boehnhardt, H., Cruikshank, D.P., Morbidelli, A. (Eds.), The Solar System Beyond Neptune. University of Arizona Press, Tucson, pp. 275-292.

Mousis, O., Chassefière, E., Holm, N.G., Bouquet, A., Waite, J.H., Geppert, W.D., Picaud, S., Aikawa, Y., Ali-Dib, M., Charlou, J.-L., Rousselot, P., 2015. Methane clathrates in the Solar System. Astrobiology 15, 308-326.

Neal, C., Stanger, G., 1983. Hydrogen generation from mantle source rocks in Oman. Earth and Planetary Science Letters 66, 315-320.

Neckel, H., 1986. The "bright stars" with UBV-colors close to those of the Sun. A&A 169, 194-200.

Nesvorný, D., Vokrouhlický, D., 2009. Chaotic capture of Neptune Trojans. AJ 137, 5003-5011.

Noll, K.S., Grundy, W.M., Stephens, D.C., Levison, H.F., Kern, S.D., 2008a. Evidence for two populations of classical transneptunian objects: The strong inclination dependence of classical binaries. Icarus 194, 758-768.

Noll, K.S., Grundy, W.M., Chiang, E.I., Margot, J.-L., Kern, S.D., 2008b. Binaries in the Kuiper Belt. In: Barucci, M.A., Boehnhardt, H., Cruikshank, D.P.,

Morbidelli, A. (Eds.), The Solar System Beyond Neptune. University of Arizona Press, Tucson, pp. 345-363.

Noll, K.S., Parker, A.H., Grundy, W.M., 2014. All bright cold classical KBOs are binary. AAS/Division for Planetary Sciences Meeting Abstracts 46, #507.05.

Olkin, C.B., Young, E.F., Young, L.A., Grundy, W., Schmitt, B., Tokunaga, A., Owen, T., Roush, T., Terada, H., 2007. Pluto's spectrum from 1.0 to 4.2 μm: Implications for surface properties. AJ 133, 420-431.

Olkin, C.B., Young, L.A., Borncamp, D., and 22 co-authors, 2015. Evidence that Pluto's atmosphere does not collapse from occultations including the 2013 May 04 event. Icarus 246, 220-225.

Oort, J.H., 1950. The structure of the cloud of comets surrounding the Solar System and a hypothesis concerning its origin. Bulletin of the Astronomical Institutes of the Netherlands 11, 91-110.

Ortiz, J.L., Sicardy, B., Braga-Ribas, F., and 53 co-authors, 2012. Albedo and atmospheric constraints on dwarf planet Makemake from a stellar occultation. Nature 491, 566-569.

Ortiz, J.L., Duffard, R., Pinilla-Alonso, N., Alvarez-Candal, A., Santos-Sanz, P., Morales, N., Fernández-Valenzuela, E., Licandro, J., Campo Bagatin, A., Thirouin, A., 2015. Possible ring material around centaur (2060) Chiron. A&A 576, A18.

Owen, T.C., Roush, T.L., Cruikshank, D.P., Elliot, J.L., Young, L.A., de Bergh, C., Schmitt, B., Geballe, T.R., Brown, R.H., Bartholomew, M.J., 1993. Surface ices and the atmospheric composition of Pluto. Science 261, 745-748.

Pál, A., Kiss, C., Müller, T.G., Molnár, L., Szabó, R., Szabó, G.M., Sárnecky, K., Kiss, L., 2016. Large size and slow rotation of the trans-Neptunian object (225088) 2007 OR_{10} discovered from Herschel and K2 observations. AJ 151, 117-124.

Parker, A.H., Buie, M.W., Grundy, W.M., Noll, K.S., 2016. Discovery of a Makemakean moon. ApJL 825, L9-L17.

Peixinho, N., Boehnhardt, H., Belskaya, I., Doressoundiram, A., Barucci, M.A., Delsanti, A., 2004. ESO large program on Centaurs and TNOs: Visible colors – final results. Icarus 170, 153-166.

Pike, R.E., Kavelaars, J.J., 2013. On a possible size/color relationship in the Kuiper Belt. AJ 146, 75-79.

Pinilla-Alonso, N., Brunetto, R., Licandro, J., Gil-Hutton, R., Roush, T.L., Strazzulla, G., 2009. The surface of (136108) Haumea (2003 EL_{61}), the largest carbon-depleted object in the trans-Neptunian belt. A&A 496, 547-556.

Pourbaix, D., Tokovinin, A.A., Batten, A.H., Fekel, F.C., Hartkopf, W.I., Levato, H., Morrell, N.I., Torres, G., Udry, S., 2004. $S^9{}_B$: The ninth catalogue of spectroscopic binary orbits. A&A 424, 727-732.

Press, W.H., Teukolsky, S.A., Vetterling, W.T., Flannery, B.P., 2007. Numerical Recipes: The Art of Scientific Computing, Third Edition. Cambridge University Press.

Prokhvatilov, A.I., Yantsevich, L.D., 1983. X-ray investigations of the equilibrium phase diagram of CH_4-N_2 solid mixtures. Soviet Journal of Low Temperature Physics 9, 94-97.

Protopapa, S., Grundy, W.M., Tegler, S.C., Bergonio, J.M., 2015. Absorption coefficients of the methane-nitrogen binary ice system: Implications for Pluto. Icarus 253, 179-188.

Protopapa, S., Grundy, W.M., Reuter, D.C., and 19 co-authors, 2016. Pluto's global surface composition through pixel-by-pixel Hapke modeling of New Horizons Ralph/LEISA data. arXiv: 1604.08468.

Quirico, E., Schmitt, B., 1997a. Near-infrared spectroscopy of simple hydrocarbons and carbon oxides diluted in solid N_2 and as pure ices: Implications for Triton and Pluto. Icarus 127, 354-378.

Quirico, E., Schmitt, B., 1997b. A spectroscopic study of CO diluted in N_2 ice: Applications for Triton and Pluto. Icarus 128, 181-188.

Rabinowitz, D.L., Barkume, K., Brown, M.E., Roe, H., Schwartz, M., Tourtellotte, S., Trujillo, C., 2006. Photometric observations constraining the size, shape, and albedo of 2003 EL61, a rapidly rotating, Pluto-sized object in the Kuiper Belt. ApJ 639, 1238-1251.

Rabinowitz, D.L., Schaefer, B.E., Tourtellotte, S.W., 2007. The diverse solar phase curves of distant icy bodies. I. Photometric observations of 18 trans-Neptunian objects, 7 Centaurs, and Nereid. AJ 133, 26-43.

Rages, K., Pollack, J.B., 1992. Voyager imaging of Triton's clouds and hazes. Icarus 99, 289-301.

Ragozzine, D., Brown, M.E., 2009. Orbits and masses of the satellites of the dwarf planet Haumea (2003 EL61). AJ137, 4766-4776.

Rayner, J.T., Toomey, D.W., Onaka, P.M. Denault, A.J., Stahlberger, W.E., Watanabe, D.Y., Wang, S.-I., 1998. SpeX: A medium-resolution IR spectrograph for IRTF. SPIE 3354, 468-479.

Rayner, J.T., Toomey, D.W., Onaka, P.M. Denault, A.J., Stahlberger, W.E., Vacca, W.D., Cushing, M.C., Wang, S., 2003. SpeX: A medium-resolution 0.8-5.5 micron spectrograph and imager for the NASA Infrared Telescope Facility. Publications of the Astronomical Society of the Pacific 115, 362-382.

Reuter, D.C., Stern, S.A., Scherrer, J., and 17 co-authors, 2008. Ralph: A visible/infrared imager for the New Horizons Pluto/Kuiper Belt mission. Space Science Reviews 140, 129-154.

Richardson, W.H., 1972. Bayesian-based iterative method of image restoration. Journal of the Optical Society of America 62, 55-59.

Rouleau, F., Martin, P.G., 1991. Shape and clustering effects on the optical properties of amorphous carbon. ApJ 377, 526-540.

Rousch, T.L., 1994. Charon: More than water ice? Icarus 108, 243-254.

Rousselot, P., Lidman, C., Cuby, J.-G., Moreels, G., Monnet, G., 2000. Night-sky spectral atlas of OH emission lines in the near-infrared. A&A 354, 1134-1150.

Sagan, C., Khare, B.N., 1979. Tholins—Organic chemistry of interstellar grains and gas. Nature 277, 102-107.

Sasaki, T., Kanno, A., Ishiguro, M., Kinoshita, D., Nakamura, R., 2005. Search for nonmethane hydrocarbons on Pluto. ApJ 618, L57-L60.

Satorre, M.A., Domingo, M., Gomis, O., Luna, R., 2004. The role of laboratory in astrophysics: Laboratory experiments on ices and astrophysical applications. Lecture Notes and Essays in Astrophysics 1, 187-196.

Schaller, E.L., Brown, M.E., 2007a. Detection of methane on Kuiper Belt Object (50000) Quaoar. ApJ 670, L49-L51.

Schaller, E.L., Brown, M.E., 2007b. Volatile loss and retention on Kuiper Belt Objects. ApJ 659, L61-L64.

Schaller, E.L., Brown, M.E., 2008. Detection of additional members of the 2003 EL61 collisional family via near-infrared spectroscopy. ApJL 684, L107-L109.

Schenk, P.M., McKinnon, W., Moore, J., Nimmo, F., Stern, S.A., Weaver, H., Ennico, K., Olkin, C., Young, L., 2015. A large impact origin for Sputnik Planum and surrounding terrains, Pluto? AAS/Division for Planetary Sciences Meeting Abstracts 47, #200.06.

Scott, P.C., Asplund, M., Grevesse, N., Sauval, A.J., 2006. Line formation in solar granulation. VII. CO lines and the solar C and O isotopic abundances. A&A 456, 675-688.

Scott, T.A., 1976. Solid and liquid nitrogen. Physics Reports 27, 89-157.

Sheppard, S.S., Jewitt, D.C., 2002. Time-resolved photometry of Kuiper Belt Objects: Rotations, shapes, and phase functions. AJ 124, 1757-1775.

Sheppard, S.S., Trujillo, C.A., 2006. A thick cloud of Neptune Trojans and their colors. Science 313, 511-514.

Showalter, M.R., Hamilton, D.P., Stern, S.A., Weaver, H.A., Steffl, A.J., Young, L.A., 2011. New satellite of (134340) Pluto: S/2011 (134340) I. IAU Circ., No. 9221, #1.

Showalter, M.R., Weaver, H.A., Stern, S.A., Steffl, A.J. Buie, M.W., Merline, W.J., Mutchler, M.J., Soummer, R., Throop, H.B., 2012. New satellite of (134340) Pluto: S/2012 (134340) I. IAU Circ., No. 9253, #1.

Sicardy, B., Boissel, Y., Colas, F., Doressoundiram, A., Lecacheux, J., Widemann, T., Frappa, E., Bath, K.-L., Beisker, W., Bernard, O., 2008. The Triton stellar occultation of 21 May 2008. EPSC, Münster, Germany, 21-25 September 2008.

Sicardy, B., Colas, F., Maquet, L., and 32 co-authors, 2010. The 2010, February 19 occultation by Varuna. AAS/Division for Planetary Sciences Meeting Abstracts 42, #23.11.

Sicardy, B., Ortiz, J.L., Assafin, M., and 59 co-authors, 2011. A Pluto-like radius and a high albedo for the dwarf planet Eris from an occultation. Nature 478, 493-496.

Slipher, V.M., 1930. Planet X – Lowell Observatory observation circular. JRASC 24, 282-284.

Smith, B.A., Soderblom, L.A., Banfield, D., and 62 co-authors, 1989. Voyager 2 at Neptune: Imaging science results. Science 246, 1422-1449.

Snodgrass, C. Carry, B., Dumas, C., Hainaut, O., 2010. Characterisation of candidate members of (136108) Haumea's family. A&A 511, A72.

Soderblom, L.A., Kieffer, S.W., Becker, T.L., Brown, R.H., Cook II, A.F., Hansen, C.J., Johnson, T.V., Kirk, R.L., Shoemaker, E.L., 1990. Triton's geyser-like plumes: Discovery and basic characterization. Science 250, 410-415.

Standish, E.M., 1993. Planet X – No dynamical evidence in the optical observations. AJ 105, 2000-2006.

Stern, S.A., Trafton, L.M., 2008. On the atmospheres of objects in the Kuiper Belt. In: Barucci, M.A., Boehnhardt, H., Cruikshank, D.P., Morbidelli, A. (Eds.), The Solar System Beyond Neptune. University of Arizona Press, Tucson, pp. 365-380.

Stern, S.A., Bagenal, F., Ennico, K., and 148 co-authors, 2015. The Pluto system: Initial results from its exploration by New Horizons. Science 350, aad1815.

Stern, S.A., Kammer, J.A., Gladstone, G.R., and 12 co-authors, 2016. New Horizons constraints on Charon's present day atmosphere. arXiv:1608.06955.

Stone, E.C., Miner, E.D., 1989. The Voyager 2 encounter with the Neptunian system. Science 246, 1417-1421.

Strazzulla, G., Palumbo, M.E., 1998. Evolution of icy surfaces: An experimental approach. Planetary and Space Science 46, 1339-1348.

Tegler, S.C., Romanishin, W.J., 2000. Extremely red Kuiper-belt objects in near-circular orbits beyond 40 AU. Nature 407, 979-981.

Tegler, S.C., Romanishin, W.J., Consolmagno, S.J., G.J., 2003. Color patterns in the Kuiper belt: A possible primordial origin. ApJ 599, L49-L52.

Tegler, S.C., Grundy, W.M., Romanishin, W., Consolmagno, G.J., Mogren, K., Vilas, F., 2007. Optical spectroscopy of the large Kuiper Belt Objects 136472 (2005 FY9) and 136108 (2003 EL61). AJ 133, 526-530.

Tegler, S.C., Bauer, J.M., Romanishin, W., Peixinho, N., 2008a. Colors of Centaurs. In: Barucci, M.A., Boehnhardt, H., Cruikshank, D.P., Morbidelli, A. (Eds.), The Solar System Beyond Neptune. University of Arizona Press, Tucson, pp. 105-114.

Tegler, S.C., Grundy, W.M., Vilas, F., Romanishin, W., Cornelison, D.M., Consolmagno, G.J., 2008. Evidence of N_2-ice on the surface of the icy dwarf planet 136472 (2005 FY9). Icarus 195, 844-850.

Tegler, S.C., Cornelison, D.M., Grundy, W.M., Romanishin, W., Abernathy, M.R., Bovyn, M.J., Burt, J.A., Evans, D.E., Maleszewski, C.K., Thompson, Z., Vilas, F., 2010. Methane and nitrogen abundances on Pluto and Eris. ApJ 725, 1296-1305.

Tegler, S.C., Grundy, W.M., Olkin, C.B., Young, L.A., Romanishin, W., Cornelison, D.M., Khodadadkouchaki, R., 2012. Ice mineralogy across and into the surfaces of Pluto, Triton, and Eris. ApJ 751, 76.

Tennyson, Jonathan, 2011. Astronomical Spectroscopy: An Introduction to the Atomic and Molecular Physics of Astronomical Spectra, 2nd Edition. World Scientific Publishing.

Tholen, D.J., Buie, M.W., Grundy, W.M., Elliott, G.T., 2008. Masses of Nix and Hydra. AJ 135, 777-784.

Tiscareno, M.S., Malhotra, R., 2003. The dynamics of known Centaurs. AJ 126, 3122-3131.

Trafton, L., 1984. Large seasonal variations in Triton's atmosphere. Icarus 58, 312-324.

Trujillo, C.A., Brown, M.E., 2001. The radial distribution of the Kuiper Belt. ApJ 554, L95-L98.

Trujillo, C.A., Brown, M.E., 2002. A correlation between inclination and color in the classical Kuiper belt. ApJ 556, L125-L128.

Trujillo, C.A., Brown, M.E., Barkume, K.M., Schaller, E.L., Rabinowitz, D.L., 2007. The surface of 2003 EL_{61} in the near-infrared. ApJ 655, 1172-1178.

Trujillo, C.A. Sheppard, S.S., Schaller, E.L., 2011. A photometric system for detection of water and methane ices on Kuiper Belt Objects. ApJ 730, 105-117.

Trujillo, C., Sheppard, S.S., 2014. A Sedna-like body with a perihelion of 80 astronomical units. Nature 507, 471-474.

Tryka, K.A., Brown, R.H., Anicich, V., Cruikshank, D.P., Owen, T.C., 1993. Spectroscopic determination of the phase composition and temperature of nitrogen ice on Triton. Science 261, 751-754.

Tryka, K.A., Brown, R.H., Cruikshank, D.P., Owen, T.C., Geballe, T.R., de Bergh, C., 1994. Temperature of nitrogen ice on Pluto and its implications for flux measurements. Icarus 112, 513-527.

Tsiganis, K., Gomes, R., Morbidelli, A., Levison, H.F., 2005. Origin of the orbital architecture of the giant planets of the Solar System. Nature 435, 459-461.

Tyler, G.L., Sweetnam, D.N., Anderson, J.D., Borutzki, S.E., Campbell, J.K., Kursinski, E.R., Levy, G.S., Lindal, G.F., Lyons, J.R., Wood, G.E., 1989. Voyager radio science observations of Neptune and Triton. Science 246, 1466-1473.

Uras, N., Devlin, J.P., 2000. Rate study of ice particle conversion to ammonia hemihydrate: Hydrate crust nucleation and NH_3 diffusion. The Journal of Physical Chemistry A 104, 5770-5777.

Veillet, C., Parker, J.M., Griffin, I., Marsden, B., Doressoundiram, A., Buie, M., Tholen, D.J., Connelley, M., Holman, M.J., 2002. The binary Kuiper-belt object 1998 WW_{31}. Nature 416, 711-713.

Verbiscer, A.J., Peterson, D.E., Skrutskie, M.F., Cushing, M., Helfenstein, P., Nelson, M.J., Smith, J.D., Wilson, J.C., 2006. Near-infrared spectra of the leading and trailing hemispheres of Enceladus. Icarus 182, 211-223.

Verbiscer, A.J., Peterson, D.E., Skrutskie, M.F., Cushing, M., Nelson, M.J., Smith, J.D., Wilson, J.C., 2007. Simultaneous spatially-resolved near-infrared spectra of Pluto and Charon. LPSC 38, 2318.

Vetter, M., Jodi, H.-J., Brodyanski, A., 2007. From optical spectra to phase diagrams—The binary mixture N_2-CO. Low Temperature Physics 33, 1052-1060.

Weaver, H.A., Stern, S.A., Mutchler, M.J., Steffl, A.J., Buie, M.W., Merline, W.J., Spencer, J.R., Young, E.F., Young, L.A., 2006. Discovery of two new satellites of Pluto. Nature 439, 943-945.

Wong, M.L., Fan, S., Gao, and 12 co-authors, 2017. The photochemistry of Pluto's atmosphere as illuminated by New Horizons. Icarus, in press.

Yanez, M.D., Holler, B.J., Young, L., Chanover, N.J., Olkin, C.B., 2016. Search for short-term temporal evolution of Pluto's surface. Joint AAS/Division for Planetary Sciences 48/European Planetary Science Congress 11 Meeting Abstracts, #224.15.

Young, L.A., 2008. New Horizons: Anticipated scientific investigations at the Pluto system. Space Science Reviews 140, 93-127.

Young, L.A., 2013. Pluto's seasons; New predictions for New Horizons. ApJL 766, L22.

Zahnle, K., Schenk, P., Levison, H., Dones, L., 2003. Cratering rates in the outer Solar System. Icarus 163, 263-289.

Zangari, A., 2015. A meta-analysis of coordinate systems and bibliography of their use on Pluto from Charon's discovery to the present day. Icarus 246, 93-145.

Zheng, W., Jewitt, D., Kaiser, R.I., 2009. On the state of water ice on Saturn's moon Titan and implications to icy bodies in the outer Solar System. The Journal of Physical Chemistry A 113, 11174-11181.